National Science Foundation ATM-8814913
Department of Energy DE-FG02-90ER61066

CONVECTIVE PARAMETERIZATION IN MESOSCALE MODELS

by Michael J. Weissbluth

William R. Cotton, P.I.

Colorado State University

DEPARTMENT OF ATMOSPHERIC SCIENCE

PAPER NO. 486

CONVECTIVE PARAMETERIZATION IN MESOSCALE MODELS

by

Michael J. Weissbluth

Department of Atmospheric Science

Colorado State University

Fort Collins, CO 80523

Research Supported by

National Science Foundation

under grant ATM-8814913

and

Department of Energy

under grant DE-FG02-90ER61066

October 28, 1991

Atmospheric Science Paper No. 486

ABSTRACT

CONVECTIVE PARAMETERIZATION IN MESOSCALE MODELS

Currently, there is no adequate cumulus parameterization that is suitable for use in mesoscale models having horizontal resolutions between five and fifty kilometers. Based on the similarity of the temporal and spatial evolution of the vertical variances between a CCOPE supercell and a generic tropical squall line as explicitly simulated by the Colorado State University Regional Atmospheric Modeling System (CSU RAMS), a modified second order closure scheme has been developed which allows the prediction of deep convective fluxes. The Mellor and Yamada 2.5 level closure has been modified to predict solely on $\overline{w'w'}$ using Zeman and Lumley's formulation of the buoyancy-driven mixed layer to close the pressure terms and the eddy-transport term. The extension to the free atmosphere has been accomplished by representing the deep cumulus fluxes as proportional to the difference between a cloud model derived property and the environmental value. This cloud model has been calibrated and generalized by comparisons with conditionally sampled data from the two explicitly simulated storms.

The deep cumulus tendencies of heat, moisture and hydrometeors are specified by a mesoscale compensation term and a convective adjustment term. As above, the convective adjustment term is specified as the difference between a cloud model derived property and its environmental value, but is modulated by a time scale determined by an integrated value of $\overline{w'w'}$. The mesoscale compensation term is a product of the vertical gradient of the appropriate scalar and a constant determined through a moist static energy balance.

One unique feature of this approach is that the parameterization is not simply a local grid column scheme; $\overline{w'w'}$ is transported by the turbulence as well as the mean horizontal and vertical winds. Thus, the scheme responds to shear and is more global in nature than current cumulus parameterizations. Furthermore, the scheme provides explicit cumulus source functions for all hydrometeor species. Results of an explicit simulation of two dimensional sea-breeze convection over the Florida peninsula will be compared to simulations on coarser grids using the generalized cumulus parameterization.

ACKNOWLEDGEMENTS

I would like to express sincere thanks and gratitude to several people who aided significantly during the course of this research. Dr. William Cotton, my advisor, provided the initial impetus for this research (whether this was good or bad has yet to be determined!), and lent invaluable guidance, advice and patience. Committee member David Randall is thanked for useful and enlightening conversations on the nature of this problem, as are the other committee members Drs. Wayne Schubert and Bogusz Bienkiewicz.

Dr. Greg Tripoli is acknowledged for many valuable discussions and advice in the early years of this research effort. Drs. Craig Tremback and Robert Walko also contributed valuable insight on this topic and help in negotiating the numerical modeling maze that is the CSU-RAMS. Further discussions and help from the rest of the Cotton gang is also recognized.

Finally, I am indebted to my friends and family who supported me during the depressing times and celebrated with me during the happy times. In particular, my parents gave unwavering and much appreciated support during the somewhat convoluted path from the Applied and Engineering Physics program at Cornell University to the Atmospheric Science program at Colorado State University.

Brenda Thompson is thanked for her help in preparing this manuscript. Some figures were drafted by Lucy McCall. Much of the computing was performed at the National Center for Atmospheric Research (NCAR) which is supported by the National Science Foundation. This research was funded by the National Science Foundation under grant ATM-8814913 and the Department of Energy under grant DE-FG02-90ER61066.

TABLE OF CONTENTS

LIST OF FIGURES

LIST OF TABLES

Chapter 1

INTRODUCTION

The primitive equations characterize all scales of motion within the atmosphere. These scales include large scale planetary Rossby waves to small scale microscopic turbulence. When numerically integrating the primitive equations, it is not practical to consider all of these scales of motion and thus several simplifying assumptions are invoked. One such assumption involves partitioning the dynamic, thermodynamic and microphysical variables into a resolved component and a fluctuating or turbulent component. The fluctuating or turbulent component is usually ensemble averaged or grid-volume averaged and is referred to as turbulence even though it may represent eddies thousands of kilometers in scale when the averaging operator is applied to large scales of motion. Of course, there is no explicit information included in the numerical model about turbulent processes, therefore, the parameterization problem can be thought of as expressing the unresolved small scale processes in terms of the resolved large scale variables. The grid-volume averaged component represents all of those physical processes occurring on scales smaller than the grid spacing in the numerical model. The ensemble averaging operator can, in principal, include scales of motion larger than the grid spacing, thus moving some of the normally resolved processes from the resolved grid. In theory, this may result in the physical process being both resolved and parameterized (double-counted); in practice the parameterization is generally robust and prohibits the physical process from appearing on the resolvable grid (Cotton, personal communication).

The small scale processes that are represented in the primitive equations depend on the motions that are resolved in the numerical model. For example, explicit simulations of eddies in the planetary boundary layer (PBL) might necessitate a numerical grid with a

100 m grid spacing. Eddies having horizontal dimensions less than about 200 m would have to be parameterized. Similarly, a regional scale simulation over Colorado's Front Range would require a 25 km grid thus forcing parameterization of all the scales of motion below around 50 km. While those sub-grid scale motions that occur in the PBL simulation technically need to be modeled in the Colorado simulation, other larger scale motions such as cumulus convection may dominate. In fact, when present, cumulus convection is the dominant transporter of heat, momentum and moisture. Therefore, unless the horizontal grid scale of the numerical model is less than 1 km so that the cumulus eddies can be explicitly resolved, the effect of cumulus must be implicitly included through its parameterization.

There is of yet no general scheme for parameterizing cumulus convection. That is to say that the scheme used to represent the cumulus convection on a regional scale grid will not function on a larger synoptic scale grid and *vice versa*. This is due to the assumptions that relate the convection to the resolved variables. The present cumulus parameterization schemes based upon a general classification of the scales of atmospheric motion first proposed by Ooyama (1982) and discussed by Frank (1983) will be stratified. This classification is based upon the Rossby radius of deformation $R_o = NH/f_o$ where N is the Brunt-Väisälla frequency, H is a scale height and f_o is the Coriolis parameter. Frank extended this to include the dynamic effects of rotation so that the dynamic Rossby radius of deformation becomes $R' = NH/\sqrt{(\zeta + f_o)(2V/R + f_o)}$ where ζ is the relative vorticity and V/R represents the solid body rotation of the system. NH is the phase speed of an internal gravity wave while $\frac{1}{\sqrt{(\zeta+f_o)(2V/R+f_o)}}$ is the time scale over which gradient balance occurs. This is similar to the time scale $\frac{1}{f_o}$ over which geostrophic balance occurs in systems where only the rotation of the earth is considered.

Therefore, if gravity waves are created by heating the atmosphere, for example, R' is simply a measure of the length scale that a gravity wave will travel before gradient balance occurs. The process can be envisioned as follows: A steady heat source disrupts the mass field and the atmosphere responds to this impulse through the excitation of a gravity wave (Bretherton and Smolarkiewicz, 1989; Nicholls *et al.* , 1991b). This wave of adjustment includes only subsident motions since the heat source does not decay, and propagates away from the disturbance. If the heat source decays to zero, then another wave of adjustment propagates from the disturbance with an equal but opposite amplitude to the initial subsident wave. Pulsing convection, then, will launch a family of gravity waves whose horizontal wavelength is proportional to the time between pulses.

The horizontal scale of the disturbance, L as compared to R' determines whether this gravity wave energy is incorporated into a balanced circulation. When $L \geq R'$, the system is balanced since the gravity wave energy excited by the heating will be in the system long enough so that gradient balance ensues. As gradient adjustment occurs, additional subsidence is forced as the mass field adjusts to the newly formed wind field. This subsidence becomes stronger as more gravity wave energy is trapped within the balanced circulation and probably interacts with the transient gravity wave motions directly associated with pulsing convection. Conversely, when $L < R'$, the system is unbalanced because the gravity waves excited by the heating escape the system before gradient balance can occur. If L falls much below 10 km, the system becomes probabilistic rather than deterministic.

1.1 Models resolving only the balanced flow

When the horizontal scale of the circulation L is comparable to or larger than R', then the motions are quasi-geostrophic or quasi-gradient. This implies that only these balanced circulations are resolved by numerical models having horizontal grid sizes of the same order as R'. Haltiner and Williams (1980) and Shapiro and Willoughby (1982) have shown that dynamically large circulations respond to heating by the adjustment of the rotational component of the wind. Vertical motions arising through divergence are small and are a result of the geostrophic or gradient adjustment process. This effectively isolates the convection from modulating the large scale divergence and insures a scale separation between the cumulus convection and the large scale forcing. There is then a sound basis for the parameterization since the resolved forcing remains relatively constant during convective episodes.

Parameterization schemes for the models resolving only the balanced flow seek to represent a statistically steady-state population of clouds because the grid size is large.

This allows the consideration of a large number of clouds, each undergoing its own growth, maturation and decay process. The parameterization problem then reduces to quantifying the average effect of this ensemble of clouds on the environment.

There are several schemes designed for the balanced flow regime. They are mainly intended for general circulation models (GCMs) since the several hundred kilometer grid spacing insures that the eddies resolved by the model are primarily the balanced circulations. The schemes are based upon either large scale convergence of mass and/or moisture or an equilibrium assumption.

The moist convective adjustment scheme (Manabe *et al.* , 1965) and the Arakawa and Schubert scheme (1974) both rely on the fact that convection acts to modify a conditionally unstable atmosphere toward some equilibrium state at a specified rate. A class of scheme first proposed by Kuo (1965) assumes that convection is related to the large scale moisture convergence. These three schemes form the basis for what is available for the GCM modeler and their performance is evaluated by Krishnamurti *et al.* (1980).

1.2 Models resolving both the balanced and unbalanced flow

As the dimensions of the system and the numerical grid shrink below R', the difficulty in parameterizing cumulus convection increases. This is because in dynamically small circulations, significant divergent circulations result as the mass field adjusts to the wind field. Stated differently, the gravity waves generated as the convection perturbs the mass field radiate outward and perturb the divergent component of the wind. This greatly complicates the parameterization problem since the convection responds to both the perturbed and ambient divergent wind component, *i. e.* the cumulus modulates itself. This is in contrast to the models resolving only the balanced flow where the divergent circulations result only from the slowly changing quasi-horizontal motions. The scale separation present in the balanced flow regime narrows considerably, thus blurring the relationships between the forcing and the convective response. Furthermore, since a balanced circulation does not develop within the scale of the disturbance, the transient gravity wave response from the convection may have to be captured. The timing as well as the magnitude and vertical distribution of the latent heat release then becomes important.

Furthermore, as the grid resolution decreases, there can no longer be a population of clouds which exist within the grid-box; indeed only part of one cell may be captured. Therefore the parameterization problem in mesoscale models reduces to specifying the effect of one cell on its environment. Statistical averages can be gleaned by considering a number of 'look-alike' clouds which would exist in certain environmental conditions or by considering one generic cloud which embodies the features present in many clouds if they were ensemble-averaged.

The several cumulus parameterization schemes which exist for models resolving both the unbalanced and balanced flow are scale specific, *i. e.* they are designed for a specific grid size. This is certainly not a desirable property of a parameterization scheme. The Fritsch and Chappell (1980) scheme recognizes that energy in the mid-latitudes can be accumulated over a long period of time and then almost instantaneously released. The cloud is assumed to remove the convective available potential energy (CAPE) that exists in a grid volume within a specified time interval.

The Kreitzberg and Perkey (1976) parameterization is a sequential plume scheme that adapts the moist convective adjustment parameterization used in balanced flow models to simulations of the atmosphere within the unbalanced flow regime. A problem this scheme shares with the Fritsch-Chappell scheme is the assumption that the cumulus clouds exist within and modify only one grid box. This constrains all of the subsidence associated with cumulus clouds to occur within the same grid box as the convection. As the grid resolution increases, this assumption becomes increasingly suspect, thus forcing a lower bound on the grid size.

1.3 Probabilistic flow

As the scale of the simulation is reduced to significantly less than 2 km, there may be no need to parameterize the cumulus eddies since they will be explicitly resolved by the numerical model. The unresolved turbulence still needs to parameterized, though, and one way is through similarity theory (Businger *et al.* , 1971). Mellor and Yamada (1974) approached the parameterization of turbulent eddies based upon scale considerations.

The cumulus parameterization scheme for mesoscale models developed here is based on the ensemble averaged approach of Mellor and Yamada. As will be discussed in later chapters, a model will also be developed to represent the cumulus scale eddies. Therefore, the cumulus parameterization schemes briefly reviewed in the introduction are more fully discussed in chapter 2 with particular attention paid to the closure assumptions. The basis for the parameterization is presented in chapter 3 as well as the general theoretical framework. The mathematical derivation of the parameterization is cast in chapter 4 while the results of prognostic tests with various grid resolutions are presented and compared with an explicit two dimensional simulation of Florida sea breeze convection in chapter 5. Finally, a summary and the conclusions are discussed in chapter 6.

Chapter 2

PARAMETERIZING THE UNRESOLVED SCALES

As mentioned in the introduction, the unresolved scale in a numerical simulation may include eddies having scales from micrometers to tens or even hundreds of kilometers. As the grid interval in a numerical simulation increases, the length scale of the unresolved eddies also increases. Therefore, the important unresolved scale in a GCM will be the cumulus scale eddies while in a large eddy simulation (LES), the parameterized scale will include the eddies having scales of tens or hundreds of meters. The parameterization of eddies spanning the length scales suitable for the small scale LES through the mesoscale to the larger scale is reviewed in this chapter. The larger scale parameterizations are designed for a GCM and rely on the numerical model resolving only the balanced circulations while parameterizations for the mesoscale rely on the model resolving both the balanced and unbalanced circulations. In order to gain a deeper understanding of how these parameterizations differ, particular emphasis is placed on the closure assumptions.

Perhaps a philosophical difference arises when cumulus parameterization for mesoscale models is compared to cumulus parameterization for GCMs and small scale turbulence parameterizations for LESs. In all cases, the parameterizations seek to represent the statistically averaged effect of the unresolved eddies, or the generalized ensemble averages (Cotton and Anthes, 1989). This is straightforward in LES and GCM work since a population of eddies and cumulus clouds exist. In GCMs, each cloud within the population may be in different stages of growth and decay so that with large enough grid sizes, it is feasible to capture the mean effect of the clouds on the grid-box variables. Since condensation in the updraft core is mostly balanced by precipitation and the heating from this condensation is balanced by adiabatic cooling, the averaged effect of the cloud on its environment is the subsidence forced by the cloud and the detrainment of the cloud into the surrounding environment.

Another way to think about this is to consider a reference numerical model with a grid spacing small enough to explicitly resolve all cumulus convection. The reference model will be run long enough to capture a statistically constant time period when cumulus convection is active. Furthermore, the reference simulation will take place over a domain large enough to include several GCM grid boxes. Let us now consider a contractible grid having the area of a GCM grid box. All cumulus convection which falls within this grid will have to be parameterized. It is easy to see that if this grid is large enough, then cumulus convection within all stages of its life-cycle will be captured. Furthermore, the population of clouds within this grid will be statistically constant as this grid is moved or the initial conditions of the reference model are slightly changed. Therefore, the ensemble averaged effect of the population of clouds is simply determined by averaging over the contractible grid.

When cumulus convection in a mesoscale model is considered, a different approach is needed for its parameterization. As the grid discussed above shrinks in size, the number of cumulus clouds captured within this grid decreases. Rather than capturing a population of clouds in a statistically steady state, the grid may now capture one or even part of one cumulus cell or no cells. Therefore, an individual cumulus cell now needs to be parameterized, depending on whether cumulus convection should occur at a particular grid box. Statistics can no longer be determined by simply averaging over the contractible grid since an ensemble of cumulus eddies no longer exists. Meaningful ensemble averages of a cell are then determined by considering the statistical average of a number of cells that develop under 'look-alike' local environmental conditions in the reference numerical model. The timing and location of the cumulus convection would presumably be well represented in the mesoscale model since aspects of the local forcing present in the reference model would be captured.

2.1 Parameterizations for LESs

As the scale of the simulation is reduced to significantly less than 2 km, there may be no need to parameterize the cumulus eddies since they will be explicitly resolved by the numerical model. There may be some exceptions, however, as in Rosenthal (1978) who explicitly simulated the convection occurring within a hurricane on a 20 km grid. However, the numerical model was initialized as a balanced vortex and, as such, evolved as a balanced circulation with or without unresolved convection. Orlanski and Ross (1977) explicitly simulated dry convection in the presence of a cold front on a twenty kilometer grid by artificially enhancing the eddy viscosity in the presence of static instability. Similarly, Orlanski and Ross (1986) performed a similar simulation with moist convection. In each case, however, convection did not play an important role in forcing the circulations since strong dynamics were present. Cram (1990), on the other hand, found that cumulus convection could not be adequately simulated on a 5 km grid. The squall line she attempted to simulate moved with a phase speed corresponding to an internal gravity wave thus underscoring the importance of a cumulus parameterization scheme designed for the unbalanced flow regime.

2.1.1 Classic LESs

The numerical simulation of the PBL represents only one realization of many possible outcomes since the resolvable terms begin to represent the turbulent eddies which are relatively random in nature. The results of such a simulation may be thought of as an ensemble average as discussed by Cotton and Anthes (1989). The unresolved turbulence still needs to parameterized, though, and one way is through similarity theory (Businger *et al.* , 1971). Here, turbulence is assumed to behave statistically similarly under 'look-alike' atmospheric conditions as determined by the dimensionless characteristics of the atmospheric flow. Quantities such as the Richardson number and the Monin-Obukhov (1954) length are valuable in determining these 'look-alike' conditions. The relevant fluxes are determined through universal similarity functions

Mellor and Yamada (1974) approached the parameterization of turbulent eddies differently, and discussed a hierarchy of second order turbulence closures based upon scale considerations. The resulting four levels of equations contain an increasing number of prognostic equations as the degree of anisotropic turbulence increases. The parameterized vertical fluxes of heat, momentum and moisture are related to the mean gradients of these quantities by diagnostically determined mixing coefficients. Moeng (1984) used the intermediate level 2.5 closure which carries one predictive equation for TKE to simulate a laboratory vortex and the evolution of the PBL, and a cloud topped convective boundary layer (Moeng, 1986). A full second order level 4 closure was also constructed by Moeng and Arakawa (1980) to study the interaction of radiation with a stratus-topped marine PBL and Chen and Cotton (1986) to study the physics of the marine stratocumulus-capped mixed layer. Finally, full third order closures which contain predictive equations for the second and third order moments have been constructed by Andre *et. al.* (1978), Moeng and Randall (1984) and others to study the PBL.

Explicitly simulating eddies allows the numerical simulation to be used as a virtually perfect data base. The data, if they are believable, represent perfect spatial and temporal coverage. Diagnostics can be recovered as in Moeng (1987), Moeng and Wyngaard (1984) and Bougeault (1981) to further understand the physics of the phenomena under study. Furthermore, averaging the data and their statistics over various space and time scales allow for the evaluation of parameterizations of physical processes, such as those carried out by Moeng and Wyngaard (1984, 1989) to evaluate closures for the pressure-scalar covariances, turbulent transport and dissipation terms, and Sommeria (1976).

2.1.2 Cumulus ensemble models

Extending the LES approach from the PBL to the free atmosphere yields cloud or cumulus ensemble models. Cloud models using a variety of simple turbulence closures have been used to study cumulus clouds for some time. Although they can describe the dynamics of the cumulus clouds, they fail to capture the feedback between the cloud and the large scale due to the limited domain size. Furthermore, due to their relatively simple turbulence closures, the interactions between the cloud and the sub-cloud layer are poorly simulated. Schlesinger (1990) used a limited domain to investigate the feedback between a simulated supercell and its near environment and calculate the cumulus fluxes of heat, momentum and moisture.

Soong and Ogura (1980) pioneered the use of cumulus ensemble models which simulate a field of cumulus and its feedback on the large scale. Although their approach was semi-prognostic because the large scale fields were specified and their domain size was limited to almost seven kilometers, cumulus ensemble models have developed into valuable tools for studying cumulus convection. Soong and Tao (1984), for example, used a 130 km grid to explicitly simulate the vertical transport of momentum within tropical rainbands.

Recently, Krueger (1988) has developed a numerical model with a full third order closure to study the response of tropical clouds to large-scale advection. The benefits of the third order closure include greater emphasis on the turbulent processes both within the cloud and the sub-cloud layer. At present, cumulus ensemble models are restricted to two dimensions due to computational limitations, however, the third order closure does provide for an accurate treatment of the PBL and, due to its generality and wide range of validity, cumulus clouds. In addition, Nicholls *et al.* (1991a) used a cumulus ensemble model covering six hundred kilometers to investigate the role that the large scale shear profiles have in the moderating organization of cumulus convection over the Florida peninsula. Gregory and Miller (1990) also used a cumulus ensemble model with a domain greater than 250 km to study the convective heat and moisture budgets and investigate several assumptions contained within the Arakawa-Schubert and Kuo cumulus parameterizations. Also, Schlesinger (1990) diagnostically determined convective feedback budgets for heat, moisture and horizontal momentum from a cloud model having a two kilometer horizontal resolution.

Thus far, relatively small scale models which parameterize the random, turbulent eddies having length scales of tens to hundreds of meters have been considered. All other scales of motion are resolved as long as they are contained within the domain. Attention is now turned to mesoscale models having horizontal resolutions of two to fifty kilometers. As mentioned in the introduction, these models characteristically resolve the divergent part of the circulation.

2.2 Parameterizations for models resolving both the balanced and unbalanced flow

The parameterization schemes to be reviewed are the Fritsch-Chappell (1980) and the Kreitzberg-Perkey (1976) approaches. Also reviewed are schemes developed by Brown (1979) and Frank and Cohen (1987). All of these schemes use one dimensional cloud models to distribute the temperature and moisture in the vertical. And, although these approaches are specifically designed for mesoscale grid sizes, they still assume that the cloud and its associated subsidence occur within the same grid box. As stated in the introduction, this assumption becomes increasingly suspect as the grid interval shrinks. Also mentioned for completeness are the wave-CISK schemes proposed by Lindzen (1974) to explain cloud clusters in the tropics and extended by Raymond (1975) and others. Unlike traditional cumulus parameterization schemes, wave-CISK assumes that convection forces gravity waves which create travelling regions of convergence and divergence which in turn influence the convection. Wave-CISK may be applied to models resolving the balanced and/or unbalanced flows.

2.2.1 Kreitzberg-Perkey

This is perhaps the first of the schemes which recognized that convective instability could build for several days before being explosively released over a time scale of several hours. They employ a series of sequential plumes which are called every twenty minutes until the CAPE is exhausted. The CAPE, as stated earlier, is related to the positive area in a skew T-ln P graph, *i. e.* the difference between the cloud and grid box temperatures. This appears similar to a soft convective adjustment scheme, mentioned later, where a lapse rate is adjusted towards greater stability.

The initial cloud radius is assumed constant, but because the cloud radius modulates the amount of entrainment, Kreitzberg and Perkey maintain that extratropical storms are handled better than their tropical counterparts since entrainment plays a less decisive role in cloud development. They note that the specification of the initial updraft radius is the weak link in their parameterization since it controls entrainment and cloud height. Possibilities for modifying the initial updraft radius include basing it on the previous convective activity within a grid box and introducing a spectrum of clouds with different initial updraft radii. Note that this is similar to the Arakawa-Schubert approach of assuming a distribution of clouds with various entrainment rates and as such would be more suitable on the coarser grids. The updraft obeys vertical mass continuity as in a steady-state cloud, with the radius decreasing with updraft acceleration and increasing broadly with updraft deceleration.

Cloud base is selected by determining the height where the maximum releasable instability is achieved. The primary closure rests on a vertically-integrated slice method. This means that the fractional updraft area at cloud base is determined by forcing the hydrostatic pressures within the cloud and the adjacent environment to be equal. Since the environmental subsidence depends upon the fractional updraft area through mass continuity, an iterative technique is used to determine the fractional updraft area and the resulting environmental subsidence. The premise in forcing the hydrostatic pressures within and outside the updraft to be equal is that convection will cease and the cloud will decay when the buoyancy within the cloud is offset by the warming due to subsidence next to the cloud. At this point the model cloud is mixed horizontally through bulk theory with the subsided environment, and, if diagnosed, further convection is allowed. Care has been taken to ensure energy conservation by forcing consistency between the heating and moistening and the computed precipitation.

2.2.2 Fritsch-Chappell

This parameterization scheme is also based on the assumption that CAPE is depleted over a time scale much shorter than the rate at which the buoyant energy is made available. The time scale over which the CAPE is depleted is the grid length divided by the mean environmental wind over the clouds depth and represents the amount of time needed for the cloud to transverse the grid.

The grid box temperatures are area-weighted averages of the updraft, downdraft and environmental temperatures which implies bulk mixing. The time rate of change of the environmental temperature is due, in this formulation, to the compensating hydrostatic subsidence and cooling due to evaporation of condensate within the anvil. Moist downdrafts are included in this formulation and are assumed to be saturated above cloud base and eighty percent saturated below cloud base. The area of the downdraft is related to the precipitation efficiency of the system which is determined by the environmental shear. All cloud types are assumed similar within a grid box so that there exists a unique updraft area at cloud base (which can easily be related to cloud fractional coverage) and associated downdraft and environmental areas which will remove all CAPE within the convective time period. This is also an iterative solution and the end result is a number of identical clouds which exist within the cloud volume. Momentum and moisture are also distributed using the same bulk theory of transport and mixing.

Tremback (1990) substantially modified the Fritsch-Chappell parameterization in several ways. The downdrafts formulation is completely reformulated to match the observational and modeling study of Knupp (1985, 1987). The updraft vertical profile and cloud top is also redefined, as is the effect of the capping inversion, if present, in determining if and how much convection will occur. Perhaps the most important modification is the requirement that water mass and energy are conserved in the parameterization.

2.2.3 Brown and Frank-Cohen

Both of these schemes assume simple relationships between the unresolved drafts and compensating subsidence mass fluxes. Unfortunately, the empirical constants which relate the unresolved mass fluxes to the resolved mass fluxes are scale dependent which limits the generality of the schemes. Brown, for example, relates the cloud mass flux to the resolved mass flux at 900 mb, while Frank and Cohen prescribe the compensating subsidence to be one fifth of the updraft mass flux. The Frank-Cohen scheme also parameterizes downdrafts which are assumed to lag the updraft formation by some calculated time interval equal to twice the time it takes for a parcel to travel from cloud base to cloud top. The factor of two is needed since they state that one dimensional cloud models overestimate the vertical velocities.

2.2.4 Wave-CISK

This theory assumes that the gravity waves forced by convection are critical in maintaining and initiating convection. The gravity waves modulate the convection by forcing areas of convergence and divergence so that a positive feedback between the convection and the subsequently forced gravity waves exists. Raymond (1975, 1976) showed that this theory successfully simulated the propagation speed of various storms. Lagged downdrafts were incorporated by Raymond (1983, 1984) and shown to significantly alter the propagation characteristics of the storm. Specifically, the inclusion of downdrafts allowed for a traditional wave-CISK propagating mode and an advective mode which moved with the speed of the mid-level steering flow. A cumulus parameterization scheme designed around wave-CISK assumes fixed profiles of convective heating whose amplitudes are modulated by the amount of lifting near cloud base. Raymond (1986) applied this theory in the context of a large scale model resolving only the balanced circulations and assumed a spectrum of non-entraining clouds similar to the Arakawa-Schubert scheme discussed below. Downdrafts were included to highlight the importance of the advective mode in mesoscale convective systems.

2.3 Parameterizations for models resolving only the balanced flow

Models in which only the balanced part of the circulation is resolved are now considered. On the one hand, this makes the parameterization problem easier since there is a distinct scale separation between the large scale forcing and the unresolved scale response. On the other hand, the divergent mesoscale circulations may have to be parameterized if they are important.

The three parameterizations reviewed here are similar in that they are based on equilibrium assumptions between the rate of stabilization by convection (the unresolved-scale response) and the rate of supply of convective fuel (the large-scale forcing). Certain assumptions about the convection are contained in all three parameterizations; perhaps the most stringent requirement in some is that the areal extent of the convection is much less than the grid area in which it is contained.

2.3.1 Arakawa-Schubert

This parameterization scheme is unique because it recognizes that clouds of various heights exist and are important in modifying the large-scale fields. To this end, the scheme specifies a spectral representation of a sub-ensemble of clouds. The clouds themselves are assumed to be of constant radius and detrain in a very thin layer near the equilibrium temperature level. The cloud types within the sub-ensemble are characterized by varying entrainment rates, with the larger clouds having the smaller entrainment rates. The larger clouds will have higher detrainment levels since they lose buoyancy less quickly than the smaller clouds with higher entrainment rates.

A predictive equation for the height of the mixed layer is also included in this parameterization. The depth of the mixed layer is important since the updrafts are assumed to incorporate the mixed layer air. The subsidence from the convection will modulate the height of this layer, and, if the convection and its associated subsidence is strong enough, the mixed layer height will decrease. There then exists a control on the strength of the convection; as the mixed layer height decreases, the fuel available to feed the convection decreases.

The cloud work function is introduced in their formulation and represents the positive area on a skew-T ln P graph spectrally weighted for each cloud type. The key closure for this parameterization is the assumption that the cloud ensemble reacts rapidly enough to the large scale changes so that the changes in the cloud work function are minimized. In other words, the cloud-ensemble consumes the energy provided by the large scale at the same rate it is supplied. Downdrafts, although not part of the original scheme, have been added by Payne (1981) who noted improvement in the vertical heating profiles and increased mass flux in middle and low clouds and Cheng (1989a,b), who found that the downdrafts reduced excessive drying through the entire cloud layer. Similarly, Kao and Ogura (1987) found that downdrafts alleviated the underestimate of condensation and evaporation rates while Ogura and Kao (1987) found that downdraft cooling reduced the circulation intensity of the simulated convective system. In addition, König and Ruprecht (1989) parameterized the effects of clouds on the large-scale vorticity budgets using the Arakawa-Schubert parameterization.

2.3.2 Kuo schemes

The Kuo schemes are easier to understand since only one cloud type is represented. This general class of scheme relates the strength of the convection to the large scale moisture convergence including evaporation from the ground. Moisture and heat are distributed vertically through a one dimensional cloud model assuming that the cloud temperature is reached for some fraction of the grid over some time interval through the condensation of water vapor and warming to balance grid-scale adiabatic cooling. The warming needed to balance the adiabatic cooling combines with the vertical advection term in the mean equations to represent the subsidence warming which occurs at the large scale. The parameter which closes the scheme is the partitioning parameter which partitions the moisture provided by the large scale into either condensation or humidification. The condensation either rains out or is carried away while the rest is assumed to evaporate and increase the relative humidity of the large scale environment. Of course, the behavior of the scheme is crucially dependent upon the partitioning parameter, and although Kuo (1974) mentions that in the tropics, the partitioning parameter is near zero so that most of the large scale moisture eventually falls as rain, the scheme will not adequately describe all types of convection until a suitably general formulation is found for the partitioning parameter.

Kanamitsu (1975) and Krishnamurti *et. al.* (1976) generalized the Kuo scheme to allow for separate fractional approaches of moisture and heat to the limiting state. These additional variables make the movement of the grid column temperature and moisture towards cloud values dependent upon such factors as the strength of the forcing, the presence of downdrafts and the moisture partitioning. The Kuo scheme then becomes a variable-rate, time dependent scheme rather than just a mixing approach. They also redefined the moisture supply to include only the vertical advection of moisture which seems to reduce the lag between the moisture supply and convection to zero.

Molinari and Corsetti (1985) included cumulus scale and mesoscale downdrafts in the Kuo formulation and assume a functional form for the moisture partition dependent upon shear as in Fritsch and Chappell (1980). The area weights of the downdrafts and updrafts are determined from observations as is the thermodynamic character of the downdrafts. The main effect of the downdraft was to stabilize the grid column more rapidly and shift the level of maximum upward motion higher. Molinari (1985) proposed a simplification of the Kuo approach which defined the fractional approaches of heat and moisture to the cloud profiles such that the cumulus heating and moistening exactly matched arbitrarily defined profiles which were derived from observations.

Tremback (1990) modified this work and arbitrarily defined the downdraft weighting with respect to the updraft. Furthermore, an anvil moistening term as well as the sub-cloud drying term was introduced. Bougeault (1985) proposed an improvement to the Kuo type schemes which is based upon the concept of cloud mass flux. The cumulus parameterization scheme presented in this paper is a modification of this approach. The cumulus scale heating and moistening budgets in this scheme are dependent upon the vertical advection of heat or moisture by the cloud scale mass flux and the detrainment of these quantities. The detrainment term is simply represented by the relaxation of the large-scale variables toward a cloud profile over a specified time constant which is independent of altitude. This time constant is determined by assuming that the vertical integral of the moist static energy is conserved and the mass flux is assumed proportional to the square root of the cloud-environmental difference of the moist static energy. The constant of proportionality is derived from equating the large-scale moisture convergence to the rainfall and the atmospheric moistening, as in the classic Kuo scheme. However, since the rainfall is related to the mass flux, the partitioning parameter is explicitly calculated. The cumulus parameterization scheme presented in this paper is a modification of part of this approach.

2.3.3 Moist convective adjustment

Perhaps the easiest of the parameterizations to implement and understand is moist convective adjustment. This class of scheme simply adjusts the lapse rate if it becomes unstable back to neutrality within a specified time interval. The underlying physics of the adjustment are ignored which may be attractive if the underlying physics are not well known. A modification to this is soft convective adjustment (Manabe *et al.* , 1965) which prescribes the changing of the lapse rate over a part of the grid box, σ, over a specified time interval, usually taken to be thirty minutes. The cloud fractional coverage must be calculated from another parameterized relationship based on relative humidity. The final grid column profile is then obtained by weighting the moist adiabatic lapse rate by σ and the unperturbed clear air profile by $(1 - \sigma)$. The percentage of the grid over which to change the lapse rate is certainly scale dependent and no general scheme for its prescription has been proposed.

Betts (1986) and Betts and Miller (1986) proposed a more sophisticated adjustment scheme where temperature and moisture profiles are relaxed toward reference profiles derived from quasi-equilibrium assumptions over some time period. The time period determines the lag between the convection and the large scale forcing. Included in this scheme are both a deep convective reference profile determined through a total enthalpy constraint and a shallow convective reference profile determined by forcing the sum of the condensation and precipitation to be zero.

2.4 Summary

Closure techniques for parameterizing small scale eddies within LESs through cumulus scale eddies within GCMs have been reviewed. Since this paper is concerned with a cumulus parameterization scheme for mesoscale models, the schemes designed for models resolving only the balanced flow are not applicable. The moist convective adjustment scheme may be applicable for smaller scale models since the lapse rate is certainly modified in the presence of cumulus convection on any scale, and this will be discussed in later chapters.

The schemes designed for models resolving the unbalanced circulations are grid dependent since they assume that the cumulus convection and the related compensating subsidence occur within the same grid box. Forcing the convection and its compensating subsidence to occur in the same grid box forces a lower limit on horizontal resolution. Most also disallow the translational motion of the storm which becomes increasingly important as the grid resolution increases. Furthermore, none of these schemes allow for the prediction of explicit hydrometeor species. Rutledge and Houze (1987) diagnostically determined that the active line of cumulus inject substantial quantities of hydrometeors into the trailing stratiform region. While many GCMs do not carry explicit microphysics, mesoscale models are able to predict a wide range of hydrometeor species. It is therefore important that a cumulus parameterization incorporate a source function of hydrometeors for mesoscale models. Therefore, a new parameterization is needed.

Considering the success of the cumulus ensemble model, it appears reasonable to extend the higher order closure technique to modeling cumulus convection in the free atmosphere. Excluding precipitation processes, the main difference between eddies in the PBL and deep cumulus clouds in the free atmosphere is the forcing. PBL eddies are driven by boundary fluxes of heat, momentum and moisture while cumulus eddies are driven by the release of latent heat in the lower and mid-troposphere. Therefore, the deep cumulus fluxes of heat and moisture will need to be separately parameterized Thus, a new parameterization is proposed in the next chapter which is based on a level 2.5 second order closure and the specification of the the cumulus heat and hydrometeor fluxes and tendencies. As in the manner that LES data are analyzed to determine statistics and validate term closures, cloud model simulations are used for determining and calibrating the proposed cumulus parameterization.

Chapter 3

THEORETICAL FRAMEWORK

As discussed in the previous chapter, LES type models explicitly resolve the large eddies and parameterize the smaller scale turbulence. Given that the numerical simulation of an event is 'correct', the model data provides an extensive data base from which analysis may be done. This data base is essentially perfect in that there is complete spatial and temporal coverage over the domain. Researchers have used data from classic LES simulations to elucidate the physical mechanisms and parameterize processes. Extensions of this approach can also be applied to cloud models and cumulus ensemble models. From cumulus ensemble models the nature of convection and its interaction with the environment can be studied.

Care needs to be exercised when interpreting the cloud model output because the numerical simulations used in this study, for example, have limited domains which capture the storm and its near environment. They are not considered true cumulus ensemble models since while the control on the storms by the environment is well represented, only the effect of the storm on its local environment is well represented, *i. e.* only half of the feedback loop is modeled.

Data from cloud models and cumulus ensemble models can also be used to study the cumulus parameterization problem. This is seen by considering the the derivation of the mean model equations. If $\mathcal{X}$ represents any scalar variable, then a generalized equation for the rate of change of $\mathcal{X}$ with time is

$$\frac{d\,\mathcal{X}}{dt} = \mathrm{PR}(\,\mathcal{X}\,) + \mathrm{S}(\,\mathcal{X}\,),$$

where PR represents all microphysical processes such as precipitation fallout, growth and decay due to accretion, auto-conversion, nucleation, melting, freezing, collection, vapor deposition, evaporation and riming (Tripoli and Cotton, 1982), and S represents all other source terms such as radiation. The total derivative can be separated into local changes and advective changes by use of tensor notation:

$$\frac{\partial \mathcal{X}}{\partial t} = -U_j \frac{\partial \mathcal{X}}{\partial x_j} + \mathrm{PR}(\mathcal{X}) + \mathrm{S}(\mathcal{X}), \tag{3.1}$$

where U_j is the three dimensional velocity.

$\mathcal{X}$ and U_j are now decomposed into a mean and fluctuating component,

$$\mathcal{X} = \overline{\mathcal{X}} + x', \tag{3.2}$$

where the overbar represents the generalized ensemble average discussed in chapter 2 and Cotton and Anthes (1989) and the prime represents deviations from this average. The averaging operator represents an average over time and space scales resolvable by the numerical model. When this is substituted into Eq. 3.1, the resulting equation becomes:

$$\begin{aligned}\frac{\partial \overline{\mathcal{X}}}{\partial t} + \frac{\partial x'}{\partial t} &= -(\overline{U}_j + u'_j)\frac{\partial}{\partial x_j}(\overline{\mathcal{X}} + x') + \mathrm{PR}(\overline{\mathcal{X}}) + \mathrm{S}(\overline{\mathcal{X}}) \\ &\quad + \mathrm{PR}(x') + \mathrm{S}(x'). \end{aligned}\tag{3.3}$$

If the traditional assumptions about the averaging operator are made, mainly

$$\begin{aligned}\overline{x'} &= 0 \\ \overline{\overline{\mathcal{X}}} &= \overline{\mathcal{X}} \\ \overline{u'_j \frac{\partial \mathcal{X}}{\partial x_j}} = \overline{U_j \frac{\partial x'}{\partial x_j}} &= 0,\end{aligned}$$

then when Eq. 3.3 is averaged, the result is

$$\frac{\partial \overline{\mathcal{X}}}{\partial t} = -\overline{U}_j \frac{\partial \overline{\mathcal{X}}}{\partial x_j} - \overline{u'_j \frac{\partial x'}{\partial x_j}} + \mathrm{PR}(\overline{\mathcal{X}}) + \mathrm{S}(\overline{\mathcal{X}}). \tag{3.4}$$

The result when this equation is expressed in total derivative form and turbulence is assumed incompressible is

$$\frac{d\,\overline{\mathcal{X}}}{dt} = \mathrm{TURB}(\overline{\mathcal{X}}) + \mathrm{PR}(\overline{\mathcal{X}}) + \mathrm{S}(\overline{\mathcal{X}}). \tag{3.5}$$

This shows that the turbulence operator represents scales of motion which are not resolvable by the model. If a mesoscale model having a horizontal resolution of twenty kilometers is used, then the averaging operator will include scales of motion less than about forty kilometers. If an explicit simulation (where the averaging operator now represents smaller scales of motion) is then performed of a cumulonimbus, for example, then the subsequent averaging of these fields over the storm scale will enable an ensemble-averaged view of convection as it is applicable to the mesoscale model.

The explicit simulations may also be used as a calibration instrument. As will be discussed later in this chapter, the cumulus parameterization scheme incorporates a one-dimensional cloud model. Parameters within the cloud model can be calibrated to match the values derived from the numerical simulations and, with enough simulations, generalized to include an array of cloud environments.

With this in mind, data from the numerical simulations of a tropical squall line and a mid-latitude supercell are analyzed and compared. It is hoped that the simulations of these different storm types in different environments yields a sufficiently broad view of the physics of cumulus convection so that a first step towards a general cloud model and cumulus parameterization scheme can be formulation. A basis for developing a generalized cumulus parameterization scheme using a predicted $\overline{w'w'}$ is then developed. This parameterization scheme will consist of a second order turbulence model to capture the small-scale eddies which occur within a deep convective cloud as well as layer-averaged stratocumulus elements, and a deep cumulus forcing term to represent the tropospheric scale thunderstorm eddies which are the major transporters of heat, momentum and moisture. The parameterization itself will be presented in chapter 4.

3.1 Data base

The numerically simulated data base includes a mid-latitude supercell and a tropical squall line. Both simulations were performed using the Colorado State University Regional Atmospheric Modeling System (CSU RAMS) which employed the non-hydrostatic, fully compressible, equations with parameterized microphysics (Tripoli and Cotton, 1982; Cotton *et al.* , 1982,1986). The supercell was observed on 2 August 1982 during the CCOPE experiment (Miller *et al.* , 1988) and was simulated using a 40 km x 40 km x 21 km domain with a grid resolution of 750 m in all directions. The storm developed along a probable synoptic surface front and was characterized by strong shear and buoyancy. The lifted index was about -10 and the winds veered nearly 120° from the surface layer to cloud base with a magnitude of 10 m/s. From cloud base to about 9 km, the winds increased to almost 40 m/s with very little directional shear. Its bulk Richardson number (Moncrieff and Green, 1972, Weisman and Klemp, 1982) was about 25. The simulation was initialized by a warm bubble which produced a relatively steady-state storm simulated for three hours.

A quasi three dimensional tropical squall line (Nicholls and Weissbluth, 1988) was also simulated over the ocean. Unlike the supercell simulation, this can be considered a cumulus ensemble simulation since the domain was 110 km x 30 km x 23 km. The horizontal grid spacing was 1 km, while in the vertical, a stretched grid with 280 m resolution near the ground increasing to 1 km aloft was used. Also, unlike the supercell, the squall line evolved with relatively weak shear and buoyancy. The lifted index was about -6 which is slightly stronger than the composite analysis of tropical squall lines observed during GATE but weaker than those of mid-latitude squall lines. The wind profile had a low level jet with winds increasing from 1 m/s to almost 12 m/s at 3.5 km and a weaker upper level jet. Its bulk Richardson number was over an order of magnitude larger than the supercell storm at around 500.

3.2 Comparison

Variances and covariances are now compared between and within the two numerically simulated storms. Perturbation values are determined by subtracting a horizontally homogeneous vertically dependent mean value of a variable from the instantaneous value of that variable. Vertically dependent profiles of variances and covariances are then determined by horizontally averaging the product of the appropriate perturbation quantities. These second order statistics can provide valuable insight if they are calculated over the lifetime of a storm, as shown below.

These two cases show striking similarity in the vertical structure and temporal evolution of $\overline{w'w'}$. Presented in Figs. 3.1a and 3.1b are time-height cross sections of the CCOPE and Florida simulations, respectively. All have centers of activity in the upper troposphere which pulse with time.

In Fig. 3.2a, a vertical profile of $\overline{w'w'}$ at 5400 sec is shown for the CCOPE storm while in Fig. 3.2b, the vertical profile is for the tropical storm at 1800 sec.

Shown in Figs. 3.3a and 3.3b are the time-03 cross-sections of turbulence kinetic energy (TKE). In these cases, the strong divergences near cloud top dominate the TKE budget. There is very little structure through most of the troposphere which strongly contrasts with the $\overline{w'w'}$ profiles.

Also shown in Figs. 3.4a,b - Figs. 3.10a,b are time-height cross-sections of the vertical flux of total water, $\overline{\Theta_{il}}$, θ, and the microphysical quantities rain, ice, graupel and aggregates for the supercell and the squall line, respectively. Total water is a good tracer except in the presence of precipitation. The profiles of total water flux bear close resemblance to the profiles of $\overline{w'w'}$ except that the maxima for total water are considerably lower in the troposphere for both storms due to precipitation effects.

The numerical model uses the thermodynamic variable Θ_{il} which is conservative for parcels undergoing adiabatic motions with phase changes. It is non-conservative, however, for all precipitation processes. The expression relating Θ_{il} and Θ is derived in Tripoli and Cotton (1981) and is

$$\Theta = \Theta_{il} \left(1 + \frac{L_{lv}}{C_p T} r_l + \frac{L_{iv}}{C_p T} r_i\right). \tag{3.6}$$

The profiles of the Θ_{il} flux also mimic the $\overline{w'w'}$ curves because Θ_{il} is conservative for phase changes. Once again, precipitation alters the levels of maxima or minima. If the vertical fluxes of Θ_{il} and Θ are compared, the relative smoothness of the Θ_{il} flux is apparent. Also, the Θ_{il} flux more closely resembles the $\overline{w'w'}$ profiles since the flux is always of the same sign and has a single minima. It appears beneficial, then, that the RAMS model uses ice-liquid potential temperature as its predictive thermodynamic variable.

The similarity of both the behavior of $\overline{w'w'}$ within storms embedded in markedly different environments and the vertical covariances with $\overline{w'w'}$ prompted speculation that

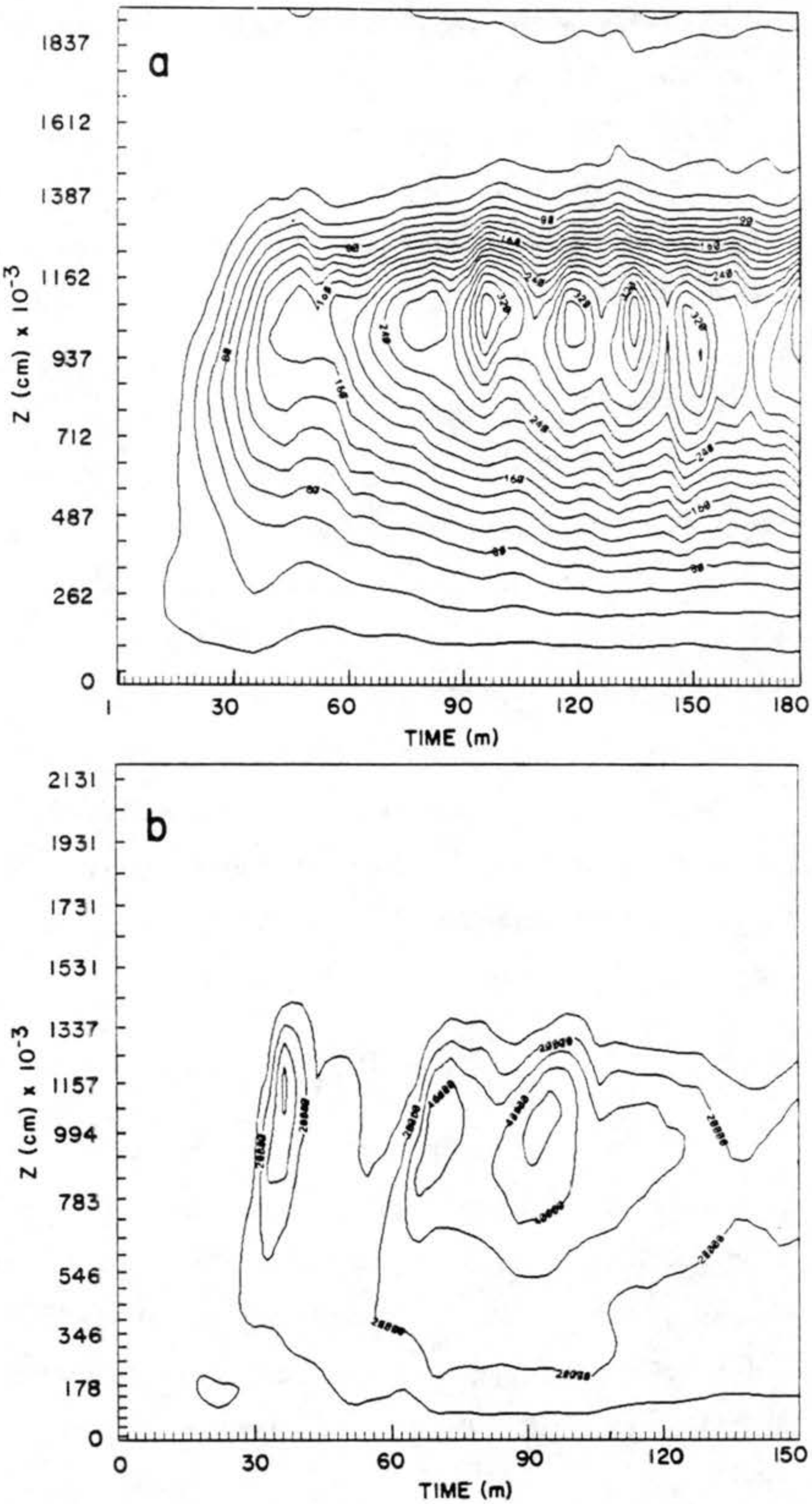

Figure 3.1: Time of series $\overline{w'w'}$ in cm^2/s^2 as a function of height for (a) the CCOPE supercell (labels scaled by 10^{-3}), and (b) the tropical squall line.

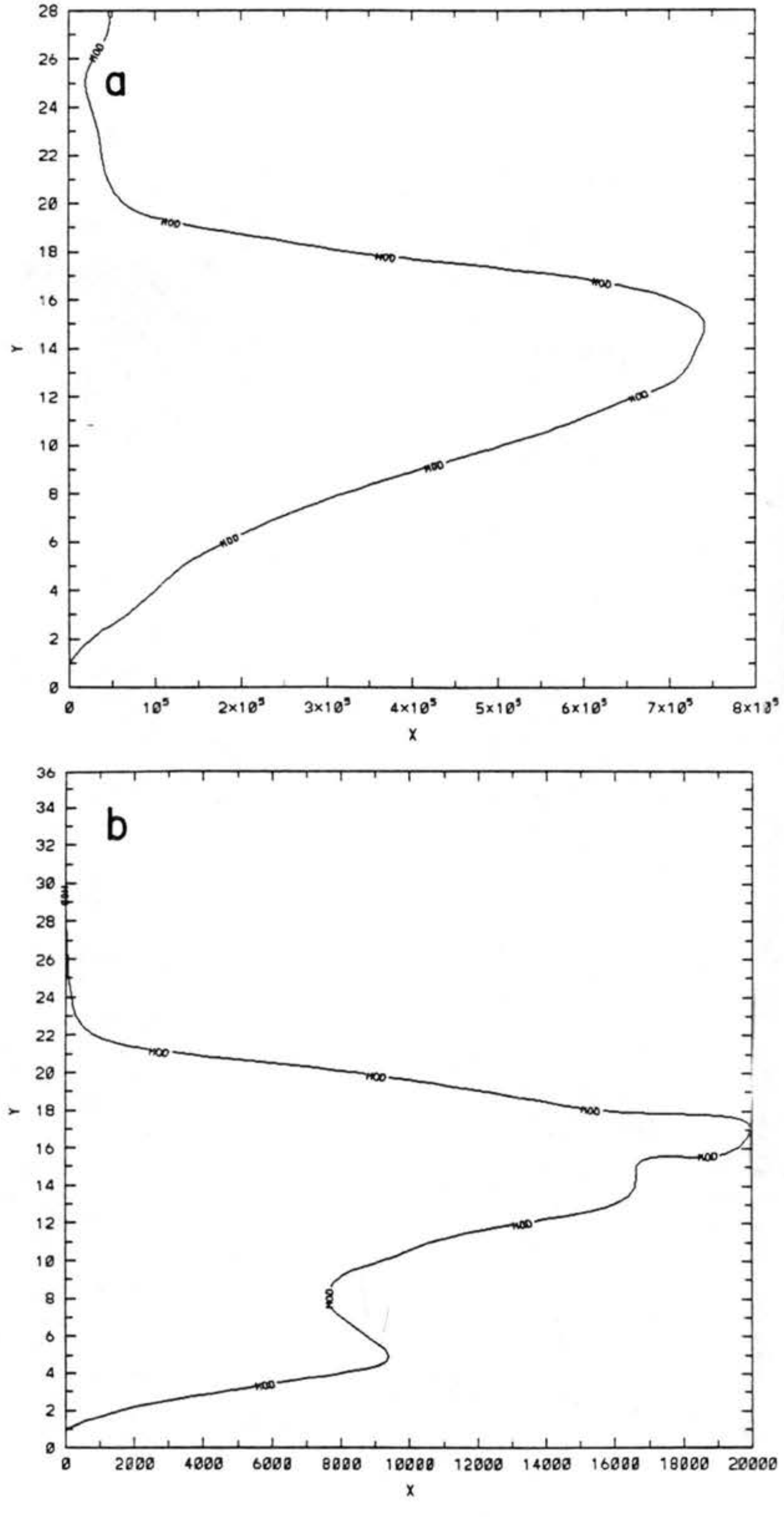

Figure 3.2: Profiles of $\overline{w'w'}$ in cm^2/s^2 as a function of model level for (a) the CCOPE supercell, and (b) the tropical squall line.

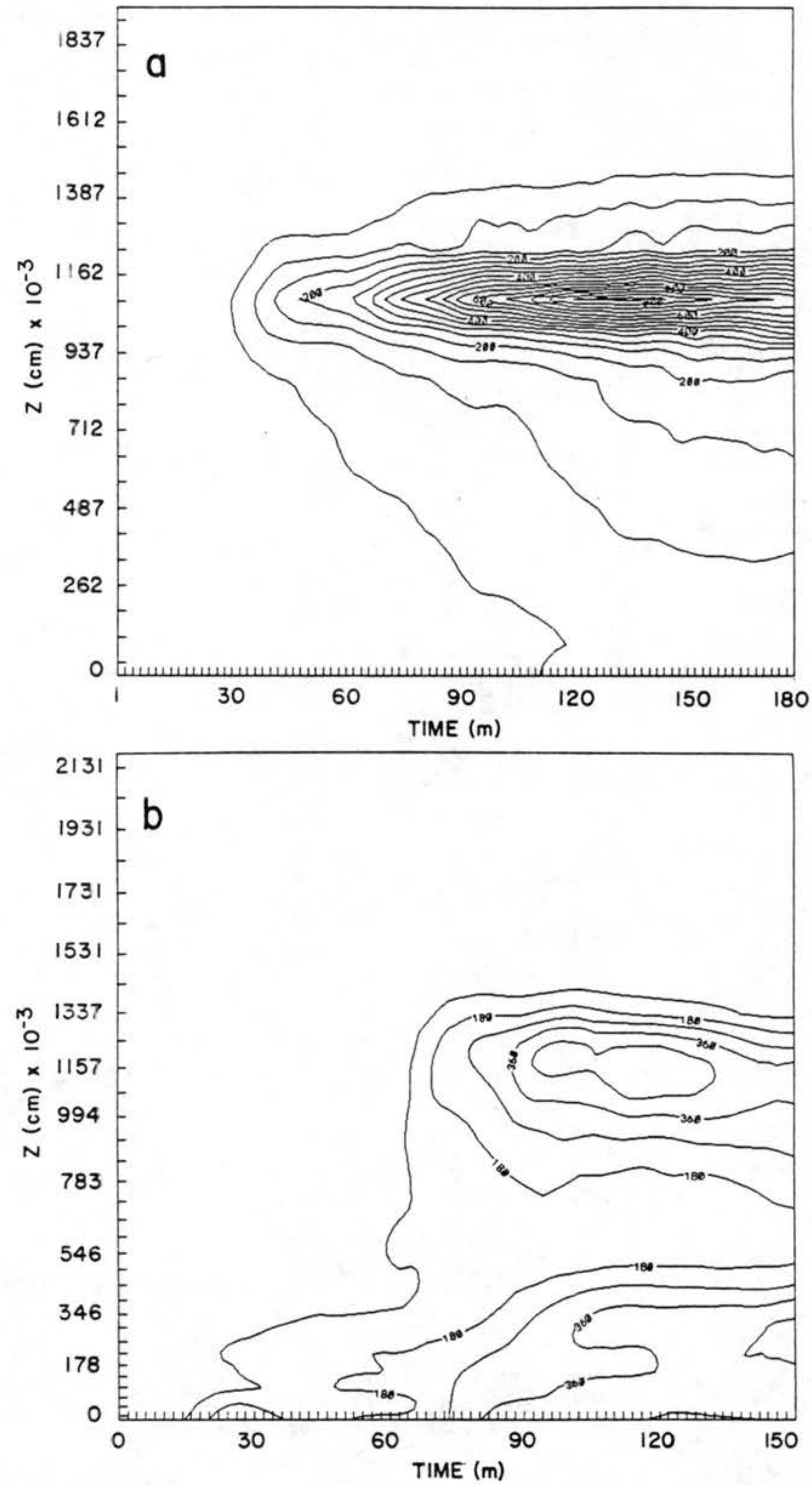

Figure 3.3: Time series of TKE in cm^2/s^2 as a function of height for (a) the CCOPE supercell (labels scale by 10^{-4}), and (b) the tropical squall line (labels scaled by 10^{-3}).

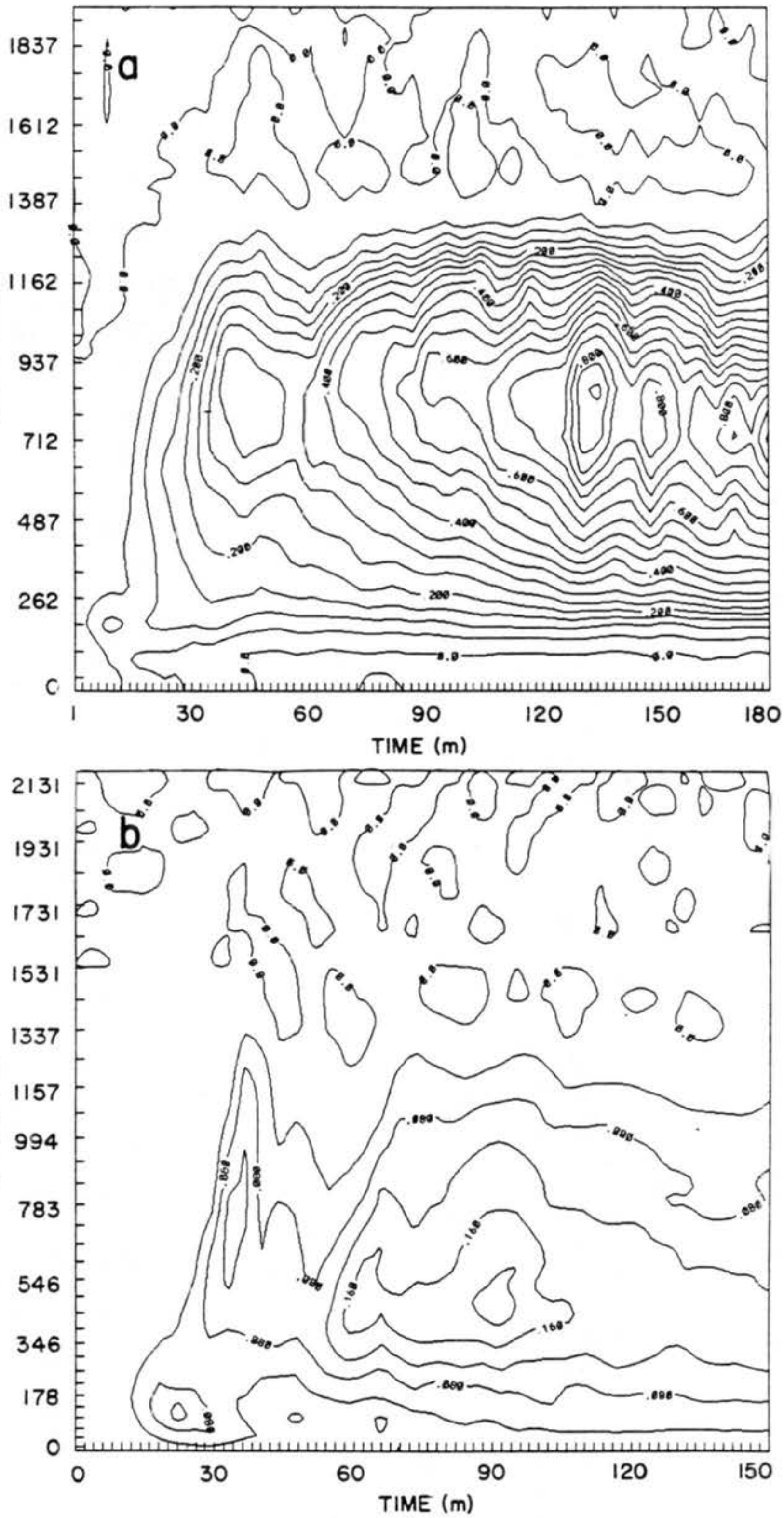

Figure 3.4: Time series of $\overline{w'r'_t}$ in cm/s as a function of height for (a) the CCOPE supercell and, (b) the tropical squall line.

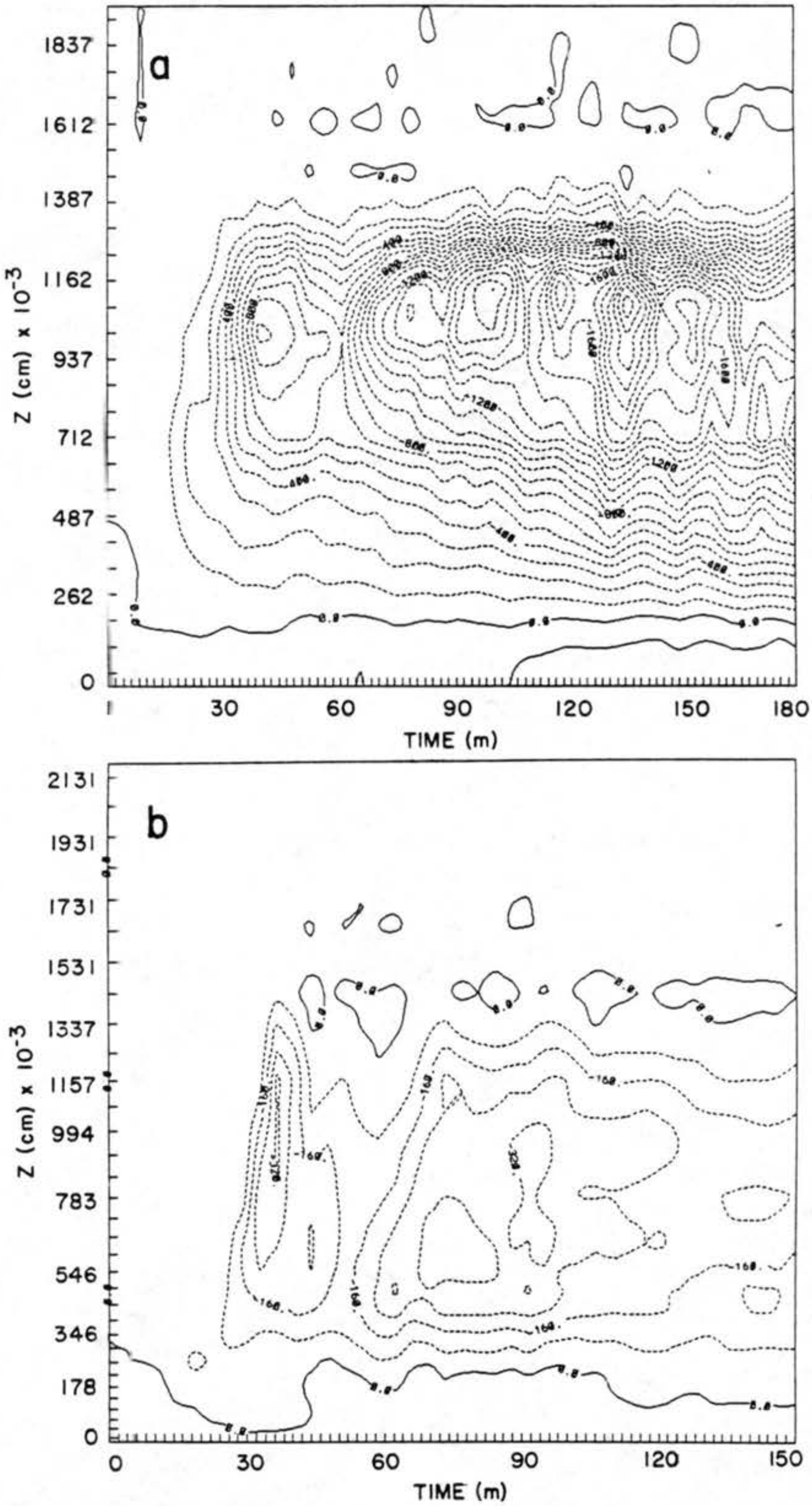

Figure 3.5: Time series of $\overline{w'\theta'_{il}}$ in cm-K/s as a function of height for (a) the CCOPE supercell, and (b) the tropical squall line.

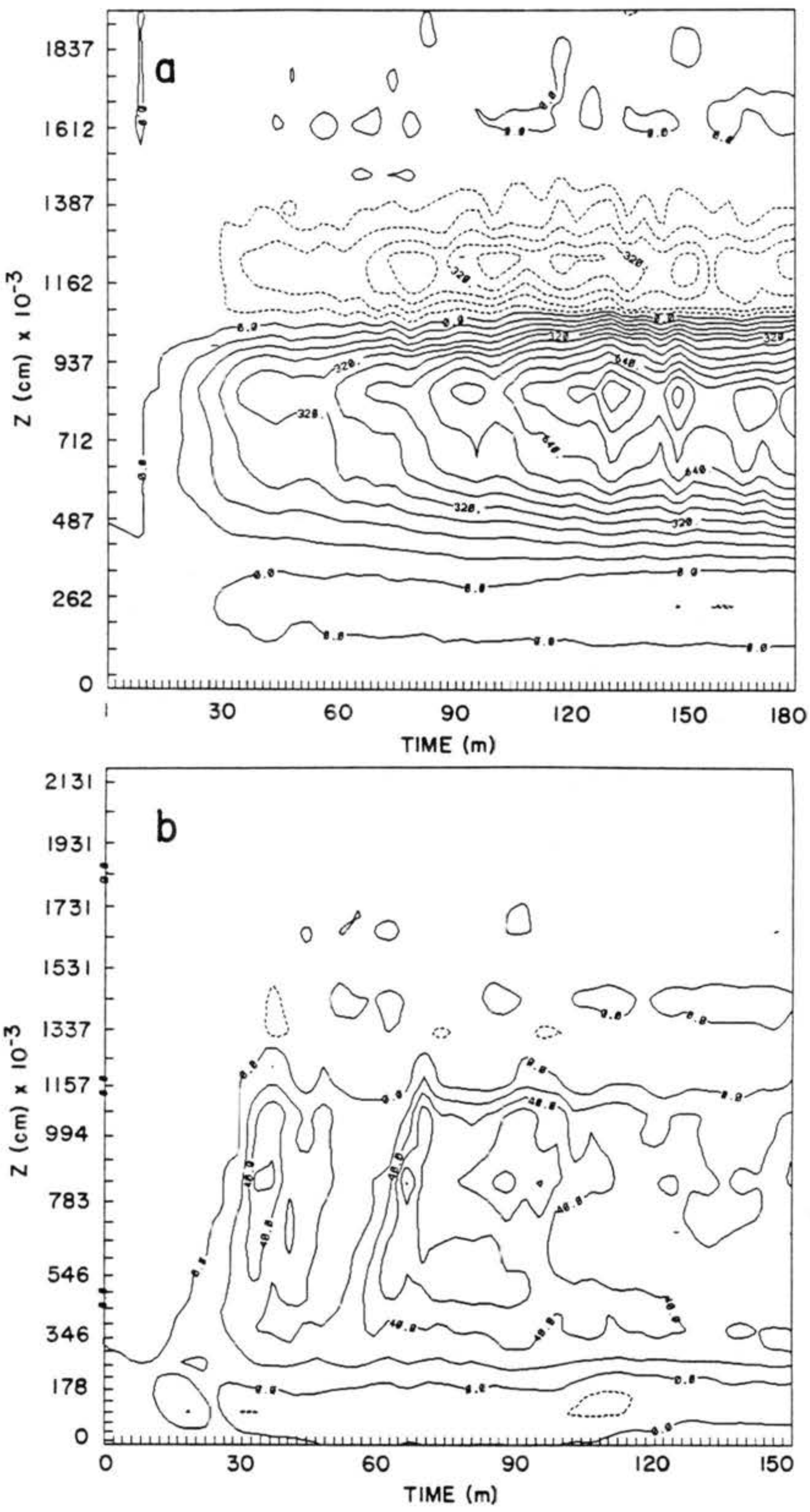

Figure 3.6: Time series of $\overline{w'\theta'}$ in cm-K/s as a function of height for (a) the CCOPE supercell, and (b) the tropical squall line.

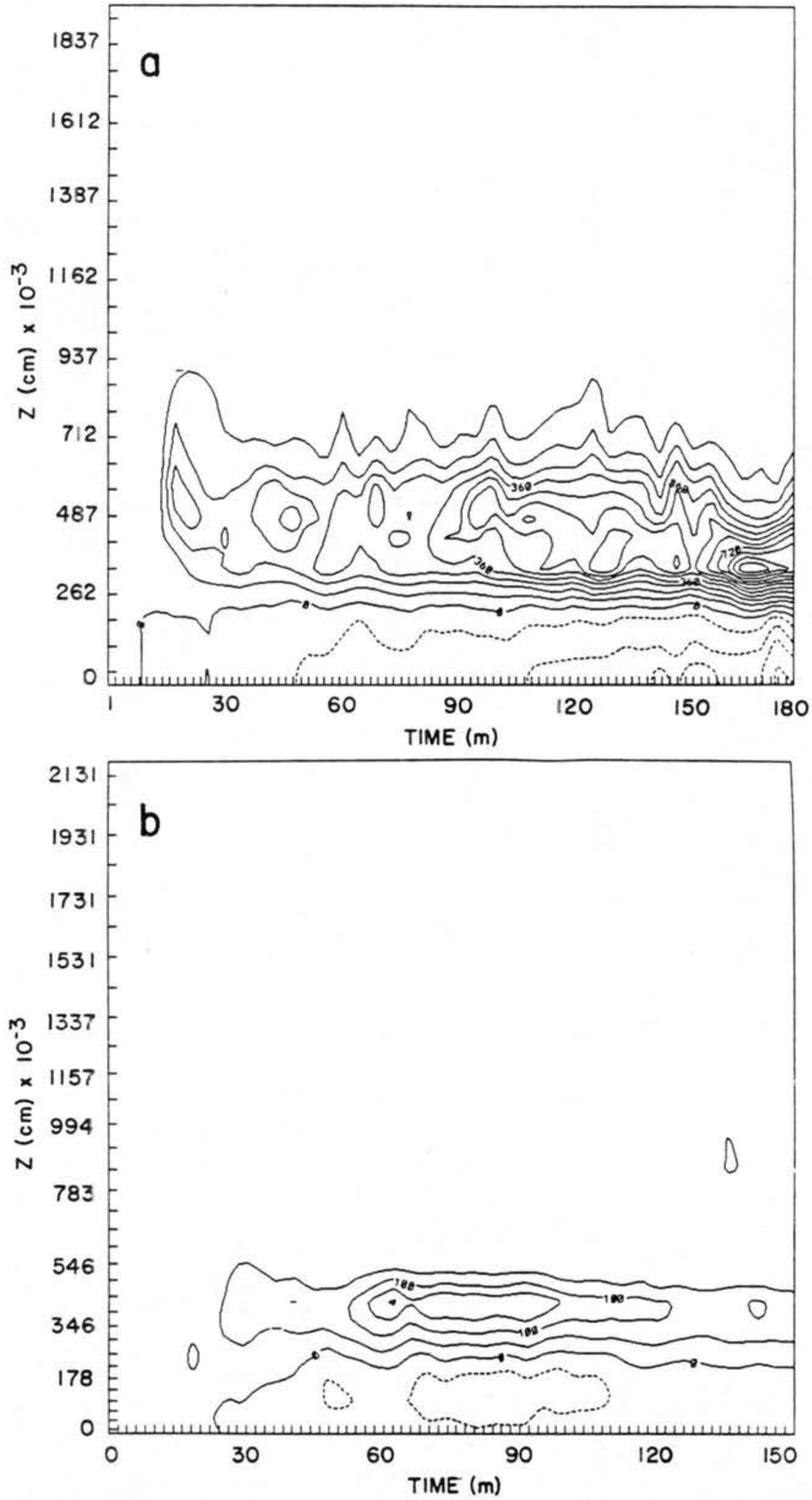

Figure 3.7: Time series of $\overline{w'r'_r}$ in cm/s as a function of height for (a) the CCOPE supercell, and (b) the tropical squall line. Labels are scaled by 10^3

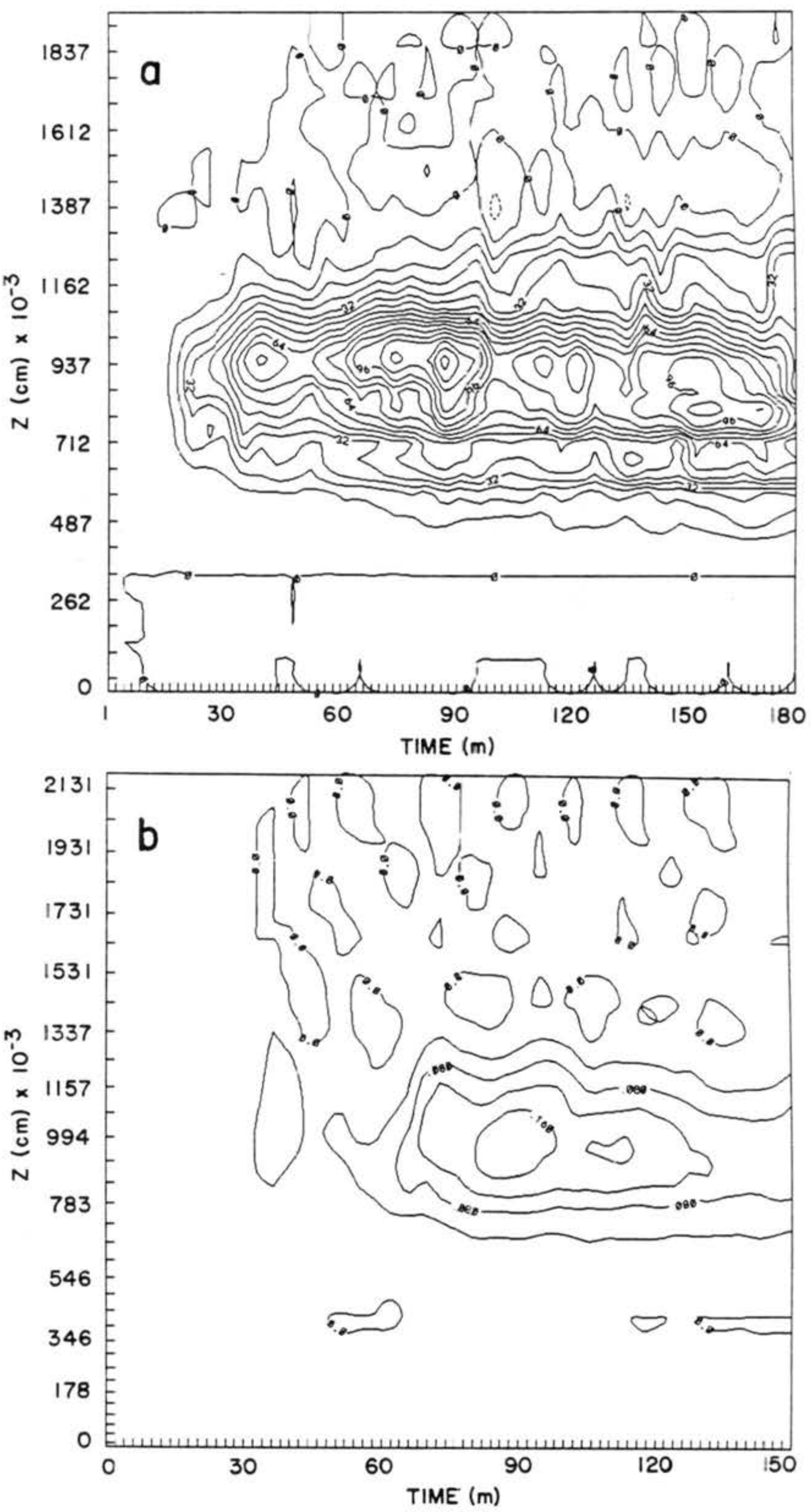

Figure 3.8: Time series of $\overline{w'r_i'}$ in cm/s as a function of height for (a) the CCOPE supercell (labels scaled by 10^3, and (b) the tropical squall line.

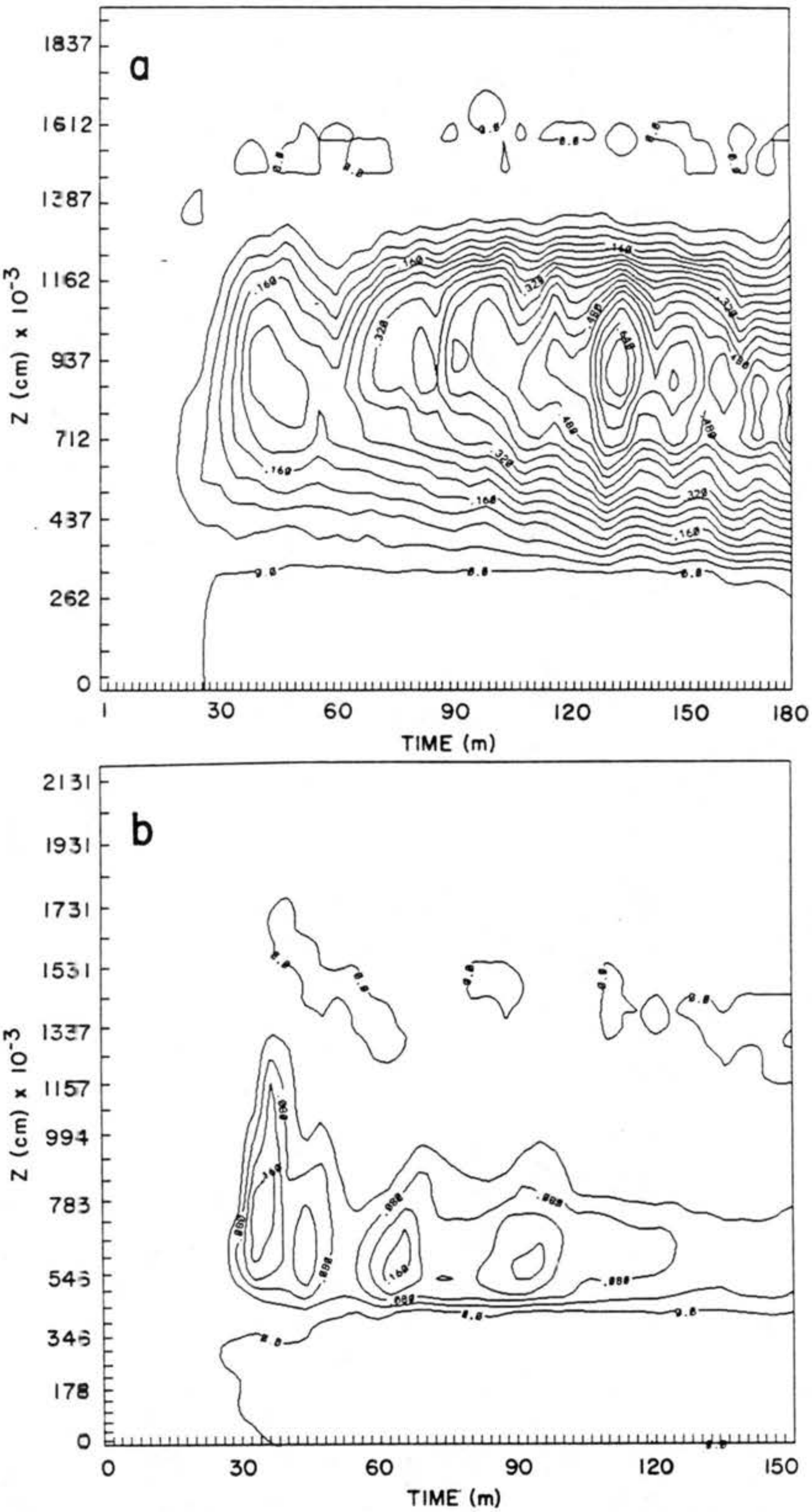

Figure 3.9: Time series of $\overline{w'r'_g}$ in cm/s as a function of height for (a) the CCOPE supercell, and (b) the tropical squall line.

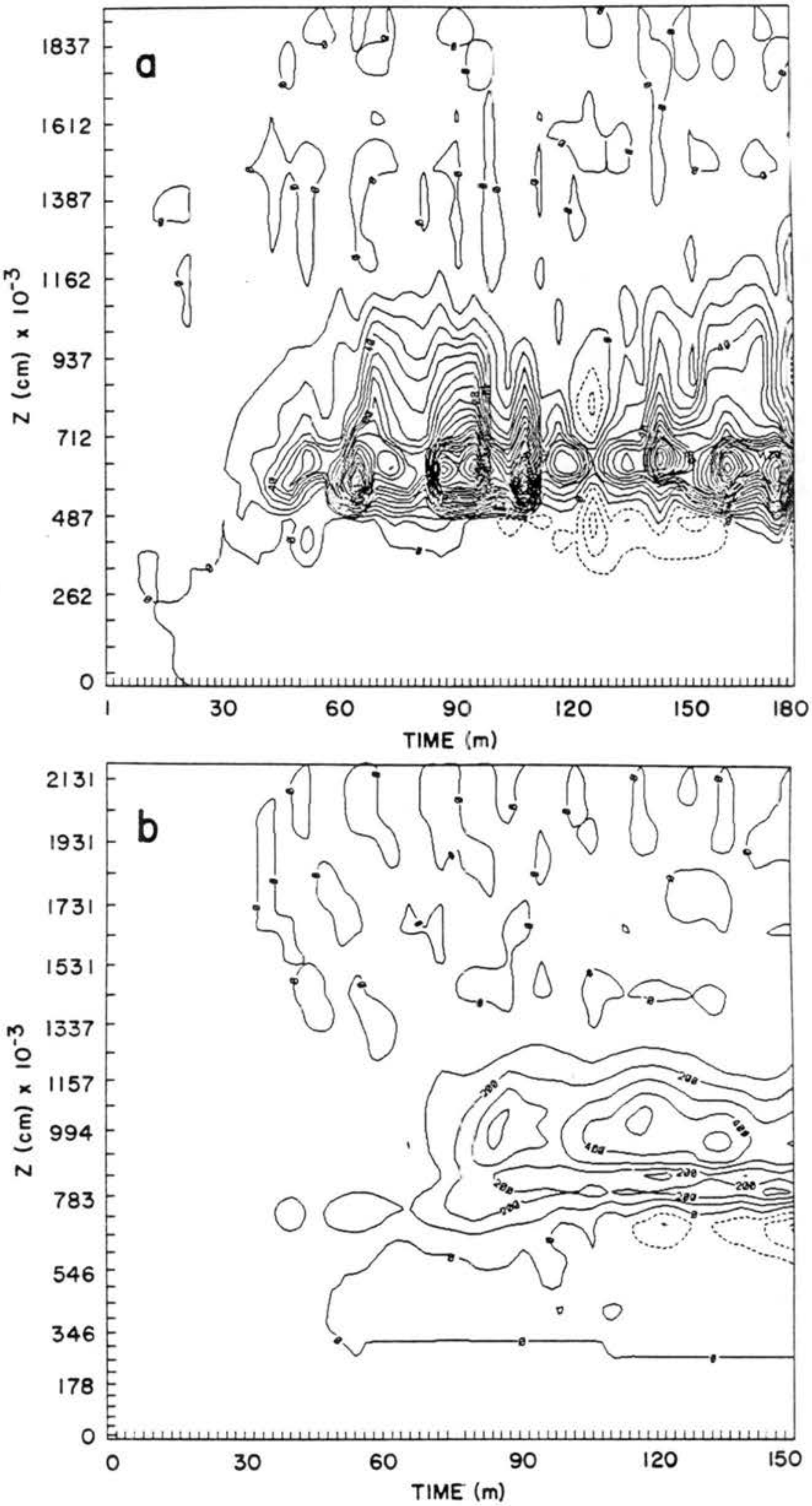

Figure 3.10: Time series of $\overline{w'r'_{ag}}$ in cm/s as a function of height for (a) the CCOPE supercell, and (b) the tropical squall line. Labels are scaled by 10^5

a cumulus parameterization scheme could be based on $\overline{w'w'}$. Therefore, the basis for the parameterization is presented below. As mentioned earlier, the scheme consists of two parts; the diagnosis of the cumulus fluxes and the closure modeling of the smaller-scale eddies.

3.3 Basis for the model components

The scheme name is based on the Mellor and Yamada (1974) hierarchy of higher order turbulence closures. In order to make the closure computationally feasible as a cumulus parameterization scheme, the number of prognostic variables is limited to one. The scheme is therefore a 2.5 level closure and, because it is based on $\overline{w'w'}$, it is termed a level 2.5w closure. As will be discussed in chapter 4, the two components of the model operate symbiotically. Conceptually, however, it will be easier to treat the parts separately.

3.3.1 The level 2.5w closure

Vertical variance is predicted for several reasons. First, the prognosis of $\overline{w'w'}$ allows for explicit vertical and horizontal advection of this quantity by the mean wind. This creates a parameterization scheme which is more global in nature since there is communication of convective activity between adjacent grid volumes. This offers a distinct advantage over all previous cumulus parameterization schemes since they all specify that convection grows, matures and decays within the same grid box. While this is an appropriate approximation for large grid sizes, as the grid size shrinks below 100 km, the approximation becomes increasingly inaccurate and is altogether invalid for grid sizes below a cloud diameter. Also by specifying the cloud existence within a given grid cell, the other schemes force compensating subsidence to occur within the same grid volume. As stated in the introduction, cloud induced subsidence remains within the grid cell when $\Delta \sim R'$ since the transient gravity waves approach gradient balance within a distance R' from the convective source. When $\Delta < R'$, transient gravity waves may affect several grid cells with subsident heating.

The vertical velocity variance is a direct and intuitive measure of convective activity. It can also explicitly respond to shear in a model since it is advected by the resolved winds.

With these points in mind, a term analysis diagnosed from the explicit simulations is performed on $\overline{w'w'}$ so that the behavior and magnitude of the terms could be investigated. A prognostic equation for $\overline{w'w'}$ will be fully derived in the next section, however the final for it is

$$\begin{aligned}\frac{\partial}{\partial t}\,\overline{w'w'} \quad = \quad & \underbrace{-\,\overline{U_j}\,\frac{\partial}{\partial x_j}\,\overline{w'w'}}_{ADV} \underbrace{-2\,\overline{w'u'_j}\,\frac{\partial\,\overline{W}}{\partial x_j}}_{SHRPRD} \underbrace{+2\,g\left(\frac{\overline{w'\theta'_v}}{\Theta_{vo}} - \overline{w'r'_w}\right)}_{BUOPRD} \\ & \underbrace{-\frac{\partial}{\partial z}\,\overline{w'w'w'}}_{EDYTRN} \underbrace{-2\,\frac{1}{\rho_o}\,\overline{w'\tfrac{\partial p'}{\partial z}}}_{PRS} \underbrace{-\,\frac{2}{3}\overline{\epsilon}}_{DIS}\,.\end{aligned} \tag{3.7}$$

ADV, SHRPRD, BUOPRD and DIS are the mean advection, shear production, buoyant production and dissipation of $\overline{w'w'}$, respectively and are relatively easy to represent. However the eddy transport and pressure terms are relatively difficult to model. Here arises one of the difficulties in predicting $\overline{w'w'}$ rather than turbulence kinetic energy; upon contraction of the Reynolds stress equation to form a TKE equation, the pressure terms drop out since they tend to distribute stress among the various components of TKE. However, they need to be modeled in the $\overline{w'w'}$ equation. In Fig. 3.11a and 3.11b, the diagnosed vertical profiles of these terms for the CCOPE supercell at 5408 sec and the tropical squall line at 1800 sec is shown. As is portrayed by the figure, the difficult terms to model are important in driving vertical variance. Note the large positive tendencies in Fig. 3.11b when the squall line exhibits strong growth. In Fig. 3.12, the term analysis is shown at 5400 sec for the squall line when it was more steady-state.

The shape of the component curves for both the supercell and squall line are similar. In particular, the eddy transport term closely balances the sum of the buoyancy production and pressure redistribution. Also note that in Fig. 3.11b, there is an imbalance in these three terms leading to a relatively large positive tendency for $\overline{w'w'}$ which is to be expected in the growing stage of a squall-line. The more steady-state behavior is represented by the closer balance and resulting smaller tendencies for $\overline{w'w'}$ in Figs. 3.11a and 3.12.

Zeman and Lumley (1976) modeled the buoyancy-driven mixed layer, including the eddy-transport and pressure terms. Their model produces vertical profiles of $\overline{w'w'w'}$ which have the characteristic shape shown in Fig. 3.13. The broad peak in the middle of

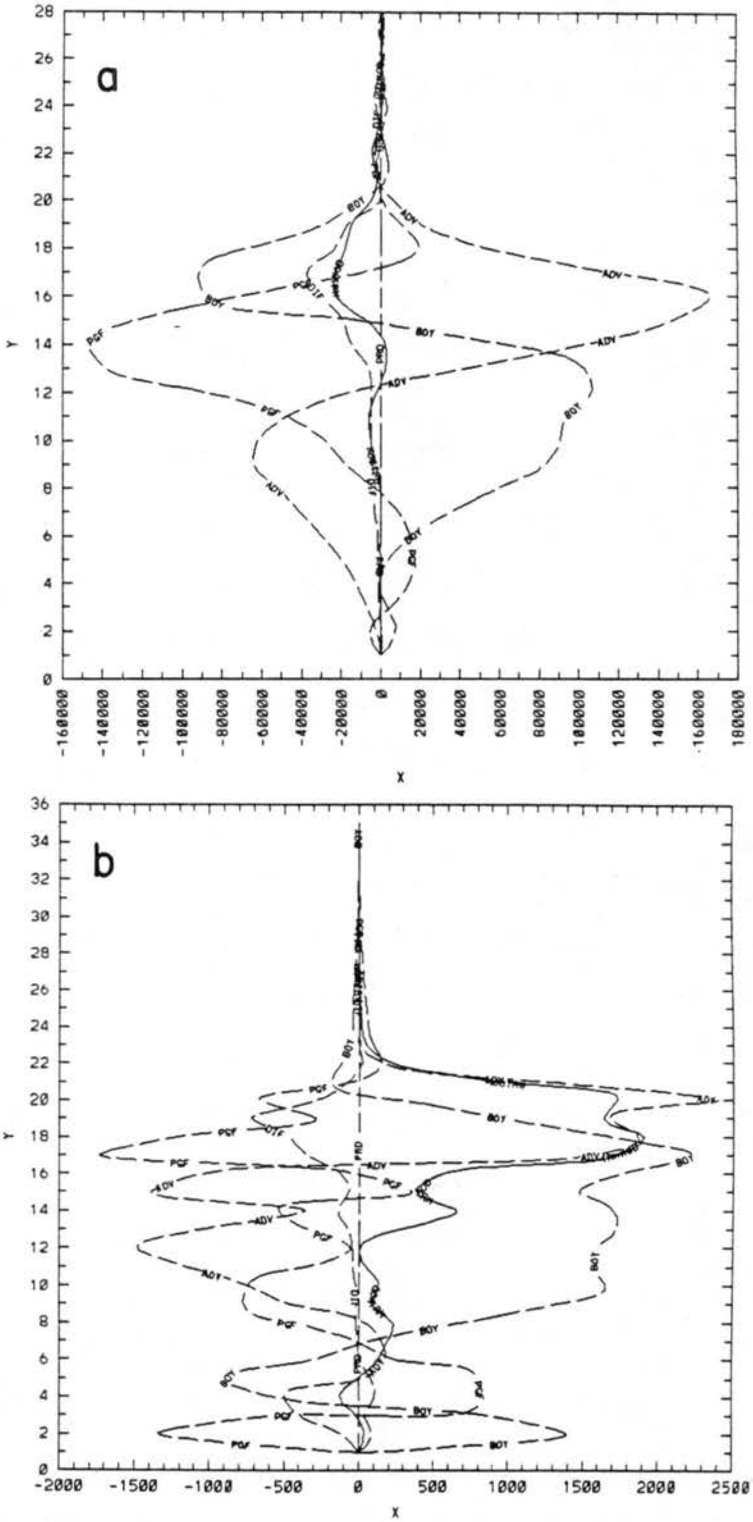

Figure 3.11: Term analysis of the time rate of change of $\overline{w'w'}$ in cm^2/s^3 as a function of model level for (a) the CCOPE supercell, and (b) the tropical squall line. The solid lines are the sum of curves (BOY) buoyancy, (PGF) pressure gradient force, (ADV) eddy transport, and (DIF) diffusion which equals the tendency as determined from numerical model.

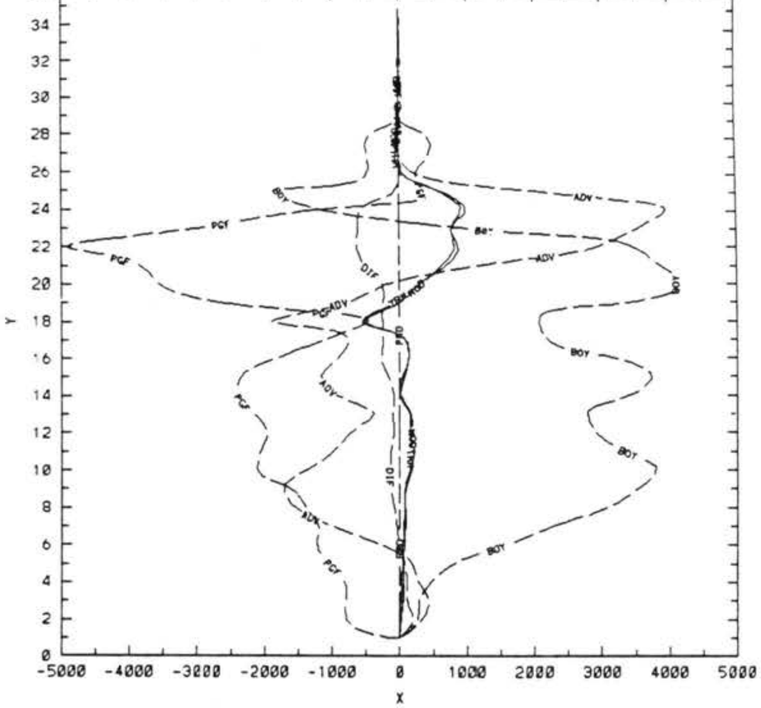

Figure 3.12: As in Fig. 3.11b except for the tropical squall line at 5400 sec when it exhibits steady-state behavior.

the mixed layer also appears in the eddy-transport curve in Figs. 3.11a, 3.11b and 3.12 when this curve is integrated from the mixed layer top to the bottom. The broad similarity between this term and the general profile of $\overline{w'w'}$ in our studies and Zeman and Lumley's study has led us to adopt their method of modeling the pressure and eddy-advection terms in Eq. 3.7. The scheme is promising since the main difference between their buoyancy driven mixed layer and our free atmosphere is that theirs is driven with a heat source located at the ground while deep convection is driven by latent heat release in the lower and mid-troposphere.

3.3.2 The cumulus fluxes

Given that $\overline{w'w'}$ can be reasonably predicted for cumulus clouds, a quantitative model is needed to retrieve the covariances. A cumulus flux model first proposed by Arakawa (1969) and developed by Betts (1975) is attractive because it is simple and intuitive. The parameterized convective flux is derived from a convective velocity and a

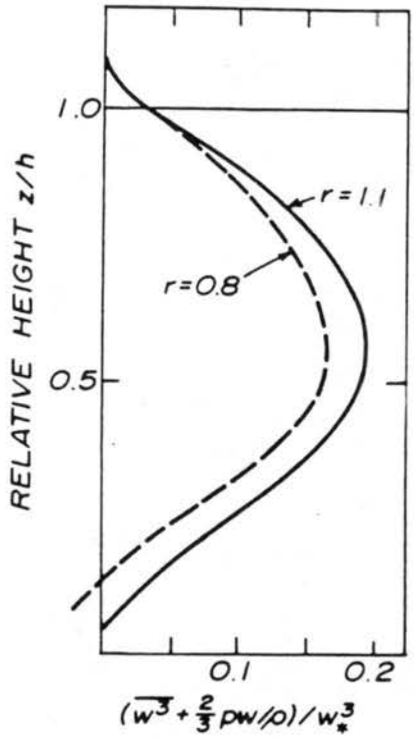

Figure 3.13: Zeman and Lumley's (1976) $\overline{w'w'w'}$ profile (from their Fig. 8).

one dimensional cloud model, *i. e.*

$$\overline{w'\chi'} \quad = \quad \sigma w^* \left(\overline{\mathcal{X}_u} - \overline{\mathcal{X}_e}\right) \tag{3.8}$$

where $\overline{w'\chi'}$ is any vertical variance, w^* is the convective velocity, and $\overline{\mathcal{X}_u}$ and $\overline{\mathcal{X}_e}$ are the updraft properties as determined from a one-dimensional cloud model and the environmental or resolved properties, respectively. The cloud fractional coverage is designated by σ. The convective flux model in this form is compared with the vertical covariances of potential temperature explicitly calculated over the model domain for the two simulations in Figs. 3.14a and 3.14b. Cloud fractional coverage was assumed to be around 10 percent, however, the actual value is unimportant since it will have to be diagnosed in the cumulus parameterization scheme. The agreement is excellent and indicates that this model can satisfactorily diagnose the convective fluxes if the fractional coverage and the convective velocity are prescribed.

Also shown in Figs. 3.15a and 3.15b are the parameterized convective fluxes for total water and the explicitly calculated total water flux. The agreement is not as good, but

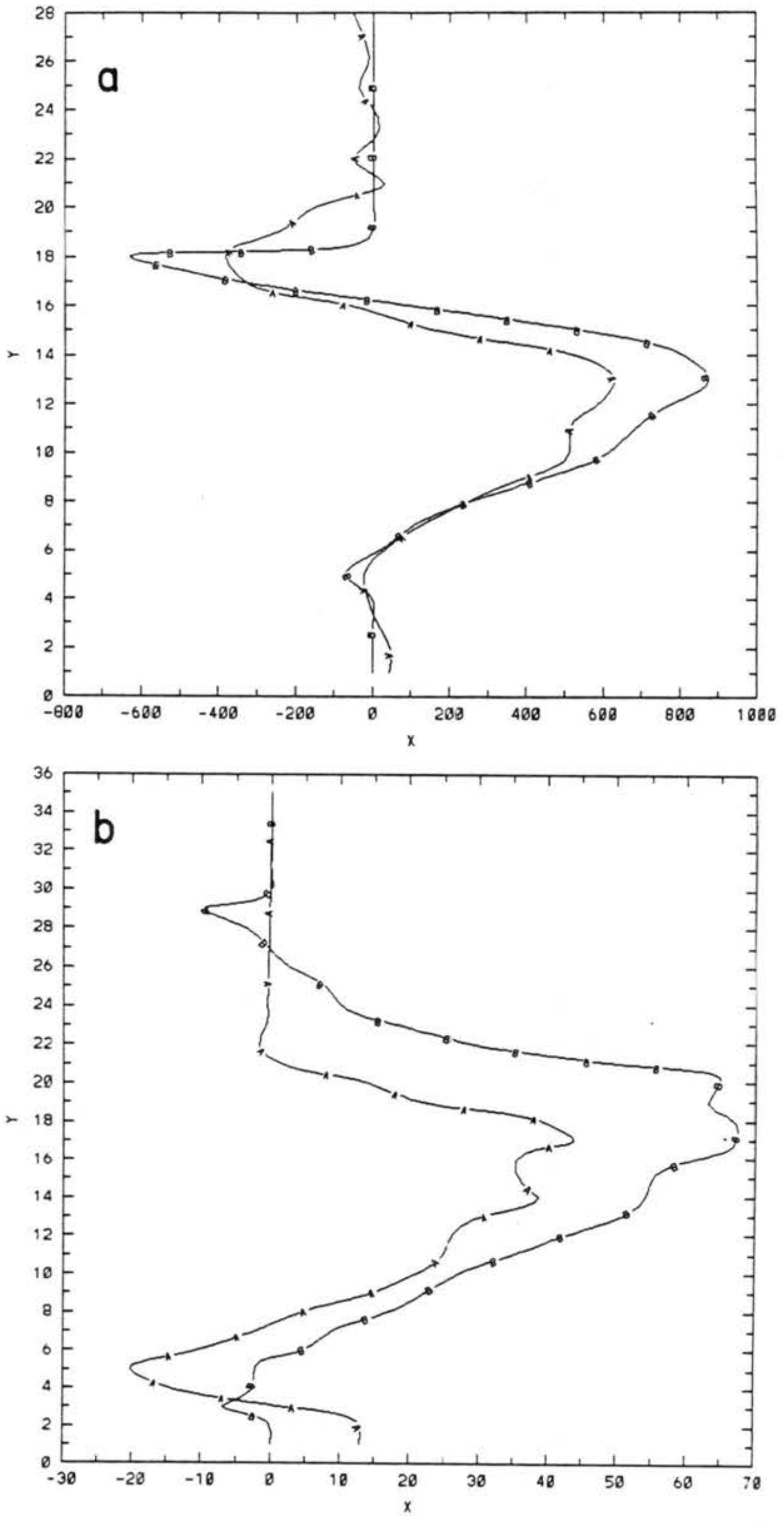

Figure 3.14: Vertical profiles of the flux of potential temperature in cm-K/s explicitly calculated from the numerical model (curve A) and the parameterized flux (curve B) for (a) the CCOPE supercell, and (b) the tropical squall line.

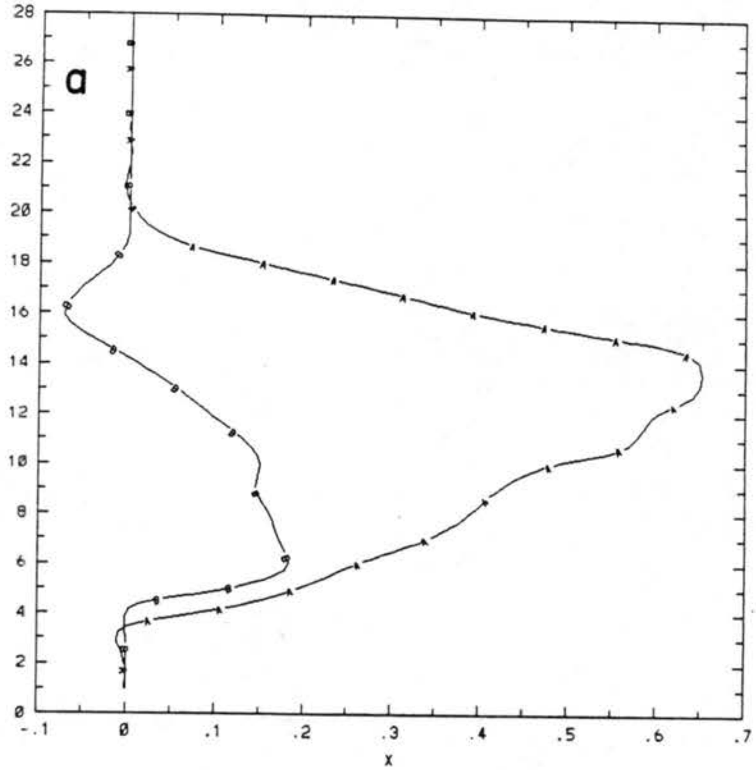

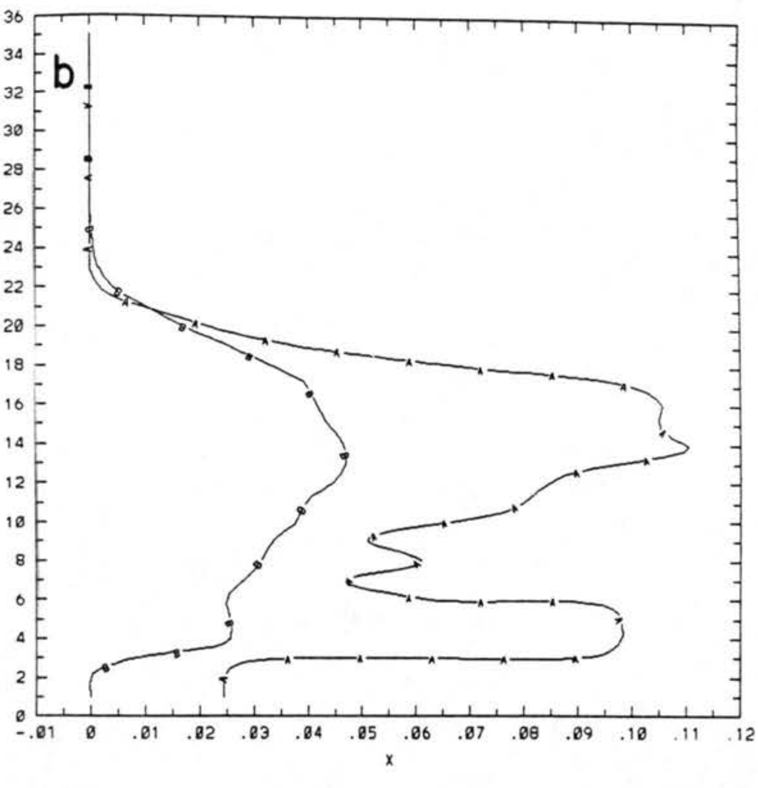

Figure 3.15: Vertical profiles of the flux of total water in cm/s explicitly calculated from the numerical model (curve A) and the parameterized flux (curve B) for (a) the CCOPE supercell, and (b) the tropical squall line.

this is to be expected since the cloud model has no precipitation scheme. The convective fluxes (determined with Eq. 3.8 and diagnosing w^* as $\sqrt{\overline{w'w'}}$), then, roughly agree with the explicitly calculated covariances.

There is now a broad basis on which to formulate the cumulus parameterization scheme. A tropical squall line and a mid-latitude supercell are shown to exhibit striking similarity in the behavior of $\overline{w'w'}$. Furthermore, the vertical convective fluxes of ice-liquid potential temperature, total water and the other microphysical variables bear resemblance to $\overline{w'w'}$. Therefore, the parameterization is based on $\overline{w'w'}$. A model for the diagnosis of the convective flux has been presented and shown to broadly represent the explicitly calculated flux for potential temperature and total water. And finally, a way to close the prognostic equation for $\overline{w'w'}$ has been proposed.

The task now is to implement the closures for the prognostic $\overline{w'w'}$ equation and develop a cloud model with precipitation that will yield the cumulus forcing terms.

Chapter 4

THE LEVEL 2.5W CUMULUS MODEL

In this chapter, the modified second order turbulence model and the cumulus model used in the cumulus parameterization are described. Although these two parts of the parameterization operate symbiotically, they will be described separately. The level 2.5w model is based on higher order closure theory and incorporates terms important to modeling buoyancy-driven mixed layers. The cumulus model incorporates a one dimensional cloud model and parameterized hydrometeor profiles derived from the explicit simulations of the CCOPE supercell and the tropical squall line described in earlier chapters. Furthermore, the cumulus model contains a parameterization for fractional updraft and downdraft core coverage based upon a bulk Richardson number.

4.1 The level 2.5w model

The turbulence model follows closely the Mellor and Yamada (1974) system of equations. They have based the number of prognostic equations in their generalized second order turbulence scheme on the degree of anisotropy of the system. Their Level 4 scheme includes prognostic equations on all variances and covariances while their Level 3 includes prognostic equations on turbulence kinetic energy (TKE) and potential temperature variance. They have also formulated a Level 2.5 model which predicts only on TKE; all other variances and covariances are diagnosed. They have found that the Level 2.5 model performs reasonably well in predicting the development of the PBL except during times when the PBL is undergoing significant change, *i. e.* at sunset and sunrise. This is to be expected since the degree of anisotropy grows large and the scaled equations no longer represent reality.

In order to maintain simplicity, only one second order quantity is predicted. Because of the behavior of $\overline{w'w'}$ discussed in the previous chapter, $\overline{w'w'}$ is predicted instead of TKE and thus the model is labeled level 2.5w. All other variances and covariances are diagnostic. Because the same problems as Mellor and Yamada are encountered when the turbulence changes quickly, several constraints were imposed on the model. These include the clipping approximation of André *et al.* (1976) and limiting the obtainable values of certain coefficients in the algebraic solution of the diagnostic equations as in Hassid and Galperin (1983).

The present formulation uses the thermodynamic variable θ_{il} as described in the previous chapter. If Eq. 3.6 is linearized by assuming $\theta_{il} = \overline{\Theta_{il}} + \theta_{il}{}'$ and the ice and liquid water mixing ratios are decomposed similarly, and the assumption $\overline{\Theta_{il}} \sim \Theta$ is used, then

$$\theta' = \theta_{il}{}' + \frac{L_{lv}\overline{\Theta}}{C_pT}r_l' + \frac{L_{iv}\overline{\Theta}}{C_pT}r_i' \tag{4.1}$$

is obtained.

The equations for the second moment quantities contain terms that involve covariances with the density perturbation. Density perturbation will therefore be expressed as a function of the model variables. From Manton and Cotton (1977), the density perturbation equation can be written as

$$\frac{\rho'}{\rho_o} = -\frac{\theta'}{\overline{\overline{\Theta_o}}} - \left(\frac{R_v}{R_a} - 1\right) r_t' + \frac{R_v}{R_a}r_l' + \frac{R_v}{R_a}r_i' + \frac{1}{\gamma}\frac{p'}{\overline{\overline{P_o}}} \tag{4.2}$$

where $\gamma = \frac{C_p}{C_v}$. After substituting Eq. 4.1 into Eq. 4.2, the expression relating density perturbations to θ_{il} perturbations is

$$\frac{\rho'}{\rho_o} = -\frac{\theta_{il}{}'}{\overline{\overline{\Theta_o}}} - \left(\frac{R_v}{R_a} - 1\right) r_t' + \left(\frac{R_v}{R_a} - \frac{L_{lv}\overline{\Theta}}{C_pT}\right) r_l' + \left(\frac{R_v}{R_a} - \frac{L_{iv}\overline{\Theta}}{C_pT}\right) r_i' + \frac{1}{\gamma}\frac{p'}{\overline{\overline{P_o}}}. \tag{4.3}$$

From 4.3 the covariance of density perturbations with any variable a' is

$$-\frac{g}{\rho_o}\overline{a'\rho'} = \beta_n\overline{a'\theta_n'},$$

where

$$\beta_n \overline{a'\theta'_n} = \begin{bmatrix} \frac{g}{\Theta_o} \\ g\left(\frac{R_v}{R_a} - 1\right) \\ g\left(\frac{L_{lv}\Theta_0}{C_p T} - \frac{R_v}{R_a}\right) \\ g\left(\frac{L_{iv}\Theta_0}{C_p T} - \frac{R_v}{R_a}\right) \\ -\frac{g}{\gamma P_o} \end{bmatrix} \begin{bmatrix} \overline{a'\theta'_{il}} \\ \overline{a'r'_t} \\ \overline{a'r'_l} \\ \overline{a'r'_i} \\ \overline{a'p'} \end{bmatrix}. \tag{4.4}$$

The correlations with pressure are appropriate for deep convective flows. The calculations done thus far do not include this term.

After decomposing the variables as $U_i = \overline{U_i} + u'_i$ where the overbar represents the grid-volume-averaged variables and the prime represents sub-grid scale deviations from this average, the fully prognostic second order equation set is as follows:

$$\begin{aligned}
\frac{\partial}{\partial t}\overline{u'_i u'_k} = & -\underbrace{\overline{U_j}\frac{\partial}{\partial x_j}\overline{u'_i u'_k}}_{ADV} - \underbrace{\left(\overline{u'_i u'_j}\frac{\partial \overline{U_k}}{\partial x_j} + \overline{u'_k u'_j}\frac{\partial \overline{U_i}}{\partial x_j}\right)}_{SHRPRD} \\
& + \underbrace{\delta_{3k}\beta_n\overline{u'_i\theta'_n} + \delta_{i3}\beta_n\overline{u'_k\theta'_n}}_{BUOPRD} \\
& - \underbrace{\frac{\partial}{\partial x_j}\left(\overline{u'_i u'_j u'_k}\right)}_{EDYTRN} - \underbrace{\frac{1}{\rho_o}\left(\overline{u'_k\frac{\partial p'}{\partial x_i}} + \overline{u'_i\frac{\partial p'}{\partial x_k}}\right)}_{PRS=\Pi_{ik}} - \underbrace{\frac{2}{3}\epsilon}_{DIS}
\end{aligned} \tag{4.5}$$

$$\begin{aligned}
\frac{\partial}{\partial t}\overline{u'_i a'} = & -\underbrace{\overline{U_j}\frac{\partial}{\partial x_j}\overline{u'_i a'}}_{ADV} - \underbrace{\left(\overline{u'_i u'_j}\frac{\partial \overline{A}}{\partial x_j} + \overline{u'_j a'}\frac{\partial \overline{U_i}}{\partial x_j}\right)}_{SHRPRD} \\
& + \underbrace{\delta_{i3}\beta_n\overline{a'\theta'_n}}_{BUOPRD} - \underbrace{\frac{\partial}{\partial x_j}\overline{u'_i u'_j a'}}_{EDYTRN} - \underbrace{\frac{1}{\rho_o}\overline{a'\frac{\partial p'}{\partial x_i}}}_{PRS=\Pi_i}
\end{aligned} \tag{4.6}$$

$$\frac{\partial}{\partial t}\overline{a'b'} = -\underbrace{\overline{U_j}\frac{\partial}{\partial x_j}\overline{a'b'}}_{ADV} - \underbrace{\left(\overline{u'_j a'}\frac{\partial \overline{B}}{\partial x_j} + \overline{u'_j b'}\frac{\partial \overline{A}}{\partial x_j}\right)}_{SHRPRD} - \underbrace{\frac{\partial}{\partial x_j}\overline{u'_j a' b'}}_{EDYTRN} - \underbrace{2\epsilon}_{DIS} \tag{4.7}$$

Here, u represents the horizontal and vertical velocities and a and b are any of the scalar variables. ADV represents the advection of the covariance or variance by the mean wind, SHRPRD and BUOPRD represents the production of these by shear and buoyancy, respectively, EDYTRN represents the transport of these quantities by the eddies, PRS represents the sub-grid scale pressure forces and DIS represents dissipative forces.

In order to clarify the behavior of the pressure term, the term is manipulated as follows:

$$
\begin{aligned}
\Pi_{ik} &= \frac{1}{\rho_o}\left(\overline{u'_k\frac{\partial p'}{\partial x_i}} + \overline{u'_i\frac{\partial p'}{\partial x_k}}\right) \\
&= \frac{1}{\rho_o}\left(\underbrace{\frac{\partial}{\partial x_i}\,\overline{u'_k p'} + \frac{\partial}{\partial x_k}\,\overline{u'_i p'}}_{PRSDIF} - \left[\underbrace{\overline{p'\frac{\partial u'_k}{\partial x_i}} + \overline{p'\frac{\partial u'_i}{\partial x_k}}}_{RTN\ TO\ ISO}\right]\right).
\end{aligned}
$$

Here, PRSDIF represents the pressure-diffusion term and RTN TO ISO is the return to isotropy term. The main effect of this term is to distribute the Reynolds stress amongst the three components of TKE.

In order to form a prognostic equation on $\overline{w'w'}$, the indexes i and k are equated in Eq. 4.5. The result is:

$$
\begin{aligned}
\frac{\partial}{\partial t}\,\overline{w'w'} &= \underbrace{-\,\overline{U_j}\,\frac{\partial}{\partial x_j}\,\overline{w'w'}}_{ADV}\ \underbrace{-2\,\overline{w'u'_j}\,\frac{\partial\,\overline{W}}{\partial x_j}}_{SHRPRD} + 2\underbrace{\beta_n\,\overline{w'\theta'_n}}_{BUOPRD} \\
&\quad \underbrace{-\left(\frac{\partial}{\partial z}\,\overline{w'w'w'} + \frac{2}{3}\frac{1}{\rho_o}\frac{\partial}{\partial x_j}\,\overline{u'_j p'}\right)}_{EDYTRN} \\
&\quad \underbrace{-\frac{1}{\rho_o}\left(2\,\overline{w'\frac{\partial p'}{\partial z}} - \frac{2}{3}\frac{\partial}{\partial x_j}\,\overline{u'_j p'}\right)}_{PRS=\Pi_{33}} - \underbrace{\frac{2}{3}\overline{\epsilon}}_{DIS}\,. \qquad (4.8)
\end{aligned}
$$

Note that in Eq. 4.8, the divergence of $\overline{u'_j p'}$ has been added to the eddy transport term and subtracted from the pressure term in anticipation of future manipulation.

To form the velocity variances and covariances, Eq. 4.5 is contracted. Furthermore, if $\overline{u'_i u'_i} = q^2$ where q^2 is the TKE and $\frac{d}{dt} = \frac{\partial}{\partial t} + \overline{U_j}\,\frac{\partial}{\partial x_j}$, the resultant TKE equation is

$$
\frac{d}{dt}q^2 = -2\,\overline{u'_i u'_j}\,\frac{\partial\,\overline{U_i}}{\partial x_j} + 2\delta_{i3}\beta_n\,\overline{u'_i\theta'_n} - \frac{\partial}{\partial x_j}\,\overline{u'_j q^2} - \frac{2}{\rho_o}\frac{\partial}{\partial x_j}\,\overline{u'_j p'} - 2\overline{\epsilon}. \qquad (4.9)
$$

Note that the return to isotropy term of the pressure term vanishes since turbulence is assumed to be incompressible. If Eq. 4.9 is multiplied by $\frac{1}{3}\delta_{ik}$, then

$$
\begin{aligned}
\frac{d}{dt}\,\tfrac{1}{3}\delta_{ik}\,q^2 &= -\,\tfrac{2}{3}\delta_{ik}\,\overline{u'_i u'_j}\,\frac{\partial\,\overline{U_i}}{\partial x_j} + \tfrac{2}{3}\delta_{ik}\,\delta_{3k}\beta_n\,\overline{u'_i\theta'_n} \\
&\quad -\,\tfrac{1}{3}\delta_{ik}\,\frac{\partial}{\partial x_j}\,\overline{u'_j q^2} - \tfrac{2}{3}\delta_{ik}\,\frac{1}{\rho_o}\frac{\partial}{\partial x_j}\,\overline{u'_j p'} - \tfrac{2}{3}\delta_{ik}\,\overline{\epsilon}. \qquad (4.10)
\end{aligned}
$$

Now, by subtracting Eq. 4.10 from Eq. 4.5, the departure from isotropy equation is

$$
\begin{aligned}
\frac{d}{dt} a_{ik} q^2 \;=\; & -\left(\overline{u_i' u_j'} \, \frac{\partial \, \overline{U_k}}{\partial x_j} + \overline{u_k' u_j'} \, \frac{\partial \, \overline{U_i}}{\partial x_j} - \tfrac{2}{3}\delta_{ik} \; \overline{u_i' u_j'} \; \frac{\partial \, \overline{U_k}}{\partial x_j} \right) \\
& + \delta_{3k}\beta_n \; \overline{u_i' \theta_n'} \; + \delta_{i3}\beta_n \; \overline{u_k' \theta_n'} \; - \; \tfrac{2}{3}\delta_{ik} \; \delta_{3k}\beta_n \; \overline{u_i' \theta_n'} \\
& - \frac{\partial}{\partial x_j} \left(\; \overline{u_i' u_j' u_k'} \; - \; \tfrac{1}{3}\delta_{ik} \; \overline{u_j' q^2} \; \right) \\
& - \frac{1}{\rho_o} \left(\; \overline{u_k' \tfrac{\partial p'}{\partial x_i}} + \; \overline{u_i' \tfrac{\partial p'}{\partial x_k}} - \frac{2}{3}\delta_{ik} \frac{\partial}{\partial x_j} \; \overline{u_j' p'} \; \right),
\end{aligned} \tag{4.11}
$$

where the departure from isotropy tensor is defined as

$$
a_{ik} = \frac{\overline{u_i' u_k'}}{q^2} - \frac{1}{3}\delta_{ik}.
$$

Note that the dissipation term has vanished. Also note the appearance of the term $-\frac{2}{3}\delta_{ik}\frac{\partial}{\partial x_j} \; \overline{u_j' p'}$ in the pressure term of Eq. 4.11. This is why the transport and pressure terms in Eq. 4.8 are formulated with the addition of the divergence of the pressure-velocity correlation.

The pressure term is modeled after Rotta (1951) who modeled the return to isotropy part and Mellor (1973) who added the effects of buoyancy. This is the 'rapid' part of the pressure term and is due to buoyancy-turbulence interactions. Terms have been added to represent virtual and water loading effects in their formulation. The diagnostic pressure term then is

$$
\begin{aligned}
\Pi_{ik} \;=\; & \frac{1}{\rho_o} \left(\; \overline{u_k' \tfrac{\partial p'}{\partial x_i}} + \; \overline{u_i' \tfrac{\partial p'}{\partial x_k}} - \frac{2}{3}\delta_{ik} \frac{\partial}{\partial x_j} \; \overline{u_j' p'} \; \right) \\
\;=\; & \frac{C_s}{\tau} a_{ik} q^2 - C_1 q^2 \left(\frac{\partial \, \overline{U_i}}{\partial x_k} + \frac{\partial \, \overline{U_k}}{\partial x_i} \right) \\
& + C_2 \left(\delta_{3k}\beta_n \; \overline{u_i' \theta_n'} \; + \delta_{i3}\beta_n \; \overline{u_k' \theta_n'} \; - \; \tfrac{2}{3}\delta_{ik} \; \delta_{3k}\beta_n \; \overline{u_i' \theta_n'} \; \right).
\end{aligned} \tag{4.12}
$$

The first and second terms on the rhs of the above equation represent the return to isotropy and shear components, respectively of the pressure term as proposed by Rotta for neutral flows. The remaining terms include buoyancy effects on the redistribution of energy amongst the three velocity components.

Zeman and Tennekes (1975) developed a self contained model for Π_{ik} which considered interactions between turbulence and the mean strain rate and the mean vorticity separately so that the Coriolis effect could be included implicitly. Sun and Ogura (1980) applied this model to the evolving convective boundary layer. The form of the pressure term then becomes

$$
\begin{aligned}
\Pi_{ik} &= \frac{C_s}{\tau} a_{ik} q^2 + C_2 \left(\delta_{3k}\beta_n \overline{u_i'\theta_n'} + \delta_{i3}\beta_n \overline{u_k'\theta_n'} - \tfrac{2}{3}\delta_{ik}\, \delta_{3k}\beta_n \overline{u_i'\theta_n'} \right) \\
&\quad - C_1 q^2 S_{ik} - q^2 \left[2\alpha_1 \left(S_{ij} a_{jk} + S_{jk} a_{ij} - \frac{2}{3} S_{jl} a_{lj} \delta_{ik} \right) \right. \\
&\quad \left. + 2\gamma_1 \left(R_{ij} a_{jk} - R_{jk} a_{ij} \right) \right],
\end{aligned}
$$

where $C_2 = \frac{3}{10}$ and $C_1 = \frac{2}{5}$. The mean strain rate and vorticity tensors are given by

$$
\begin{aligned}
S_{ik} &= \frac{1}{2} \left(\frac{\partial \overline{U_i}}{\partial x_k} + \frac{\partial \overline{U_k}}{\partial x_i} \right) \\
R_{ik} &= \frac{1}{2} \left(\frac{\partial \overline{U_i}}{\partial x_k} - \frac{\partial \overline{U_k}}{\partial x_i} \right) - 2\epsilon_{ijk}\Omega_k .
\end{aligned}
$$

The Eq. 4.12 will be used as the formulation for the pressure term and the possible improvement in model results by using the more general formulation above is noted.

If steady-state is assumed, advection and eddy-transport terms are neglected and Eq. 4.12 with $\frac{q}{3l_1}$ for $\frac{C_s}{\tau}$ (as in Mellor, 1973) is substituted into Eq. 4.11, the following relationship for the velocity variances and covariances is

$$
\begin{aligned}
\frac{q}{3l_1} a_{ik} q^2 &= -\left(\overline{u_i'u_j'} \frac{\partial \overline{U_k}}{\partial x_j} + \overline{u_k'u_j'} \frac{\partial \overline{U_i}}{\partial x_j} - \tfrac{2}{3}\delta_{ik}\ \overline{u_i'u_j'} \frac{\partial \overline{U_i}}{\partial x_j} \right) \\
&\quad + C_1 q^2 \left(\frac{\partial \overline{U_i}}{\partial x_k} + \frac{\partial \overline{U_k}}{\partial x_i} \right) \\
&\quad (1 + C_2) \left[\delta_{3k}\beta_n \overline{u_i'\theta_n'} + \delta_{i3}\beta_n \overline{u_k'\theta_n'} - \tfrac{2}{3}\delta_{ik}\, \delta_{3k}\beta_n \overline{u_i'\theta_n'} \right] .
\end{aligned}
\tag{4.13}
$$

The remaining diagnostic equations are formed by assuming that the covariances or variances are constant in time and that advection, eddy transport and any precipitation effects are negligible in Eqs. 4.6 and 4.7. Furthermore, the pressure term in Eq. 4.6 is modeled as

$$
\Pi_i = \frac{C_\theta}{\tau} \overline{u_i'a'} + \frac{1}{3}\delta_{i3} \overline{a'\theta_n'} . \tag{4.14}
$$

As in the formulation for Π_{ik}, a more general expression for Π_i is

$$
\begin{aligned}
\Pi_i &= \frac{C_\theta}{\tau} \overline{u_i'a'} - \frac{4}{5} \frac{\partial \overline{U_k}}{\partial x_j} \left[\overline{u_j'a'}\, \delta_{ik} - \frac{1}{4} \left(\overline{u_i'a'}\, \delta_{kj} - \overline{u_k'a'}\, \delta_{ji} \right) \right] \\
&\quad + \frac{1}{3}\delta_{i3} \overline{a'\theta_n'} .
\end{aligned}
$$

Zeman and Lumley (1976) note that the constant of $\frac{1}{3}$ in front of the buoyancy terms may be as small as $\frac{1}{5}$ for strongly anisotropic flows. Formulating the pressure term like this allows vector covariances with scalars to be expressed as a balance between the production of the covariance and its redistribution through pressure forces. Substituting Eq. 4.14 into Eq. 4.6 and assuming steady-state and neglecting advection and eddy-transport yields

$$\frac{q}{3l_2}\,\overline{u_i'a'} \;=\; -\left(\overline{u_i'u_j'}\,\frac{\partial\,\overline{A}}{\partial x_j} + \overline{u_j'a'}\,\frac{\partial\,\overline{U_i}}{\partial x_j}\right) + \frac{2}{3}\delta_{i3}\beta_n\,\overline{a'\theta_n'}\,. \tag{4.15}$$

Similarly, scalar covariances with scalars can be formed by assuming a length scale Λ_2 for dissipation such that

$$\epsilon \;=\; \frac{q}{\Lambda_2}\,\overline{a'b'}\,,$$

thus forcing a balance between production and dissipation, *i. e.*

$$2\frac{q}{\Lambda_2}\,\overline{a'b'} \;=\; -\left(\overline{u_j'a'}\,\frac{\partial\,\overline{B}}{\partial x_j} + \overline{u_j'b'}\,\frac{\partial\,\overline{A}}{\partial x_j}\right). \tag{4.16}$$

All length scales are assumed proportional to each other and a master length scale l, with the constants of proportionality gleaned from turbulence data. Therefore,

$$\begin{aligned}(l_1, \Lambda_1, l_2, \Lambda_2) \;&=\; l\,(A_1, B_1, A_1, B_1) \qquad (4.17)\\ &=\; l\,(0.78, 15., 0.78, 8)\,.\end{aligned}$$

Furthermore, although $C_2 = \frac{3}{10}$ and $C_1 = \frac{2}{5}$, an error in programming has produced $C_2 = 0.056$ and $C_1 = 0$. These are applicable for neutrally buoyant layers, however the exclusion of the buoyancy term occurs only in the pressure term parameterization. Therefore, it is hoped that this omission is insignificant.

The master length scale which is modeled similarly to Chen and Cotton (1987), where, in their formulation,

$$\frac{1}{l} \;=\; \frac{1}{l'} + \mathrm{MAX}\left(\frac{1}{l_b}, \frac{1}{l_c}\right),$$

where l' accounts for the generalized length scale, l_b is Blackadar's (1962) length scale and l_c is the length scale in an unstable cloud layer. The generalized length scale is represented by

$$\frac{1}{l'} \;=\; \begin{cases} \frac{1}{l_0} & \text{when } \frac{\partial}{\partial z}\frac{1}{\beta_1}\beta_n\,\overline{\Theta_n} \le 0 \\ \frac{1}{l_d} & \text{when } \frac{\partial}{\partial z}\frac{1}{\beta_1}\beta_n\,\overline{\Theta_n} > 0 \end{cases},$$

where l_0 is the characteristic length scale defined as

$$l_0 = 0.1\frac{\int qzdz}{\int qdz}$$

and l_d is the turbulent length scale defined as

$$l_d = \frac{3}{4}\sqrt{\frac{q^2}{2\frac{\partial}{\partial z}\beta_n \overline{\Theta_n}}}.$$

Finally, in accord with observations that within a buoyant layer, the dissipation is around sixty percent of the dominant buoyancy production,

$$\frac{1}{l_c} = \begin{cases} 0 & \text{when } \beta_n \overline{w'\theta'_n} \leq 0 \\ \frac{0.6\sqrt{8}}{c_1 q^3}\beta_n \overline{w'\theta'_n} & \text{when } \beta_n \overline{w'\theta'_n} > 0 \end{cases},$$

where $c_1 = 0.102$.

All the variances and covariances can now be solved for algebraically. The algebra is extensive, therefore the symbolic algebra program REDUCE 3 (Hearn,1984) is used for the algebraic manipulations. In order to make the final form of the solution physically meaningful, the following non-dimensional parameters, as in Flatau (1985), are introduced:

$$\begin{aligned} K_m &= lqS_m \\ K_h &= lqS_h \\ G_m &= \frac{l^2}{q^2}\left(\frac{\partial \overline{U}}{\partial z}^2 + \frac{\partial \overline{V}}{\partial z}^2\right) \\ G_h &= -\frac{l^2}{q^2}\beta_n \frac{\partial \overline{\Theta_n}}{\partial z} \\ \alpha &= \frac{\frac{\partial \overline{U}}{\partial z}^2}{\left(\frac{\partial \overline{U}}{\partial z}^2 + \frac{\partial \overline{V}}{\partial z}^2\right)}. \end{aligned}$$

The eddy exchange coefficients for this system of equations then become:

$$\begin{aligned} S_m &= \frac{S_m^n}{S^d} \\ S_h &= \frac{S_h^n}{S^d}, \end{aligned}$$

where

$$\begin{aligned} S_m^n &= 9A_1A_2G_h\left(3A_2\,\overline{w'w'} + B_2C_1q^2 - B_2\,\overline{w'w'}\right) + 3A_1\left(\overline{w'w'} - C_1q^2\right) \\ S_h^n &= -\left(27A_1A_2^2G_h\,\overline{w'w'} - 3A_2\,\overline{w'w'}\right) \\ S_d &= 27A_1A_2^2B_2G_h^2q^2 + 3A_2G_hq^2\left(-3A_1 - B_2\right) + q^2. \end{aligned}$$

As in Mellor and Yamada (1974), the values of these mixing coefficients are restricted to be positive. This then restricts the diagnostic quantities to be down-gradient. The values that G_h can attain are also restricted as in Hassid and Galperin (1983) in order to retain physically meaningful solutions to the Reynolds stress equation. The expression for S_h can be simplified to

$$S_h = \frac{-3\delta A_2}{3A_2B_2G_h - 1},$$

where $\delta = \frac{\overline{w'w'}}{q^2}$. If $S_h > 0$, then G_h can only assume the values

$$G_h < \frac{1}{3A_2B_2}.$$

This restriction also keeps the mixing coefficients finite. By placing limitations on the model, the mean fields are allowed to adjust to the turbulence, *i. e.* the turbulence is restricted to values that can be assimilated by the model. When turbulence changes quickly, this level 2.5w model no longer represents reality and the forcing conditions need to be modified in order that the scaled equations operate within the assumptions used in their derivation. As long as turbulence changes relatively slowly, these limitations should not impact the solution significantly.

The final set of equations become:

$$\begin{aligned}
\overline{u'u'} &= q^2\left(\frac{1}{3} + A_1\delta S_m G_m - 2A_1 S_h G_h\right) \\
\overline{v'v'} &= q^2\left(\frac{1}{3} + A_1\beta S_m G_m - 2A_1 S_h G_h\right) \\
\overline{u'v'} &= 6A_1 l^2 S_m \frac{\partial \overline{U}}{\partial z}\frac{\partial \overline{V}}{\partial z} \\
\overline{u'w'} &= -lqS_m \frac{\partial \overline{U}}{\partial z} \\
\overline{v'w'} &= -lqS_m \frac{\partial \overline{V}}{\partial z} \\
\overline{u'\theta'_{il}} &= 3A_2 l^2 (S_m + S_h) \frac{\partial \overline{U}}{\partial z}\frac{\partial \overline{\Theta_{il}}}{\partial z} \\
\overline{v'\theta'_{il}} &= 3A_2 l^2 (S_m + S_h) \frac{\partial \overline{V}}{\partial z}\frac{\partial \overline{\Theta_{il}}}{\partial z} \\
\overline{w'\theta'_{il}} &= -lqS_h \frac{\partial \overline{\Theta_{il}}}{\partial z} \\
\overline{\theta'_{il}\theta'_{il}} &= B_2 l^2 S_h \frac{\partial \overline{\Theta_{il}}}{\partial z}^2,
\end{aligned}$$

where $\delta = 2(3\alpha - 1)$, $\beta = 2(2 - 3\alpha)$, $A_1 = A_2 = 0.78$ and $B_2 = 8$.

The one prognostic equation for $\overline{w'w'}$ now needs to be expressed in a tractable form; this involves closing the transport term, the pressure term and dissipation in Eq. 4.8. The dissipation term will be closed by simply assuming

$$\epsilon = \frac{c_1}{\sqrt{8}}\frac{q^3}{l}.$$

The pressure and transport term closure will be modeled after the approach taken by Zeman and Lumley (1976) who closed these terms for a buoyancy-driven mixed layer. The pressure term is handled as in Eq. 4.12 with the coefficient in front of the return to isotropy component expressed as $\frac{C_1}{\tau}$ with $C_1 = 1$ and $C_2 = \frac{3}{10}$ and τ representing some mechanical time scale. In their original formulation, the shear components were not included since they studied an environment without shear; in our formulation, contributions to $\overline{w'w'}$ from shear will be included.

The transport term is handled in a relatively sophisticated way in order to include counter-gradient transports in the mixed layer. The present formulation extends the original theory to include the virtual and rainwater effects on the buoyancy terms. Only the part of the Zeman and Lumley analysis pertinent to closing the $\overline{w'w'w'}$ term are retained here. First, the third order fluxes, F_i, are expressed as

$$\begin{aligned} F_i &= \left[\overline{w'w'w'}\,,\ \overline{w'w'\theta'}\,,\ \overline{w'\theta'\theta'}\right], i = 1,2,3 \text{ without water loading} \\ &= \left[\overline{w'w'w'}\,, \frac{\beta_n}{\beta_1}\,\overline{w'w'\theta'_n}\,, \frac{1}{\beta_1^2}\,\overline{w'\left(\beta_n\theta'_n\right)^2}\right], i = 1,2,3 \text{ with water loading.} \end{aligned}$$

Then, express the rate equation for these fluxes as

$$\frac{\partial}{\partial t}F_i = S_{G_i} + S_{B_i} - \frac{F_i}{T_3} - D_i,$$

where S_{G_i} represents the non-buoyant or neutral source terms, S_{B_i} represent the buoyant source terms, D_i represents dissipation and the remaining term models the pressure contributions. The time scale T_3 represents a time scale for the third order terms.

The expression for the buoyant source term can be extracted from the expanded expression for F_i; if $F_i = \overline{w'\phi'}$, where ϕ is $\overline{w'w'}$, $\frac{\beta_n}{\beta_1}\,\overline{w'\theta'_n}$ or $\frac{1}{\beta_1^2}\,\overline{(\beta_n\theta'_n)^2}$, then

$$S_{B_i} = \left[\frac{\partial F_i}{\partial t}\right]_B = \left[\overline{w'\frac{\partial}{\partial t}\phi' + \phi'\frac{\partial}{\partial t}w'}\right]_B.$$

The buoyancy contributions to $\frac{\partial}{\partial t}\phi'$ and $\frac{\partial}{\partial t}w'$ are known so that S_{B_i} can be found. For example, if $F_i = F_1 = \overline{w'w'w'}$, then

$$
\begin{aligned}
S_{B_1} &= \left[\overline{w'\frac{\partial}{\partial t}w'w'} + \overline{w'w'\frac{\partial}{\partial t}w'}\right]_B \\
&= \overline{w'\left(2\beta_n w'\theta'_n - \frac{2}{5}\beta_n w'\theta'_n\right)} + \overline{\beta_n w'w'\theta'_n} \\
&= \frac{13}{5}\beta_n \overline{w'w'\theta'_n},
\end{aligned}
$$

if the pressure terms in Eq. 4.12 are included. The matrix for S_{B_i} then becomes

$$
S_{B_i} = \begin{bmatrix} \frac{13}{5}\beta_n \overline{w'w'\theta'} \\ \frac{5}{3}\frac{1}{\beta_1}\overline{w'\left(\beta_n\theta'_n\right)^2} \\ \frac{1}{\beta_1^2}\overline{\left(\beta_n\theta'_n\right)^3} \end{bmatrix}
$$

Note that modelling $\overline{w'w'w'}$ in this manner leads to terms containing $\beta_n\ \overline{w'w'\theta'_n}$. These then lead to terms containing $\overline{w'\left(\beta_n\theta'_n\right)^2}$ and then to terms containing $\overline{\left(\beta_n\theta'_n\right)^3}$. These terms are finally closed by forming a rate equation on $\overline{\left(\beta_n\theta'_n\right)^3}$ and assuming steady state:

$$
\frac{1}{\beta_1^3}\frac{\partial}{\partial t}\overline{\left(\beta_n\theta'_n\right)^3} = -\frac{1}{\beta_1^2}\overline{w'\left(\beta_n\theta'_n\right)^2}\frac{\partial\Theta}{\partial z} - \frac{\beta_n}{\beta_1}\overline{w'\theta'_n}\frac{\partial}{\partial z}\frac{1}{\beta_1^2}\overline{\left(\beta_n\theta'_n\right)^2} - \frac{2\mu}{\tau_\theta}\frac{1}{\beta_1^3}\overline{\left(\beta_n\theta'_n\right)^3} = 0.
$$

The mean temperature gradient enters into the closure for the third order fluxes here and τ_θ is some thermal time scale. In convective regions, Zeman and Lumley state that $\frac{\tau_\theta}{\tau} = 0.5$ with the ratio increasing with the stratification.

Zeman and Lumley express the neutral source terms in the invariant form

$$
S_{G_i} = \begin{bmatrix} -3\ \overline{w'w'}\ \frac{\partial}{\partial z}\ \overline{w'w'} \\ -2\ \overline{w'w'}\ \frac{\partial}{\partial z}\frac{\beta_n}{\beta_1}\ \overline{w'\theta'_n} - \frac{\beta_n}{\beta_1}\ \overline{w'\theta'_n}\ \frac{\partial}{\partial z}\ \overline{w'w'} \\ -\ \overline{w'w'}\ \frac{\partial}{\partial z}\frac{1}{\beta_1^2}\ \overline{\left(\beta_n\theta'_n\right)^2} \end{bmatrix}
$$

and the dissipation terms are represented as

$$
D_i = \begin{bmatrix} 4\frac{\mu}{\tau}\ \overline{w'w'w'} \\ \frac{4}{3}\frac{\mu}{\tau}\frac{\beta_n}{\beta_1}\ \overline{w'w'\theta'_n} \\ 2\frac{\mu}{\tau}\frac{1}{\beta_1^2}\ \overline{w'\left(\beta_n\theta'_n\right)^2} \end{bmatrix},
$$

where $\mu = \frac{4}{13}$ as in Zeman and Lumley.

Lumley *et al.* (1976) have shown that the mixing coefficients are also subject to buoyancy effects. Therefore, terms like $T_3(\,\overline{w'w'}\,)$ are modified by

$$T_3(\,\overline{w'w'}\, + b\beta_n\tau_\theta\,\overline{w'\theta'_n}\,).$$

As in Zeman and Lumley, $T_3 = r\frac{\tau}{C_\theta}$ with $r = 1.1$.

Finally, the pressure part of the transport term is modelled in the simplest invariant form, *i. e.*

$$\frac{1}{\rho}\,\overline{u'_i p'} = \frac{1}{5}\,\overline{u'_i q^2}\,.$$

Expressions for the third order moments can be formed by assuming local equilibrium so that

$$F_i \;=\; T_3\,(S_{G_i} + S_{B_i} - D_i)\,.$$

Then if F_1 is now $\overline{w'w'w'} + \frac{2}{3}\frac{1}{\rho}\,\overline{w'p'}$,

$$F_i \;=\; \begin{bmatrix} K'_m & \beta_1\tau K'_m & \frac{3}{4}\beta_1^2\tau^2 K'_t \\ \frac{1}{2.2}\tau\frac{\beta_n}{\beta_1}\,\overline{w'\theta'_n} & \frac{1}{1.1}K'_m & \frac{3}{4}\beta_1\tau K'_t \\ 0 & 0 & K'_t \end{bmatrix} \begin{bmatrix} \frac{\partial}{\partial z}\,\overline{w'w'} \\ \frac{\partial}{\partial z}\frac{\beta_n}{\beta_1}\,\overline{w'\theta'_n} \\ \frac{\partial}{\partial z}\frac{1}{\beta_1^2}\,\overline{(\beta_n\theta'_n)^2} \end{bmatrix}.$$

The mechanical and thermal eddy mixing coefficients K'_m and K'_t are:

$$\begin{aligned} K'_m &= \tau\left(\,\overline{w'w'}\, + b\beta_n\tau_\theta\,\overline{w'\theta'_n}\,\right) \\ K'_t &= \tau_c\frac{\tau\left(\,\overline{w'w'}\, + (b+1)\beta_n\tau_\theta\,\overline{w'\theta'_n}\,\right)}{1+\frac{1}{3}\tau_c\tau_\theta N^2}, \end{aligned}$$

where the compounded time scale is

$$\tau_c \;=\; \frac{1}{\frac{C_\theta}{\tau} + \frac{2\mu}{\tau_\theta}}.$$

In studies of the dry buoyancy-driven mixed layer, Zeman and Lumley point out that this formulation allows the counter-gradient transport of $\overline{w'w'}$ in the lower part of the mixed layer. Since $\overline{w'w'}$ exhibits a broad peak in the middle of the mixed layer, $-K_m\frac{\partial}{\partial z}\,\overline{w'w'} < 0$ and the principal gradient term contributes to a local decrease of $\overline{w'w'}$. However, since the vertical gradients of $\overline{w'\theta'}$ and $\overline{\theta'\theta'}$ tend to be negative in the mixed layer, the contributions to $\overline{w'w'}$ are positive and counteract the negative contributions from the principal gradient term. This then yields the correct shape of the $\overline{w'w'w'}$ profiles. Furthermore, they point out that the thermal mixing coefficient is associated with transport of $\overline{w'w'}$ through the gradient of $\overline{\theta'\theta'}$, is more sensitive to buoyancy effects than the mechanical mixing coefficient and is a function of N, the Brunt-Väisälla frequency.

It is important to note that there are two classes of mixing coefficient; those related to the second order closure (K_m and K_h) and those related to the third order closure (K'_m and K'_h). The third order mixing coefficients tends to be several orders of magnitude larger than the second order coefficients due to their direct dependence on $\overline{w'w'}$. Furthermore, the linear stability criterion for the diffusion equation

$$K_x \frac{\Delta t}{\Delta x^2} \leq \frac{1}{4}$$

is used to determine the small time step where K_x represents the maxima of all the mixing coefficients.

Thus far, pressure effects have not been considered, *i. e.* $\beta_5 = 0$.

4.2 The convective adjustment model

The model as it stands predicts the evolution of horizontally homogeneous convection over land and water. This includes, for example, convection within the PBL and convection forced by the radiative destabilization of statiform cloud layers in the PBL and in the middle and upper troposphere. However, the theory fails to simulate the ensemble-averaged effects of deep convective activity when applied to the free atmosphere. This is because the PBL, for example, is driven by the parameterized heat flux at the ground. The divergence of this heat flux creates an unstable lapse rate which implies strong mixing and an upward transport of heat. The PBL grows slowly by vertically communicating the heat flux upwards until the inversion can no longer be eroded by the PBL eddies. When deep moist convective cells are present in the free atmosphere, however, this theory of contiguous mixing is no longer valid since information about the buoyant parcel is carried from the lifted condensation level (LCL) to the equilibrium temperature level (ETL). Some way is needed to conserve the parcels buoyancy through the depth of the free atmosphere in order to represent the effects of deep moist convection.

Two methods of determining the cumulus buoyancy are investigated. The cumulus flux method, first proposed by Arakawa (1969) and developed by Betts (1975) is an attractive way to represent convection since the fluxes of heat and moisture are simply represented by a convective velocity and the difference between the updraft and environmental characteristics of a parcel as determined from a one dimensional cloud model. Alone, the cumulus flux model represents the required magnitudes of the convective buoyancy fluxes properly, but since there is no vertical communication of this buoyancy flux, the model fails to convectively mix the free atmosphere. Therefore, a cumulus component will be added to the original formulation in the presence of deep convection so that the Betts model will supply the required buoyancy flux and the mixing coefficient model will distribute this buoyancy flux vertically, *i. e.*

$$\overline{w'\chi'} = -K\frac{\partial\overline{\mathcal{X}}}{\partial z} + \sigma_{u,d}w^{*}\left(\mathcal{X}_{u,d} - \overline{\mathcal{X}_e}\right) \tag{4.18}$$

Here, $\sigma_{u,d}$ represent cloud core fractional coverage of the updraft or downdraft, $\mathcal{X}$ represents a scalar variable and u, d, e are the updraft, downdraft and environmental values of $\mathcal{X}$. When no deep moist convection is present, the model reduces to the classic second order form. The level 2.5w model and the cumulus flux model act together when deep convection is present. Presumably, changes in the algebraic manipulations to include shear and water loading effects in the level 2.5w model would produce insignificant changes in the hybrid scheme since the main driving terms are the fluxes by cumulus towers.

However, after numerical experimentation, the cumulus flux model was found to do a poor job of transporting the scalar quantities through the free atmosphere. The strong scalar transports by cumulus convection are seen in the following Chapter in Figs. 5.11d and 5.22d where six and 21 km running averages of the perturbation total water mixing ratio from an explicit simulation of sea-breeze cumulus convection over the Florida peninsula are respectively shown. The cumulus flux model, conversely, yields drying below the mid-troposphere and only slight moistening aloft when incorporated into the mesoscale model. This can be seen by taking the divergence of the cumulus part of Eq. 4.18 to determine the tendency of $\overline{\mathcal{X}}$:

$$\begin{aligned}\left(\frac{\partial \overline{\mathcal{X}}}{\partial t}\right)_{\text{cumulus}} &= -\frac{\partial}{\partial z}\,\overline{w'\chi'} \\ &= -\sigma_{u,d}\frac{\partial w^*}{\partial z}\left(\mathcal{X}_{u,d} - \overline{\mathcal{X}_e}\right) - \sigma_{u,d}w^*\frac{\partial}{\partial z}\left(\mathcal{X}_{u,d} - \overline{\mathcal{X}_e}\right)\end{aligned}$$

For clarity, assume a non-entraining updraft with a mass flux profile independent of height. The above equation then becomes

$$\left(\frac{\partial \overline{\mathcal{X}}}{\partial t}\right)_{\text{cumulus}} = \sigma_{u,d}w^*\frac{\partial \overline{\mathcal{X}_e}}{\partial z}. \tag{4.19}$$

This clearly indicates that by casting the deep cumulus effects in a mass flux framework, the only effect non-entraining convection can have is warming and drying if the environmental temperature and moisture profile decreases with height. This is appropriate in large-scale models since the interest lies in determining the effects of a population of convective elements, each passing through its own life-cycle. Since the adiabatic cooling of the updraft is largely offset by condensation and the moistening is offset by precipitation, the mass flux present in the unresolved updraft induces compensating subsidence and subsequent warming and drying outside the cumulus core.

In mesoscale models, on the other hand, individual convective elements can be at least partially resolved so that the interest lies in capturing an ensemble-averaged single convective element. Thus strong scalar transports within the core of the convection must be parameterized. As shown above, this cannot be accomplished by a mass flux model. Therefore, a convective adjustment scheme first proposed by Manabe *et. al.* (1965) and investigated by Betts (1986), Bougeault (1985) and others is proposed. It should be noted that the above formulation for the covariances is used for the determination of $\overline{w'w'}$.

Here, the tendencies to the model variables are specified rather than the fluxes. Then, the cumulus forcing becomes

$$\left(\frac{\partial \overline{\mathcal{X}}}{\partial t}\right)_{\text{cumulus}} = \sigma_{u,d}\left[w^{**}\frac{\partial \overline{\mathcal{X}}}{\partial z} + \frac{1}{T}\left(\mathcal{X}_{u,d} - \overline{\mathcal{X}_e}\right)\right]. \tag{4.20}$$

The second term on the rhs of Eq. 4.20 is the convective adjustment term where T is the time scale over which convection modifies the environment. It is simply specified as

$$\frac{1}{T} = \frac{1}{\rho H} \int_{lcl}^{ct} \sqrt{\overline{w'w'}}\, \rho dz$$

where H is the total cloud height. The first term on the rhs of Eq. 4.20 is as in Bougeault (1985), except w^{**} is determined from forcing the moist static energy of the convective tendencies to be nil, *i. e.*

$$w^{**} = \frac{1}{T} \frac{\int_{lcl}^{ct} [L(r_{su} - \overline{r_v}) - L(r_{tu} - \overline{r_t}) + C_p(T_u - \overline{T})] \rho dz}{\int_{lcl}^{ct} [L\frac{\partial \overline{r_t}}{\partial z} - L\frac{\partial \overline{r_v}}{\partial z} - C_p \frac{\partial \overline{T}}{\partial z}] \rho dz}. \tag{4.21}$$

There are several interpretations of Eq. 4.20 which can be made. When cumulus forcing is diagnosed, the first term on the rhs combines with the resolvable advection. Bougeault (1985) then interprets the first term on the rhs as a subsidence term since the resolvable vertical motion in large-scale models is negligible compared to w^{**}. The second term is then interpreted as the detrainment term. In large scale models, then, the subsidence term prompts warming and drying while the detrainment term prompts warming and moistening.

In mesoscale models, the resolved vertical motion may be comparable to w^{**} and a different interpretation of the term is needed. In this case, the advection by the resolved motions and the first term on the rhs (now called the compensation term) combine to give near zero net advection which is desirable since the advection of the scalars is now being accomplished by the convective adjustment term. Double counting is then explicitly eliminated since the convective adjustment term wholly handles the updraft core warming and moistening.

In Eq. 4.20, either w^{**} or T could be specified and the remaining coefficient determined from a moist static energy balance. Bougeault specified the convective flux as a function of height and diagnosed the detrainment time scale. Here, the convective adjustment time scale is prescribed and the mass flux is diagnosed. This is an artifact of the methodology used to construct Eq. 4.20; only the convective adjustment term was initially included in the calculations. Due to the difficulty in balancing the moist static energy of the tendencies, the compensation term was later added. The effect of prescribing w^{**} and diagnosing T on the parameterization scheme is unknown and will be relegated to future research.

Finally, the mass balance of total water is accomplished by equating the depletion of water vapor within the PBL to the total water tendency within the parameterized cloud. Updraft and downdraft properties must now be determined including the hydrometeor mixing ratios in order to obtain the correct cumulus fluxes.

4.2.1 Modeling the updraft

The cloud updraft and downdraft values of the scalar variables must be specified in order to close the parameterization scheme. Once again this closure is based on the model output diagnostics from the explicit numerical simulations. The one dimensional cloud model is described fully in Tremback (1990) and includes an updraft and downdraft. Briefly, the drafts are assumed to be steady-state entraining plumes which travel from the lifting condensation level to the equilibrium temperature level for the updraft and from the level of free sink (the level where the environmental Θ_e is at a minima) to the ground for the downdraft. In order to calibrate the cloud model, the updraft and downdraft characteristics of each explicitly simulated storm are conditionally sampled. After several different sampling criteria were tried, updrafts greater than 5 m/s with condensate present were chosen to generally represent the updrafts in the different storm types. Figs. 4.1a and 4.1b delineate the areal coverage of the sampled updraft portions of the CCOPE supercell at 5580 sec and the tropical squall line at 3000 sec.

The updraft core

Simple cloud models depict the updraft core as undergoing undiluted ascent from cloud base to cloud top. It is well known, however, that entrainment can modify the thermodynamics of the updraft. Shown in Figs. 4.2a and 4.2b are the potential temperature profiles of the updraft incurring entrainment rates which doubled the mass flux from the base of the cloud to the detrainment level for the CCOPE supercell and the tropical squall line. Increasing the entrainment rate so that the mass flux quadrupled within the cloud

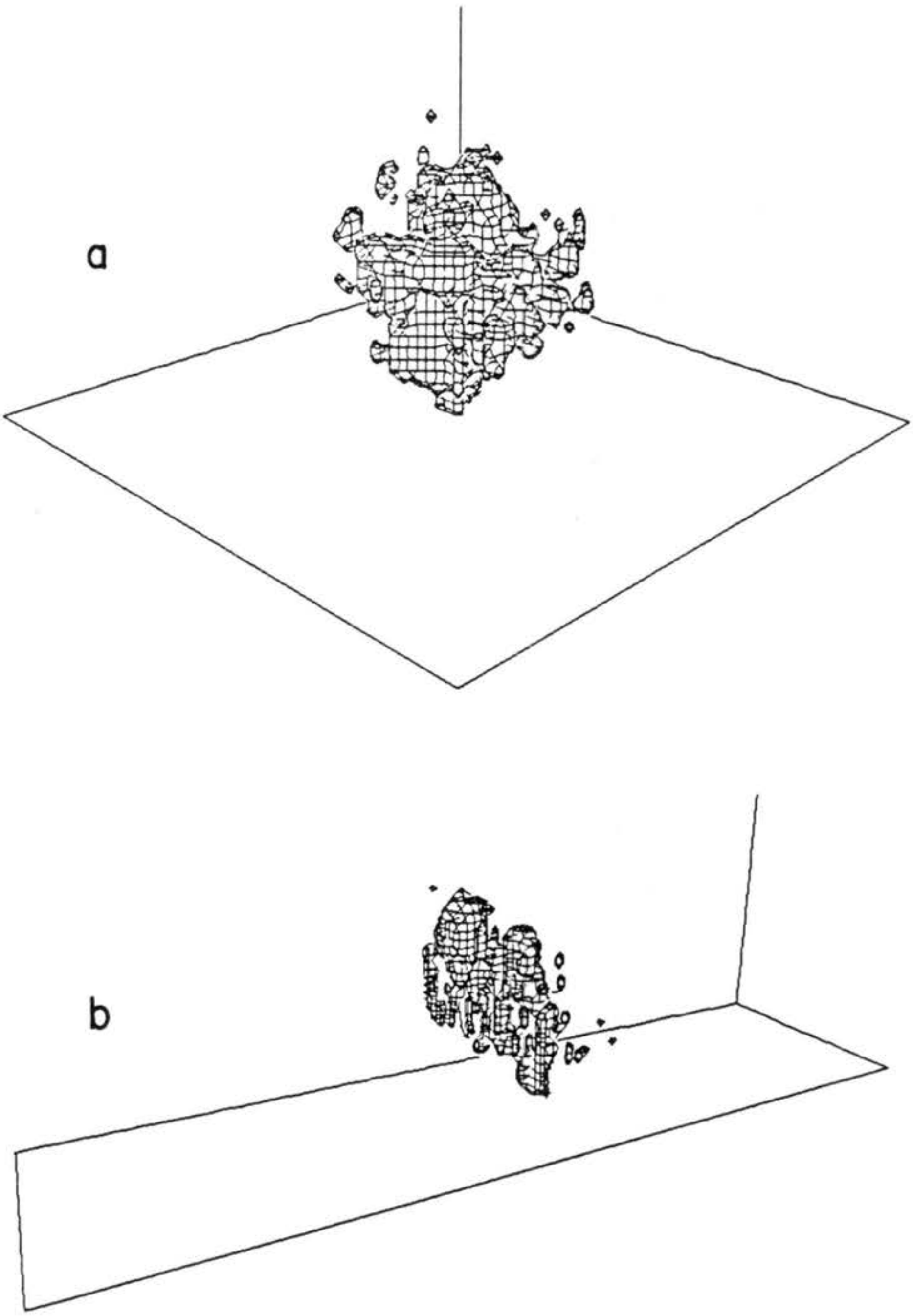

Figure 4.1: Conditionally sampled updraft cores with $W \geq 5$ m/s for (a) the CCOPE supercell at 5580 sec, and (b) the tropical squall line at 3000 sec.

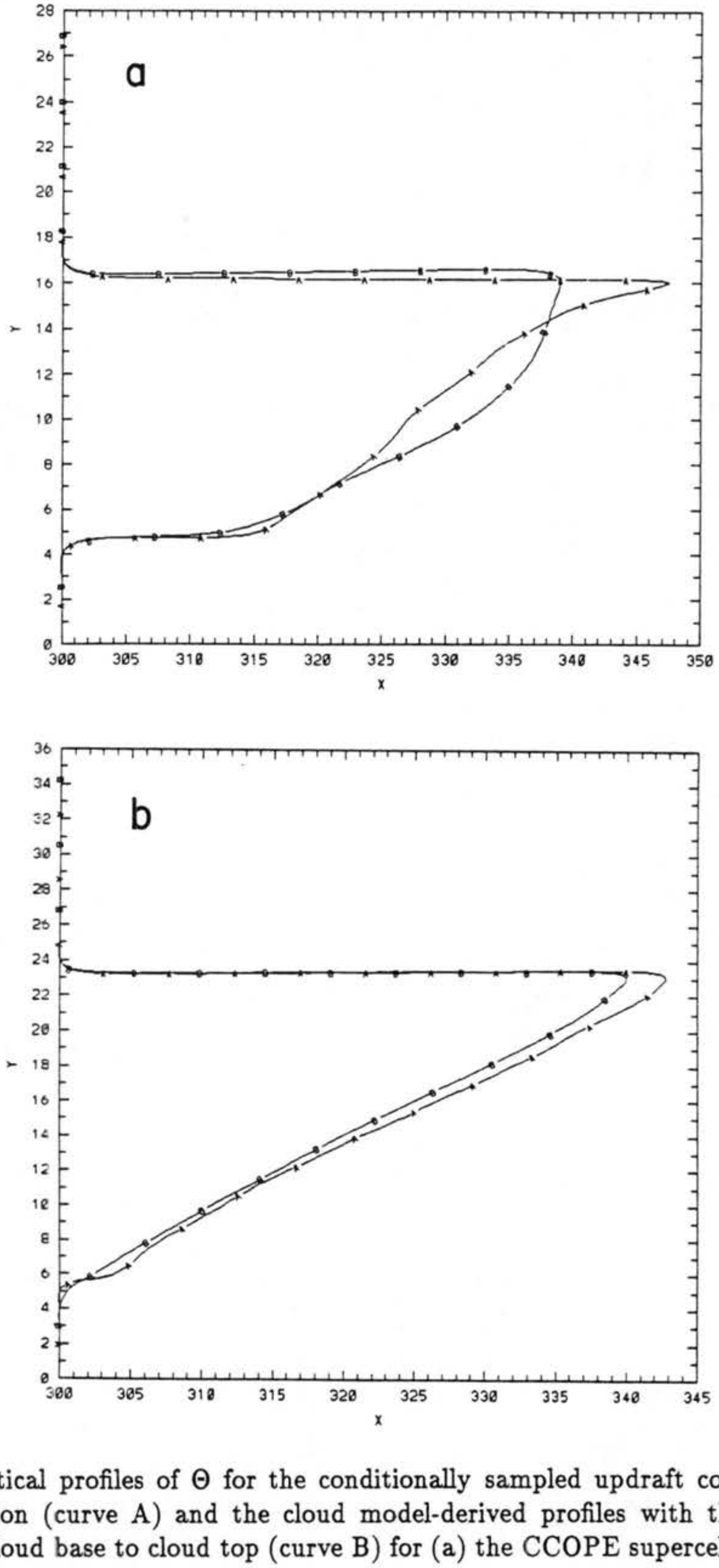

Figure 4.2: Vertical profiles of Θ for the conditionally sampled updraft cores from the explicit simulation (curve A) and the cloud model-derived profiles with the mass flux doubling from cloud base to cloud top (curve B) for (a) the CCOPE supercell at 5460 sec and, (b) the tropical squall line at 4200 sec.

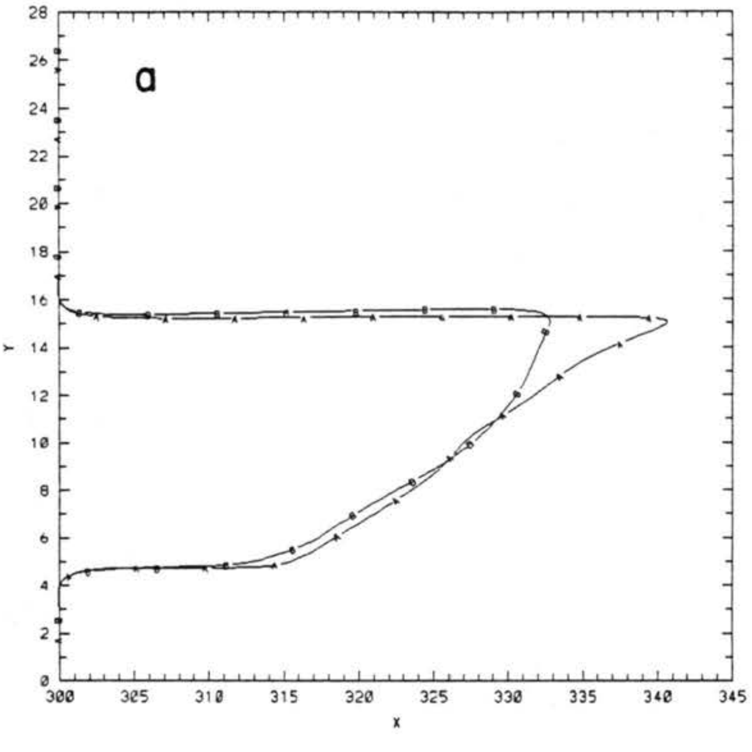

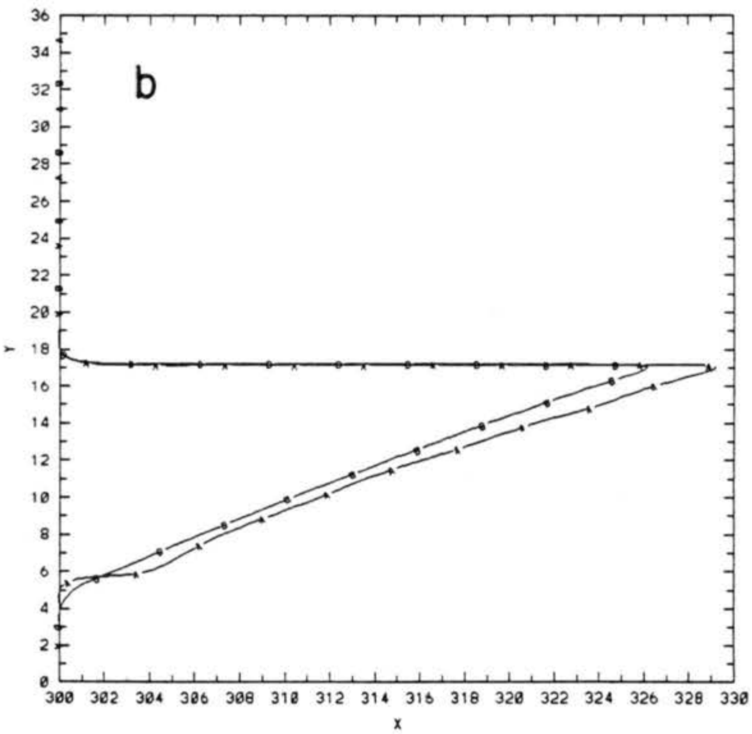

Figure 4.3: Vertical profiles of Θ for the conditionally sampled updraft cores from the explicit simulation (curve A) and the cloud model-derived profiles with the mass flux quadrupling from cloud base to cloud top (curve B) for (a) the CCOPE supercell at 5460 sec and, (b) the tropical squall line at 4200 sec.

yields the thermodynamic profiles shown in Figs. 4.3a and 4.3b. It appears that mass flux quadrupling more accurately describes the mid-latitude storm while mass flux doubling is slightly more accurate for the tropical storm, cloud top height notwithstanding. It is of interest to note the relative insensitivity of the thermodynamic profiles to the entrainment rate in the tropical storm. This contrasts with the Kreitzberg-Perkey assertion in Section 2.2.1 that mid-latitude storms are not as affected by the entrainment rate as tropical storms.

Also shown in Figs. 4.4a and 4.4b are the conditionally sampled vertical velocities compared to two modeled updraft velocities with entrainment rates leading to mass flux doubling within the cloud. Curve B is the updraft profile determined from a steady-state plume model including the 'virtual mass coefficient' while curve C is the profile with the English (1973) modifications. This involves normalizing an observationally-derived updraft profile with the maximum updraft speed derived from the parcel calculations. In Figs. 4.5a and 4.5b, the profiles derived from entrainment rates leading to mass flux quadrupling are shown. It appears that again, the larger entrainment rates better describe the vertical velocity profile of the conditionally sampled updraft profiles of the mid-latitude storm.

It should be noted that the updraft velocity profiles are not used within the parameterization, but the figures are presented for completeness.

Condensate efficiency of the updraft core

There are two ways to calculate the amount of water in the cloud that contributes to hydrometeors. The first is to define a condensate efficiency for the cores of the storm such that

$$\epsilon_{u,d} = \frac{\text{explicit conditionally sampled condensate}}{\text{columnar adiabatic EWC from cloud model}}. \tag{4.22}$$

If $\mathcal{X}$ represents the mixing ratio of any hydrometeor species, or, in this case, the sum of all the condensate (*i. e.* the difference between the water vapor mixing ratio at cloud base and the saturation vapor mixing ratio at any level within the cloud), the EWC (equivalent

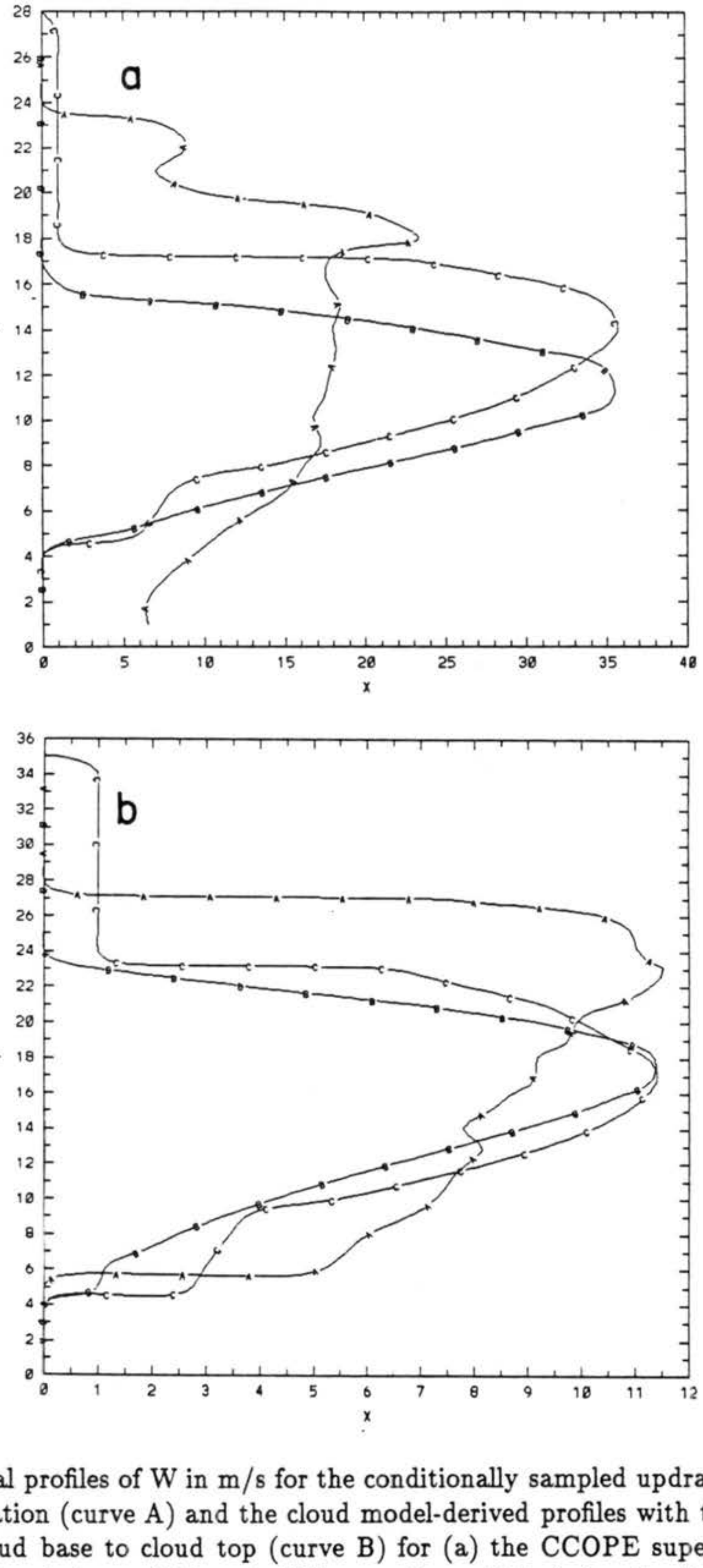

Figure 4.4: Vertical profiles of W in m/s for the conditionally sampled updraft cores from the explicit simulation (curve A) and the cloud model-derived profiles with the mass flux doubling from cloud base to cloud top (curve B) for (a) the CCOPE supercell at 5460 sec and, (b) the tropical squall line at 4200 sec. Curve C includes the English (1973) modifications to curve B.

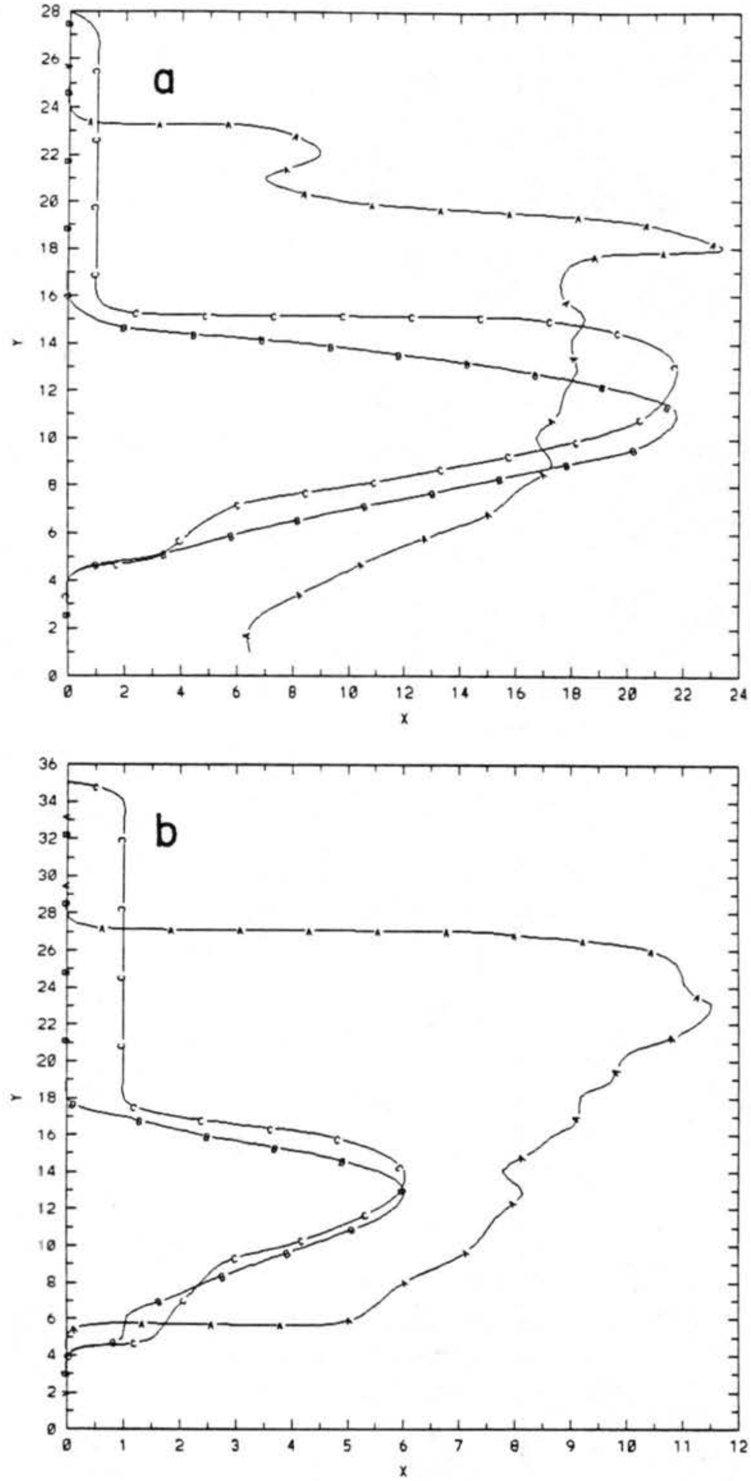

Figure 4.5: Vertical profiles of W in m/s for the conditionally sampled updraft cores from the explicit simulation (curve A) and the cloud model-derived profiles with the mass flux quadrupling from cloud base to cloud top (curve B) for (a) the CCOPE supercell at 5460 sec and, (b) the tropical squall line at 4200 sec. Curve C includes the English (1973) modifications to curve B.

water content) is defined simply as

$$\mathrm{EWC} \;=\; (\mathcal{X})(\rho_{air}). \tag{4.23}$$

The columnar EWC is the integral of Eq. 4.23 over the depth of a column. Note that Eq. 4.22 is different from the traditional interpretation of precipitation efficiency which relates the total precipitation rate observed at the ground to the water vapor moisture convergence at cloud base. The term condensate efficiency is chosen so that all condensed water including cloud water is represented rather than that just the precipitation which reaches the ground.

The evolution of the diagnosed condensate efficiency is shown in Figs. 4.6a and 4.6b for the CCOPE supercell and the tropical squall line, respectively. The time series for the supercell indicates relatively steady state behavior and an average value of 90% is representative. This is considerably higher than what may be expected from the traditional definition of precipitation efficiency. From data on various High Plains thunderstorms, Marwitz (1972) clearly showed the inverse relationship between wind shear and precipitation efficiency. From his Fig. 1, a precipitation efficiency of between 20% and 40% should be expected for this storm in view of the large value of wind shear. However, Marwitz believes that the high wind shear causes a tilted updraft which contributes to a low precipitation efficiency through hydrometeor evaporation within the clear air below the updraft. When sampling only the updraft core, the evaporation of hydrometeors detrained from the storm is not considered, thus leading to high condensate efficiencies of the updraft core.

Because the squall line is composed of many convective cells, each undergoing a growth and decay process, forty minute running averages of the fields are taken to represent an ensemble-averaged cloud field. Because the cloud model indicated no convection beyond 4680 s (time file #39), the curves are valid between time files #10-#29. A condensate efficiency of 48% is representative of the tropical storm.

These two cases underscore the strong variability of the precipitation, and condensation and condensate efficiency (defined traditionally and by Eq. 4.22, respectively) within

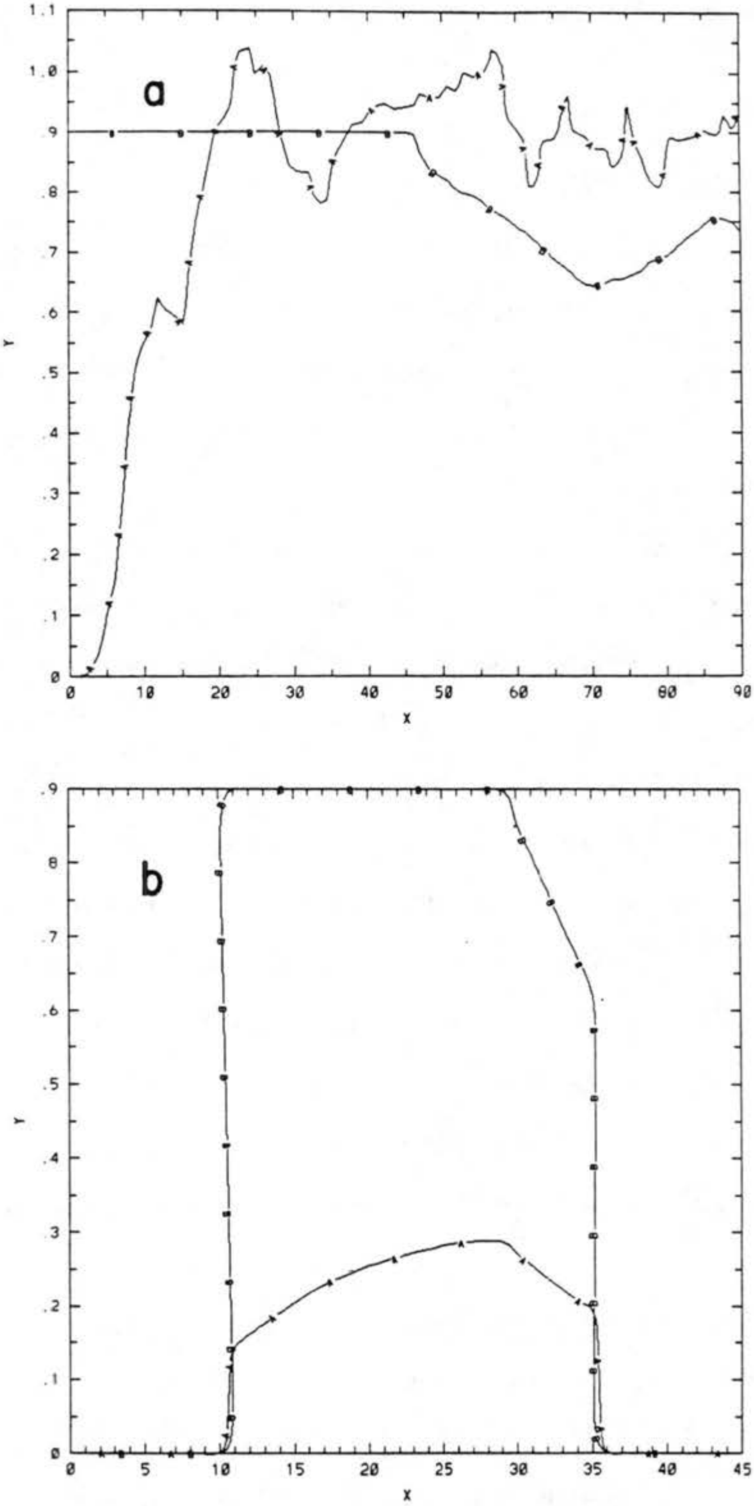

Figure 4.6: Time series in min of the condensate efficiency (curve A) for the conditionally sampled updraft core of (a) the CCOPE supercell at 5460 sec and, (b) the tropical squall line at 4200 sec. Curve B represents the storm precipitation efficiency as determined from the empirical formula in Fritsch and Chappell (1980).

different storm types. Indeed, Weisman and Klemp (1982) and, as noted above, Marwitz (1972) found precipitation efficiency to vary according to the mean shear profile and bulk Richardson numbers within similar storm types.

The second method for determining the amount of water that contributes to the hydrometeors within the cloud is simply to integrate the difference between the total water mixing ratio and the saturation mixing ratio through the cloud depth as determined from the one dimensional cloud model. For the simulations in Chapter 5, this method agreed closely with the condensate efficiency method described above and this method is chosen for its simplicity.

Hydrometeor profiles within the updraft core

All hydrometeor mixing ratios within the parameterized cloud are needed in order to determine the water loading effects on the cloud buoyancy. Furthermore, hydrometeor mixing ratios within the cloud are needed so that the cumulus tendencies can be determined and fed back into the large-scale fields, thus providing a parameterized source of hydrometeors.

The vertical profiles of the various hydrometeor mixing ratios are approximated by parabolic curves. The curve shape is determined by the appropriate general cloud criteria (which will be discussed later in this section) and is normalized by the columnar EWC of each hydrometeor species (Eq. 4.22) as determined from the explicit simulations.

Therefore, conditionally sampled vertical profiles of cloud water, rain, ice, graupel and aggregates are examined in the updraft region for both storms. From these, a total columnar EWC is calculated which is the sum of the columnar EWC of cloud water, rain, ice graupel and aggregates. We then calculate the percent contribution of each species, PCT, to the total columnar EWC. The time series in Figs. 4.7a and 4.7b indicate the PCT cloud, rain, ice, graupel and aggregates in the updraft of the supercell and the tropical squall line, respectively. Because rain and cloud water did not form until time file #7 in the tropical storm, the percentages are only valid between time files #17-#29. Similarly, the valid time files for ice, graupel and aggregates are #23-#29. The partition percentages

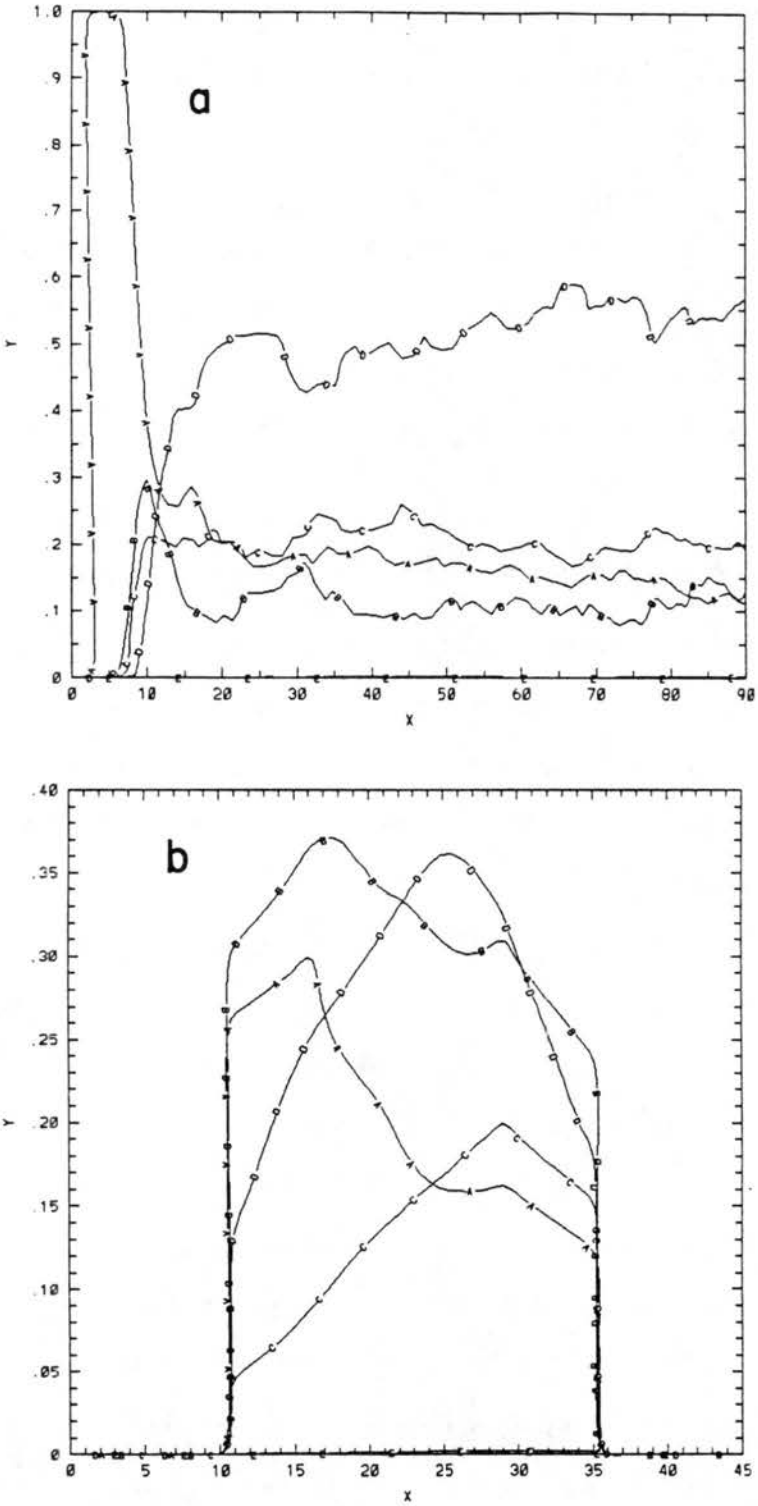

Figure 4.7: Time series in min of the percent contribution from cloud water (curve A), rain water (curve B), ice water (curve C), graupel (curve D) and aggregates (curve E) to the total conditionally sampled condensate within the updraft for (a) the CCOPE supercell at 5460 sec and, (b) the tropical squall line at 4200 sec.

representing the squall line are taken at time file #26 as were the condensate efficiencies. Again, note the temporal steadiness of the condensate partitioning.

The normalization of the parameterized hydrometeor mixing ratio is completed by assuming the columnar EWC of each species can be determined from the condensate efficiency of the updraft core, the columnar EWC of an adiabatic updraft core assuming that all supersaturated water is condensed (ADEWC) and PCT *i. e.*

$$\mathcal{X}_{u,d} \quad = \quad (\epsilon_{u,d})(\mathrm{ADEWC})(\mathrm{PCT}). \tag{4.24}$$

The shape of the vertical profiles of the hydrometeor EWC is specified in terms of general cloud parameters like the lifting condensation level (LCL), the melting, freezing and ice levels (ML, FL, IL, respectively), the equilibrium temperature level (ETL) and cloud top (CT).

Parabolic curves are then constructed based on the general cloud parameters. These are shown in Figs. 4.8a and 4.8b through Figs. 4.12a and 4.12b for the supercell and squall line, respectively. The general cloud criteria used to construct these profiles are shown in Table 4.1.

Table 4.1: The generalized criteria for constructing the hydrometeor profiles within the updraft core.

Hydrometeor species	Z_{low}	Z_{mid}	Z_{high}
cloud	LCL	ML	IL
rain	LCL	ML	FL
ice	FL	ETL	CT
graupel	ML	IL+2	CT
aggregates	ETL-IL	IL	ETL

As seen in these figures, the fit is fairly good considering the variability between the storms and their environments. These curves are combined with the updraft and downdraft values of potential temperature to yield updraft and downdraft values of Θ_{il} . These are then placed into Eq. 4.18 to yield the cumulus flux forcing to $\overline{w'w'}$. In addition the parameterization also provides source functions for the hydrometeor equations in the mesoscale model as seen in 4.20.

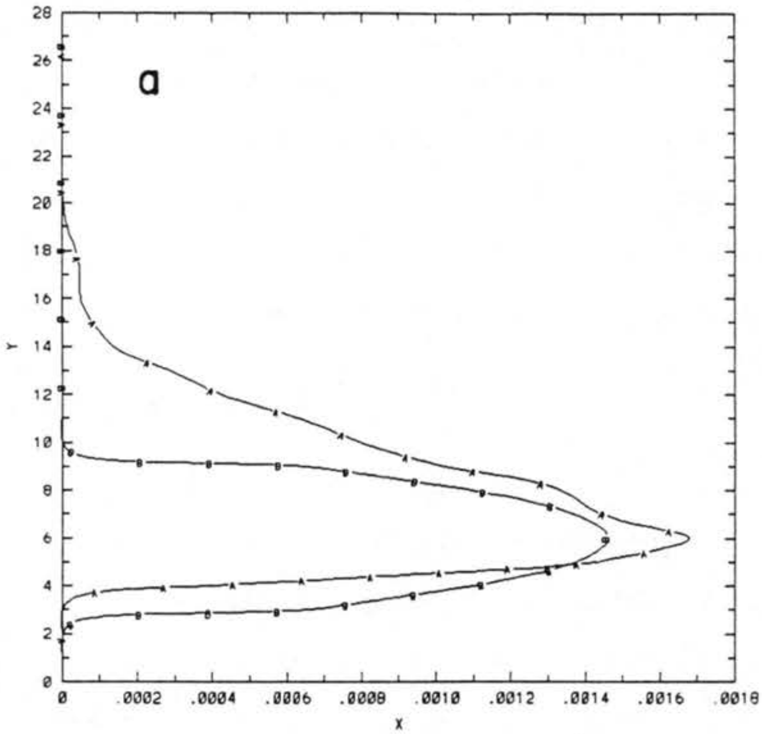

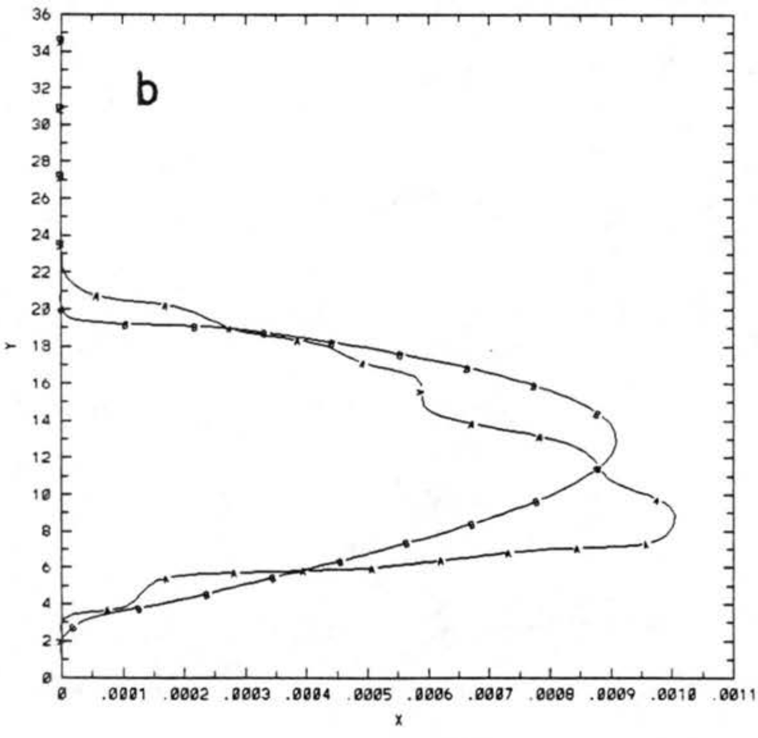

Figure 4.8: Vertical profiles of cloud water in kg/kg for the conditionally sampled updraft (curve A) and the parameterized updraft (curve B) for (a) the CCOPE supercell at 5460 sec and, (b) the tropical squall line at 4200 sec.

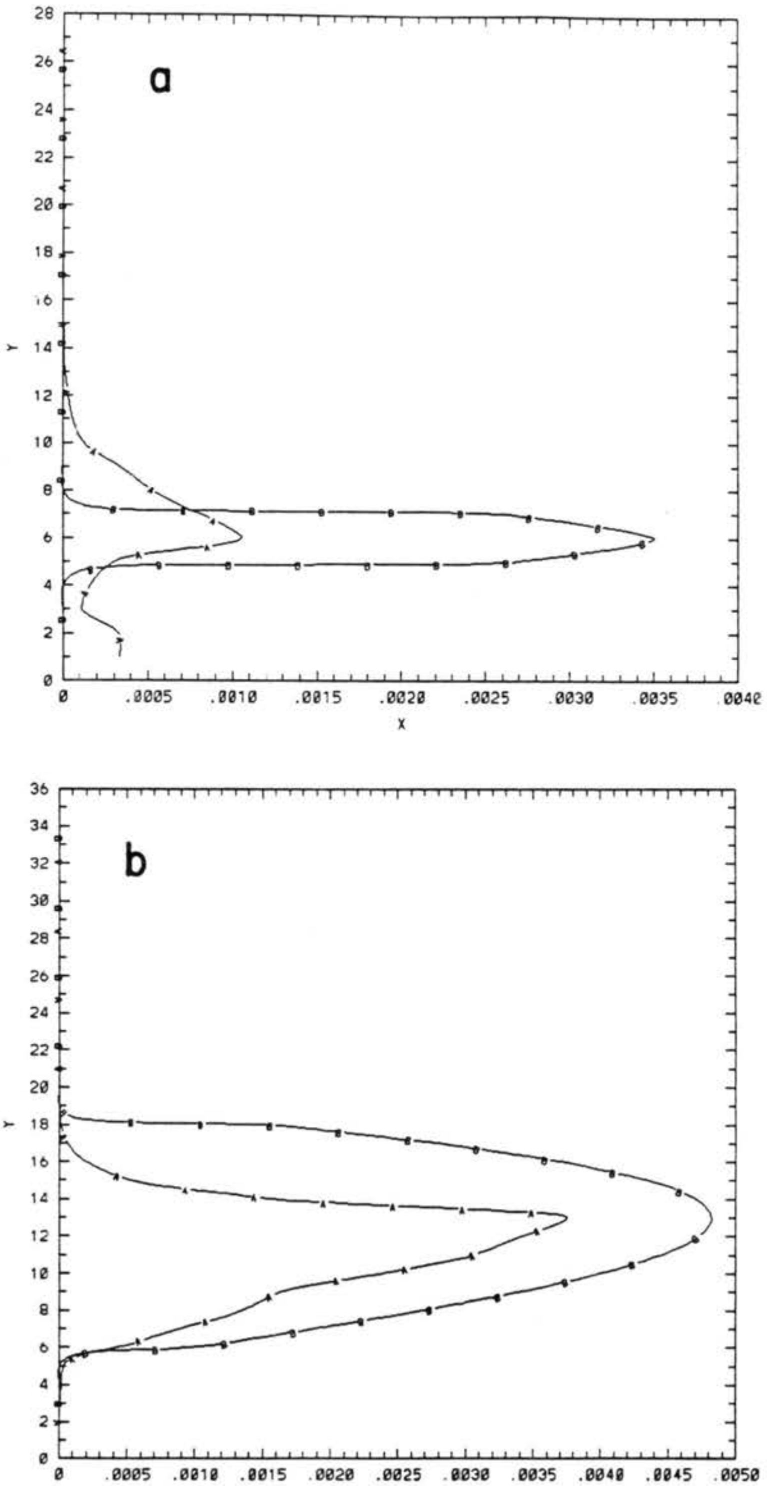

Figure 4.9: Vertical profiles of rain water in kg/kg for the conditionally sampled updraft (curve A) and the parameterized updraft (curve B) for (a) the CCOPE supercell at 5460 sec and, (b) the tropical squall line at 4200 sec.

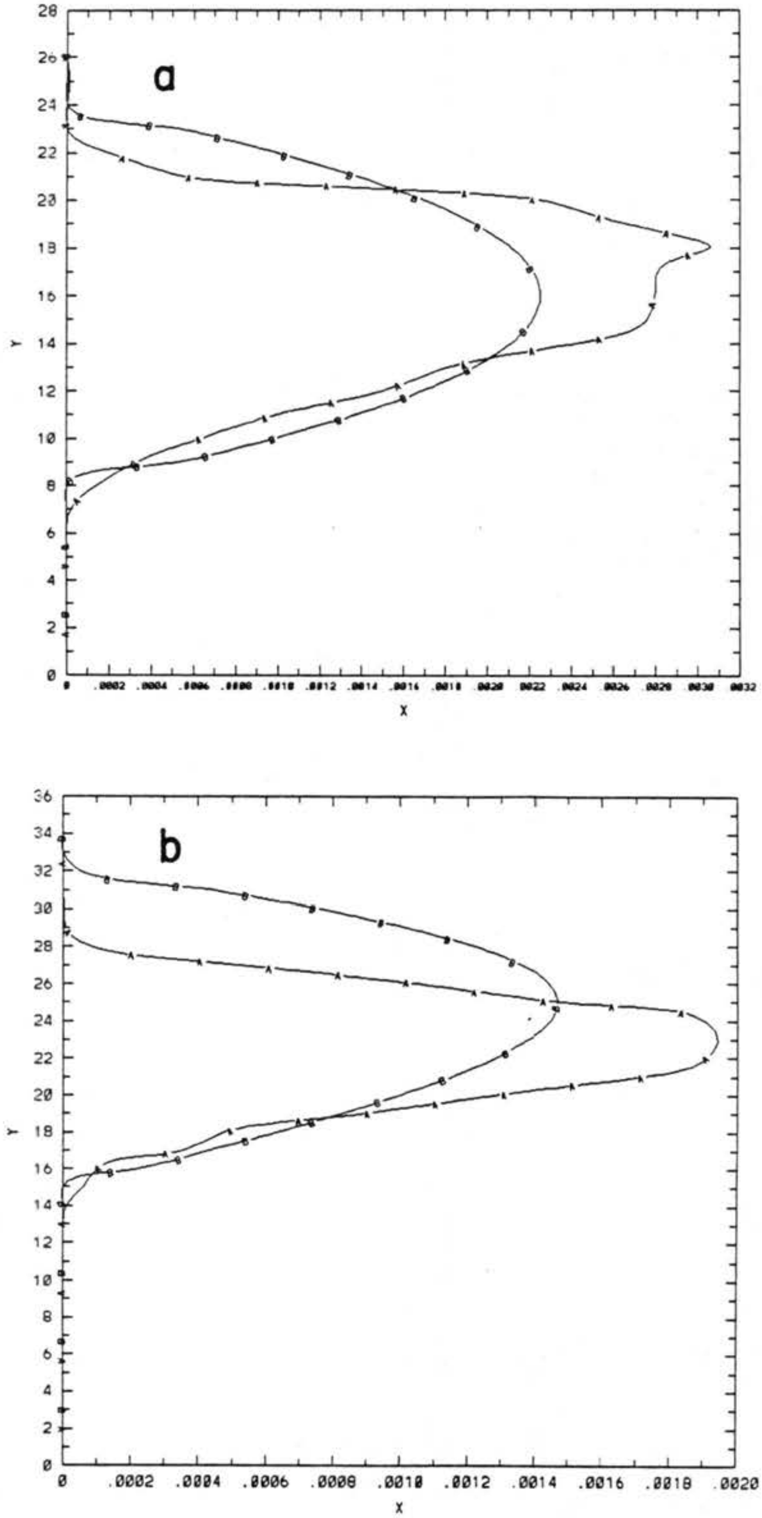

Figure 4.10: Vertical profiles of ice water in kg/kg for the conditionally sampled updraft (curve A) and the parameterized updraft (curve B) for (a) the CCOPE supercell at 5460 sec and, (b) the tropical squall line at 4200 sec.

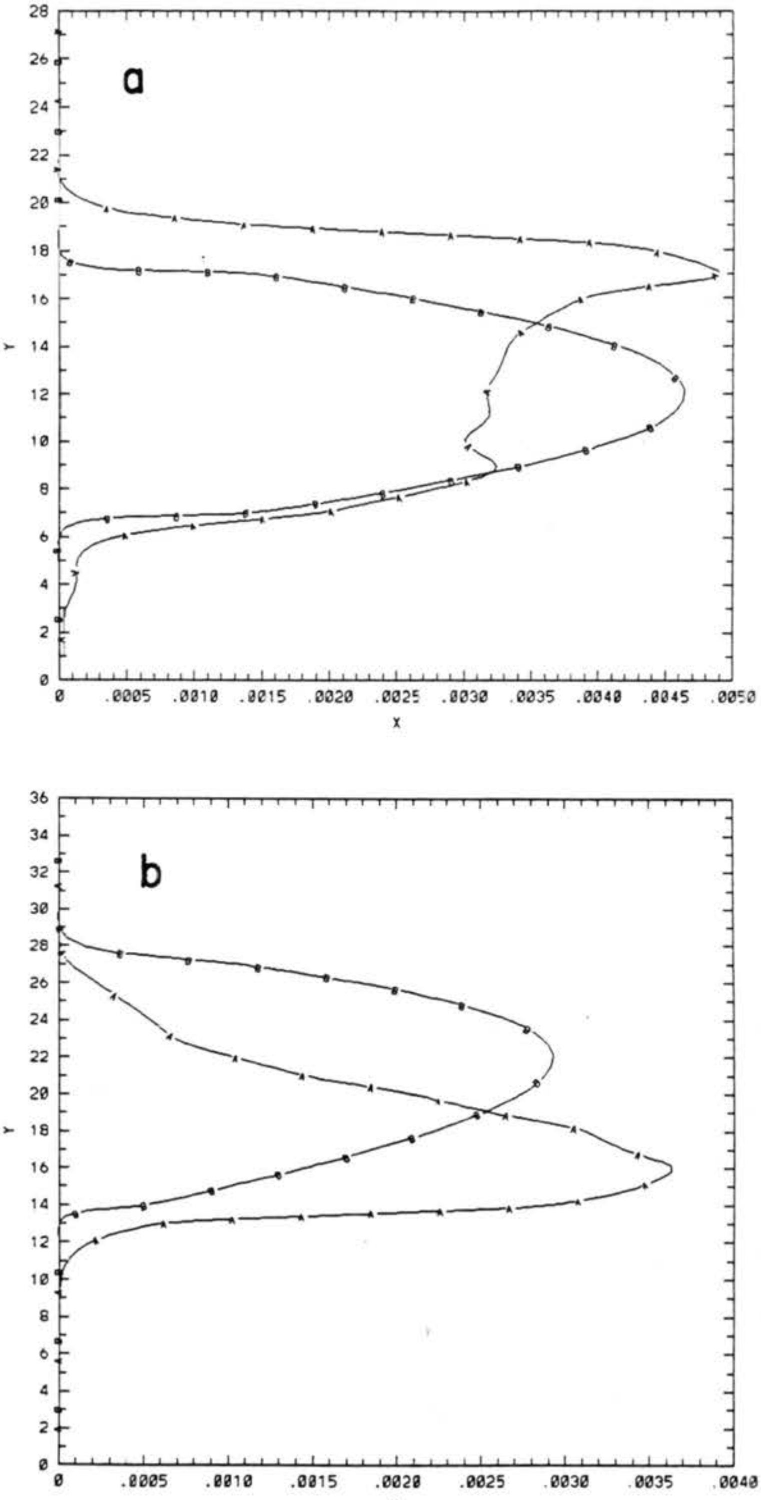

Figure 4.11: Vertical profiles of graupel in kg/kg for the conditionally sampled updraft (curve A) and the parameterized updraft (curve B) for (a) the CCOPE supercell at 5460 sec and, (b) the tropical squall line at 4200 sec.

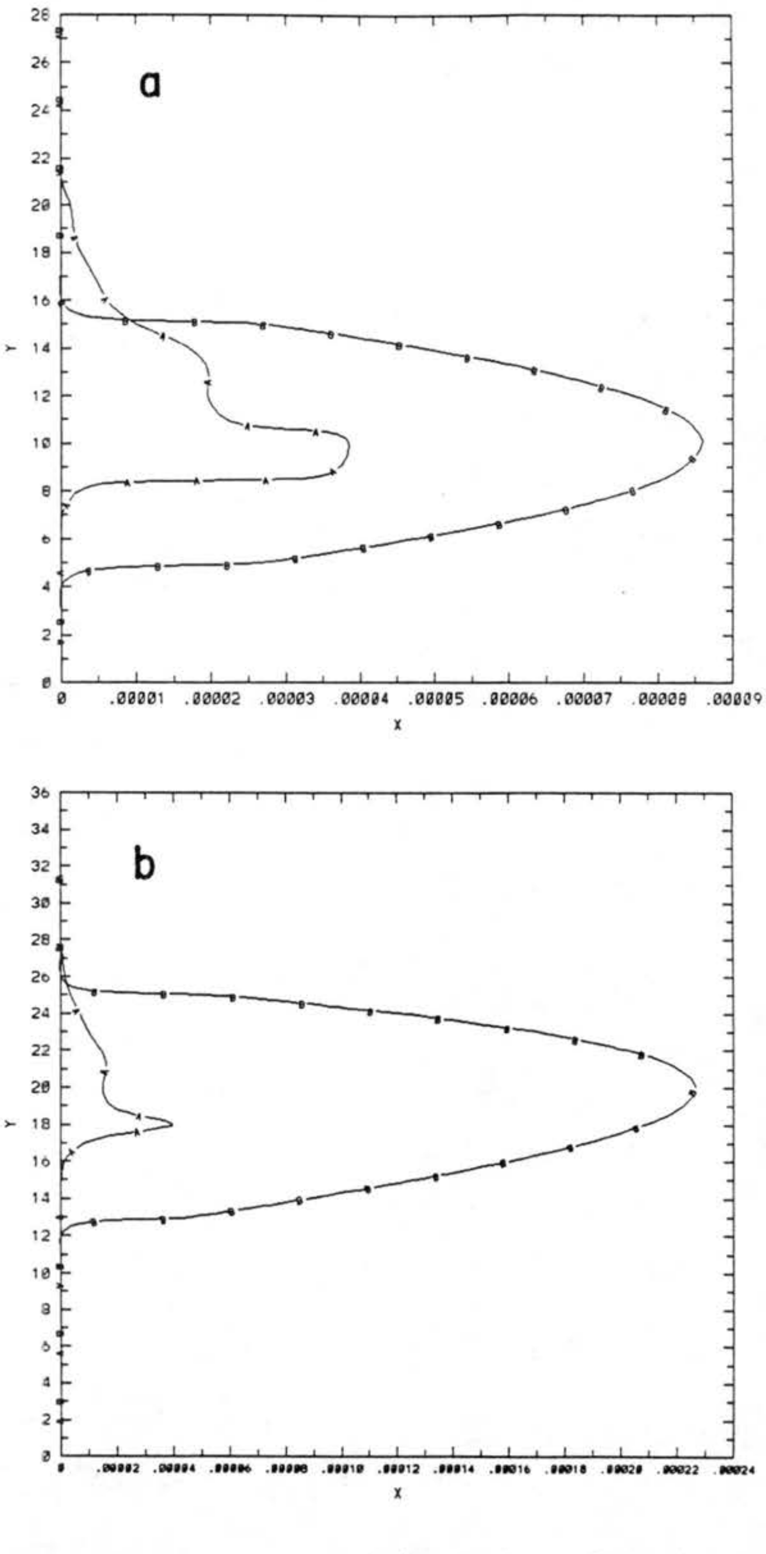

Figure 4.12: Vertical profiles of aggregates in kg/kg for the conditionally sampled updraft (curve A) and the parameterized updraft (curve B) for (a) the CCOPE supercell at 5460 sec and, (b) the tropical squall line at 4200 sec.

4.2.2 Modeling the downdraft

The sampling criterion for the downdrafts is vertical velocities less than -2 m/s with condensate present. Figs. 4.13a and 4.13b delineate the areal coverage of the sampled downdraft portions of the CCOPE supercell and the tropical squall line.

The downdraft core

The downdraft model is taken from Tremback (1990) and assumes that downdrafts are driven by the evaporation of precipitation and entrainment. In calibration tests, cloud model profiles better matched the explicitly calculated profiles if the additional cooling effects of melting and sublimation were neglected. The Betts and Silva Dias (1979) evaporative pressure scale is used to determine some of the downdraft characteristics. This crudely accounts for the evaporation rate of precipitation falling through the downdraft. Shown in Figs. 4.14a and 4.14b are the potential temperature profiles determined with evaporative pressure scales of 60 mb for the CCOPE supercell and the tropical squall line.

Increasing the evaporative pressure scale to 240 mb in the mid-latitude case and 180 mb for the tropical case yield the thermodynamic profiles shown in Figs. 4.15a and 4.15b.

Also shown in Figs. 4.16a and 4.16b are the conditionally sampled vertical velocities compared to two modeled downdraft velocities with the evaporative pressure scale set to 60 mb. Similarly, shown in Figs. 4.17a and 4.17b are the profiles with an evaporative pressure scale of 240 mb for the supercell and 180 mb for the squall line. As can be seen, the vertical velocities of the downdraft are not well predicted by the cloud model even though the potential temperature is handled well. Again, the downdraft velocities are not used in the parameterization except in the graupel parameterization which will be discussed later.

Condensate efficiency of the downdraft core

The evolution of the condensate efficiency of the downdraft core is shown in Figs. 4.18a and 4.18b for the CCOPE supercell and the tropical squall line, respectively. The

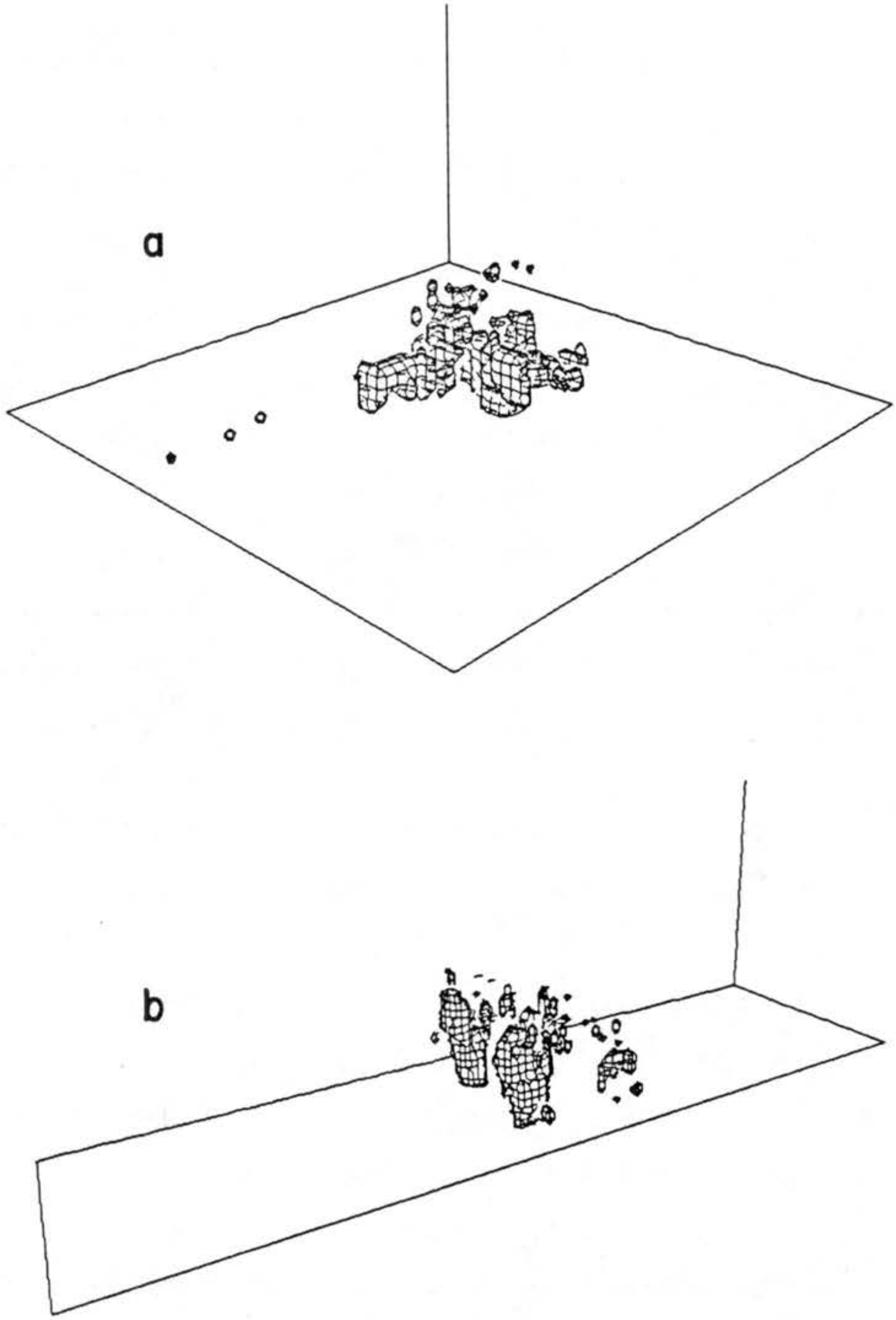

Figure 4.13: Conditionally sampled downdraft cores with $W \leq -2$ m/s for (a) the CCOPE supercell at 5580 sec, and (b) the tropical squall line at 3000 sec.

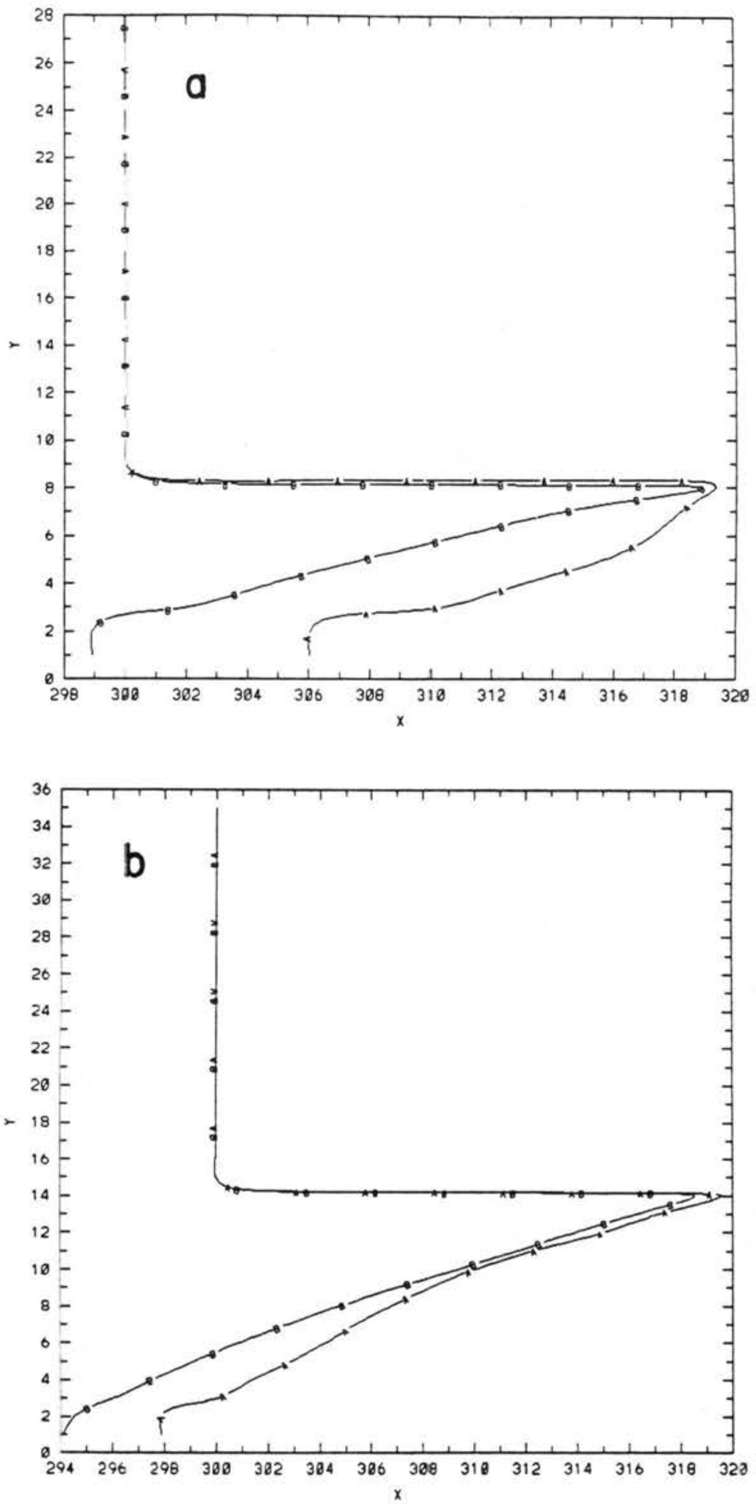

Figure 4.14: Vertical profiles of Θ for the conditionally sampled downdraft cores from the explicit simulation (curve A) and the cloud model-derived profiles with the the evaporative pressure scale equal to 60 mb (curve B) for (a) the CCOPE supercell at 5460 sec and, (b) the tropical squall line at 4200 sec.

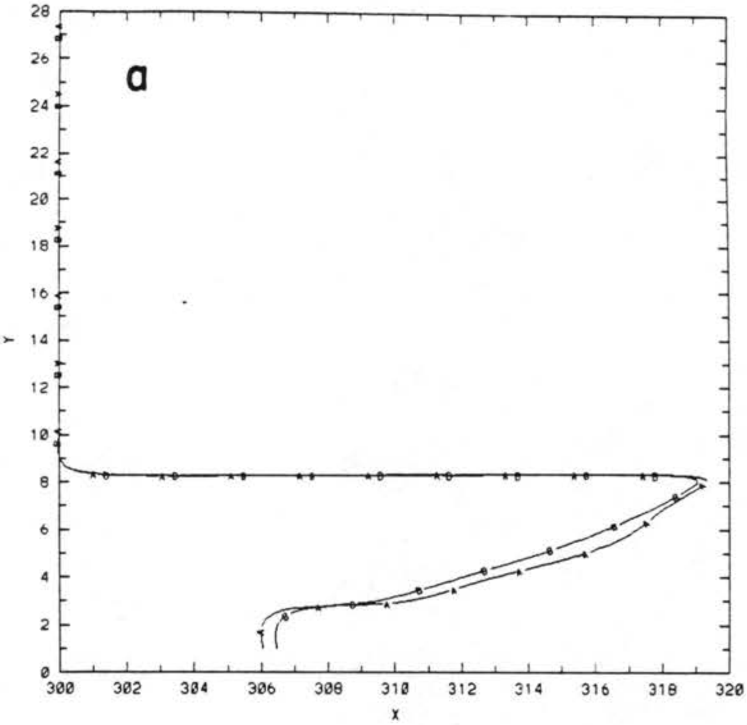

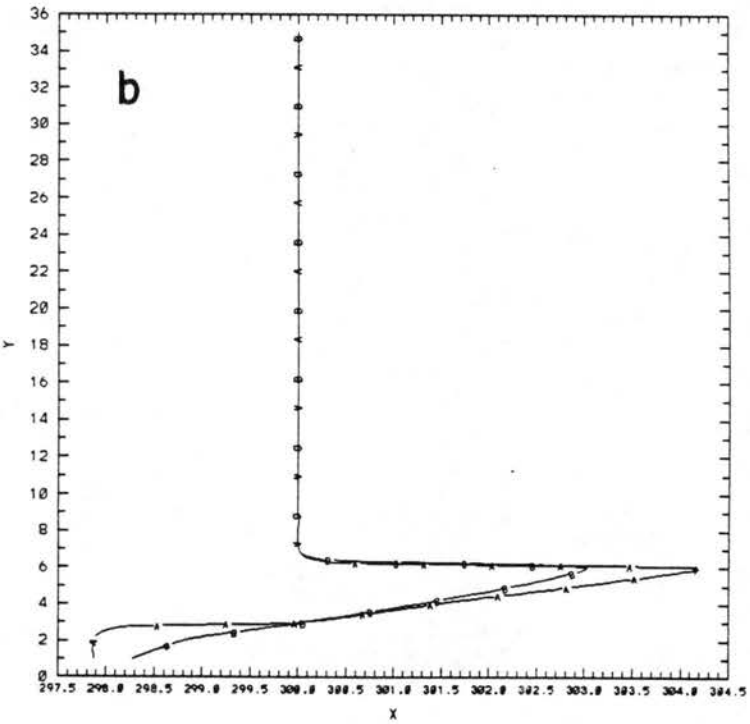

Figure 4.15: Vertical profiles of Θ for the conditionally sampled downdraft cores from the explicit simulation (curve A) and the cloud model-derived profiles (curve B) in (a) the CCOPE supercell at 5460 sec with the evaporative pressure scale equal to 240 mb, and (b) the tropical squall line at 4200 sec with the evaporative pressure scale equal to 180 mb.

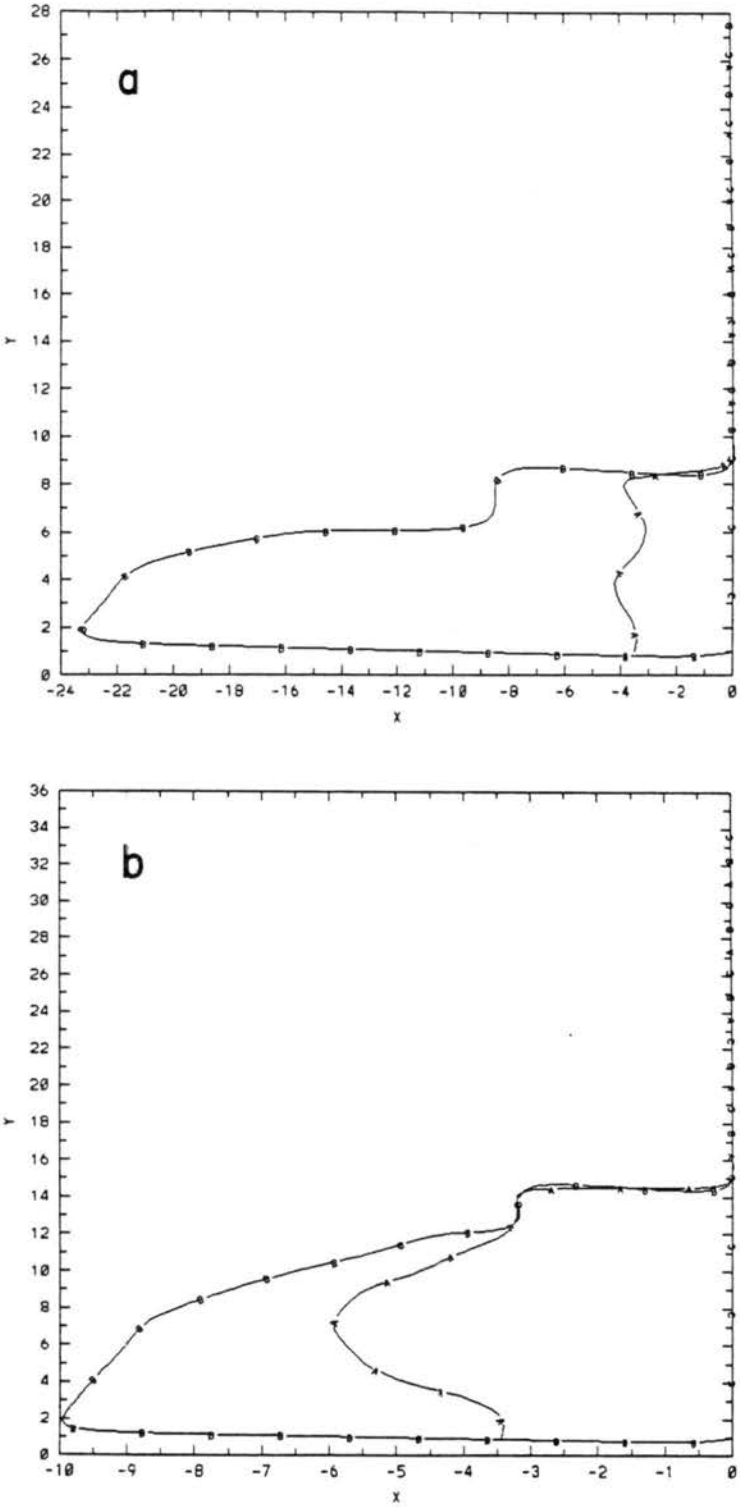

Figure 4.16: Vertical profiles of W in m/s for the conditionally sampled downdraft cores from the explicit simulation (curve A) and the cloud model-derived profiles with the evaporative pressure scale set to 60 mb (curve B) for (a) the CCOPE supercell at 5460 sec and, (b) the tropical squall line at 4200 sec.

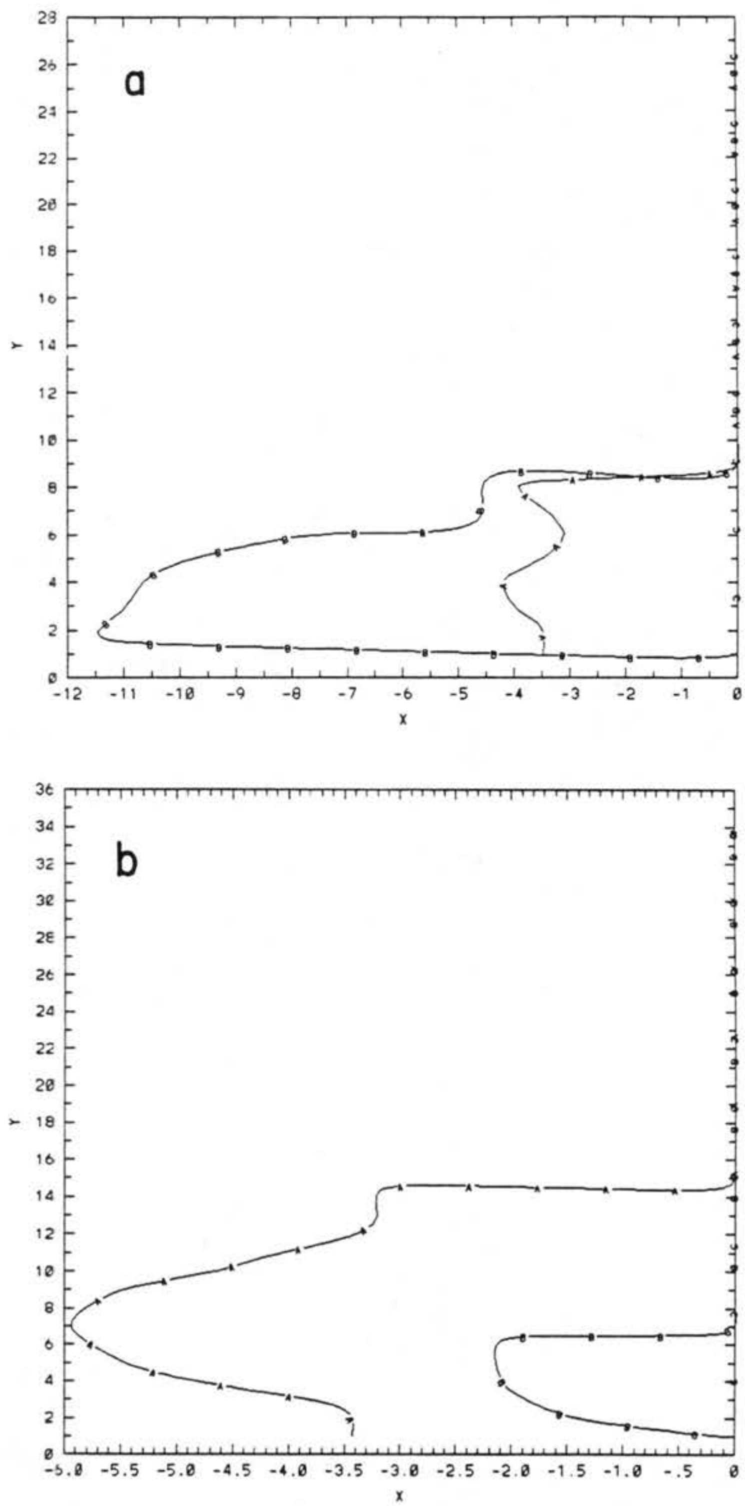

Figure 4.17: Vertical profiles of W in m/s for the conditionally sampled downdraft cores from the explicit simulation (curve A) and the cloud model-derived profiles (curve B) in (a) the CCOPE supercell at 5460 sec with the evaporative pressure scale equal to 240 mb, and (b) the tropical squall line at 4200 sec with the evaporative pressure scale equal to 180 mb.

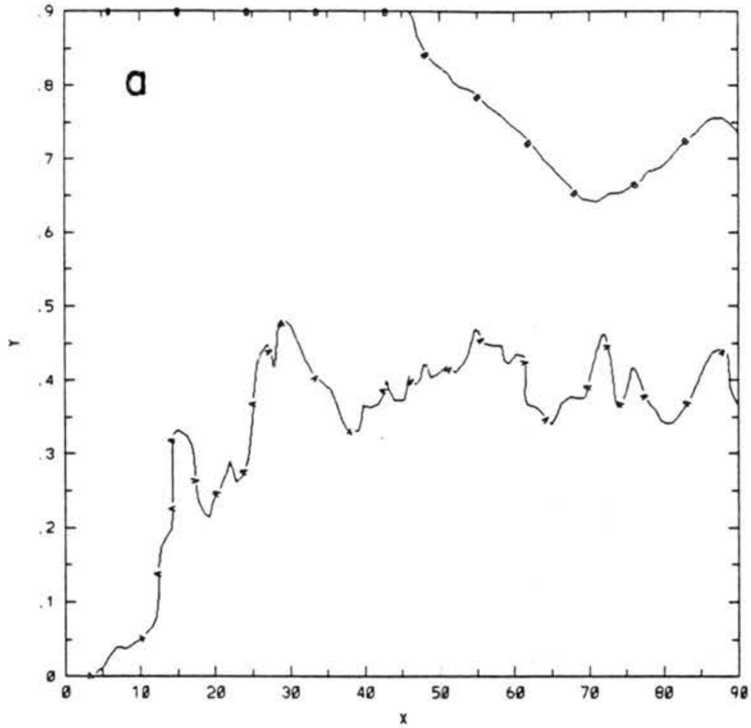

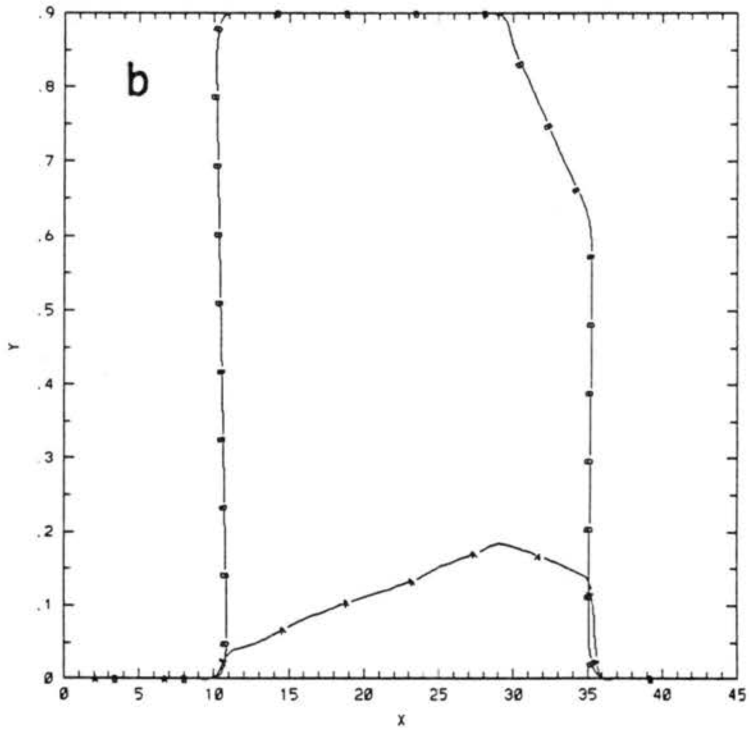

Figure 4.18: Time series in min of the condensate efficiency (curve A) for the conditionally sampled downdraft core of (a) the CCOPE supercell at 5460 sec and, (b) the tropical squall line at 4200 sec. Curve B represents the storm precipitation efficiency as determined from the empirical formula in Fritsch and Chappell (1980).

time series for the supercell indicates relatively steady state behavior and an average value of 42% is chosen as representative. A downdraft condensate efficiency of 23% is chosen to represent the tropical storm.

The total amount of water calculated in the downdraft is then taken from the updraft profile of rain since it is presumably the falling rain which contributes to the formation of the downdraft. If there is not enough rain in the updraft, then additional water is taken from the cloud water profiles within the updraft. This ensures that the total condensed water present in both the updraft and downdraft is equivalent to the total condensed water present within the cloud.

Hydrometeor profiles within the downdraft core

The time series in Figs. 4.19a and 4.19b indicate the percentage of rain and graupel in the downdraft of the supercell and the tropical squall line, respectively.

The parabolic curves for rain water is shown in Figs. 4.20a and 4.20b the supercell and squall line, respectively. Table 4.2 indicates the generalized criteria for constructing the parabolic curves.

Table 4.2: The generalized criteria for constructing the hydrometeor profiles within the downdraft core. fdis represents the distance a graupel particle will fall within the downdraft. See the text for an explanation.

Hydrometeor species	Z_{low}	Z_{mid}	Z_{high}
rain	1	1	ML
graupel (see text)	ML-fdis	ML	LFS

The parameterization of graupel is complicated by the fact that the graupel may or may not melt before it reaches the ground. The work is based on Mason (1956) who looked at factors influencing the melting of hailstones and graupel. He assumed the melting is due to the heat diffused from the environment and the heat of condensation. A more complete formulation should have included the heat diffused from the accreted cloud drops at the ambient temperature, but the treatment is kept simple. The initial radius of the graupel particle was calculated to be around 3 mm based on the mixing ratio of graupel near the

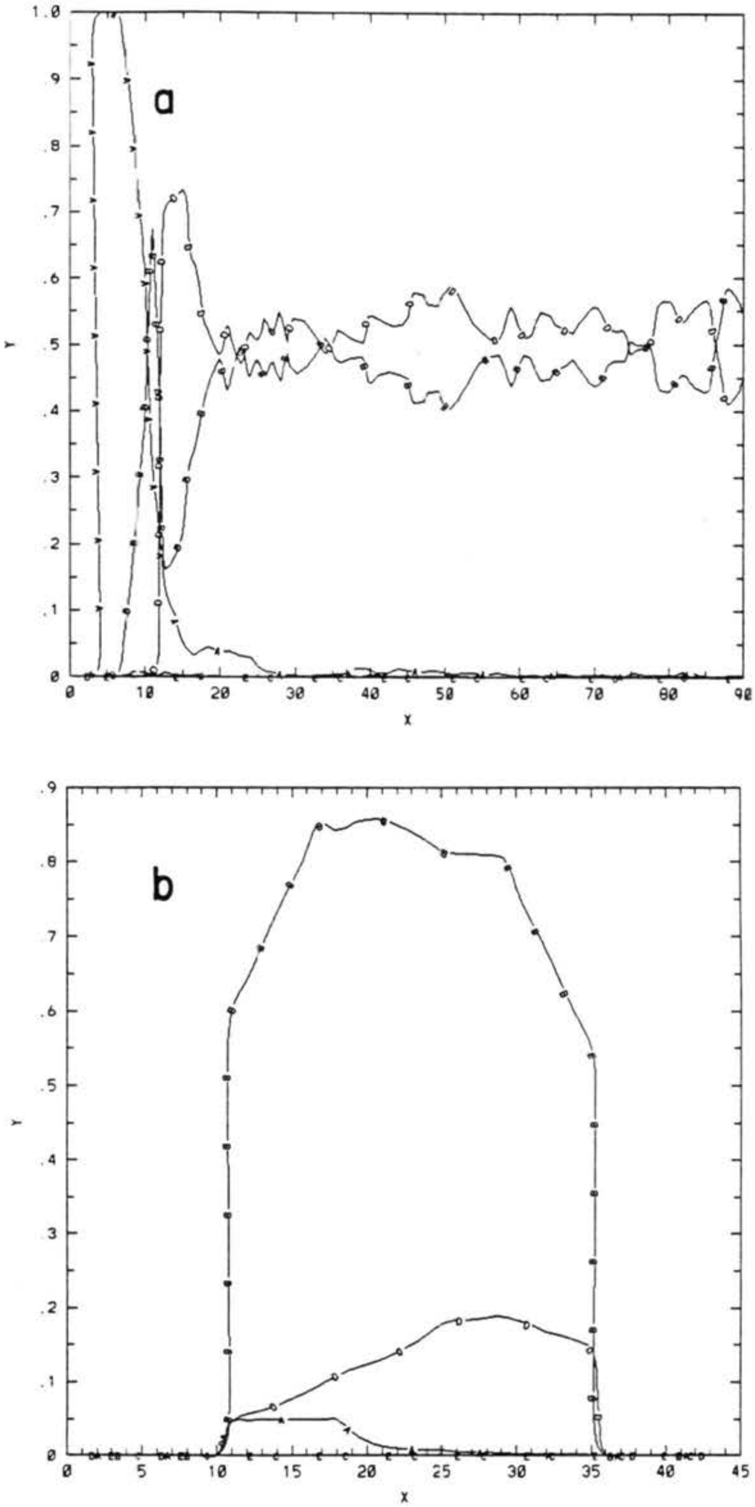

Figure 4.19: Time series in min of the percent contribution from cloud water (curve A), rain water (curve B), ice water (curve C), graupel (curve D) and aggregates (curve E) to the total conditionally sampled condensate within the downdraft for (a) the CCOPE supercell at 5460 sec and, (b) the tropical squall line at 4200 sec.

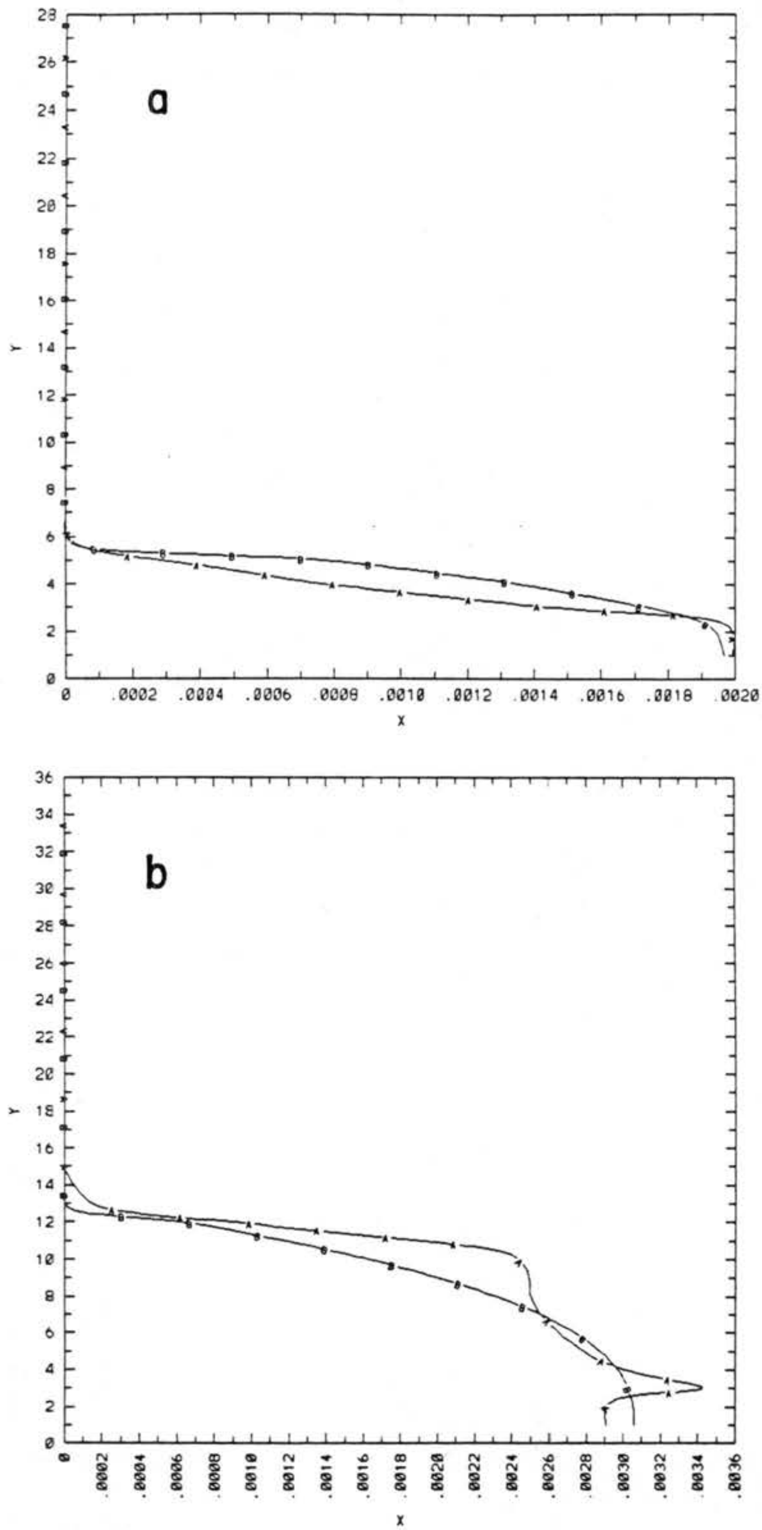

Figure 4.20: Vertical profiles of rain water in kg/kg for the conditionally sampled downdraft (curve A) and the parameterized downdraft (curve B) for (a) the CCOPE supercell at 5460 sec and, (b) the tropical squall line at 4200 sec.

ground for the supercell and the level where all the graupel had melted in the squall line. From the family of curves Mason deduced, a graupel particle with a 3 mm radius would fall 1.2 km in a saturated downdraft and 1.7 km in an unsaturated downdraft. Therefore, these distances are multiplied by $1 + W_d/V_t$ where the terminal velocity is assumed to be 5 m/s for graupel and the downdraft speed is the average over the depth of the downdraft of the cloud model predicted downdraft. The downdraft is considered saturated if the the relative humidity averaged over the downdraft depth exceed 80%. These new fall distances are subtracted from the melting level to give the lower penetration height of the graupel. This new height may be below ground level which would indicate graupel falling at ground level.

Unfortunately, the downdraft speeds are poorly estimated which could lead to erroneous graupel profiles. For the mid-latitude storm and the tropical storm, the parameterized graupel profiles are shown in Figs. 4.21a and 4.21b.

4.2.3 Cloud core fractional coverage

The final parameter to be determined is cloud core fractional coverage, *i. e.* $\sigma_{u,d}$ in Eq. 4.18. This parameter should be dependent upon the grid resolution as well as environmental conditions. At this point σ_d = f(σ_u). The closure of the updraft core fractional coverage is based on the observational evidence of the diameter of the updraft core and its associated environment, which is assumed to be comprised of weaker updrafts and downdrafts as well as any compensating subsidence around the cloud. Zipser and Lemone (1980) sampled updraft cores of greater than 1 m/s in the GATE area and found that they occupied about 5% of a 100×100 km^2 grid box from 2.5-4.3 km. Since each core has a diameter of approximately 2 km, the average area encompassed by one core and its associated environment is $\eta = 65$ km^2.

Similar diagnostics can be gleaned from Byers and Braham (1949) who studied thunderstorms in Florida and Ohio. Unfortunately, they based their fractional coverage on radar echos and thus a threshold value for the updraft core is difficult to determine. However, the maximum fractional coverage of the radar echos occurred at an altitude of 3 km

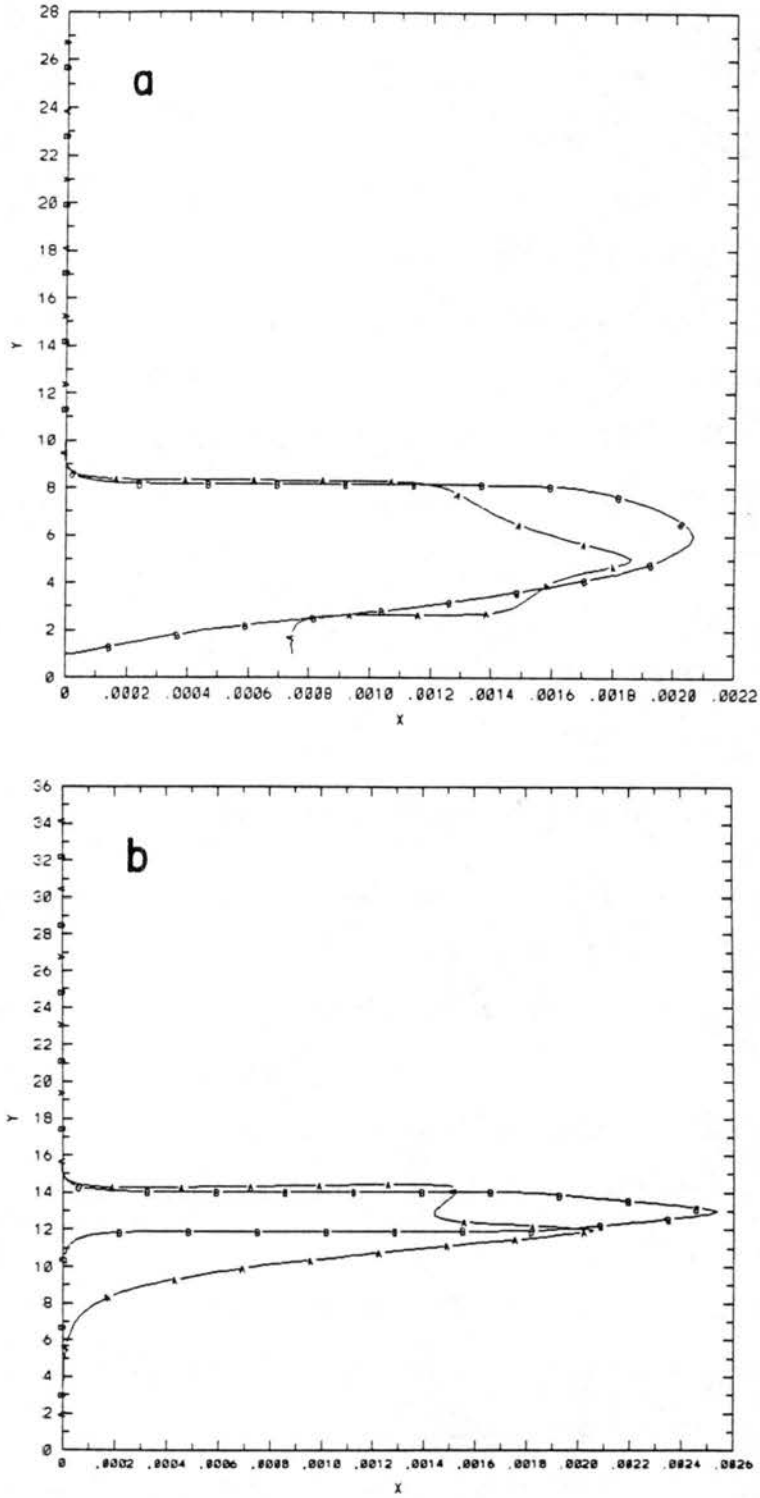

Figure 4.21: Vertical profiles of graupel in kg/kg for the conditionally sampled downdraft (curve A) and the parameterized downdraft (curve B) for (a) the CCOPE supercell at 5460 sec and, (b) the tropical squall line at 4200 sec.

and covered about 15% of a 400×400 km^2 area. If a diameter of 1.5 km is assumed, the average area encompassed by one core is $\eta = 13$ km^2.

The core and its associated environmental area is stratified according to a bulk Richardson number as defined by Weisman and Klemp (1982). In their formulation, Ri depends on CAPE, the positive area in a skew-T ln P plot and the mean shear over some of the storm's depth.

$$Ri = \frac{g \int \frac{\Theta_c(z)-\overline{\Theta}(z)}{\overline{\Theta}(z)} dz}{\frac{1}{2}\left(\frac{1}{\overline{\rho}\Delta z}\int_0^{6km} \rho(z)\overline{U}(z)dz - \frac{1}{\overline{\rho}\Delta z}\int_0^{\frac{1}{2}km} \rho(z)\overline{U}(z)dz\right)} \tag{4.25}$$

The GATE Ri were computed by Weisman and Klemp as well as a FACE Ri which was chosen to represent the thunderstorm projects η. The results are plotted in Fig. 4.22 and show that the core and cloud area vary inversely with the bulk Richardson number. This

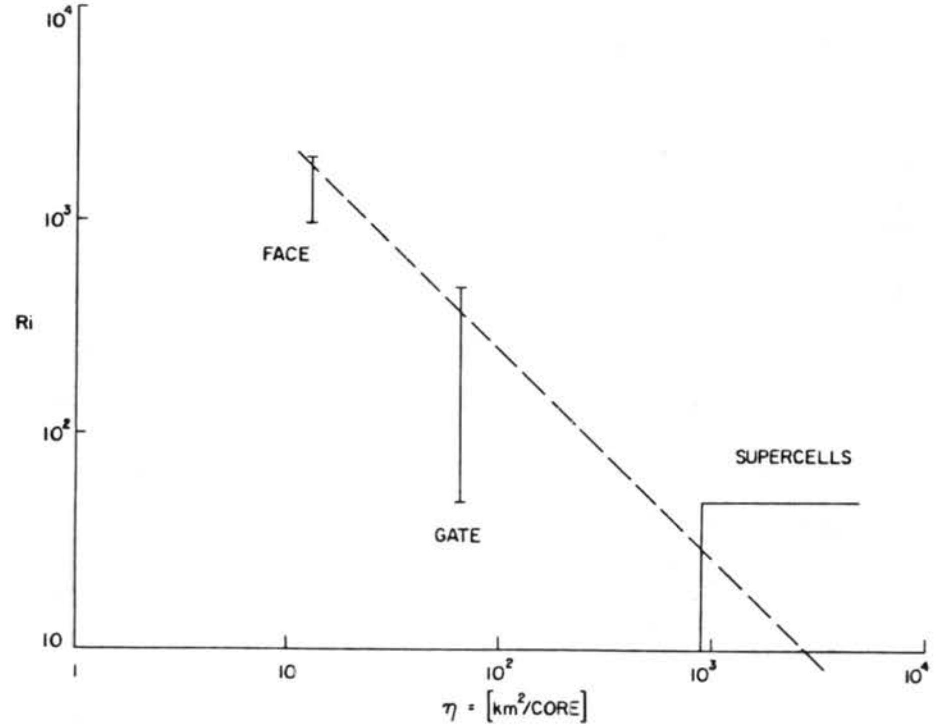

Figure 4.22: Cloud core updraft area (η) as a function of the bulk Richardson number (Ri).

makes sense since the larger storms, which occur at smaller Richardson numbers, have more area associated with them. The general relation then becomes

$$\eta = \frac{2x10^{11}}{Ri^2} + 10^7 \ [\mathrm{m}^2]. \tag{4.26}$$

If n is the number of cores in a grid area $\Delta x \Delta y$, then $\sigma_u = nA_{up}/\Delta x \Delta y = A_{up}/\eta$. Therefore, the updraft core fractional area is only dependent upon grid area if $\Delta x \Delta y < \eta$, *i. e.*

$$\sigma_u \;=\; MAX\left(\frac{A_{up}}{\eta}, \frac{A_{up}}{\Delta x \Delta y}\right). \tag{4.27}$$

For two dimensional simulations, the radius rather than the area of the updraft is considered:

$$\sigma_u \;=\; MAX\left(\frac{r_{up}}{\sqrt{\eta}}, \frac{r_{up}}{\Delta x}\right). \tag{4.28}$$

The fractional area of the downdraft is a simple function of the updraft fractional coverage. As in Tremback (1990) who based the downdraft mass flux on the observational studies of Knupp (1987), the downdraft mass flux is assumed to be equal to one half the cloud base updraft mass flux at the level of maximum downward vertical motion. The downdraft mass flux then decreases linearly with height to the LFS where its value is one third of the maximum value. This assumption is implemented by setting the maximum downdraft core fractional coverage equal to the updraft core fractional coverage at cloud base and decreasing the downdraft core fractional coverage appropriately with height.

A relationship between draft fractional coverage, the environment in which the cloud is growing and the grid area now exists if the updraft core radius is known . From Cotton and Anthes, (1989) the mean updraft radius varies between 1 km for tropical convection (high Ri) and 2 km for mid-latitude convection (low Ri). If an inverse linear relationship between cloud radius and Ri is assumed, then $A_{up} = \pi r^2 = \frac{50000}{Ri} + 1000$

4.2.4 The cumulus parameterization decision

The final parameters which need to be specified are those related to the activation of the cumulus fluxes. In general, the cloud model indicates that there is enough CAPE to support cumulus convection over a large area. In reality, the cumulus convection is focused through various triggers and is concentrated over a much smaller area. These triggers may include upward motion caused by synoptic or mesoscale fronts, propagating gust fronts or cold pools, gravity waves or other mechanisms. Ideally, the decision to activate the deep cumulus component should be related to properties of the mean flow which are not related to grid size. In the previous cumulus parameterization schemes designed for mesoscale models, resolved vertical motion at cloud base has to exceed a threshold value for the representation of deep cumulus. Since this cumulus parameterization scheme includes a measure of the sub-grid scale vertical motion, it seems appropriate to include $\overline{w'w'}$ in the cumulus decision. As will be discussed in the next Chapter, both the mean and sub-grid scale vertical motion are used in the cumulus decision.

4.3 Summary

A generalized cumulus parameterization based upon higher order turbulence closure is presented. The scheme is based on the prognosis of $\overline{w'w'}$ and is a hybrid of a level 2.5w scheme modeled after the level 2.5 scheme of Mellor and Yamada (1974) using Zeman and Lumley's (1976) closure for the eddy transport and pressure terms and the Betts (1975) method for the diagnosis of cumulus fluxes based upon a one dimensional cloud model. The cloud model has been calibrated to model output diagnostics from explicit numerical simulations of a CCOPE supercell and a tropical squall line. condensate efficiencies and condensate partition percentages are found and used in normalizing general parabolic curves representing the hydrometeor distribution within the parameterized cloud. The inclusion of hydrometeor profiles allows for an accurate treatment of the buoyancy flux within the cloud (which is crucial for the correct prognosis of $\overline{w'w'}$) and provides cumulus source functions of hydrometeors for the mesoscale model.

The variables which are thus far 'tunable' are; (1) the entrainment rate; (2) the evaporative pressure scale; (3) the condensate efficiency (which can be bypassed by using the total water values generated by the cloud model); and (4) the condensate partitioning parameter. One last detail which will be addressed in the following Chapter is the cumulus parameterization decision, *i. e.* the criteria which need to be satisfied in order to initiate deep cumulus convection.

Chapter 5

PERFORMANCE OF THE CUMULUS PARAMETERIZATION SCHEME

The mathematical framework for the parameterization has been described in chapter 4. Here, evaluation of the non-entraining cumulus parameterization scheme is performed for both one dimensional and two dimensional simulations. The one dimensional simulations are performed in the context of a mesoscale model with a very large horizontal grid spacing of 1000 km and cloud fractional coverage of unity. There is necessarily no mean vertical motion and feedback between the scheme and the numerical model so that the one dimensional simulations then indicate the limiting state to which the cumulus parameterization scheme tends. The two dimensional simulations, on the other hand, allow the parameterization and mesoscale model to develop concurrently, thus allowing the scheme to be evaluated as an interactive entity.

5.1 One dimensional simulations

The one dimensional simulations will be presented here in order to delineate the final or limiting state the cumulus parameterization scheme would reach. This scheme is placed within a mesoscale model with a large horizontal grid spacing of 1000 km in order to simulate a one dimensional model. Areal coverage of the cumulus is assumed to be unity and the parameterized cumulus is active for 5400 seconds. Since a one-dimensional simulation does not allow for the horizontal convergence of water vapor, this quantity will not be depleted by the cumulus convection. Figures in this section will include the initial and final total water mixing ratio profiles, initial and final potential temperature and final Θ_{il} profiles, and the time evolution of the condensate rate for simulations with and without downdrafts and with and without precipitation. The condensate rate is defined as the total liquid and ice which is produced within the parameterized cloud. In order to produce these limiting states, only the convective adjustment term (the second term on the rhs of Eq. 4.20) is retained since there can be no vertical motion to offset the compensation term.

The limiting state for a non-entraining cumulus cloud with no downdrafts and no precipitation is indicated in Figs. 5.1a - 5.1c. The final total water mixing ratio (Fig. 5.1a) is well mixed through the depth of the cloud as is the final $\overline{\Theta_{il}}$ profile in Fig. 5.1b. Note that the potential temperature profile in the same figure indicates the atmosphere has warmed at all levels in response to the convection. The condensate rate in Fig. 5.1c peaks at 310 mm/hr soon after cumulus convection is initiated and assymptotes to near 20 mm/hr. The condensate rates are large since the parameterized cumulus has a fractional coverage of unity. These profiles adequately characterize the expected changes in the environment when a deep, non-entraining, non-precipitating cloud with no downdrafts fills a grid volume.

When downdrafts are added to the cumulus parameterization (Figs. 5.2a - 5.2c) with an evaporative pressure scale of 180 mb, the final total water mixing ratio shows a decrease in value where the downdrafts are present. Furthermore, cooling below model level 12 in Fig. 5.2b is apparent. The condensate rate peaks 50 mm/hr higher at 460 mm/hr and assymptotes to a similar value as the no downdraft case.

The final states when the parameterization is run with precipitation and no downdrafts is indicated in Figs. 5.3a - 5.3c. The total water mixing ratios in Fig. 5.3a are not constant with height since there is now precipitation forming and falling. The final $\overline{\Theta_{il}}$ in Fig. 5.3b is no longer well mixed due to the precipitation processes, yet the potential temperature profiles are similar to the simulation with no precipitation since the in-cloud potential temperatures are only affected by precipitation through the energy released by the freezing process. The condensate rate peaks at 365 mm/hr and assymptotes near 60 mm/hour.

When both downdrafts and precipitation are added to the cumulus parameterization (Figs. 5.4a - 5.4c), slightly more total water accumulates near the lower layers as evidenced by Fig. 5.4a. Also slight cooling is seen in the lowest layers in Fig. 5.4b. The condensate

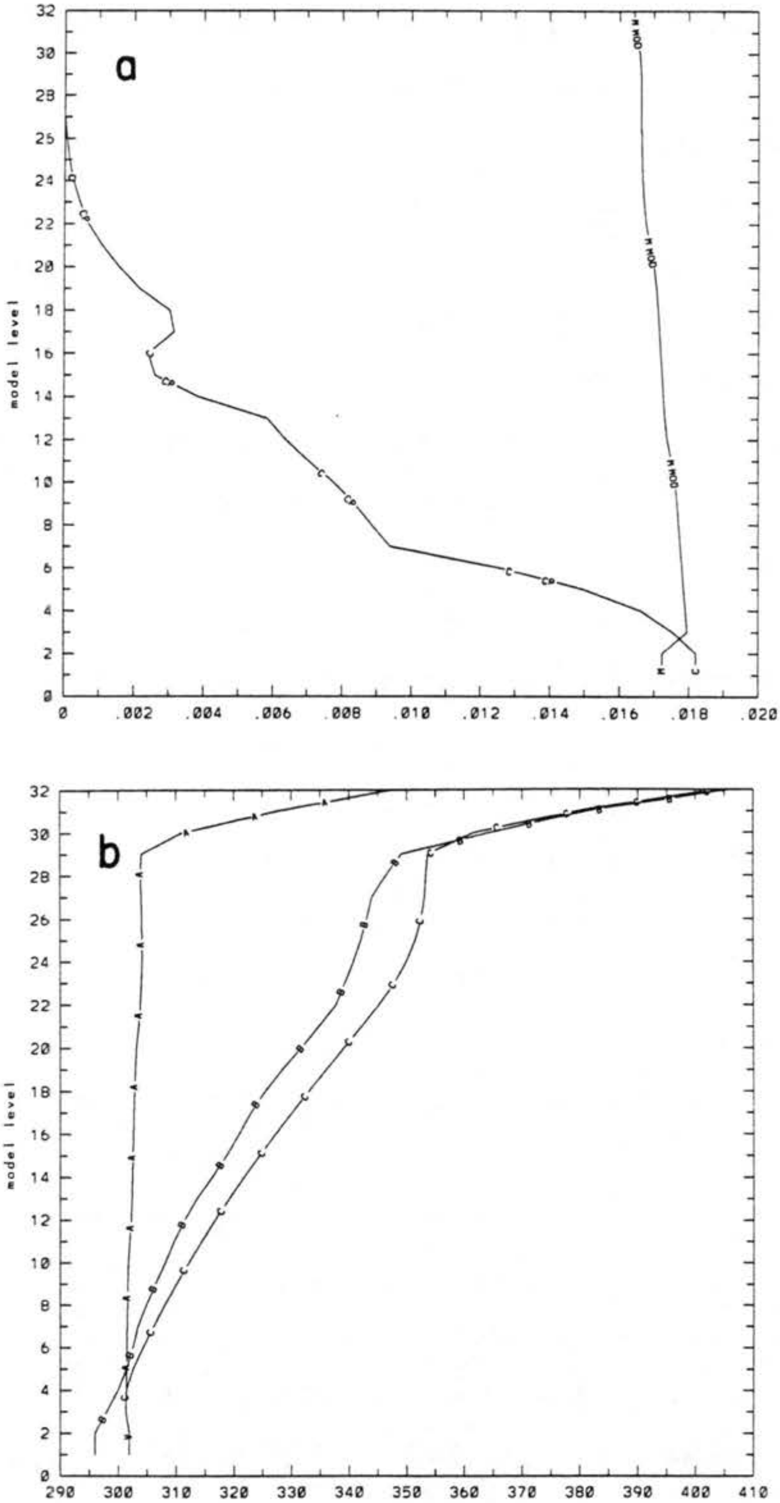

Figure 5.1: One dimensional simulation without downdrafts and without precipitation. (a) initial R_T (curve CP) and final R_T (curve MOD) in g/kg after 5400 s, (b) initial Θ (curve B), final Θ (curve C) and final $\overline{\Theta_{il}}$ (curve A) after 5400s.

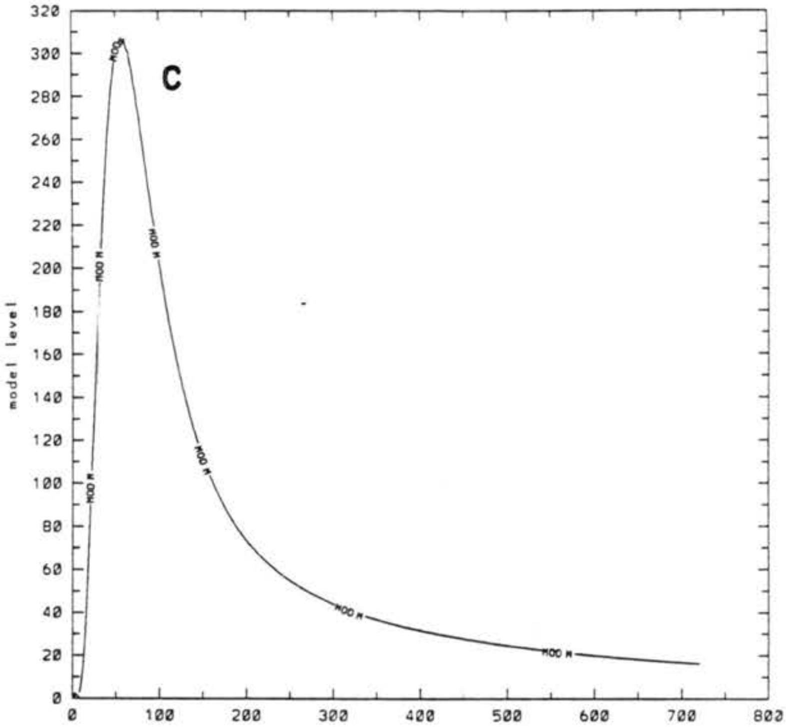

Figure 5.1: Continued. (c) Time series of condensate rate in mm/hr

rate is higher than the no downdraft case through the whole simulation with a peak rate of 460 mm/hour and an asymptotic rate of 140 mm/hour.

These limiting solutions indicate that the cumulus parameterization scheme is functioning as desired. The next step is incorporating the scheme in a fully two dimensional simulation.

5.2 Two dimensional simulations

The results of the cumulus parameterization on a five and a twenty kilometer grid are now compared to a two dimensional explicit simulation on a 1.5 km grid of Florida sea breeze convection. The explicit simulation follows closely the experimental design of Nicholls *et al.* (1991b) who examined the effect of varying initial wind and thermodynamic profiles on the evolution and structure of deep convection initiated by the propagating sea-breezes. They examined three wind profiles from which their Type I, discussed below, is chosen. The domain size is 600 km with land in the center third of the domain and water on either side and includes a stretched vertical grid having a resolution of 250 m near the

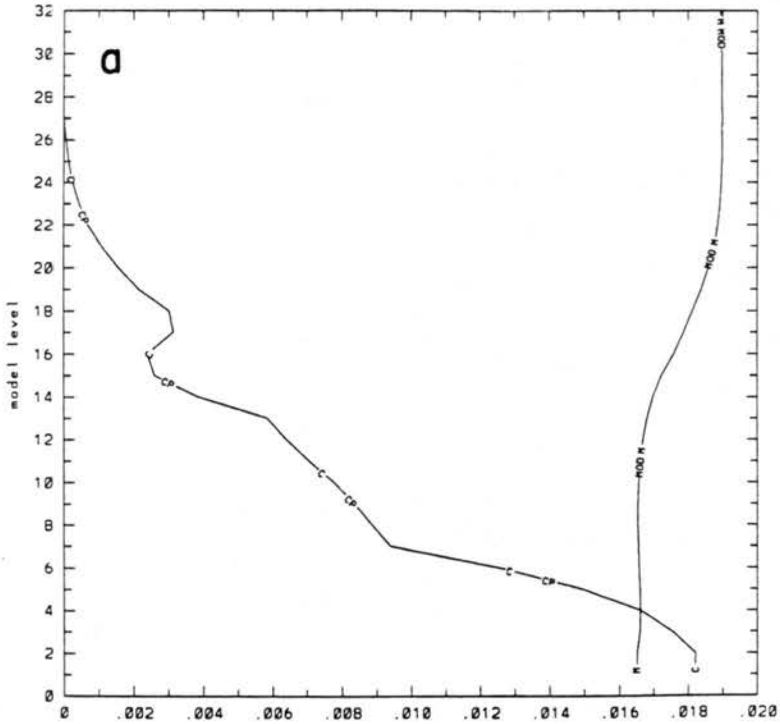

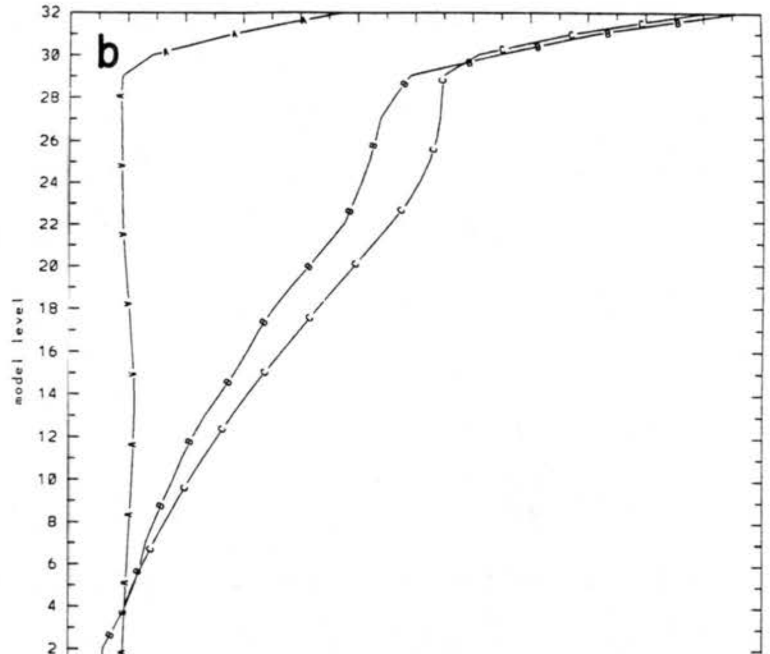

Figure 5.2: As in Figs. 5.1a-c except for a one dimensional simulation with downdrafts and without precipitation.

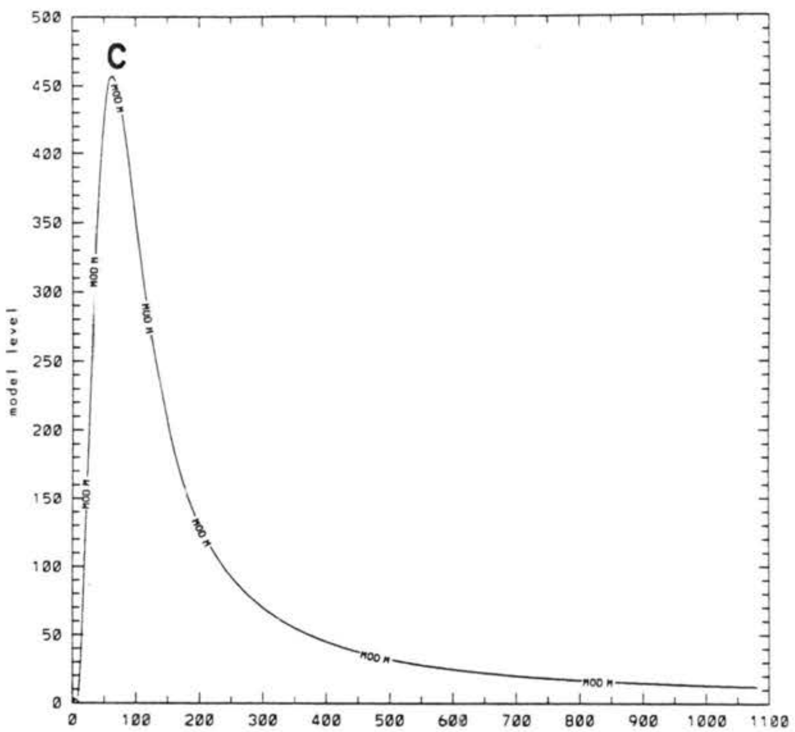

Figure 5.2: Continued.

surface and increasing to 1 km up to 21 km. There is a Rayleigh friction layer in the uppermost 7 km of the domain and Klemp-Wilhelmson (1978) radiative lateral boundary condition with a very large phase speed to effectively create a zero-gradient outflow condition. Full microphysics including rain, ice, graupel and aggregates are included. The simulation is run for 12 hours starting at 0800 local time in order to properly capture the development of the sea breeze. The Type I thermodynamic profile has a lifted index of about -4° (Fig. 5.5a) while the wind profile (Fig. 5.5b) indicates easterlies through the depth of the troposphere with a slight jet near the ground and near the troposphere.

The sea breezes develop fairly early in the day as the solar radiation heats the ground more strongly than the water. A relative low pressure forms over the peninsula which draws in the relatively cooler and denser oceanic air over both coasts. The result is an eastward propagating sea-breeze front over the western coast and a westward propagating front on the east coast. As noted in Nicholls *et al.* in their review of the Florida sea breeze phenomenon, this Type I situation is characterized by by development of deep convection along both coasts due to low level uplift at the sea breeze fronts. The east coast convection

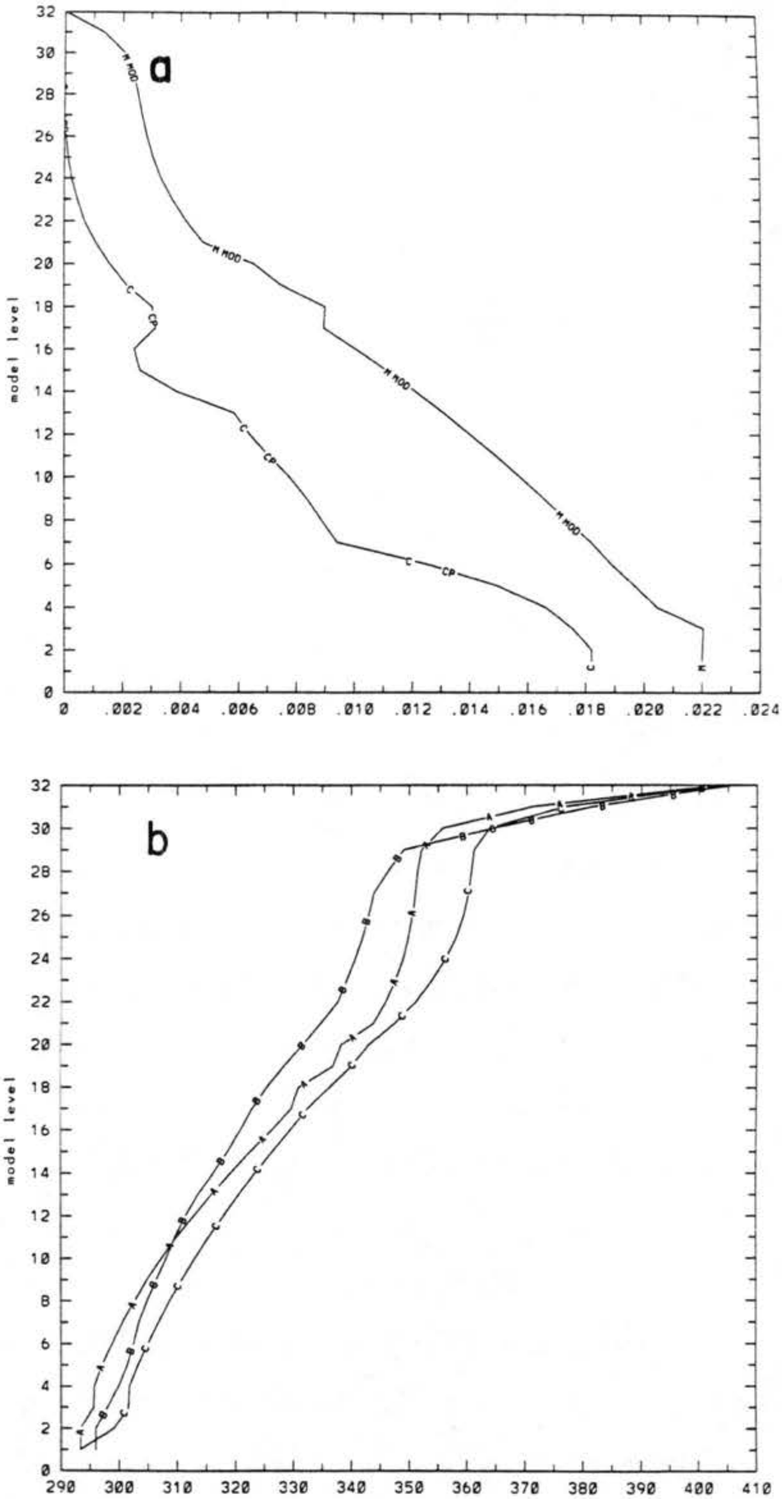

Figure 5.3: As in Figs. 5.1a-c except for a one dimensional simulation without downdrafts and with precipitation.

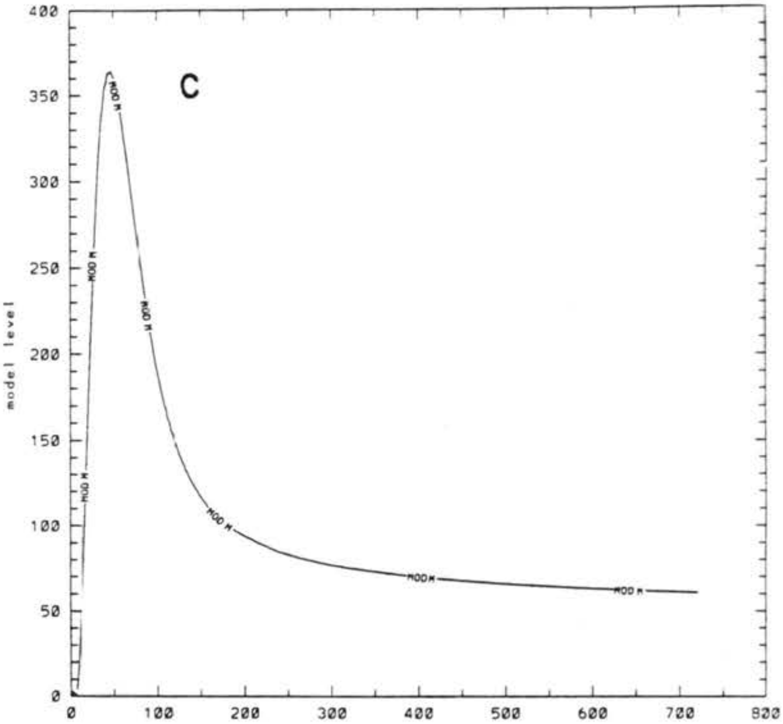

Figure 5.3: Continued.

moves inland fairly rapidly, whereas the west coast convection moves more slowly due to the presence of an easterly component in the wind. The sea breeze fronts collide to the west of the center of the peninsula producing the strongest convection which diminishes in the early evening.

Before the explicit and parameterized simulations are compared, the decision criteria for activating the cumulus parameterization scheme are discussed. Traditional parameterizations generally rely on a grid-dependent threshold value of mean vertical motion in order to determine whether to activate the cumulus parameterization scheme. For example, the Fritsch-Chappell schemes checks for resolved upward motion greater than an arbitrarily specified threshold; as the grid resolution increases, the threshold value must increase as well since the resolved vertical motions are necessarily stronger. Kuo (1974) also triggers deep cumulus when the low-level velocity reaches some threshold value while the Arakawa-Schubert scheme diagnoses the existence of convection whenever the large-scale variables increase the cloud-work function. Another problem with using vertical velocity as the decision trigger is that gravity waves excited by convection or other mechanisms may force

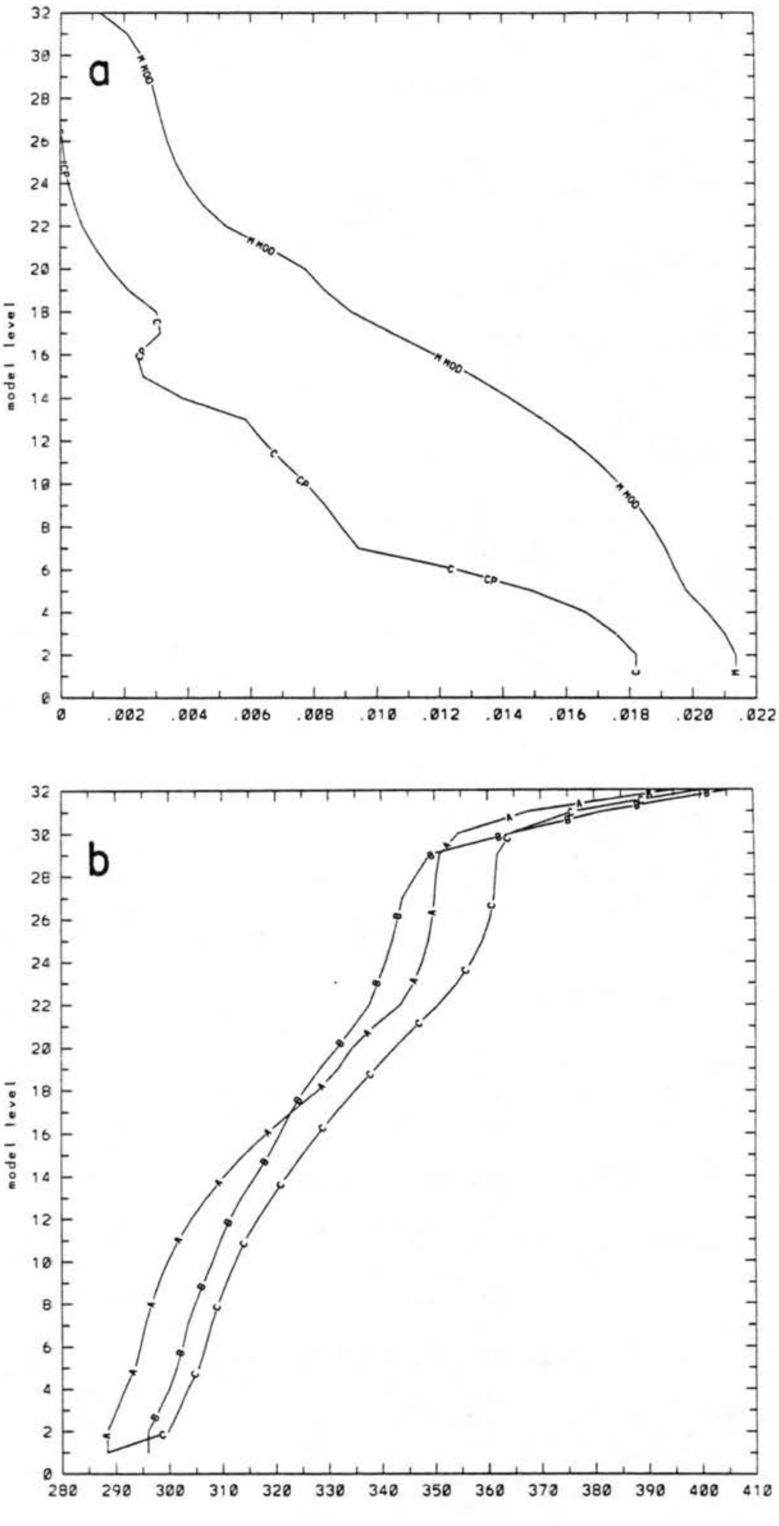

Figure 5.4: As in Figs. 5.1a-c except for a one dimensional simulation with downdrafts and with precipitation.

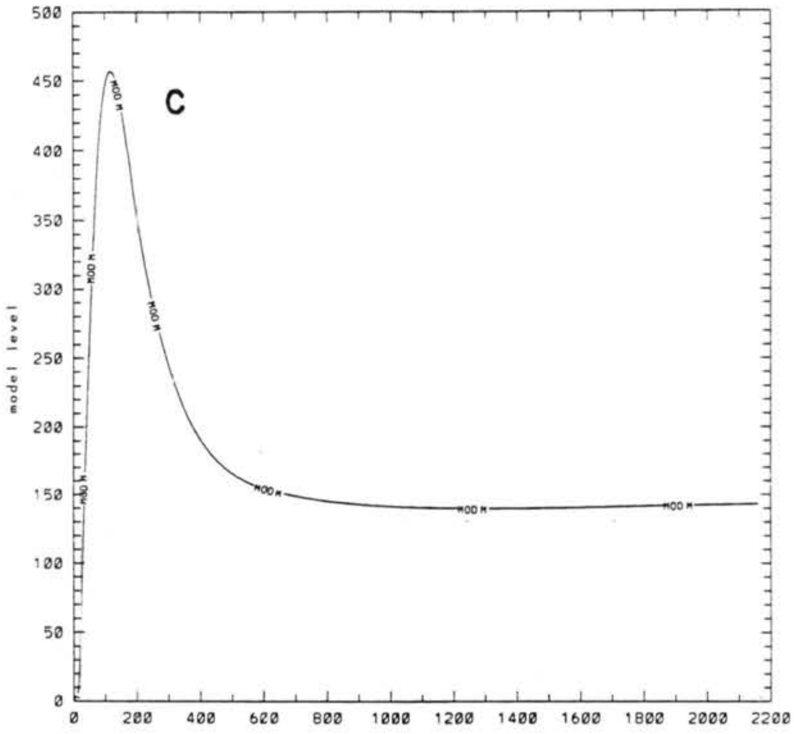

Figure 5.4: Continued.

activation of the cumulus parameterization scheme. This may produce propagation rates of the convection similar to the phase speed of the gravity wave which may or may not be the case (Tripoli and Cotton, 1989) and also produce convection in undesirable locations. The decision criteria is therefore based on there being any upward motion in the presence of a calibrated value of $\overline{w'w'}$. The advantages of using $\overline{w'w'}$ are that gravity waves are not represented in this formulation of the vertical variance and the magnitude of threshold value of $\overline{w'w'}$ should vary less than the mean vertical motion.

Unfortunately, it was necessary to adopt a threshold value of mean vertical motion since there was insufficient $\overline{w'w'}$ generated when the sea-breeze fronts collided to support deep convection. Cumulus convection can therefore be triggered in this scheme by mean vertical motion or $\overline{w'w'}$, both of which are grid-dependent. Furthermore, the convection rapidly depleted the boundary layer moisture so that convection ceased soon after it was initiated. Perhaps this is due to the nature of the parameterization; it was constructed from three dimensional steady-state storms. The source of moisture was the PBL and moisture depletion there was probably replenished through moisture convergence in both

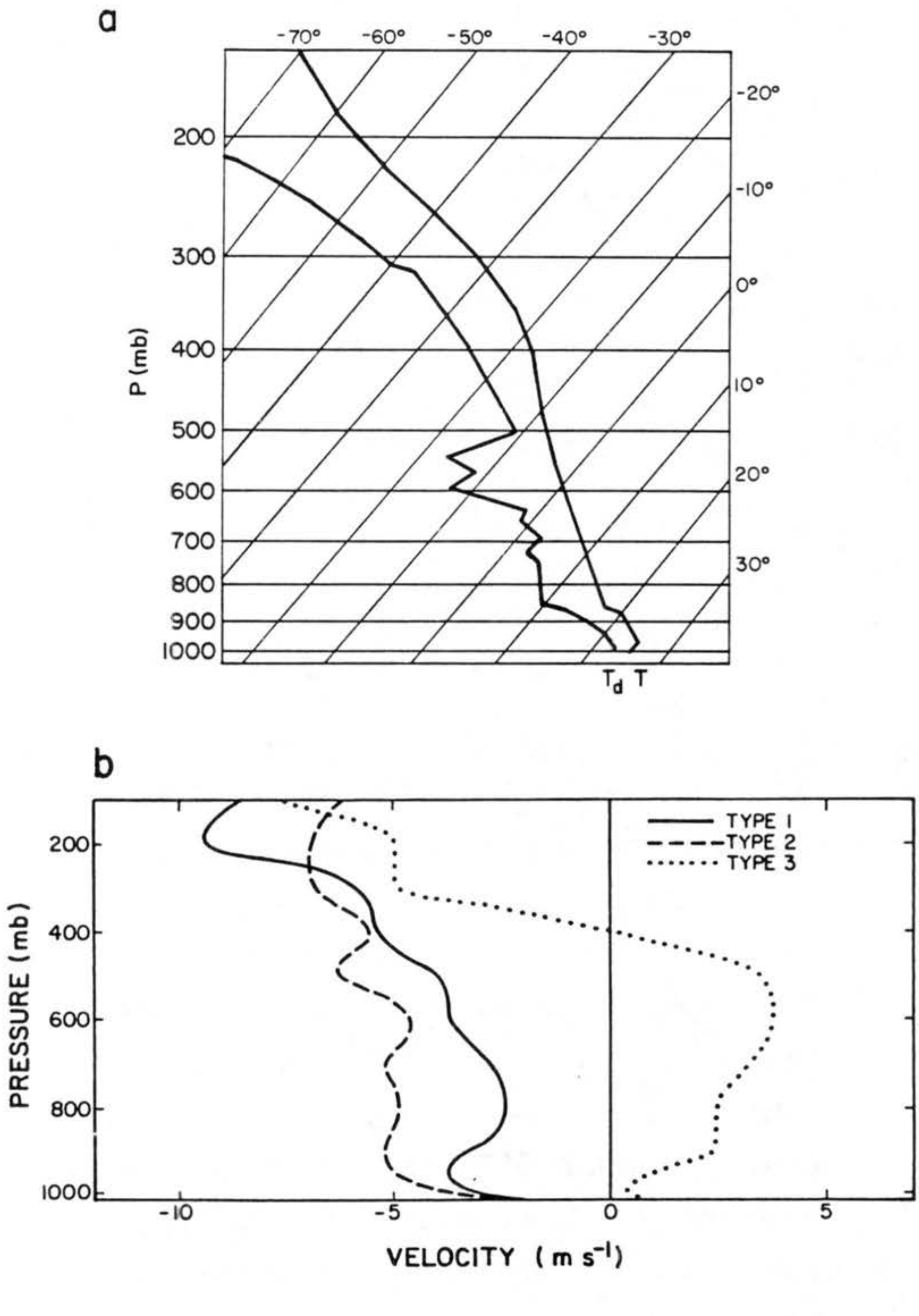

Figure 5.5: (a) Thermodynamic sounding taken from Nicholls *et al.* (1991a), and (b) the vertical profile of horizontal wind used in the two dimensional simulations.

horizontal directions. In this two dimensional study, three dimensional convection basically draws from a two dimensional boundary layer so that the parameterized storms will always be short of available moisture. Therefore, the PBL moisture is not depleted by the parameterized cumulus convection in the two dimensional test simulations and thus there is no mass balance of total water.

Four numerical simulations are performed with a five and twenty kilometer resolution; a precipitation simulation with and without downdrafts and a condensation only simulation with and without downdrafts. All simulations with downdrafts used an evaporative pressure scale of 180 mb which was found in the previous section to adequately characterized the potential temperature profile of downdrafts in tropical convection. These will be analyzed at 1400 local time when the transient convection is active along the sea-breeze fronts and 1700 local after the fronts collide and initiate steadier, longer-lived convection.

5.2.1 The explicit and parameterized simulations on a 20 km grid

This section will analyze the explicit simulation analyzed with 20 km running averages and the parameterized simulation on a 20 km grid. This will be done separately at 1400 local time and 1700 local time. Since the running averages must be an integral number of the 1.5 km grid resolution of the explicit simulation, these averages will not correspond exactly to the parameterized runs.

The explicit simulation at 1400 local time

In order to compare the explicit simulation and the simulation with the cumulus parameterization, running averages over appropriate lengths are applied to the fields of horizontal and vertical wind, perturbation temperature, perturbation total mixing ratio, condensate mixing ratio and the vertical variance on the sub-averaging-scale. Shown in Figs. 5.6a - 5.6f are the 21 km running averages of these quantities at 1400 local time.
At this time, transient convection is only present on the east coast with averaged vertical motions as high as 1 m/s. Apparent is the warming of the PBL through radiational heating and the drying of the PBL as the cumulus draws from the moisture reservoir. Interestingly, $\overline{w'w'}$ values are small; the values of 2.1 $\frac{m^2}{s^2}$ which are found in the cumulus

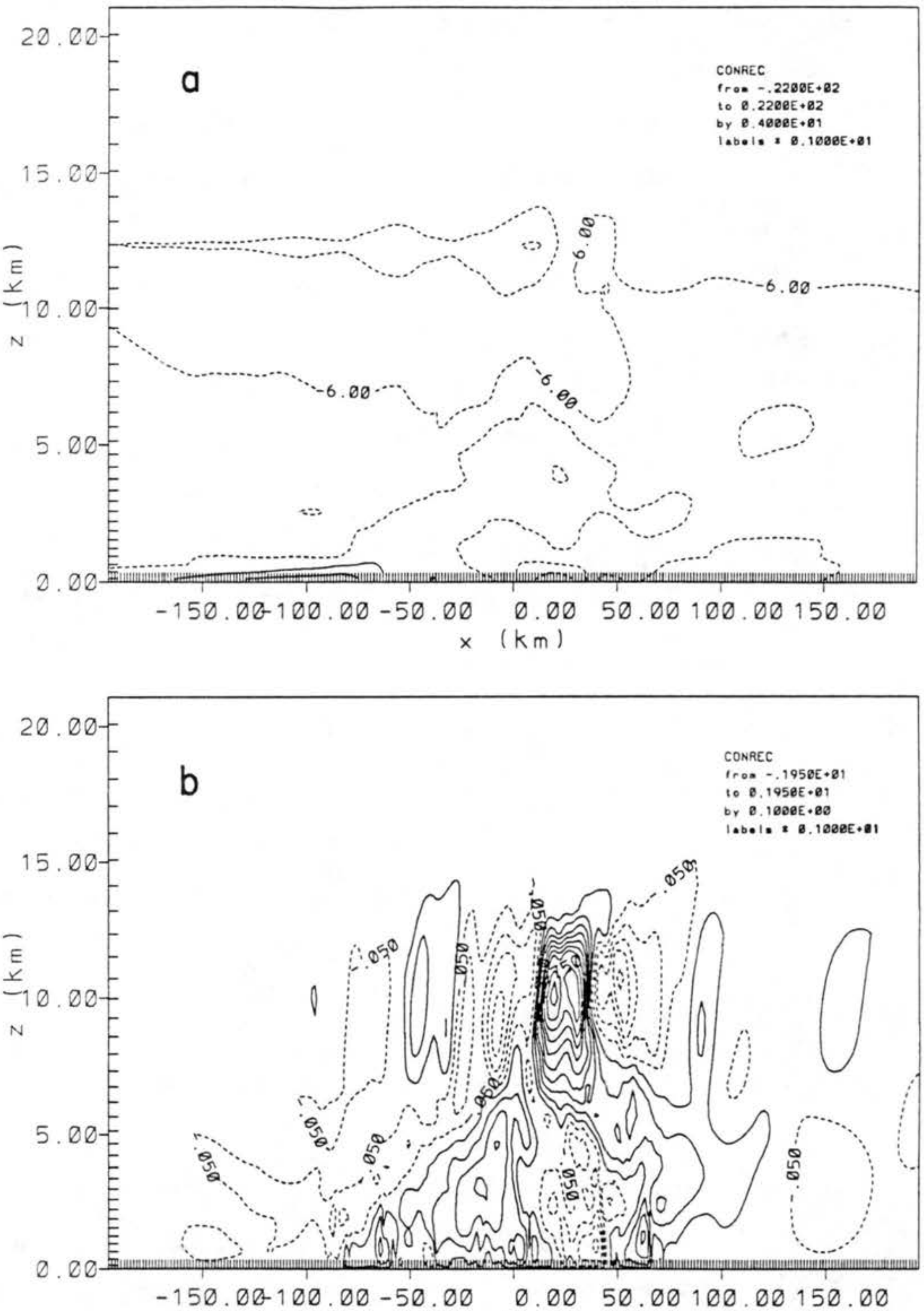

Figure 5.6: 21 km running averages of the explicit two dimensional simulation for the inner 400 km of the domain at 1400 local time. (a) horizontal velocity in m/s, (b) vertical velocity in m/s.

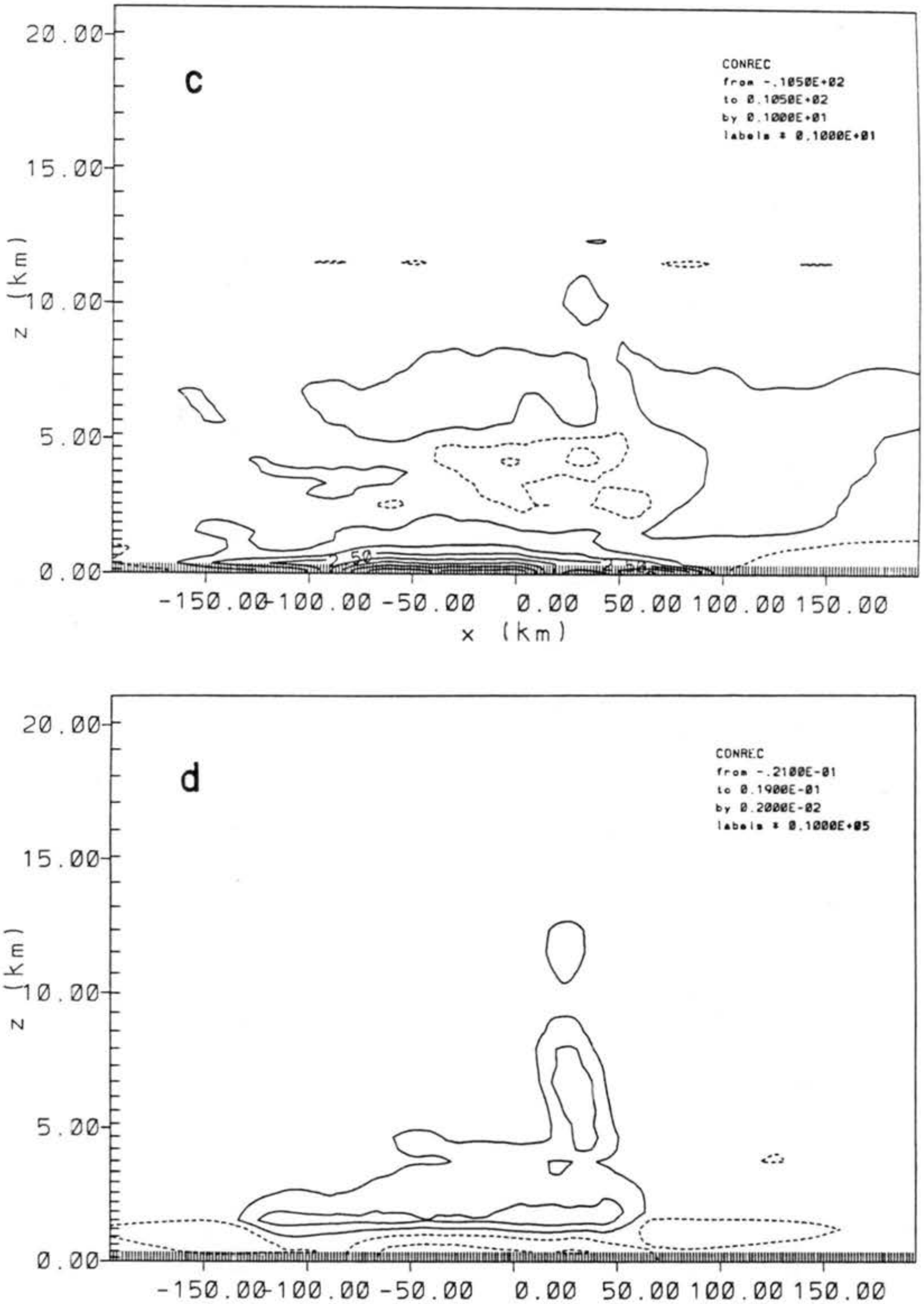

Figure 5.6: Continued. (c) perturbation temperature in K, (d) perturbation total water mixing ratio in kg/kg.

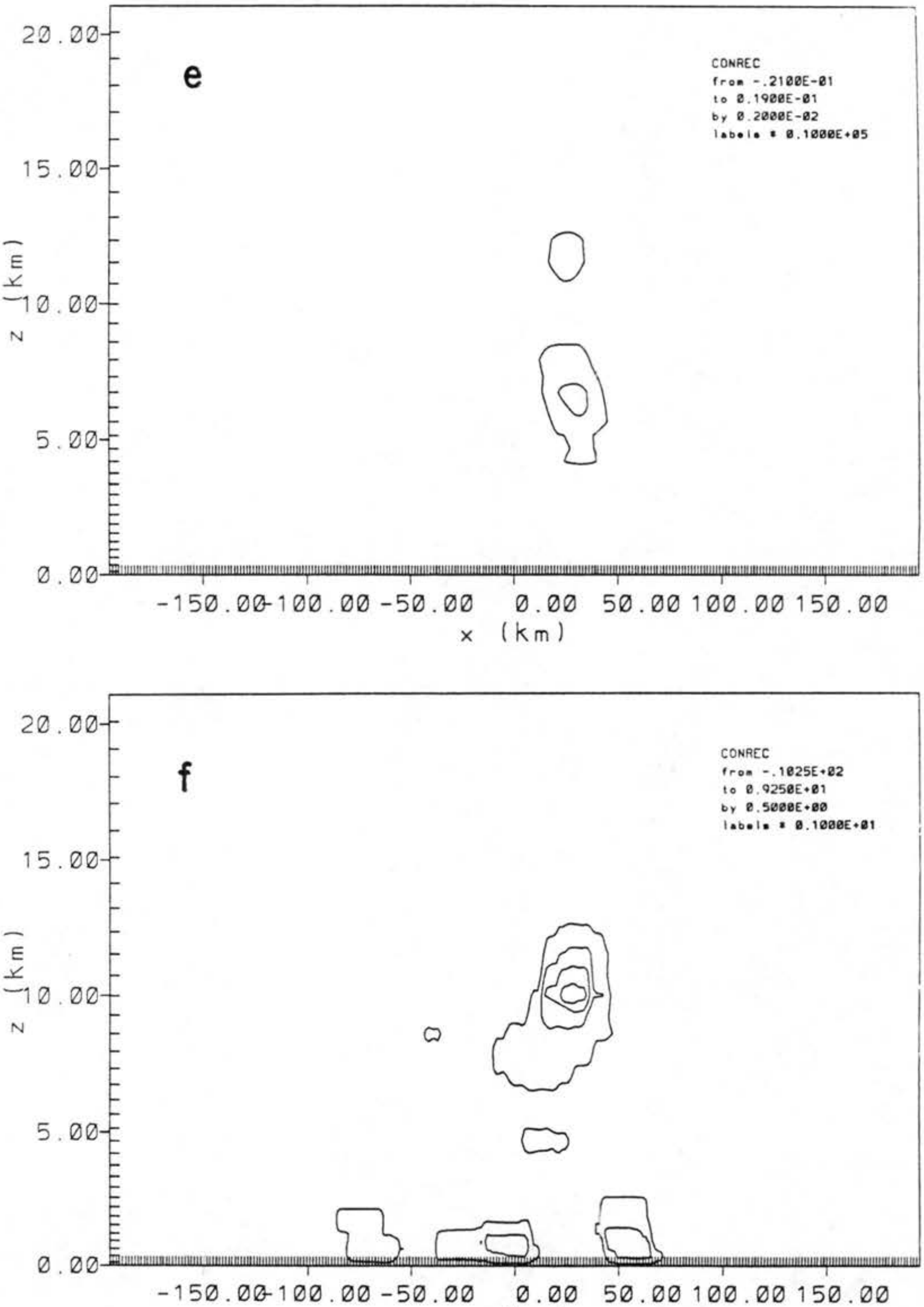

Figure 5.6: Continued. (e) condensate mixing ratio in kg/kg, (f) vertical variance in m^2/s^2.

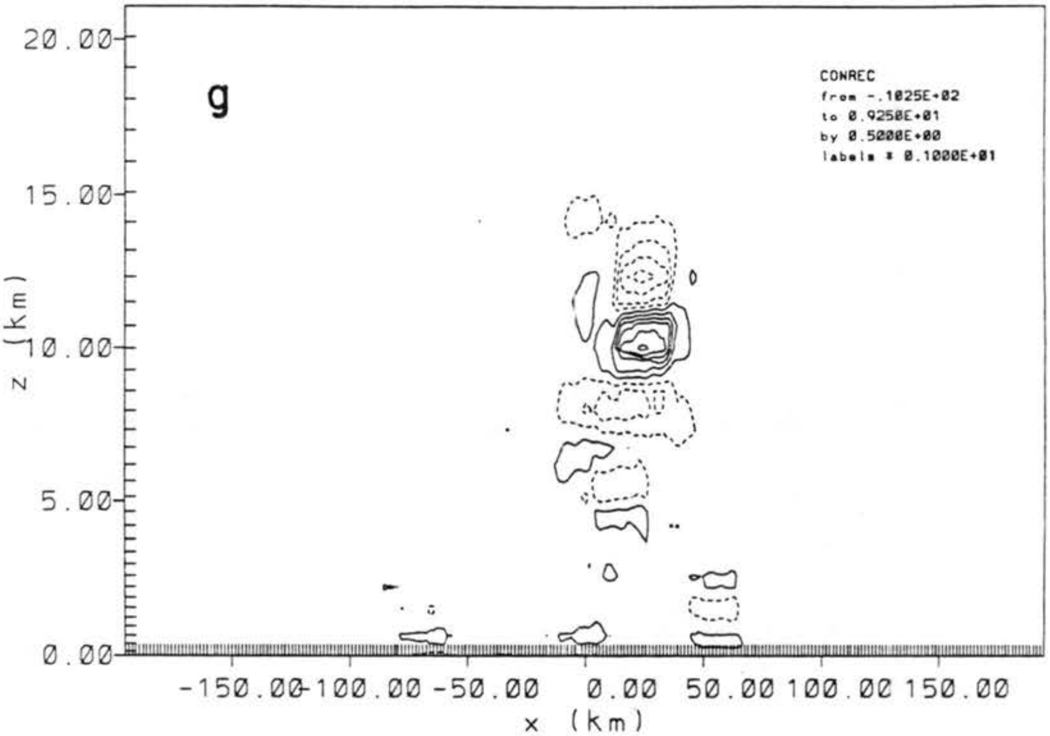

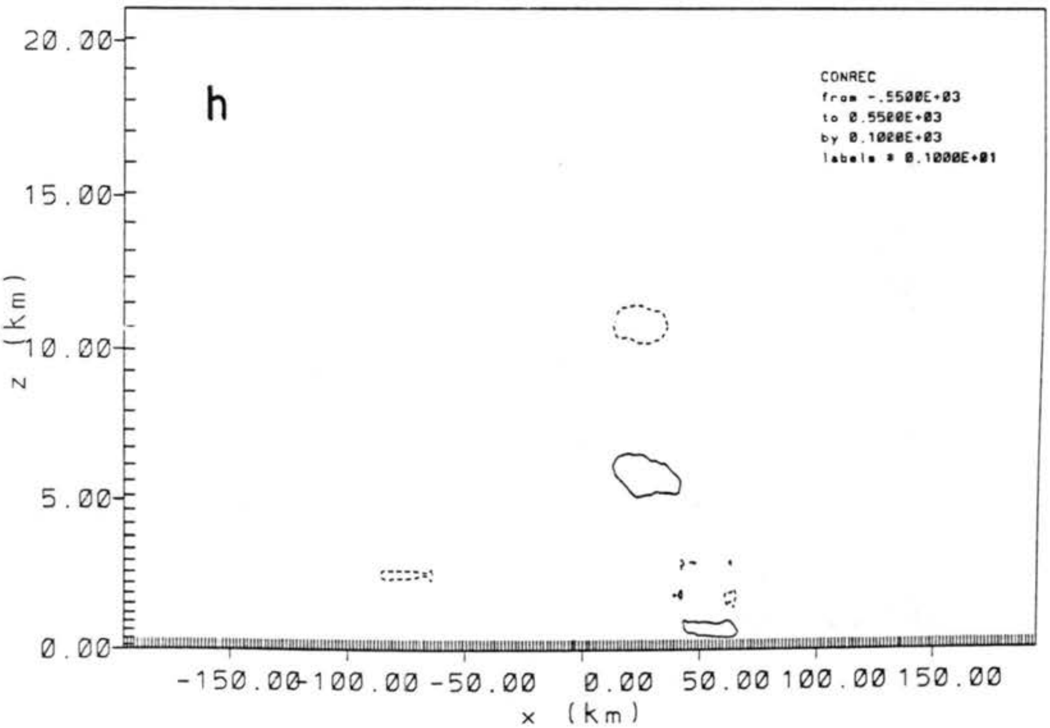

Figure 5.6: Continued. (g) heating rate in K/da, and (h) moistening rate in g/kg/da.

cores are of the same order of magnitude as the vertical variance within the PBL. The peak values of mean vertical motion, perturbation temperature, perturbation total water mixing ratio, condensate mixing ratio and $\overline{w'w'}$ are summarized for the explicit and the four parameterized simulations at 1400 local time in Table 5.1 for easy reference and comparison.

Table 5.1: Peak values of mean vertical motion, perturbation temperature aloft, perturbation total water mixing ratio, condensate mixing ratio and vertical variance for the explicit and four parameterized simulations on the 20 km grid at 1400 local time. dn/nodn refers to simulations with/without downdrafts and mc/nomc refers to simulations with/without precipitation.

Simulation	W (m/s)	T (K)	Rt (g/kg)	COND (g/kg)	$\overline{w'w'}$ ($\frac{m^2}{s^2}$)
explicit	1.0	1.0	4.5	3.6	2.1
nodn/nomc	1.7	4.0	7.2	7.6	119
dn/nomc	0.50	1.5	3.6	3.8	42
nodn/ mc	1.6	7.0	4.0	1.9	270
dn/ mc	1.3	3.6	2.4	1.1	150

Eddy heating and moistening rates for the sub-twenty kilometer averaging scale are shown in Figs. 5.6g and 5.6h, respectively. The maximum heating rate is only 2.7 K/day and the maximum moistening rate is only 110 g/kg/day. These small values indicate the limited strength of the cumulus convection at this time.

The cumulus parameterization at 1400 local time

In Figs. 5.7a - 5.7h, the fields from the 20 km grid cumulus parameterization simulation with only condensation (explicit and parameterized) and without downdrafts are shown at 1400. Note the strong upward motion and associated outflow near x=-20 km. The resolved upward motion is comparable to the average explicit value. Areas of compensating subsidence around the dominant cumulus cell are also clearly visible on Fig. 5.7b. The temperature perturbation is far too strong and elevated as are the perturbation total and condensate mixing ratios. Of course, there is no precipitation so that these high magnitudes are to be expected. Perhaps the most obvious discrepancy between the explicit and parameterized simulations is the two celled cumulus structure and the magnitude of

$\overline{w'w'}$ in the parameterized simulations. The two-celled structure is not surprising since cumulus convection on both sea-breeze fronts is expected; however it doesn't conform to the explicit simulation at this time period.

Values for $\overline{w'w'}$ are also over an order of magnitude higher than they should be and may contribute to the high temperature perturbations. This is substantiated by the large values of the cumulus heating and moistening rates shown in Figs. 5.7g and 5.7h. Strong cumulus drying is also indicated within the PBL. The absence of moisture depletion within the PBL by the parameterized cumulus may lead to excessively strong convection. In reality, the transience of cumulus convection along the propagating sea-breezes may be due to exhaustion of water vapor within the PBL. Indeed, the reason why the PBL moisture is not allowed to be removed by parameterized cumulus in these two dimensional simulations is the resulting dryness of the PBL after transient convection is triggered. Restoring moisture depletion, then, in a three dimensional simulation may well induce weaker and more transient cumulus convection along the propagating sea-breeze fronts.

Another explanation for this discrepancy may lie in the basis of the parameterization. It was conceived for and designed around simulating large steady-state storms; the convection along the sea-breeze fronts is necessarily transient and may never reach a steady-state. The parameterization, then, may be too robust for the more transient cumulus events. The end result is that the cumulus convection along the west coast in the parameterized simulations does not decay as quickly as in the explicit simulations. Furthermore, allowing entrainment would also weaken the parameterized cumulus clouds.

Unfortunately, it is difficult to interpret the large values of cumulus heating and drying and their profiles in the context of a mesoscale model. This is because the resolved motions act in tandem with the parameterization. The very stable lapse rate near the tropopause is directly responsible for the high heating rates through the compensation term in Eq. 4.20 (first term on the rhs). Presumably, the resolved vertical motions would create strong cooling to offset the strong cumulus warming. However, the strength of the temperature perturbations indicate that this is not happening as completely as it should. It could be that choosing a vertical distribution for the coefficient of the compensation

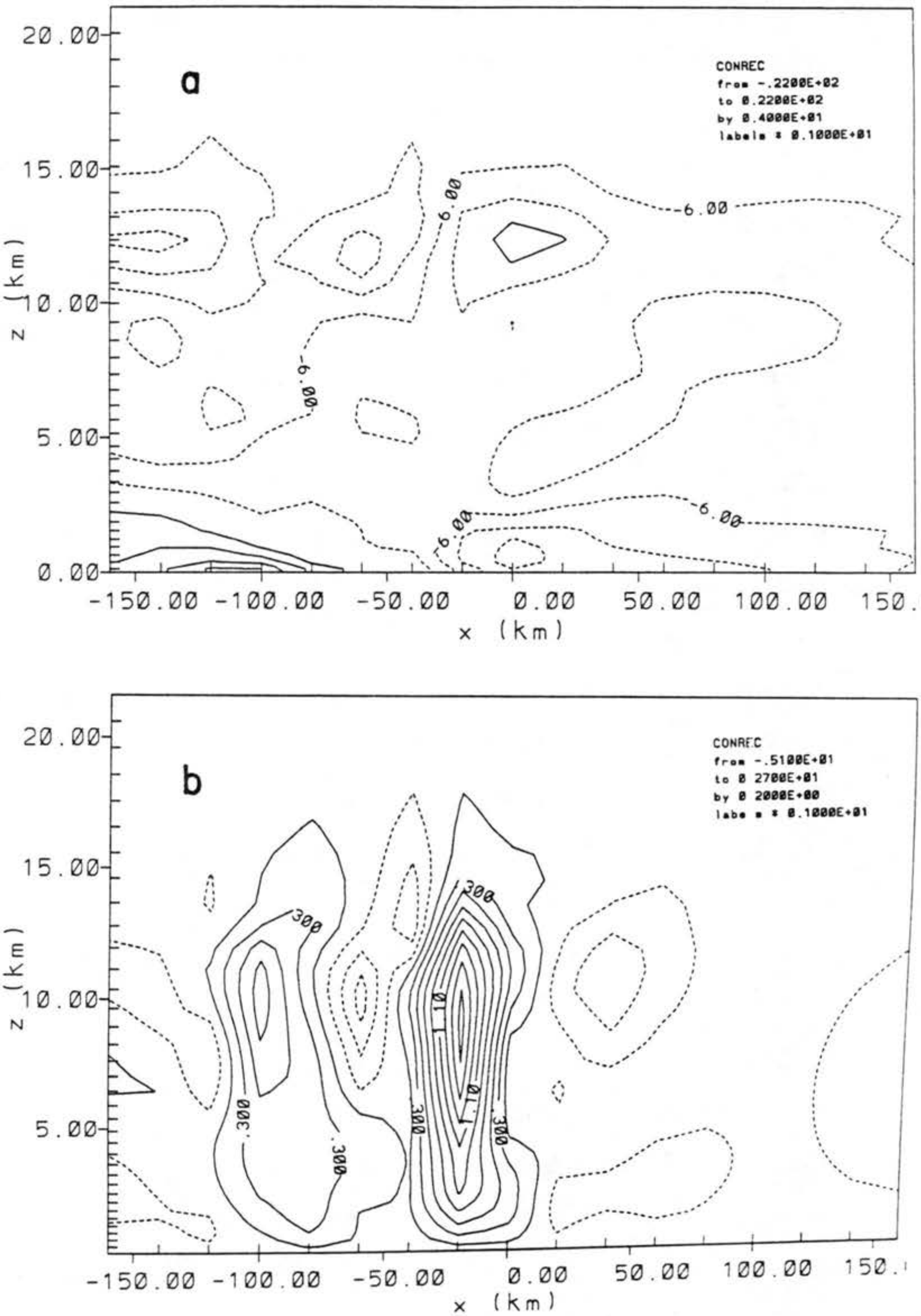

Figure 5.7: As in Figs. 5.6a-h except for the 20 km parameterized simulation without downdrafts and without precipitation.

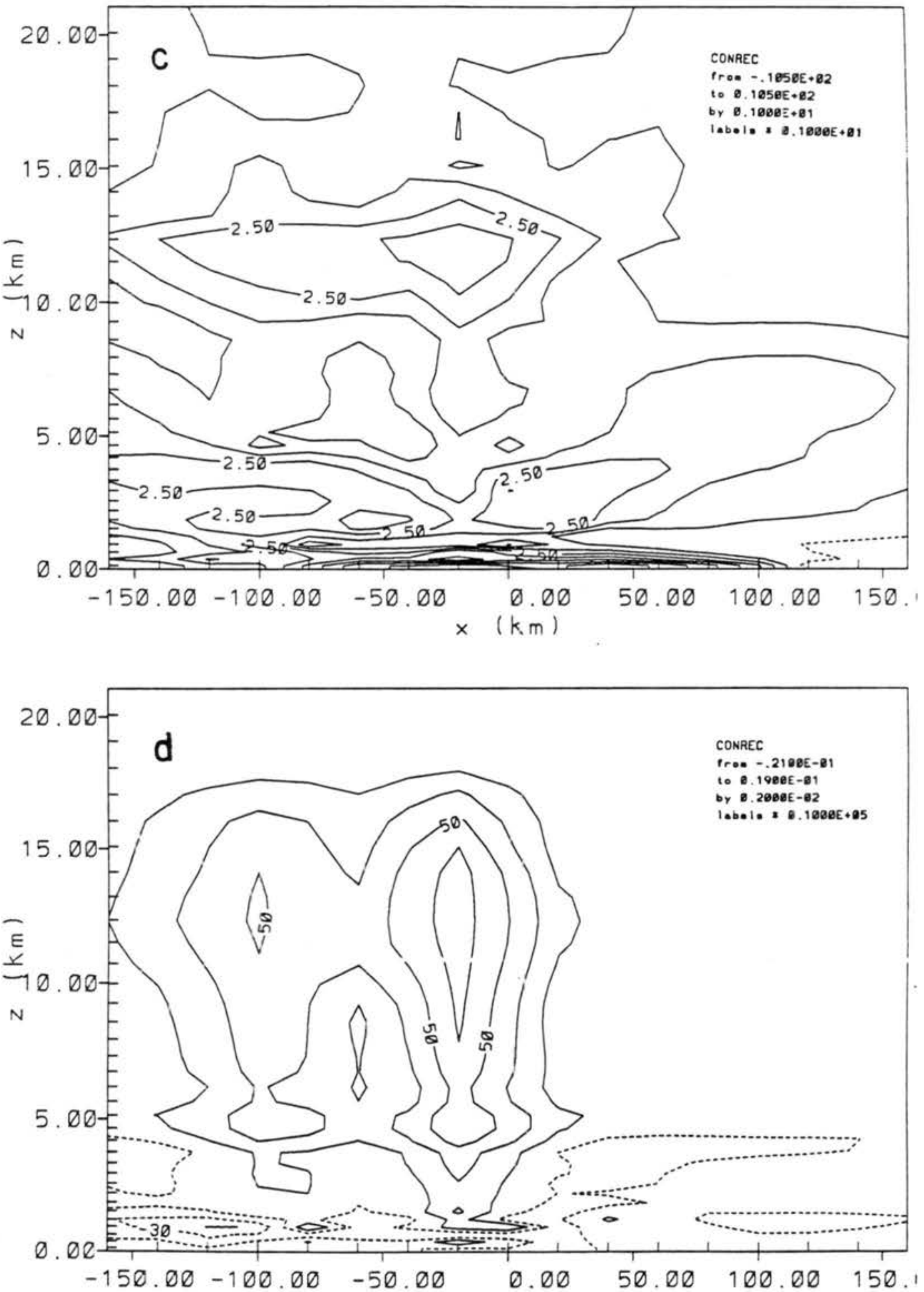

Figure 5.7: Continued.

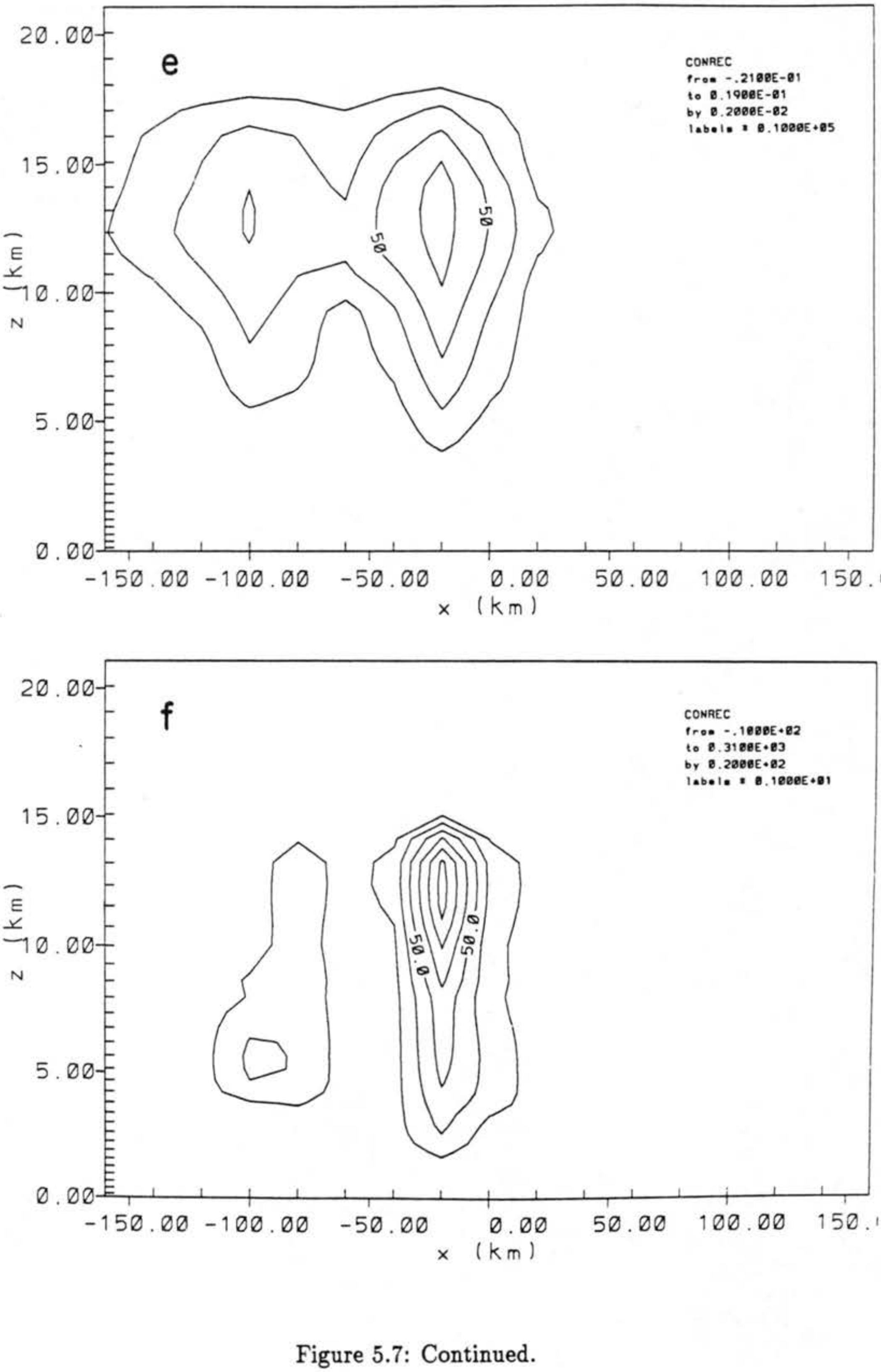

Figure 5.7: Continued.

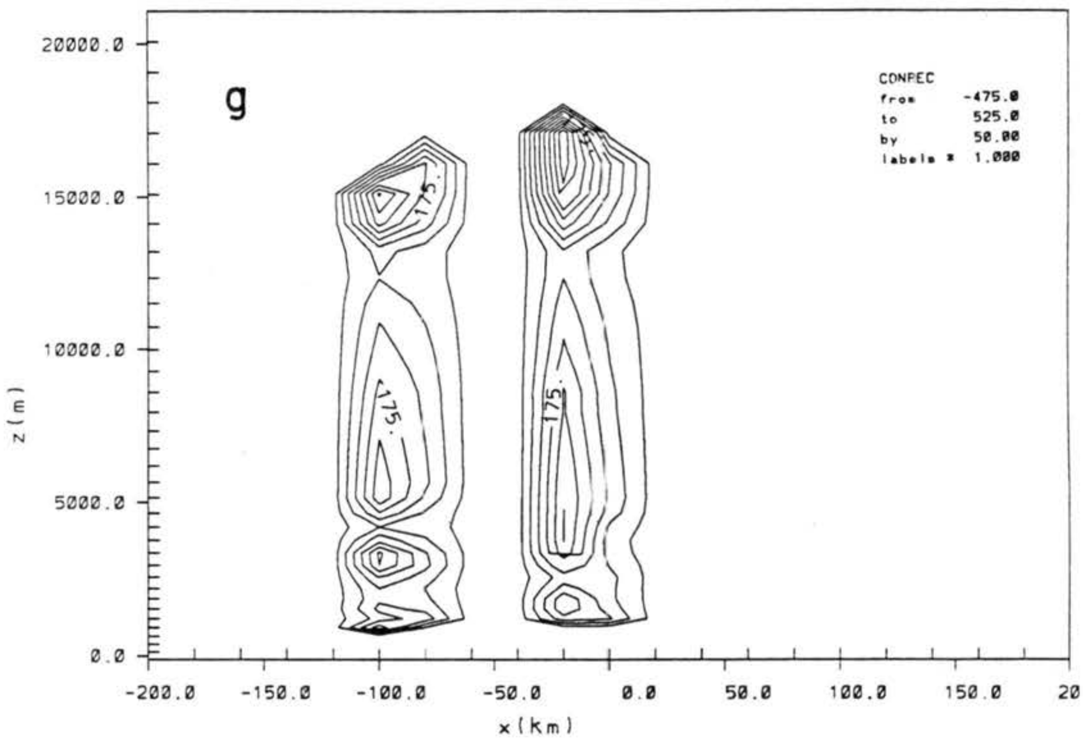

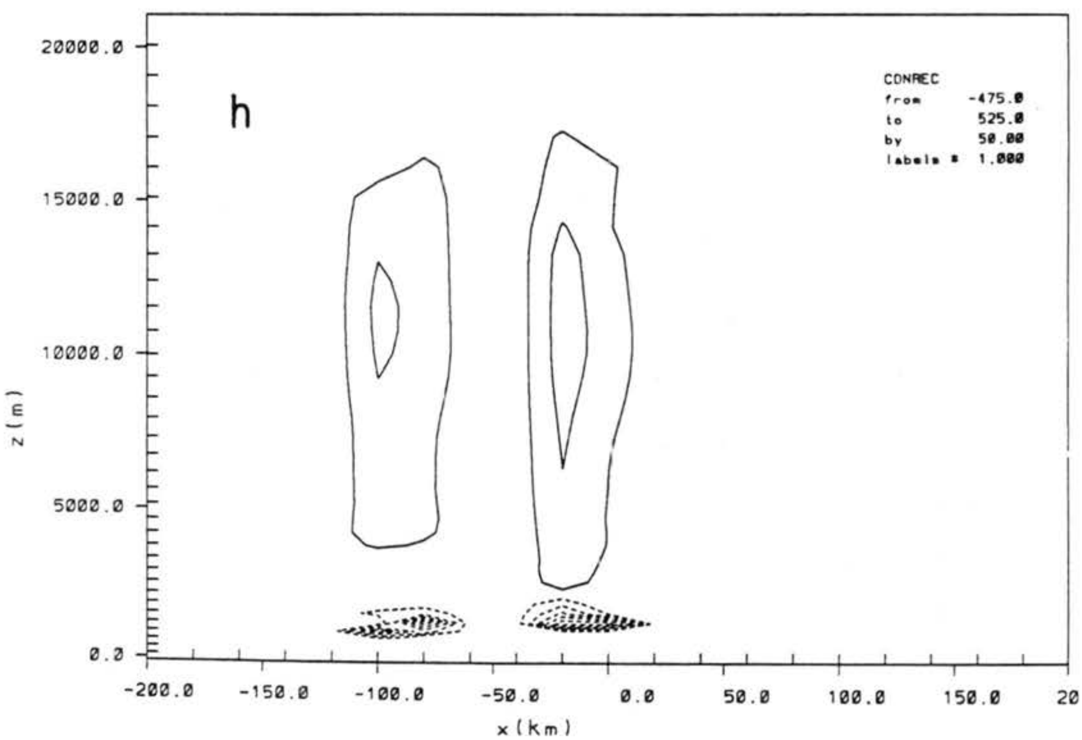

Figure 5.7: Continued.

term (first term on the rhs of Eq. 4.20) rather than assuming it to be independent of height would lead to more realistic fields in the mesoscale model. Also, if entrainment were included, the compensation term near cloud top would be considerably smaller since the cloud would not penetrate as far into the stable layers near the tropopause.

When downdrafts are added to the condensation only simulation (Figs. 5.8a - 5.8h), dramatic differences occur. Peak values of mean vertical motion at 1400 are half those which occur with no downdrafts. Furthermore, peak values of perturbation temperature, and perturbation total water and condensate mixing ratios, shown in Table 5.1, are about half of the no downdraft simulation. The reason for this general decrease of magnitude may be due to the decrease of moist static energy within the PBL when downdrafts are present. The decrease in moist static energy is accomplished by cooling and also drying since the PBL humidity is not depleted by the parameterized convection. The most obvious effect on $\overline{w'w'}$ is the lowering of the center of greatest sub-grid scale convective activity from 13 km to about 5 km.

The previous two simulations are unrealistic since no precipitation is allowed to form and fall. In Figs. 5.9a - 5.9h, the parameterized simulation with precipitation and no downdrafts is shown. Comparing these to the no precipitation simulation (Figs. 5.7a - 5.7h), several points become apparent. The mean vertical motion associated with the convection, although of the same magnitude, extends through more of the troposphere. Furthermore, the perturbation temperature in the upper troposphere is twice as large. These differences can be simply explained by the added heat release due to the freezing process which is not included in the condensation only runs. The peak perturbation total water mixing ratios are close to those predicted by the explicit simulation. The peak condensate mixing ratio is half of that predicted by the explicit simulation. Peak $\overline{w'w'}$ values are far too robust and considerably stronger than the no precipitation simulation.

When downdrafts are added to the simulation with precipitation (Figs. 5.10a - 5.10h), peak values of all variables are reduced as they were when downdrafts were added to the no precipitation simulations. Peak vertical motions fall to 1 m/s which are the 20 km-averaged

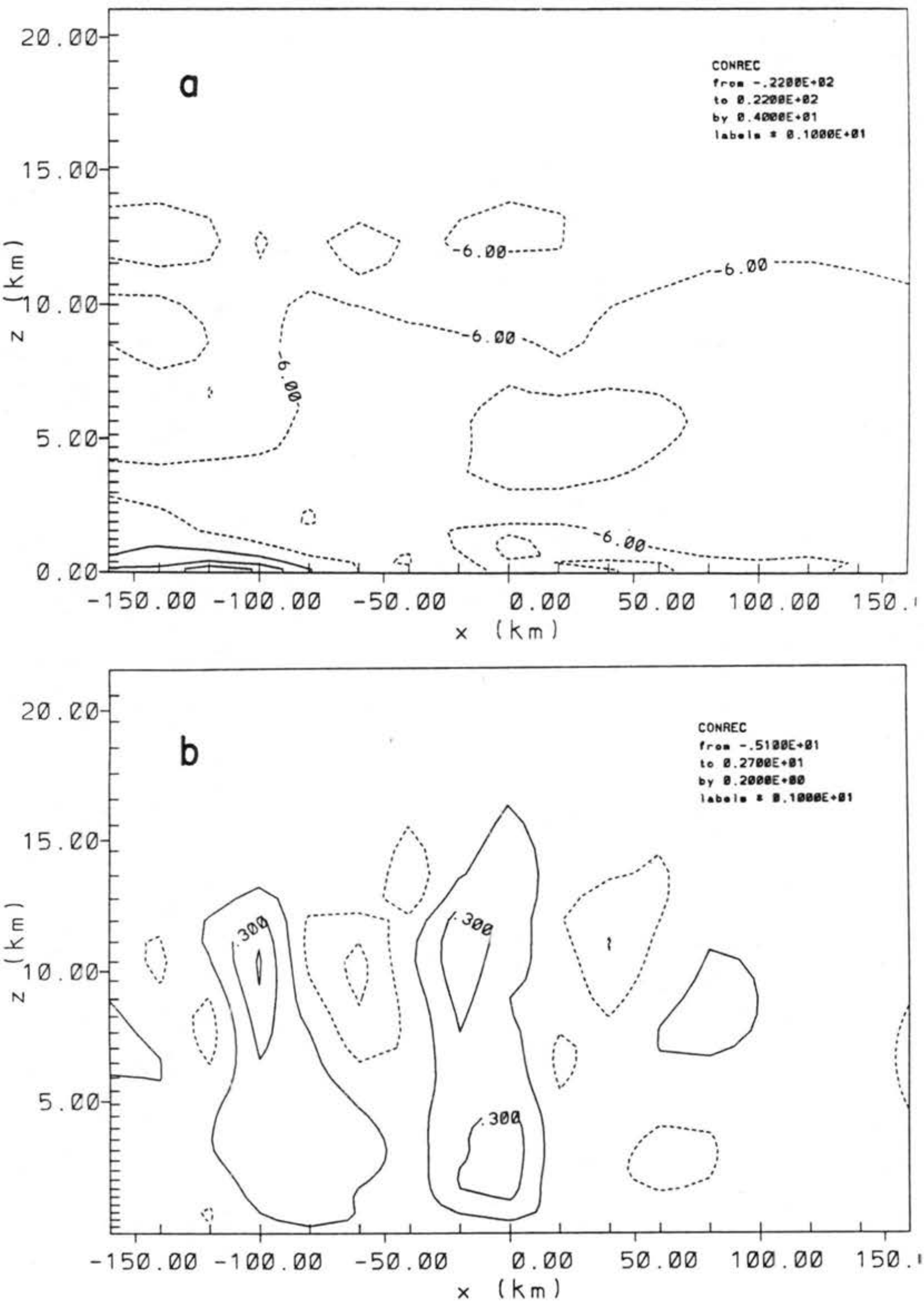

Figure 5.8: As in Figs. 5.6a-h except for the 20 km parameterized simulation with downdrafts and without precipitation.

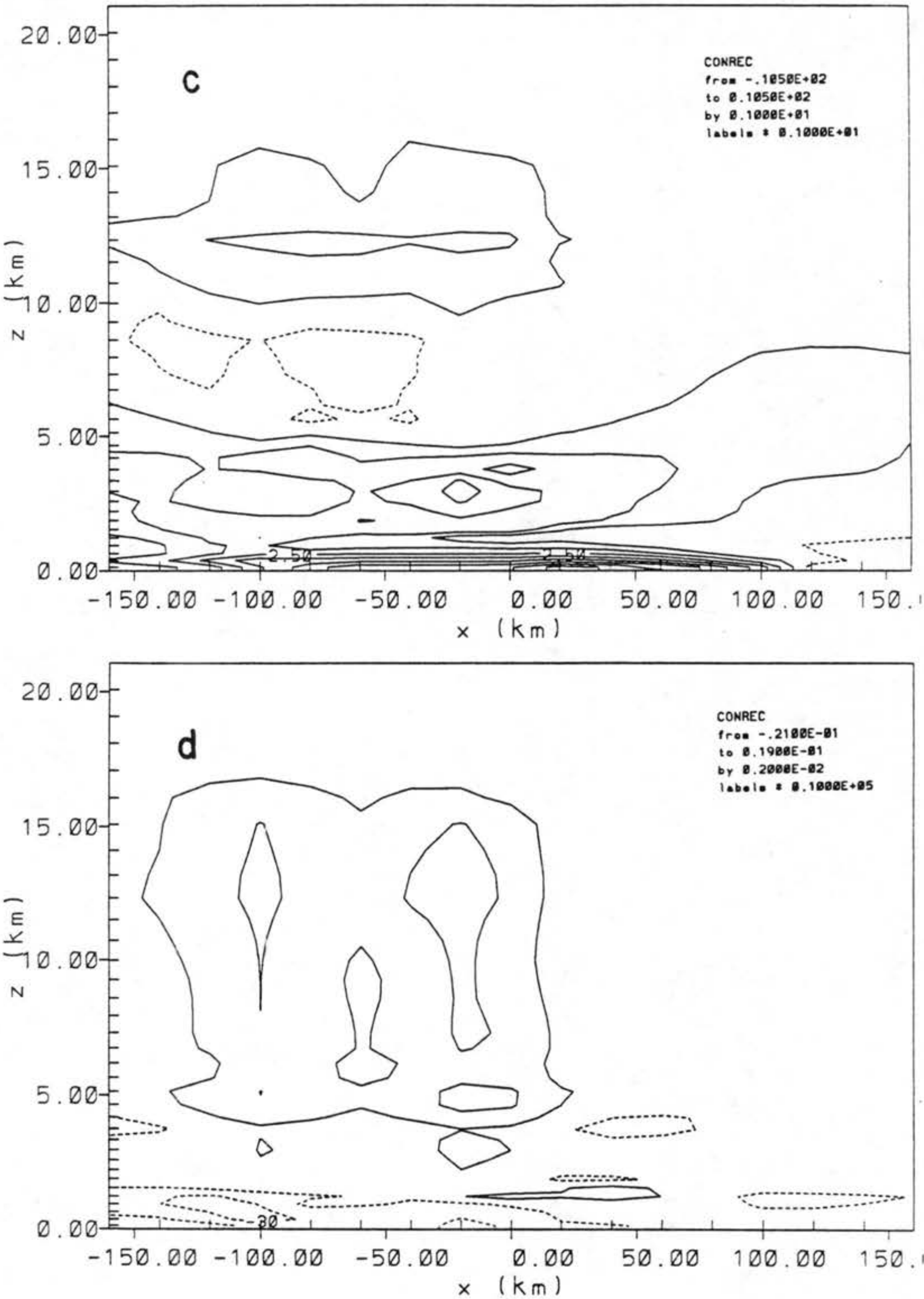

Figure 5.8: Continued.

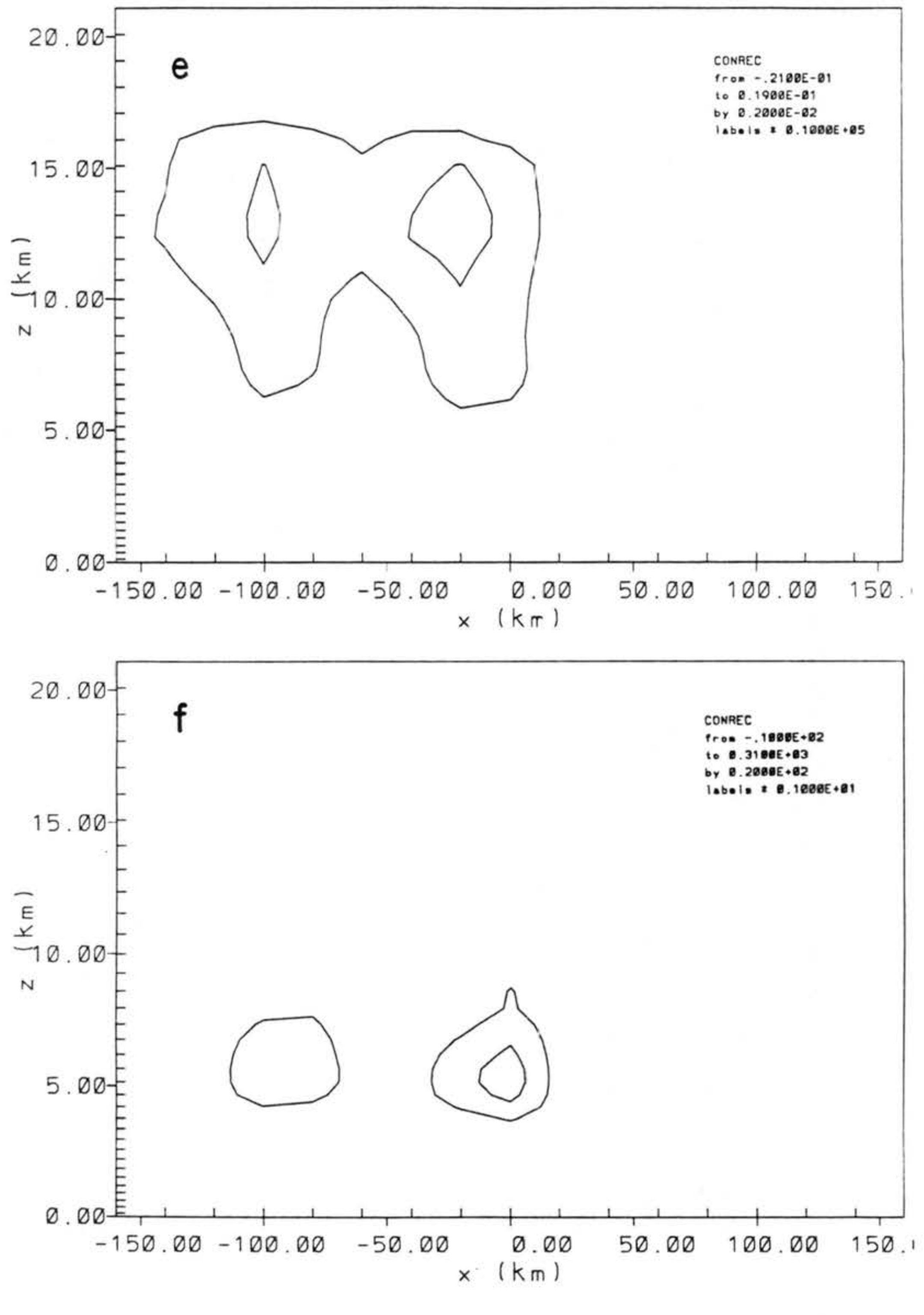

Figure 5.8: Continued.

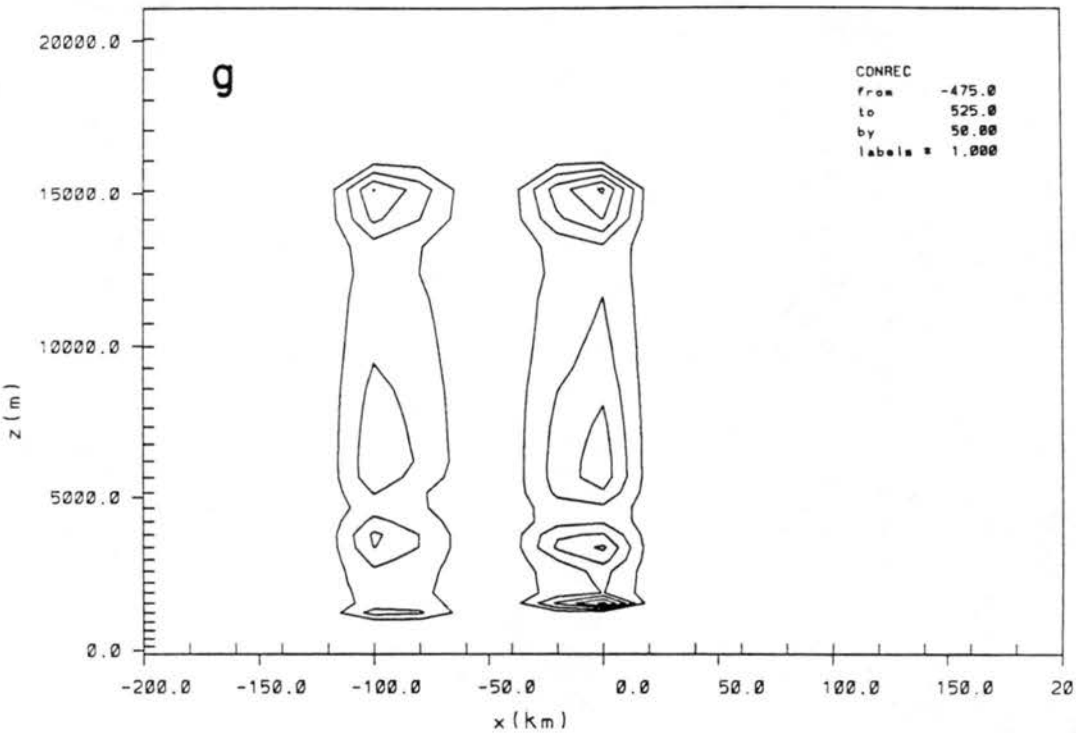

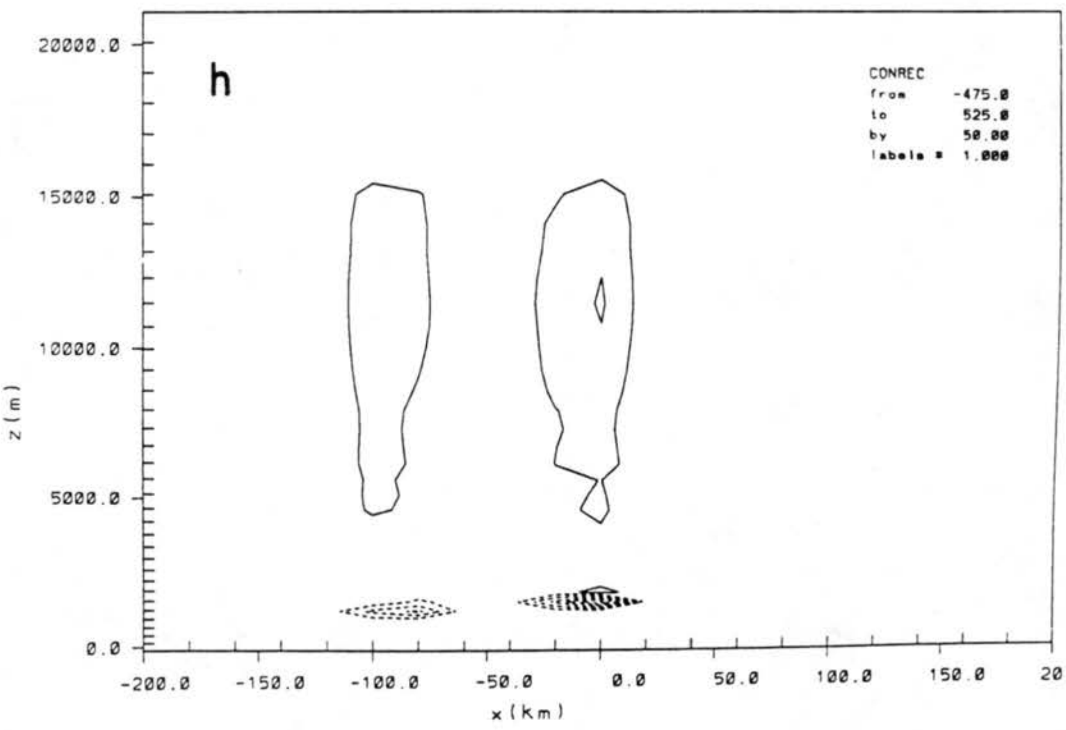

Figure 5.8: Continued.

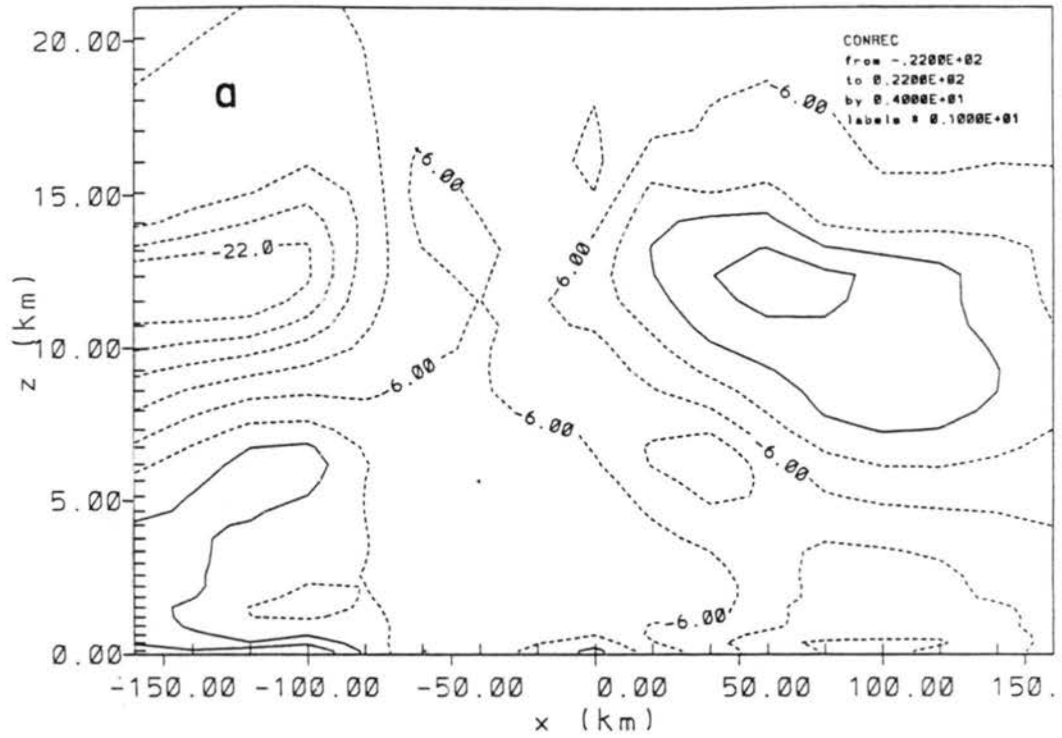

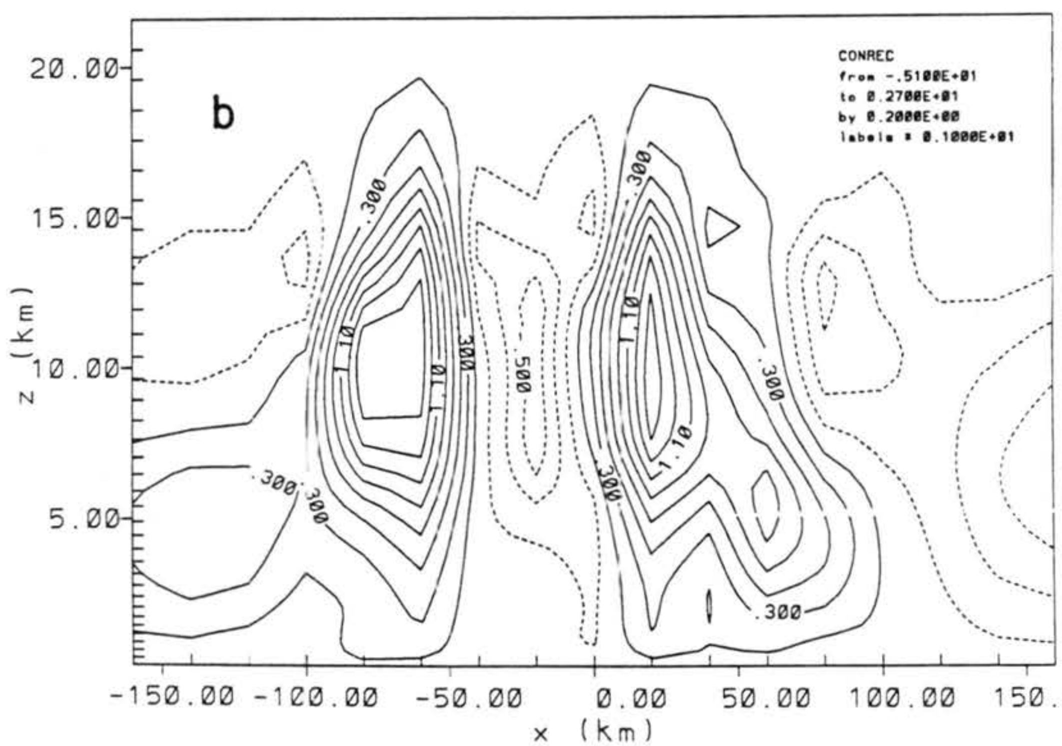

Figure 5.9: As in Figs. 5.6a-h except for the 20 km parameterized simulation without downdrafts and with precipitation.

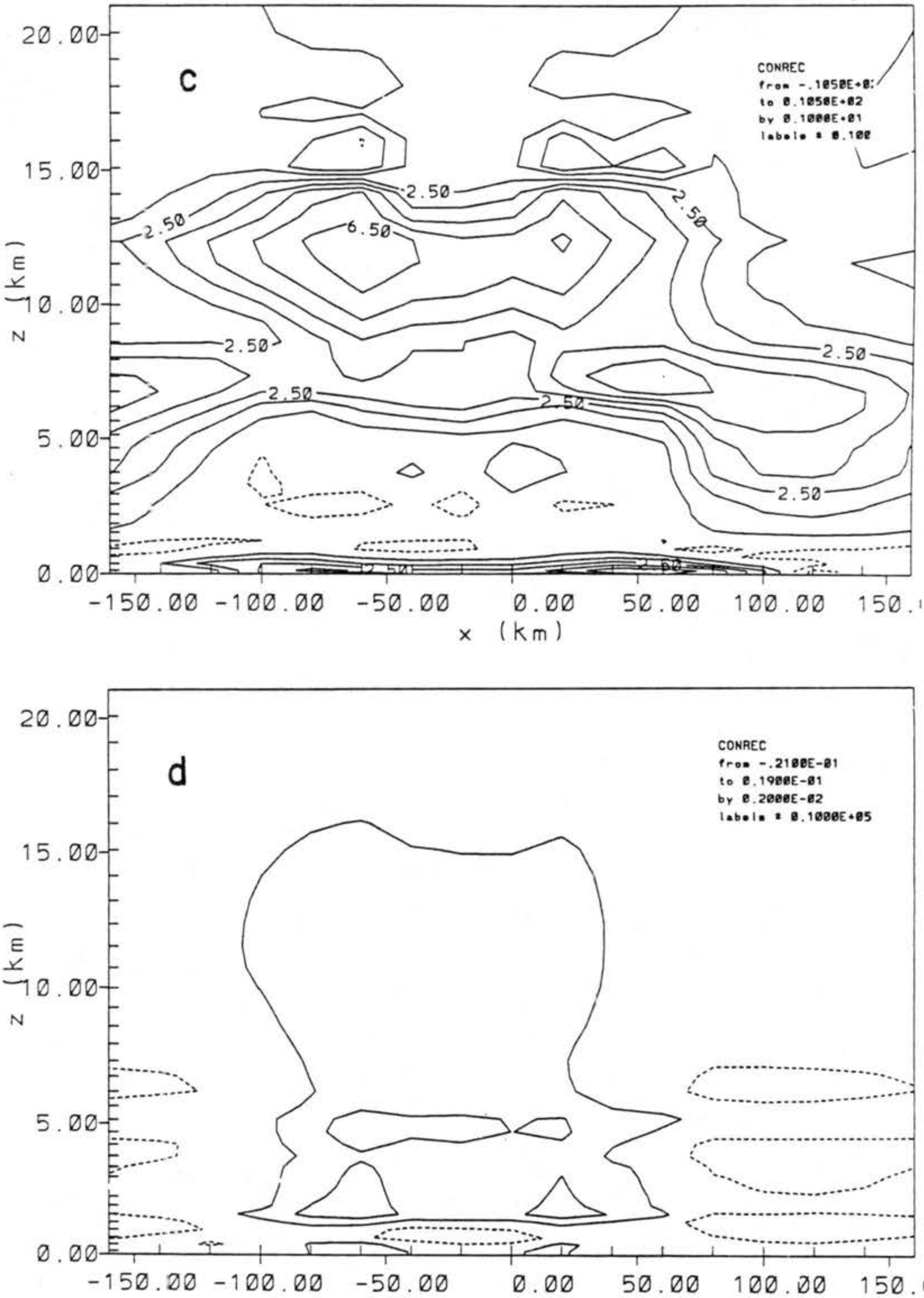

Figure 5.9: Continued.

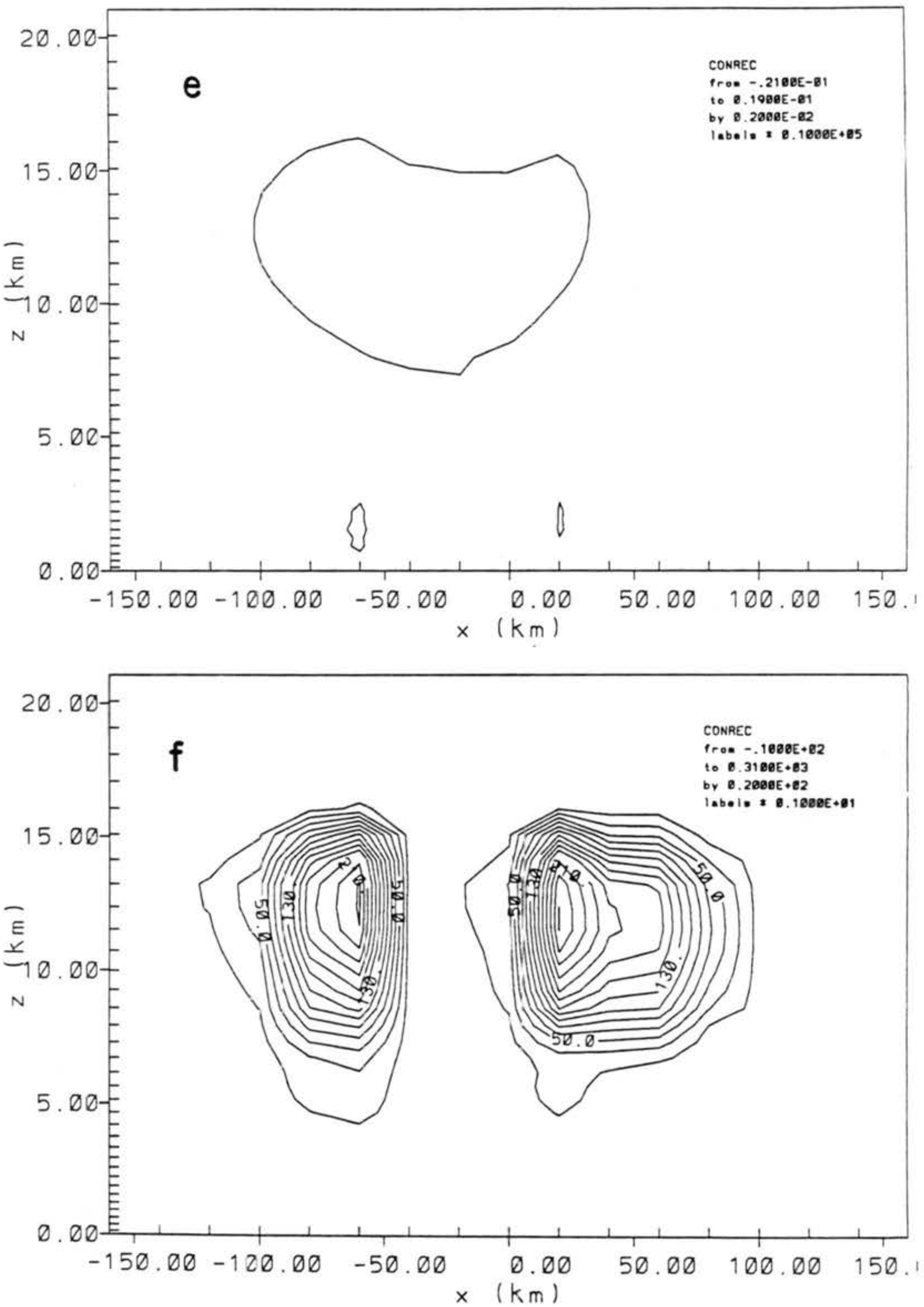

Figure 5.9: Continued.

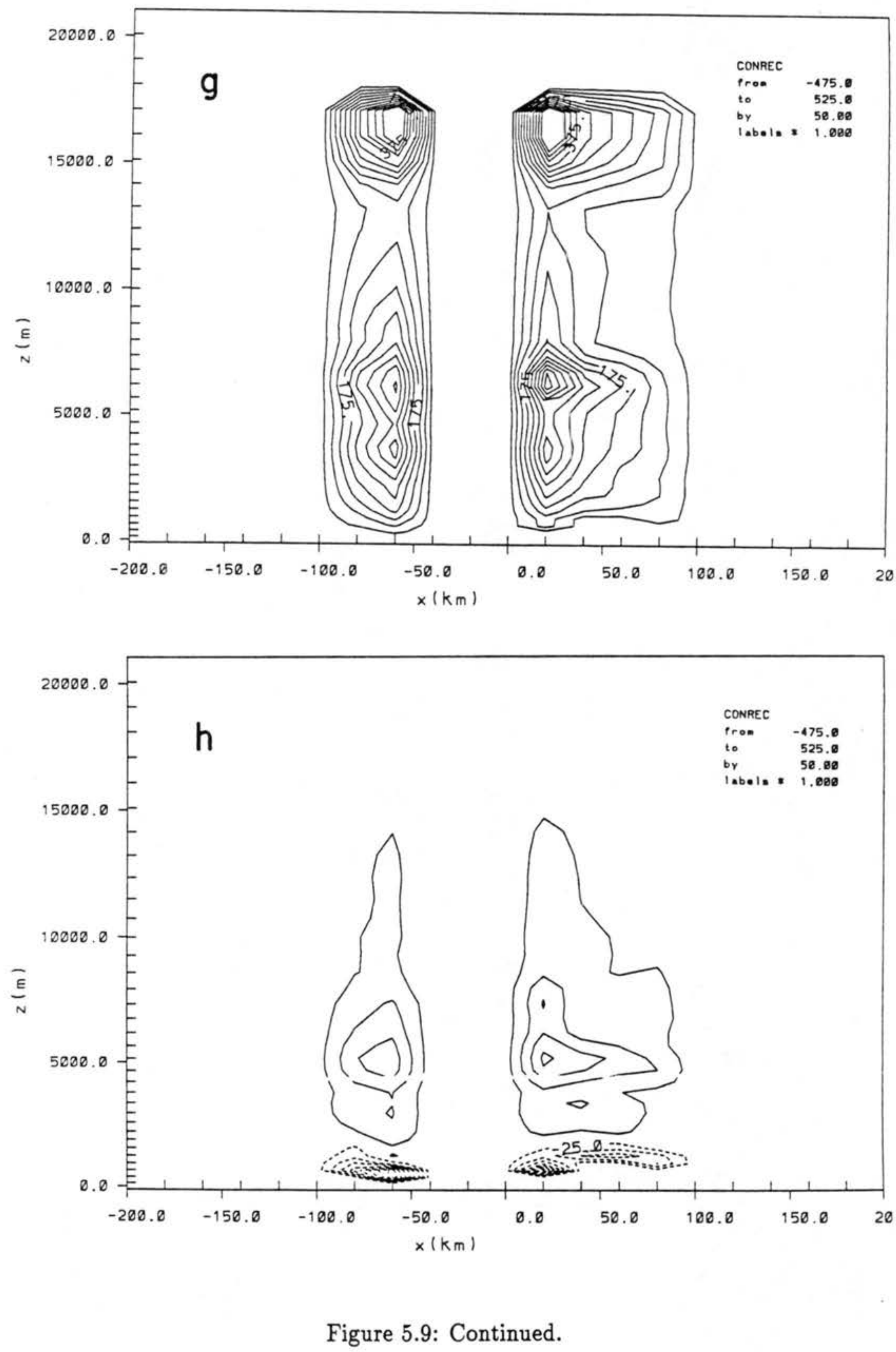

Figure 5.9: Continued.

peak values as predicted by the explicit simulation. Once again, the peak temperature perturbation is reduced by half from the no downdraft simulation, but it is still so high. Also, $\overline{w'w'}$ is too robust as in all other parameterized simulations.

The explicit simulation at 1700 local time

The explicit fields three hours later at 1700 local time are shown in Figs. 5.11a - 5.11h and the peak values of the salient fields are shown in Table 5.2. Note that cumulus convection is active west of the center of the peninsula with deep vertical motion. Apparent is the large solenoidal circulation caused by the convection with upward motion of 2.8 m/s. Also indicated is the warming and moistening of the upper troposphere and the cooling and drying of the PBL. The temperature perturbations extend higher in the troposphere and are as large as 2.5 K near 10 km. Deep transport of moisture through the cumulus cores are indicated in the perturbation total water mixing ratio and condensate mixing ratio fields. Furthermore, the vertical variance on a 20 km averaging scale is 32 $\frac{m^2}{s^2}$ and considerably stronger than during the transient convection three hours earlier.

Table 5.2: As in Table 5.1 except for the 20 km simulation at 1700 local time.

Simulation	W (m/s)	T (K)	Rt (g/kg)	COND (g/kg)	$\overline{w'w'}$ ($\frac{m^2}{s^2}$)
explicit	2.8	2.5	5.0	3.5	32
nodn/nomc	1.1	4.5	11.	11.	32
dn/nomc	0.75	2.8	6.3	6.0	27
nodn/ mc	2.8	7.0	6.5	4.0	140
dn/ mc	0.60	3.6	4.5	1.4	80

The eddy-averaged fields on the twenty kilometer averaging scale, shown in Fig. 5.11g and 5.11h, respectively, indicate that the cumulus heating and moistening rates are an order of magnitude larger that at 1400 local time. This is to be expected since the convection is stronger at this time period.

The cumulus parameterization at 1700 local time

When the parameterization scheme is run with no downdrafts and no precipitation, (Figs. 5.12a-5.12h) the general area of convection due to the colliding sea-breezes is west of

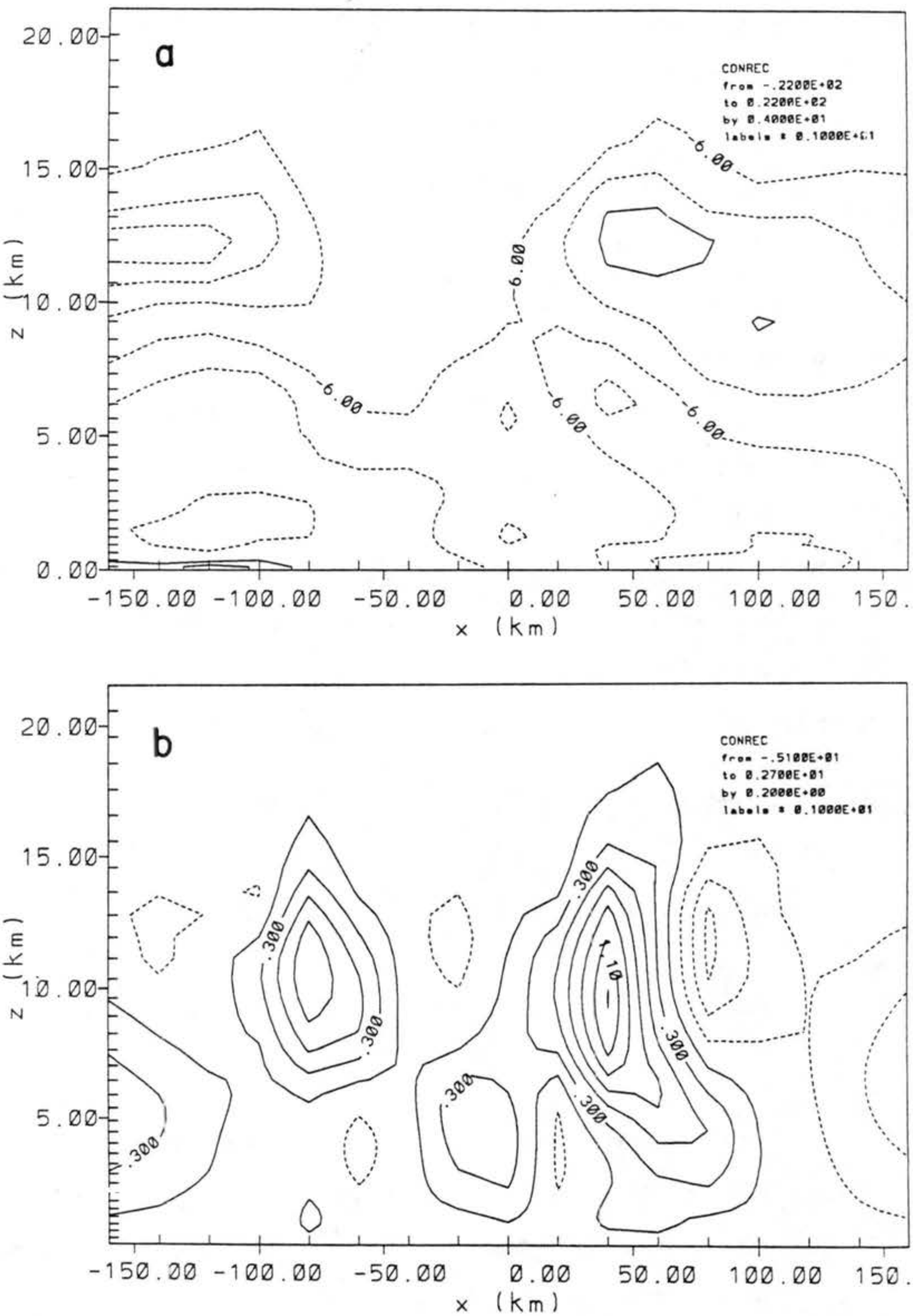

Figure 5.10: As in Figs. 5.6a-h except for the 20 km parameterized simulation with downdrafts and with precipitation.

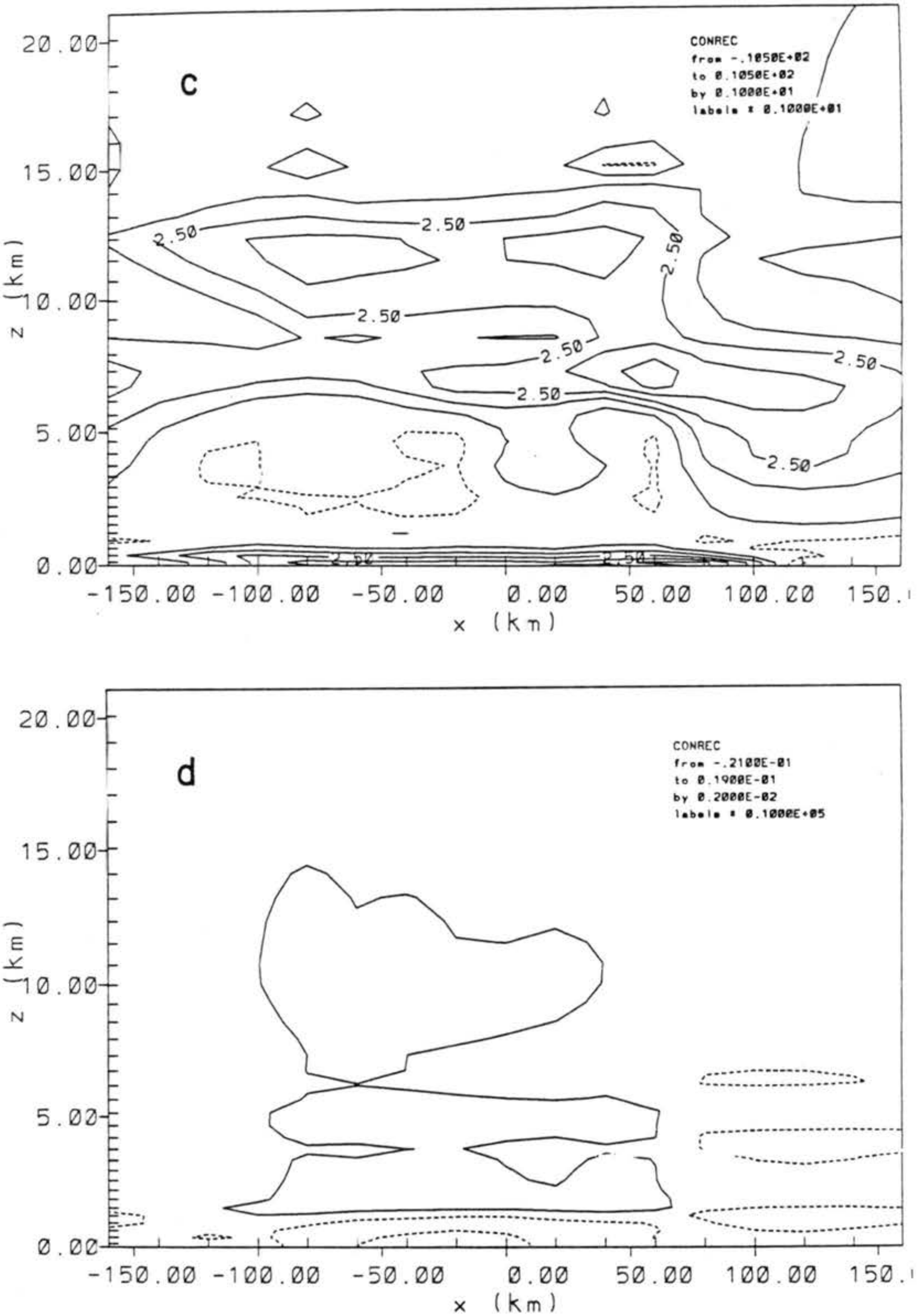

Figure 5.10: Continued.

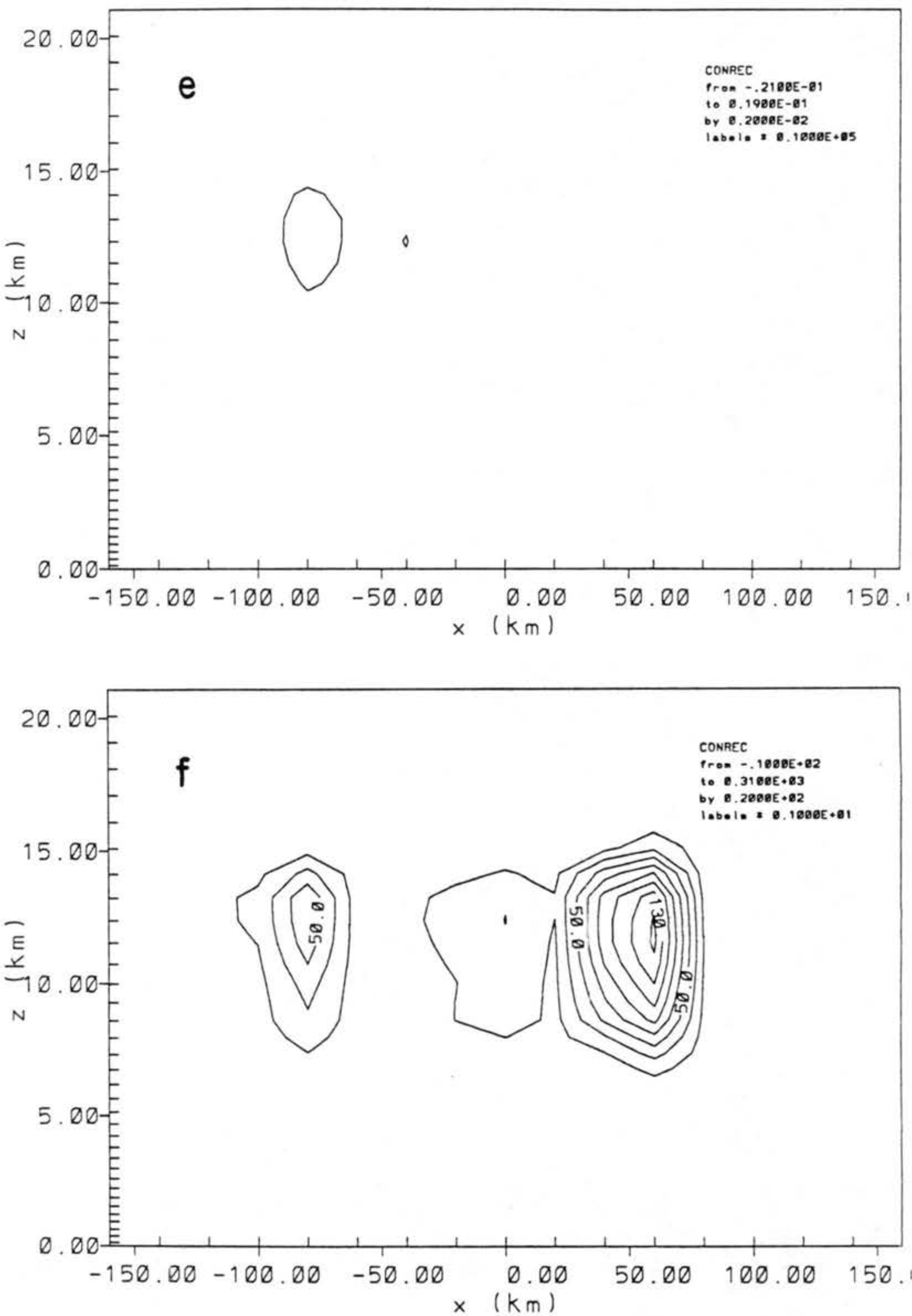

Figure 5.10: Continued.

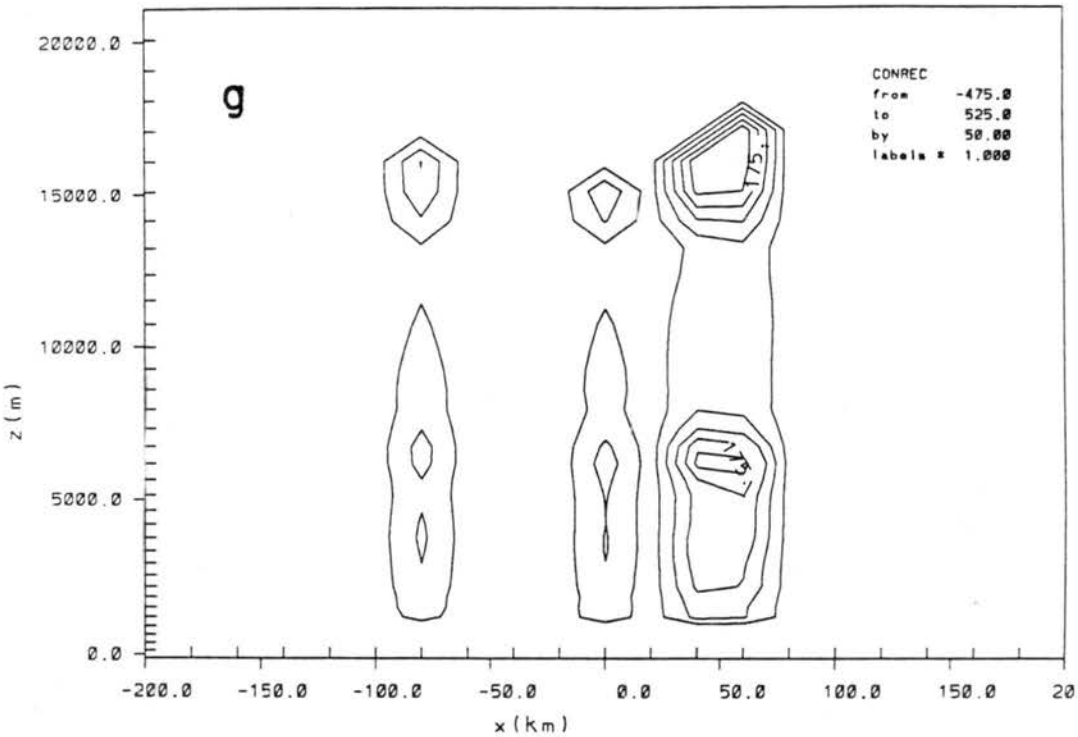

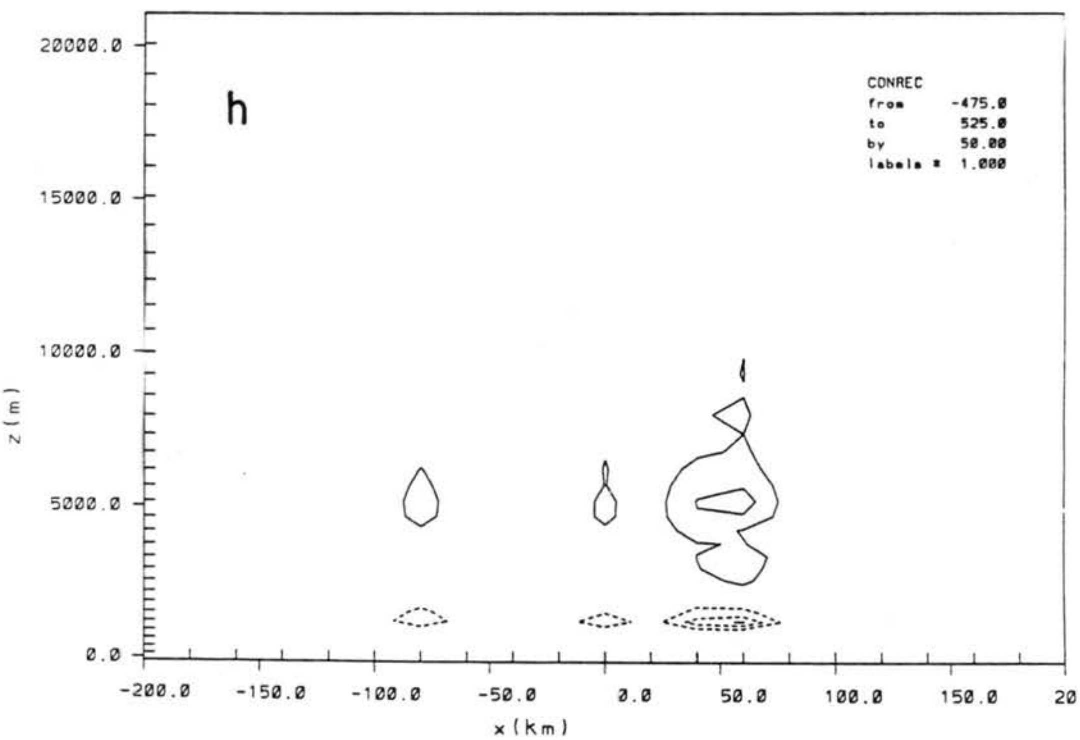

Figure 5.10: Continued.

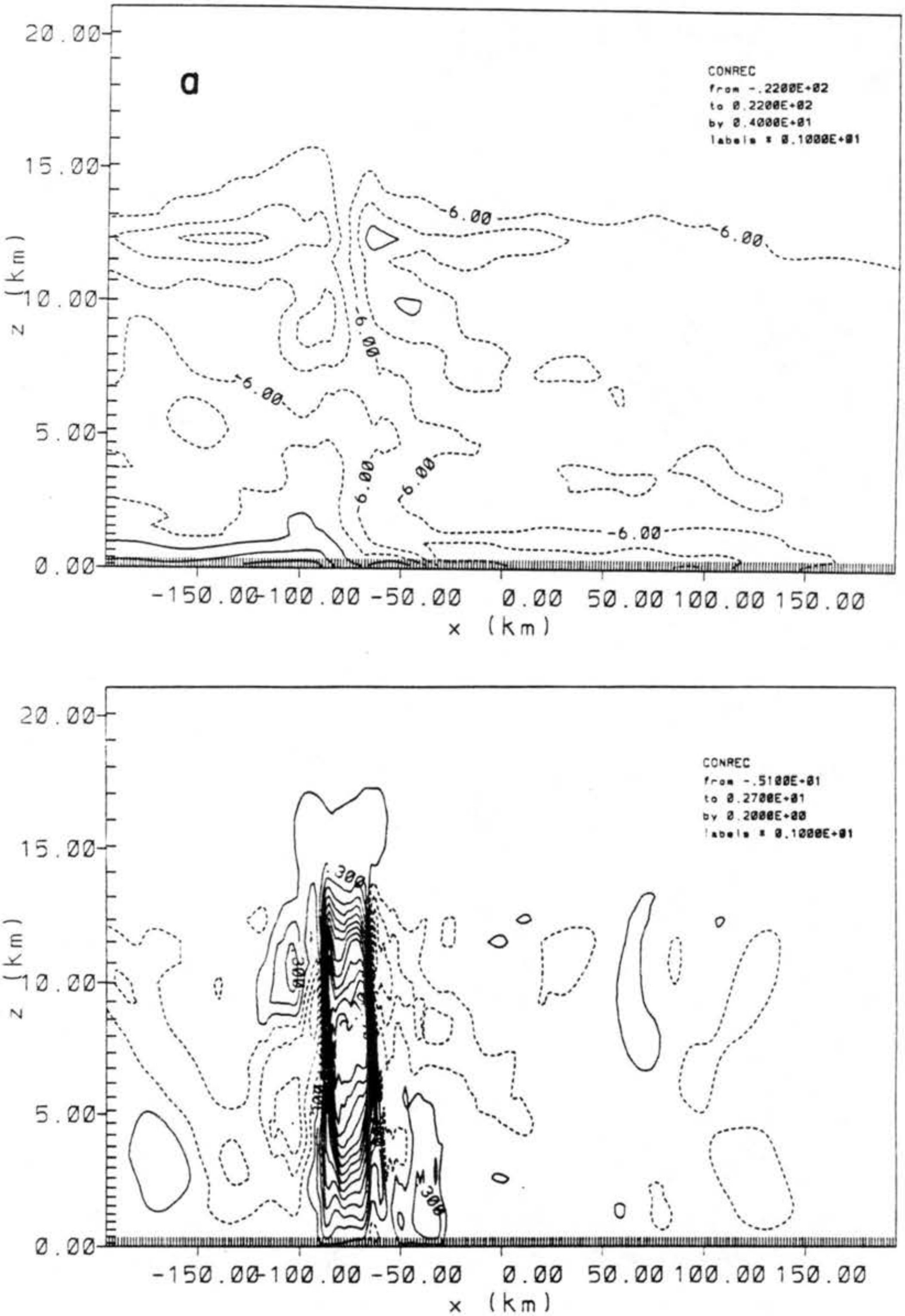

Figure 5.11: As in Figs. 5.6a-h except for 21 km running averages of the explicit simulation at 1700 local time.

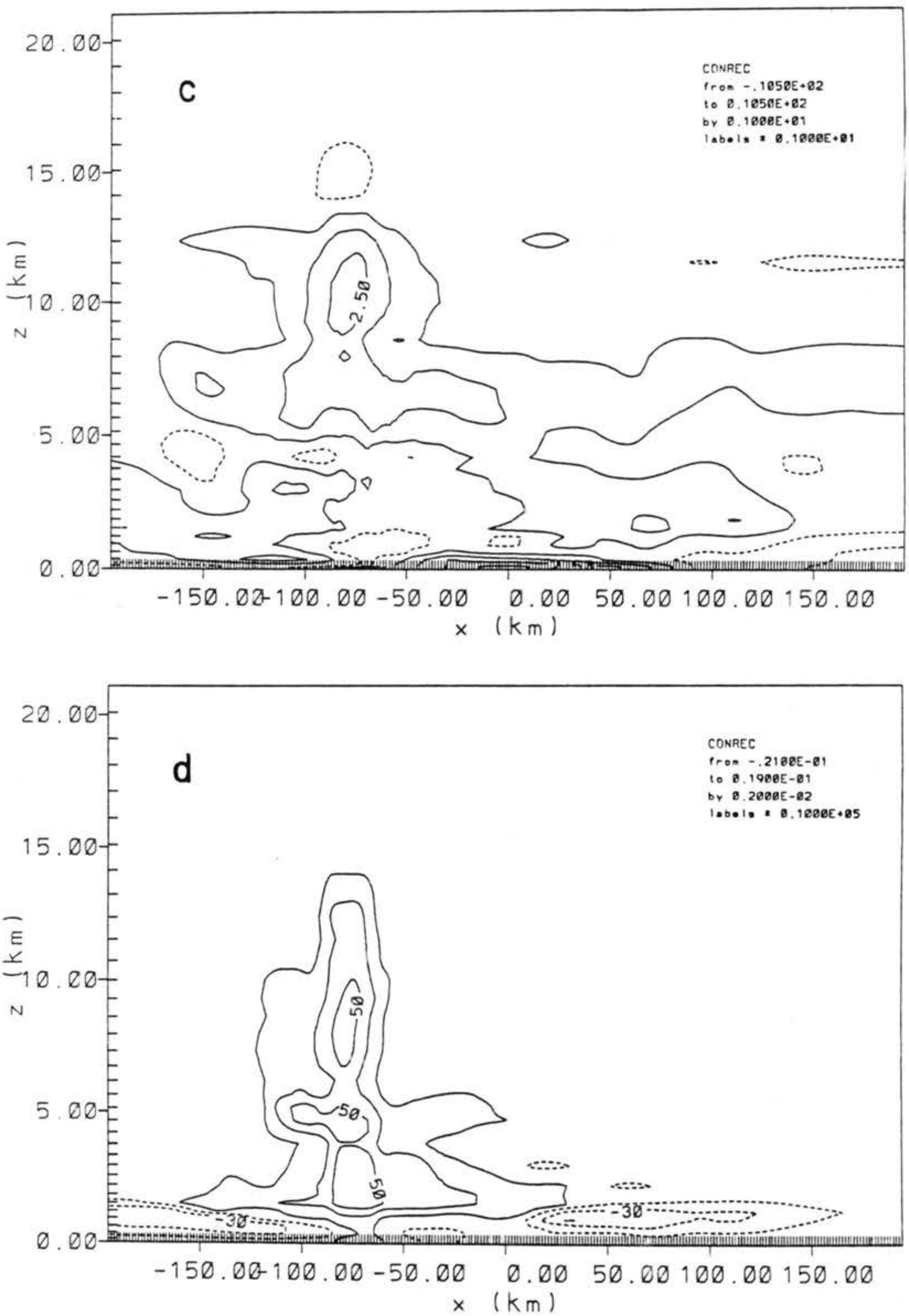

Figure 5.11: Continued.

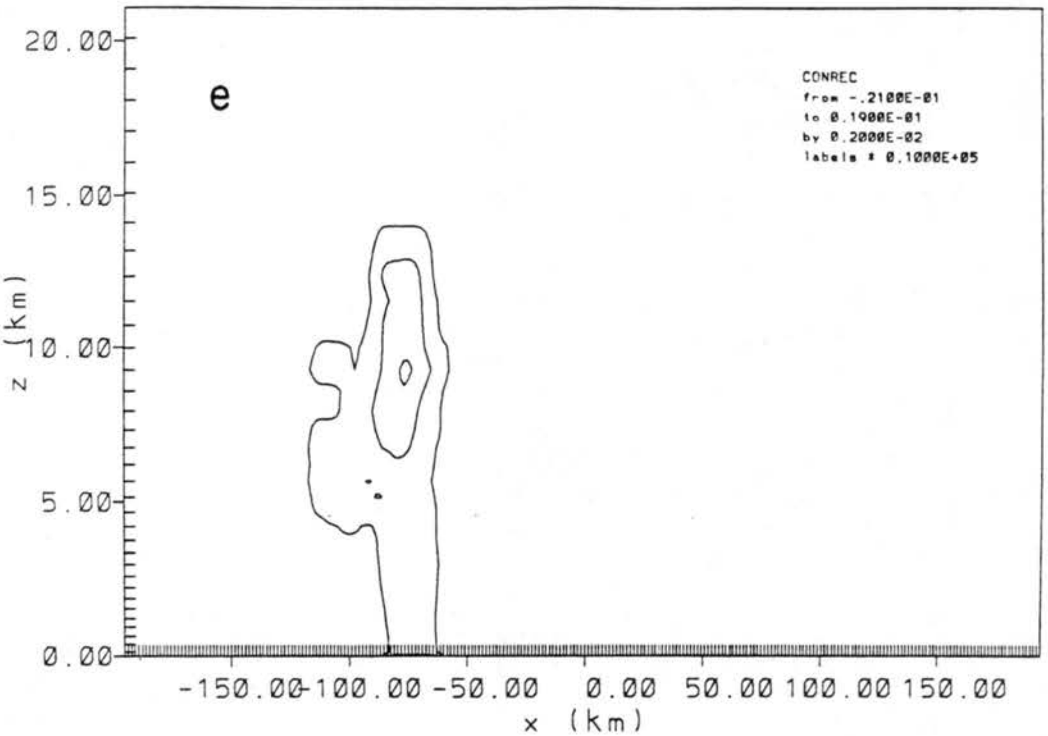

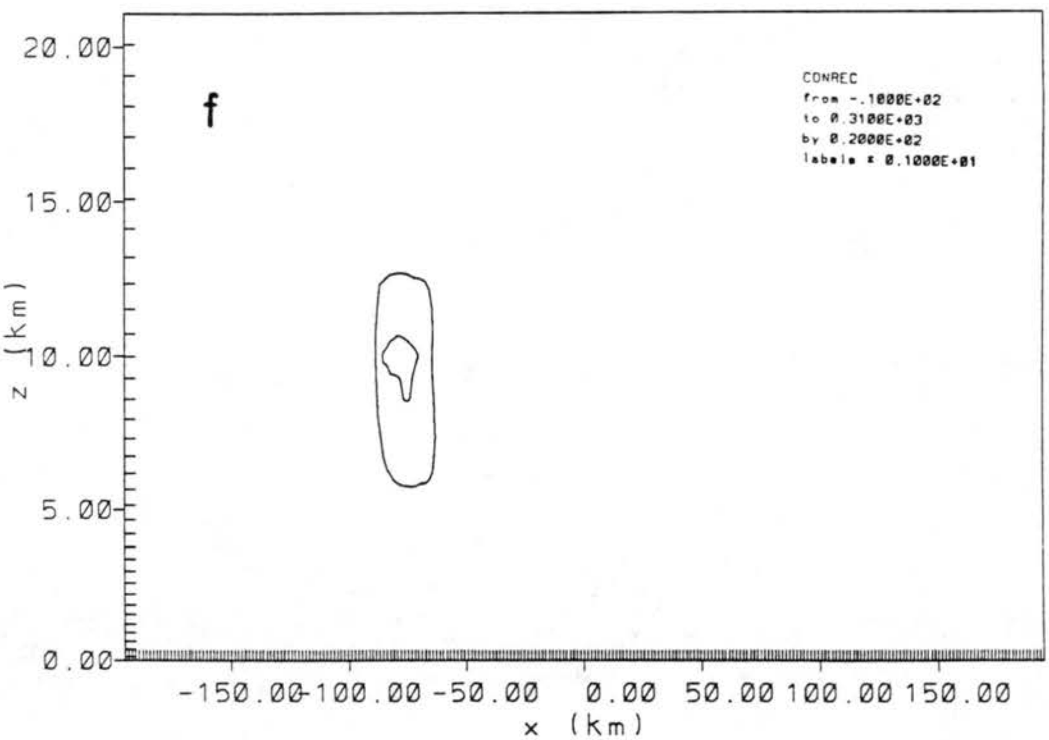

Figure 5.11: Continued.

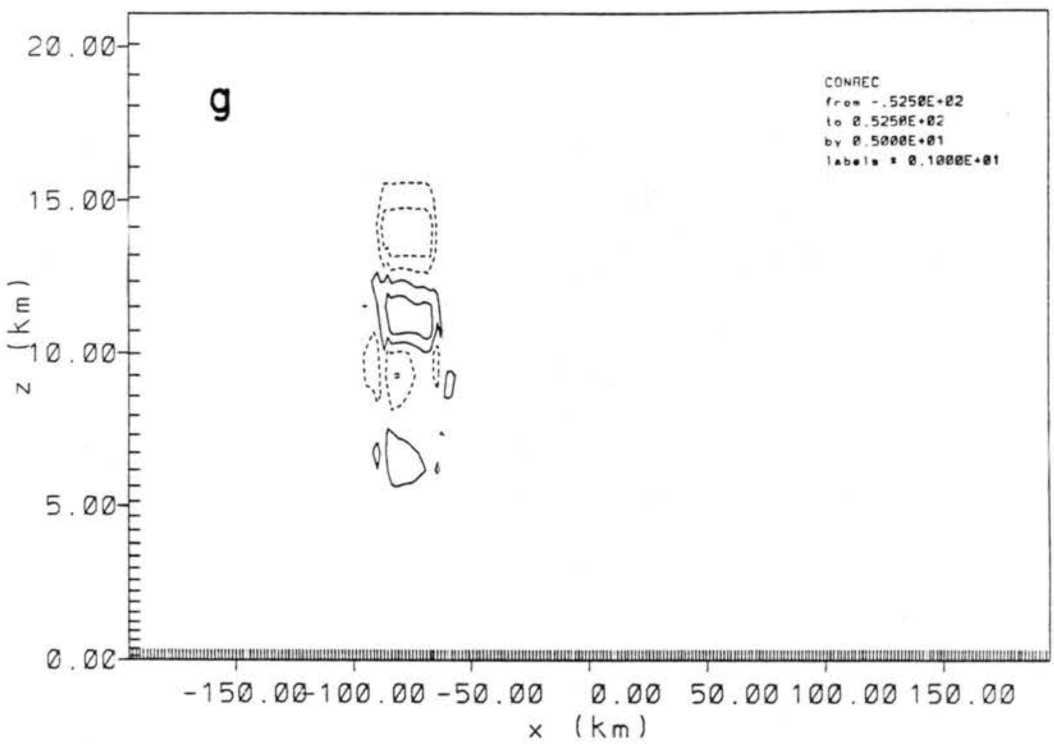

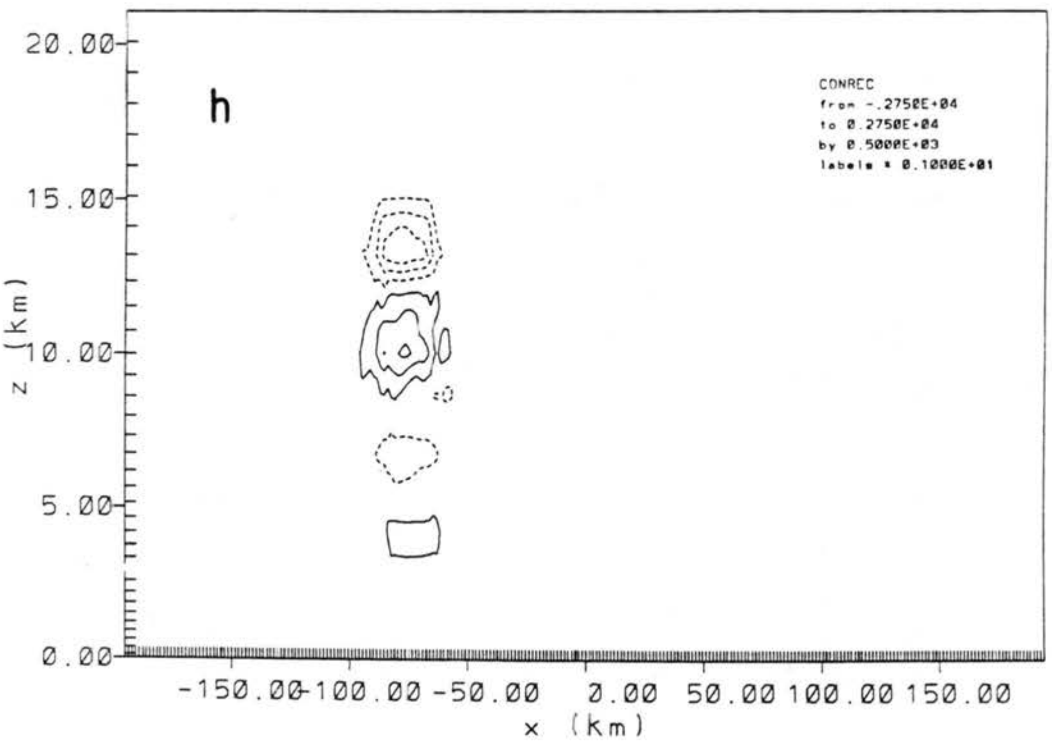

Figure 5.11: Continued.

the center of the peninsula by 40 km although the explicit simulation has the convergence localized around 80 km west of the center. Deep outflow near 13 km is present and extends over the peninsula and ocean even though the explicit simulation has the outflow considerably more localized. Resolved vertical motion resulting from the parameterization scheme is half as strong as the explicit simulation while the perturbation temperatures and total water mixing ratios are twice as strong as the explicit simulation. These fields also exhibit, along with the perturbation horizontal velocity, too much spatial coverage. Also obvious is the large amount of condensate injected into the troposphere. The magnitudes of $\overline{w'w'}$ are similar to the explicit simulation although the parameterization scheme confines the vertical variance to under 10 km. It is not clear why this restriction occurs.

Adding downdrafts to the parameterization appears to anchor the convection to a location near its initial activation, as seen in Figs. 5.13a-5.13h. This is similar to the wave-CISK result of Raymond (1983) where he obtained a propagating mode and advecting mode with downdrafts. Here, the advecting mode dominates over the propagating mode and has a phase speed near zero. The convection is also weaker with downdrafts, with the salient parameters summarized in Table 5.2 being about half the magnitude as when the simulation is run without downdrafts. This is consistent with the analysis at 1400 local time.

When precipitation is included in the parameterization without downdrafts (Figs. 5.14a-5.14h), peak values of mean vertical motion, perturbation total water mixing ratio and condensate mixing ratio are comparable to the explicit values even though the peak temperature perturbation is too large by almost three times. In addition, the vertical variance is also overestimated by the parameterization by almost five times. The injection of moisture by the core of the updraft is clearly seen in Figs. 5.14d and 5.14e.

When downdrafts are added to the simulation with precipitation, a two-celled structure emerges again as seen in Figs. 5.15a-5.15h. However, the west cell appears to have moved considerably closer to the east cell than one would expect if the convection was truly anchored to one location. The mean vertical motion has weakened by half of the

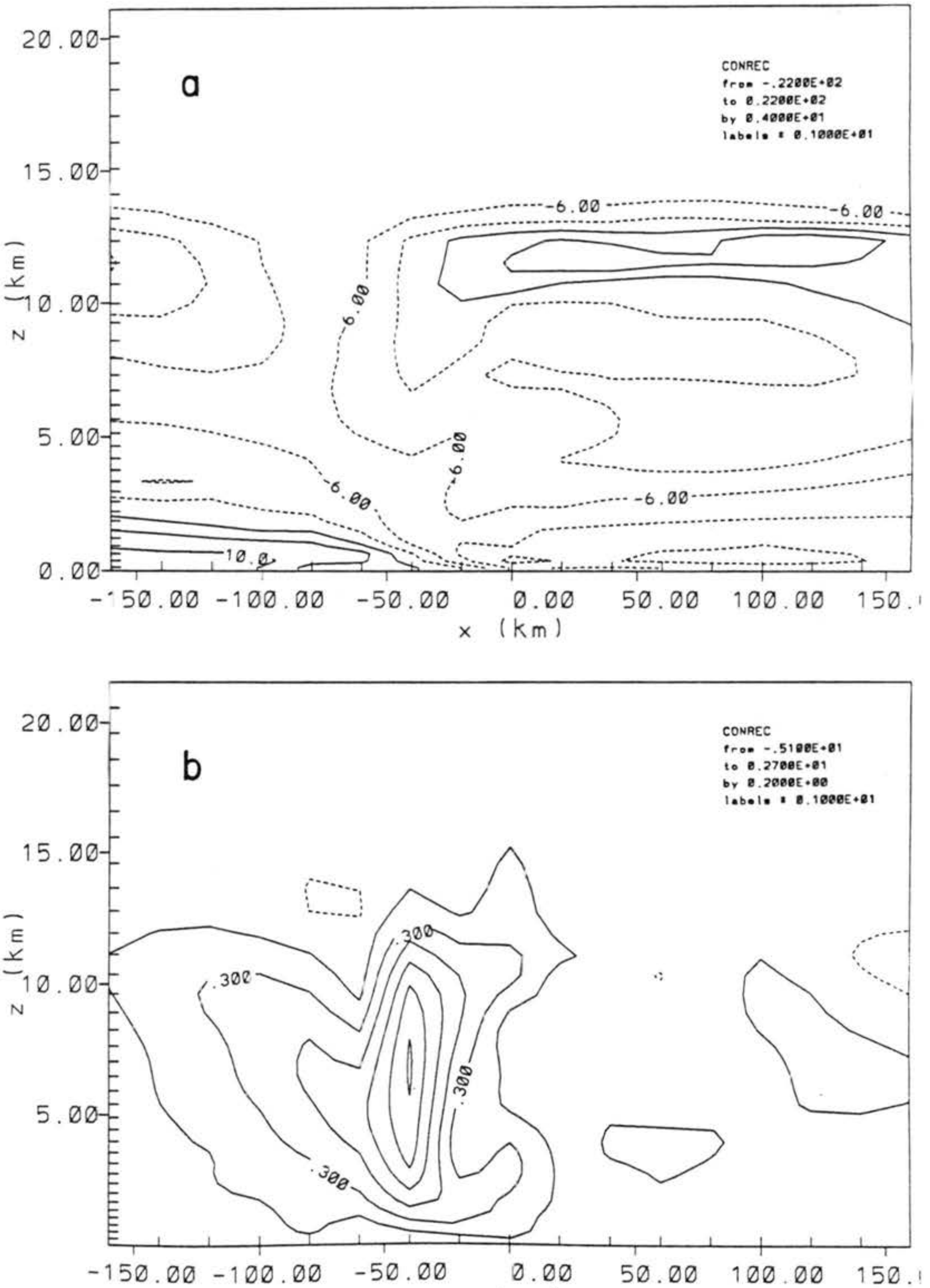

Figure 5.12: As in Figs. 5.6a-h except for the 20 km parameterized simulation without downdrafts and without precipitation.

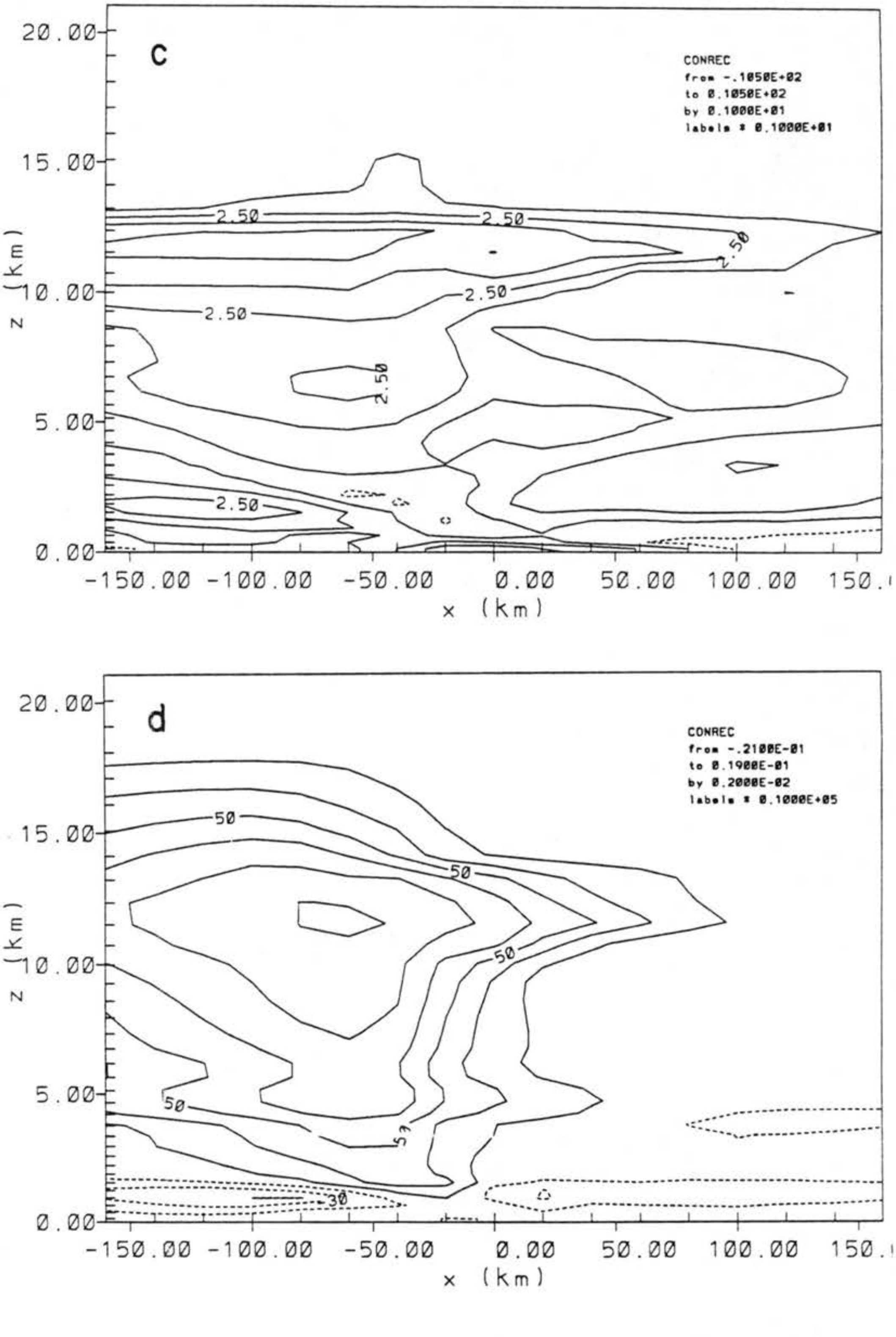

Figure 5.12: Continued.

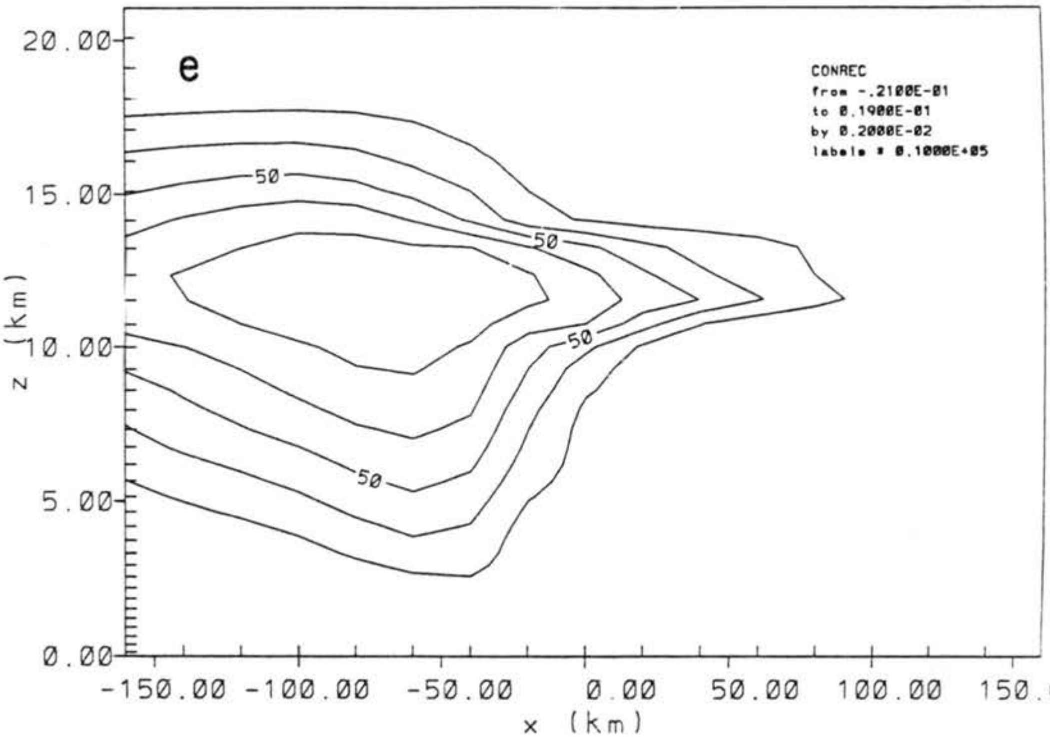

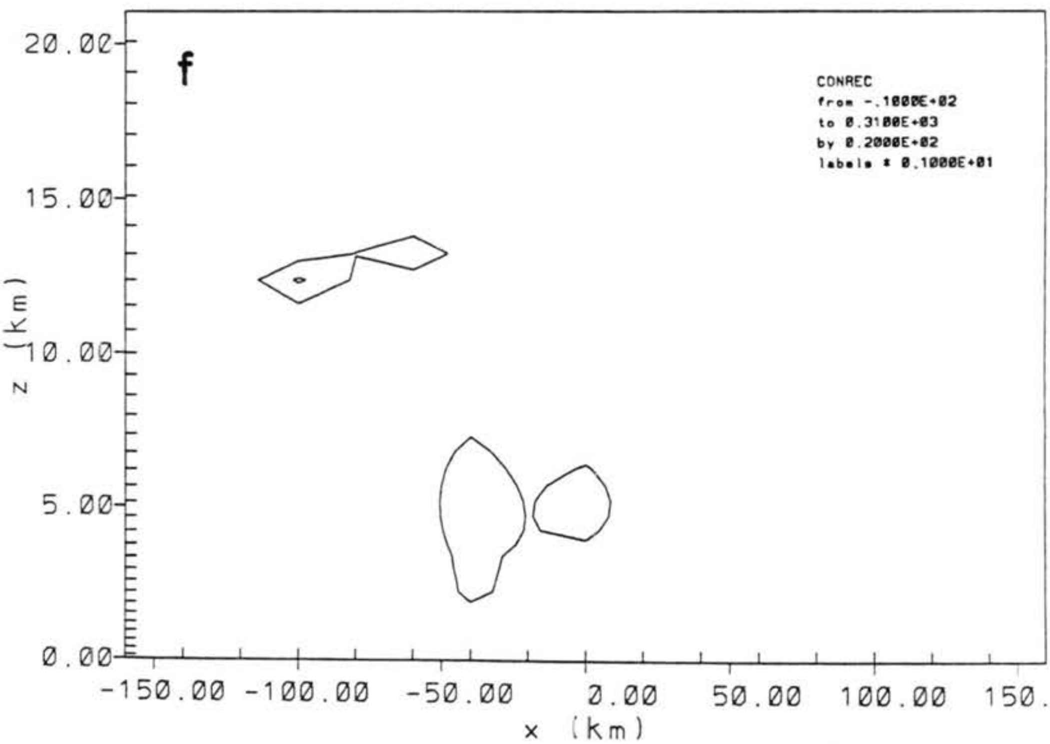

Figure 5.12: Continued.

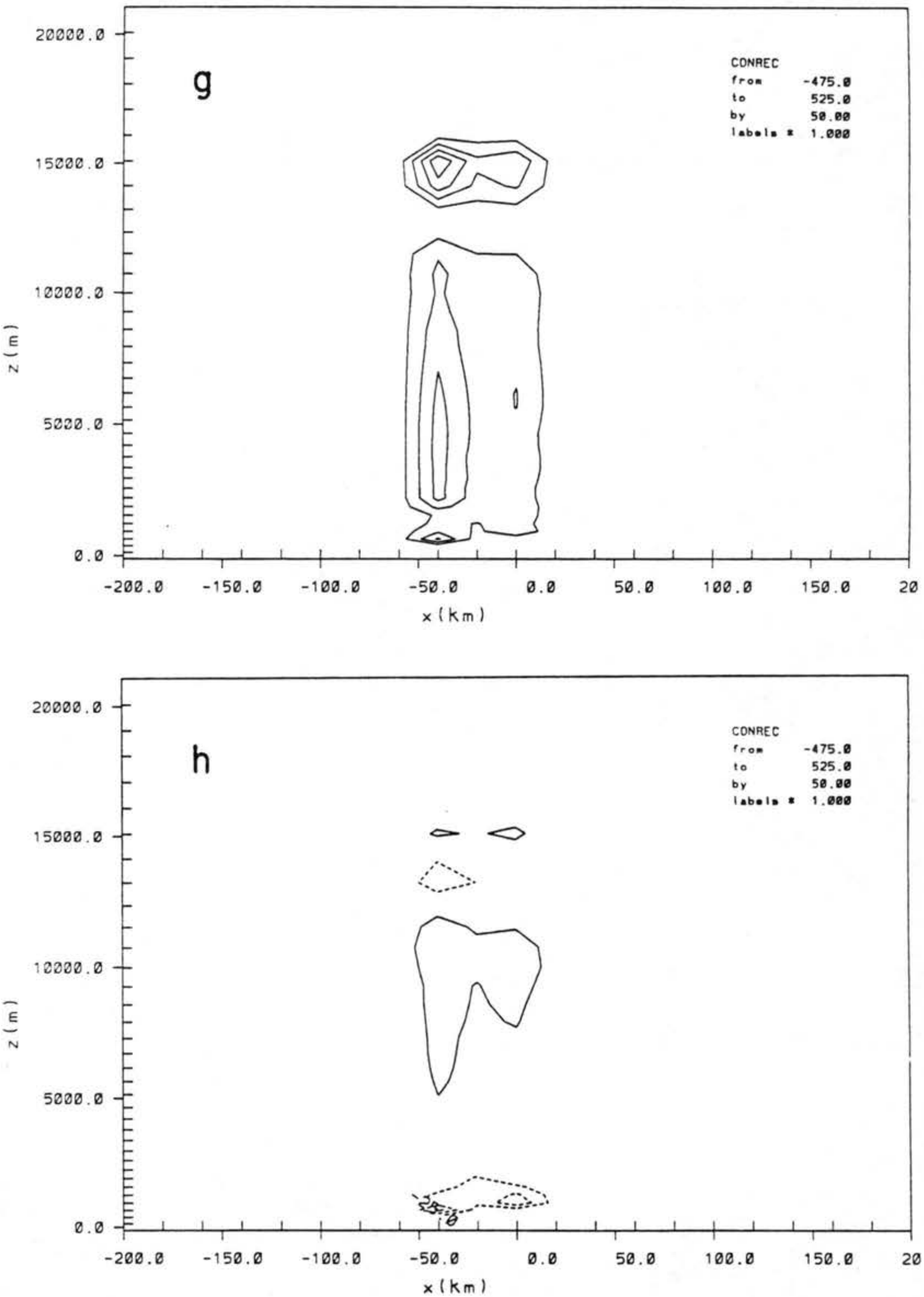

Figure 5.12: Continued.

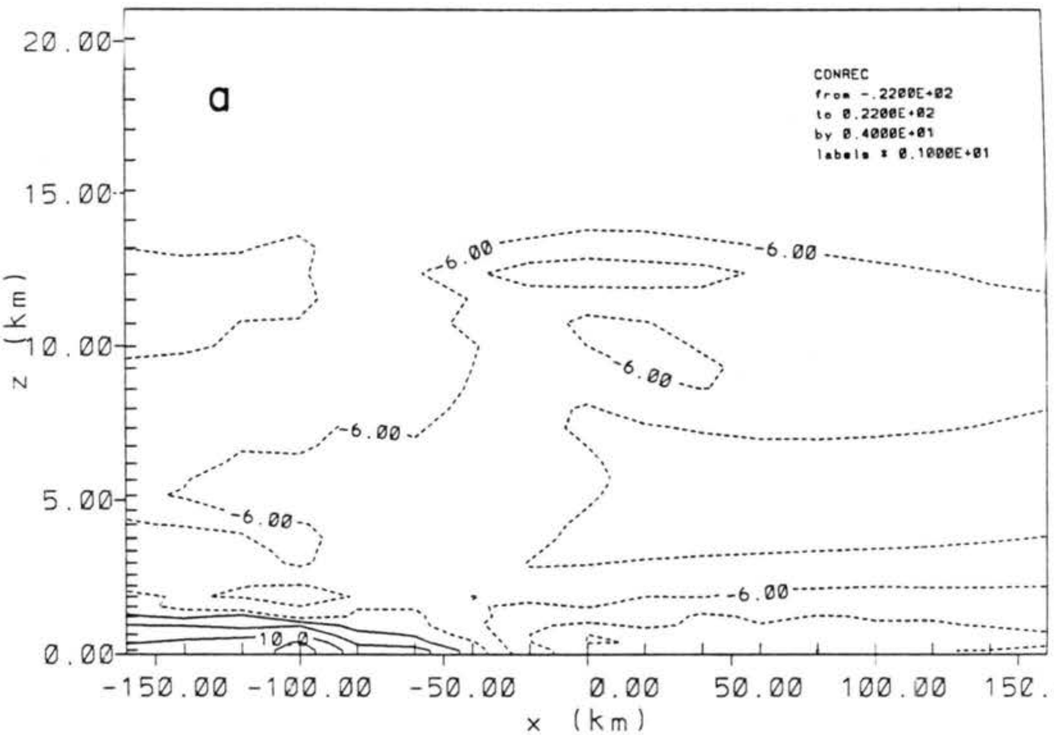

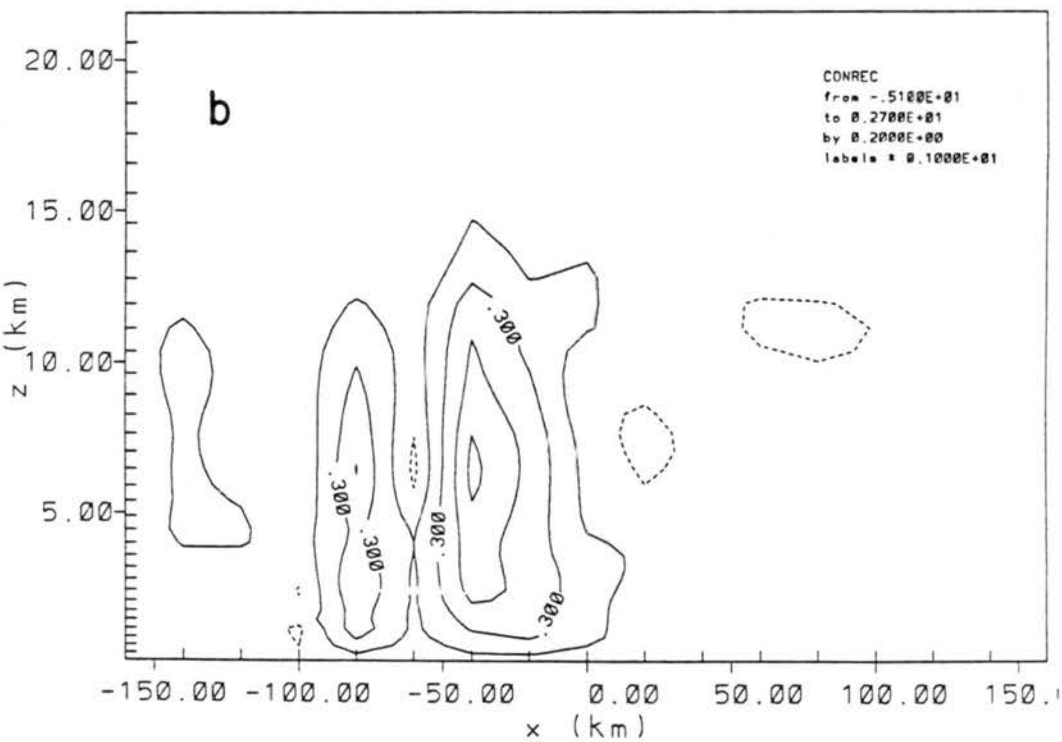

Figure 5.13: As in Figs. 5.6a-h except for the 20 km parameterized simulation with downdrafts and without precipitation.

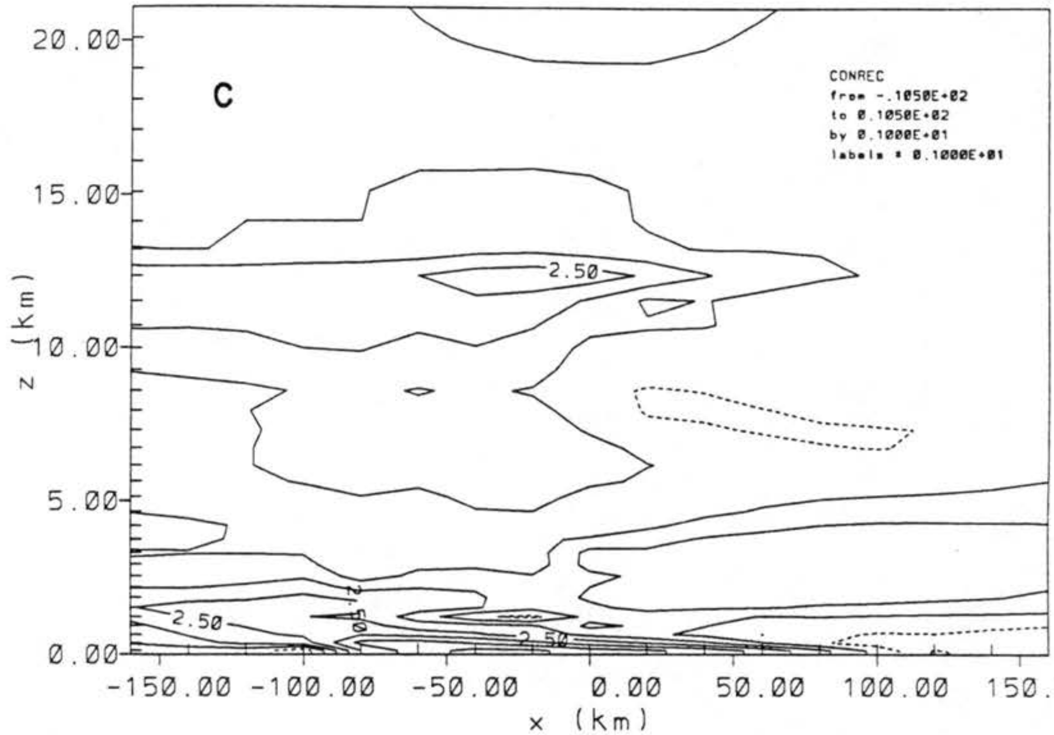

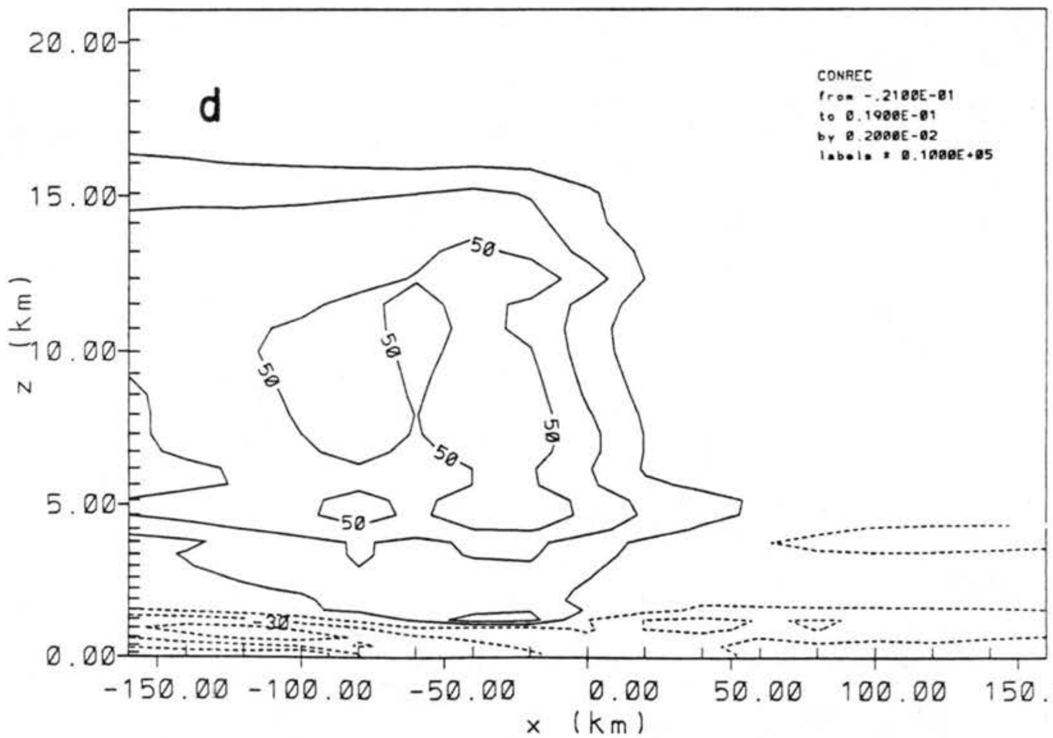

Figure 5.13: Continued.

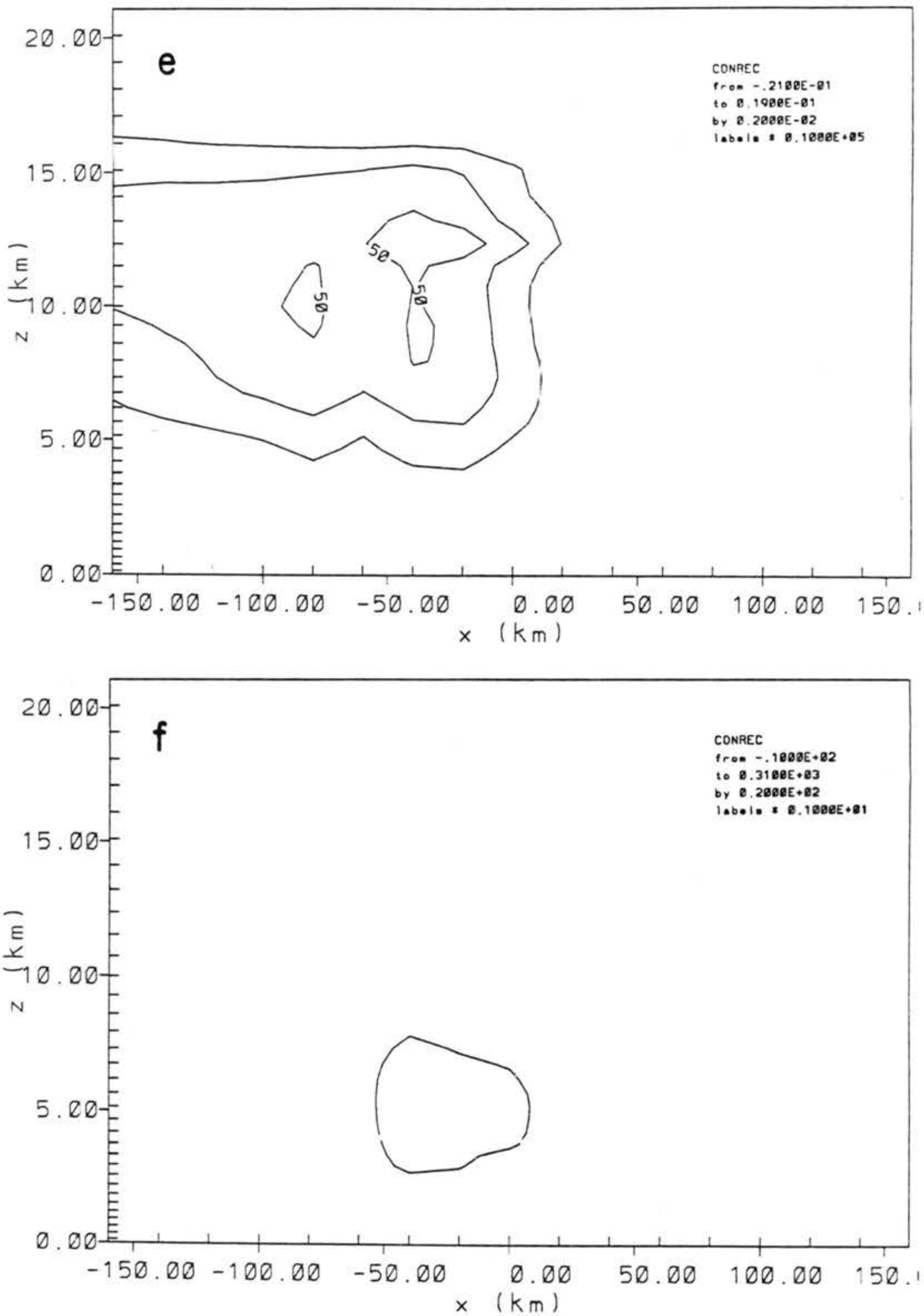

Figure 5.13: Continued.

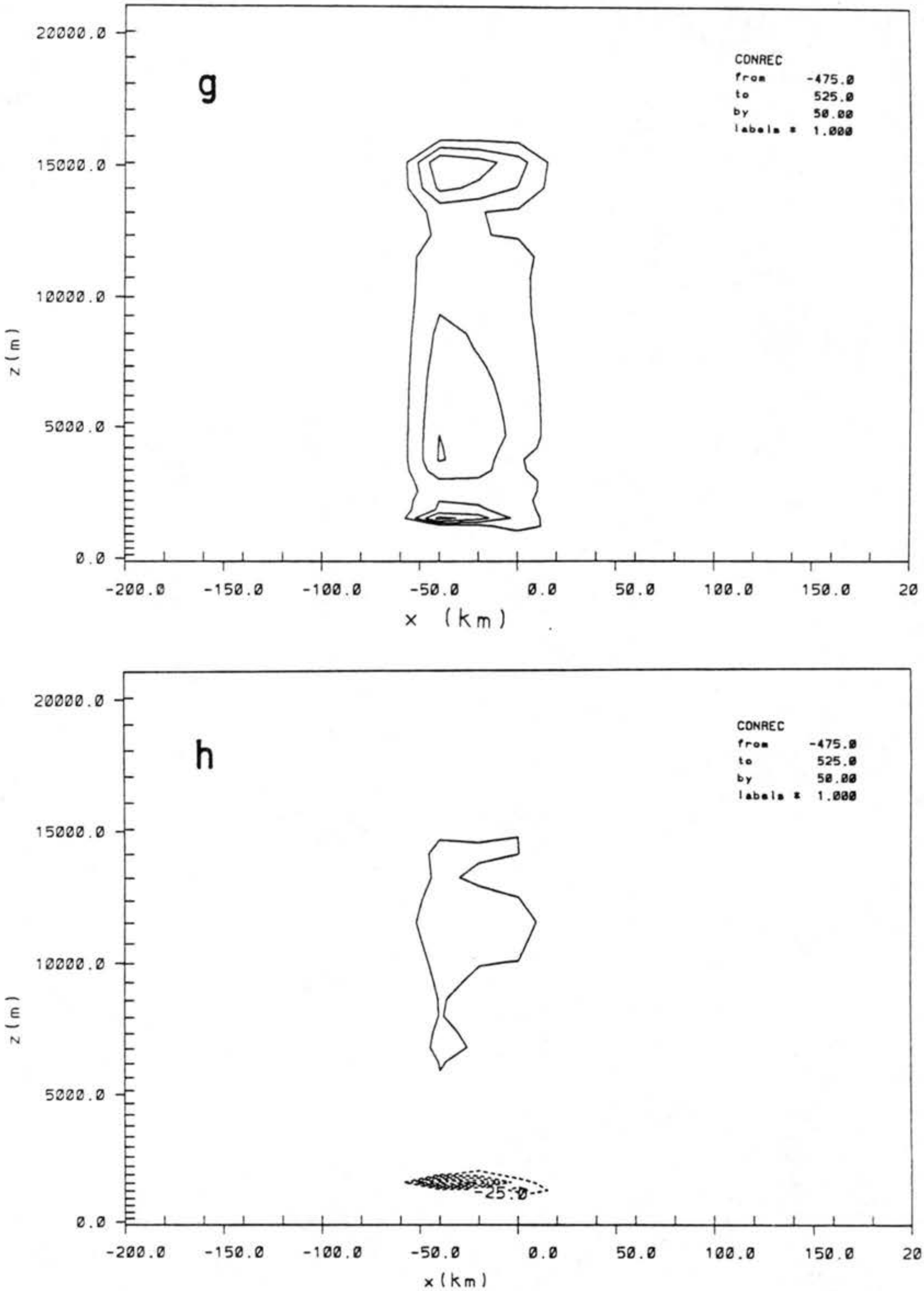

Figure 5.13: Continued.

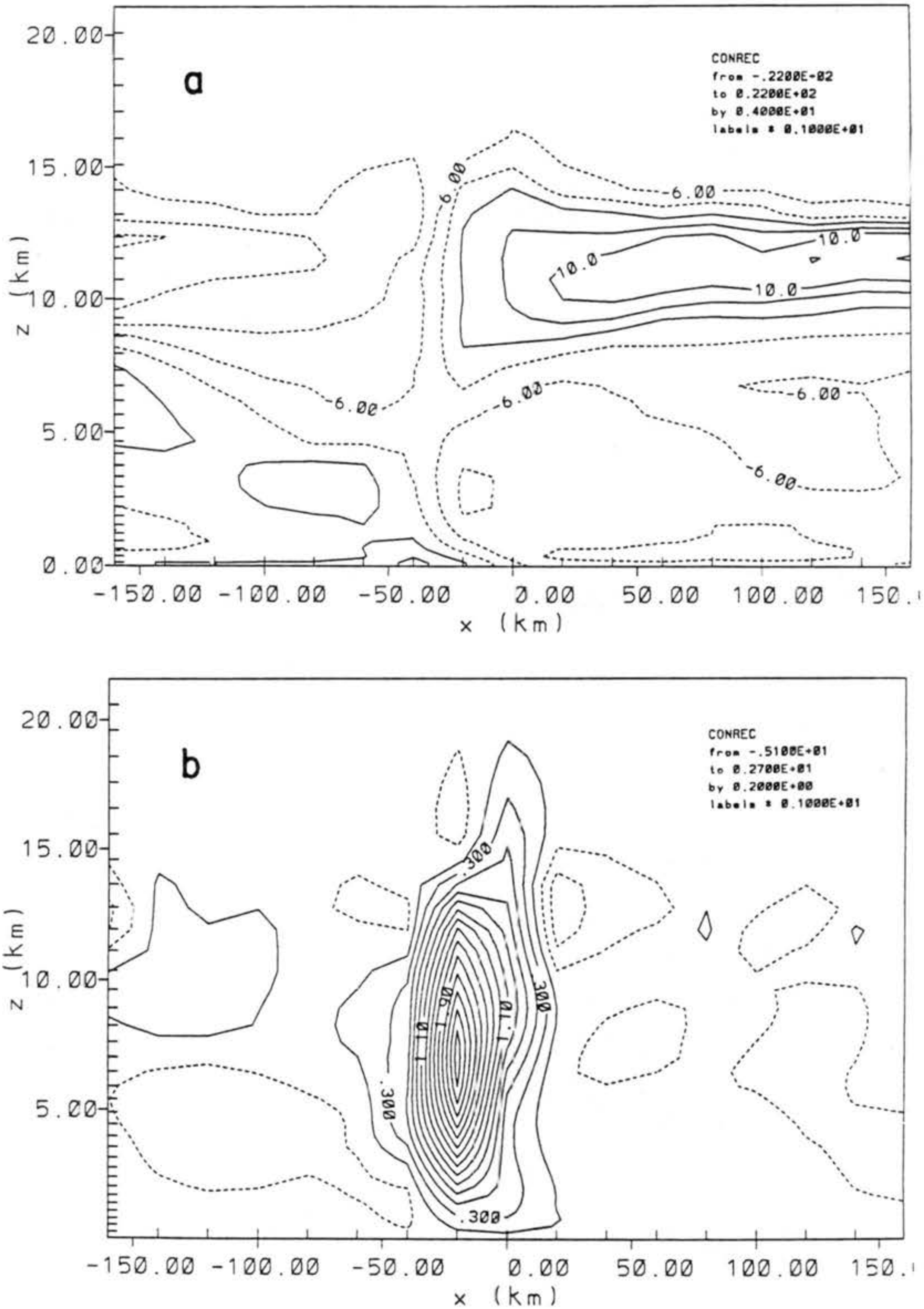

Figure 5.14: As in Figs. 5.6a-h except for the 20 km parameterized simulation without downdrafts and with precipitation.

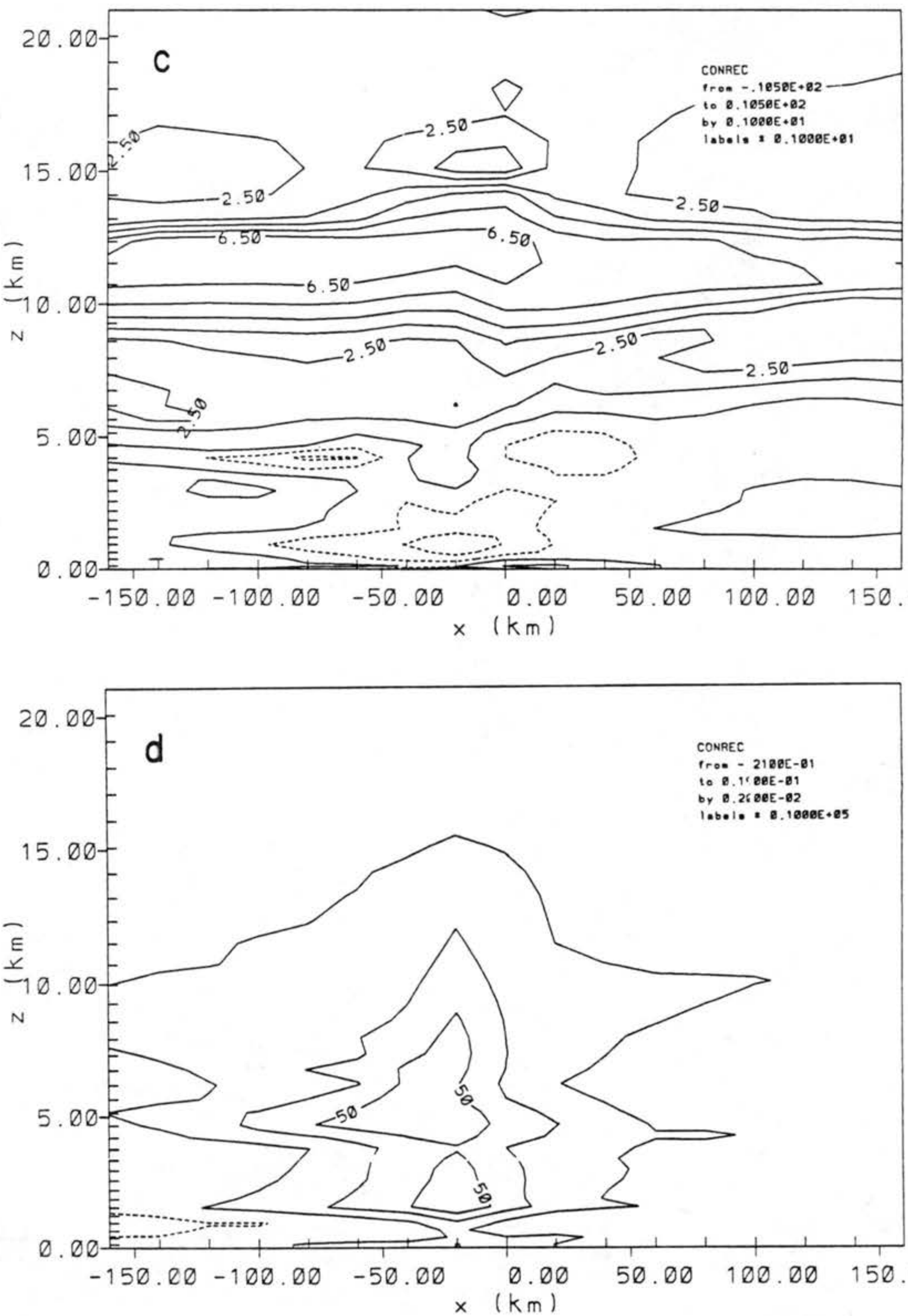

Figure 5.14: Continued.

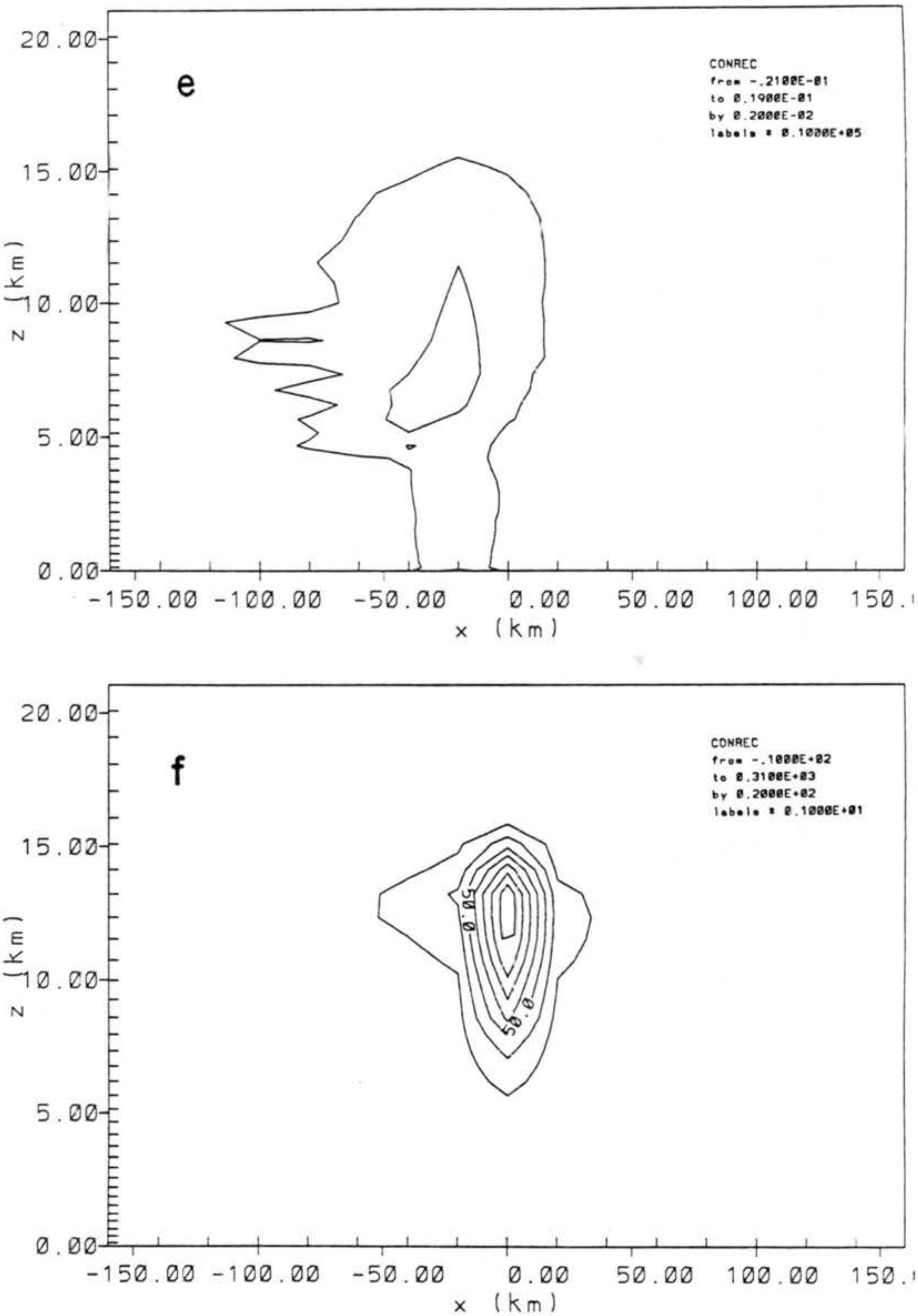

Figure 5.14: Continued.

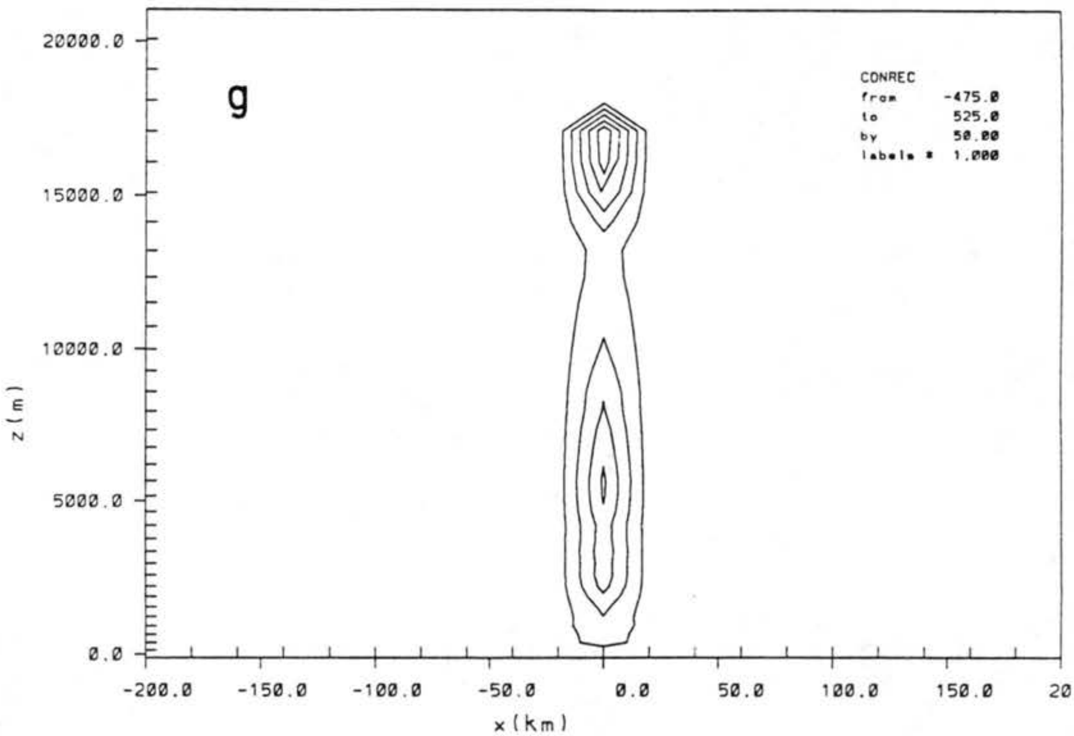

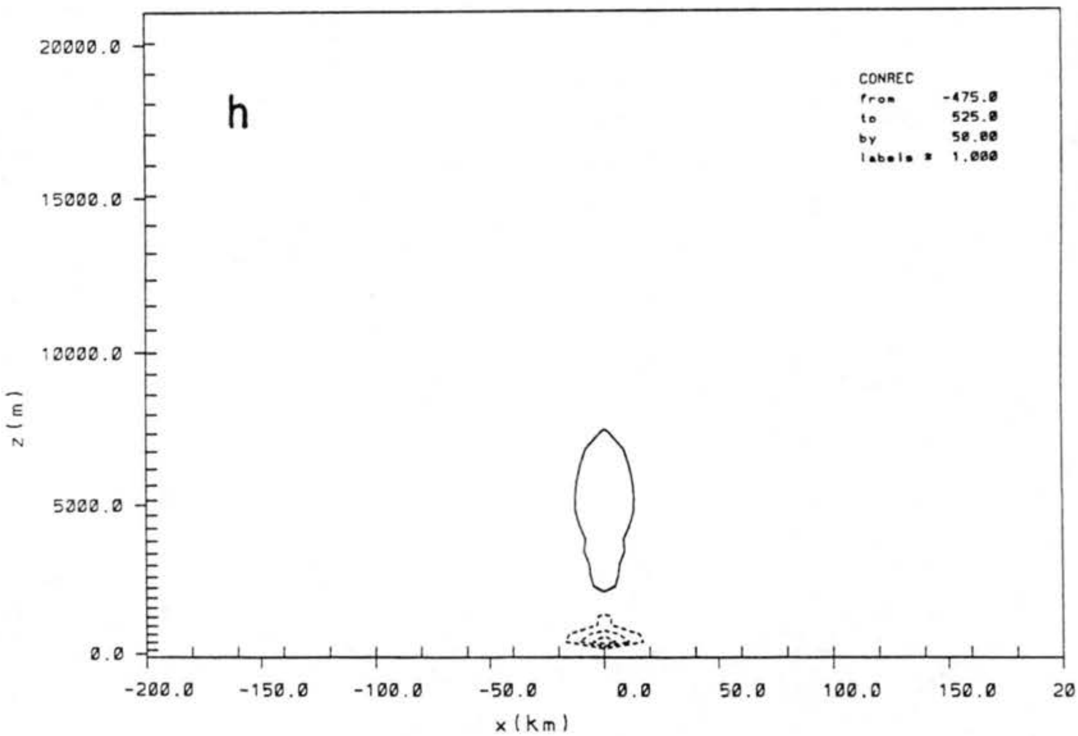

Figure 5.14: Continued.

no downdraft simulation and is one seventh of the explicit simulation value. Perturbation temperature and total water mixing ratio are similar to the explicit values, although the condensate mixing ratio is small by one half and the vertical variance is large by a factor of two.

Since the cumulus parameterization scheme communicates microphysical information to the mesoscale model, precipitation rates of the parameterization are unavailable. Therefore, condensate rates at a particular grid point near the center of the peninsula are shown in Figs. 5.16a - 5.16d for each of the four parameterized simulations. Condensate rates here are defined as the total condensate including cloud water, rain water, ice, graupel and aggregates which is produced by the parameterization scheme. Peak condensate rates when cumulus convection is first activated approach 70 mm/hr for both no downdraft simulations and are less than a third of that for the parameterized runs with downdrafts. This agrees with the previous discussions which indicate that downdrafts weaken the convection. The high frequency oscillations when downdrafts are present in the condensation only case in Fig. 5.16b are due to the cloud model indicating cumulus convection on only alternating groups of time steps. The reason for this is not known at this time. The temporal evolution of the condensation rates indicate that all simulations evolve differently.

In general, best agreement with the explicit simulations appears to be when the parameterization is run with precipitation but without downdrafts. The downdrafts appear to anchor the convection so that its propagation is less influenced by the movement of the sea breeze front and weaken convection through the decrease of moist static energy within the PBL. Because the parameterized cumulus convection is prevented from depleting the moisture in the PBL, this decrease in moist static energy is accomplished through cooling and possibly drying since the moisture content within the downdraft is less than the unperturbed humidity in the PBL. Temperature perturbation are too strong, though, as is the value of the vertical variance during the transient phase of the cumulus convection at 1400. Furthermore, temperature perturbations appear to influence too large an area about the convection. However, temperature perturbations and vertical variances are similar to the explicit simulation three hours later when the explicit simulation has indicated the

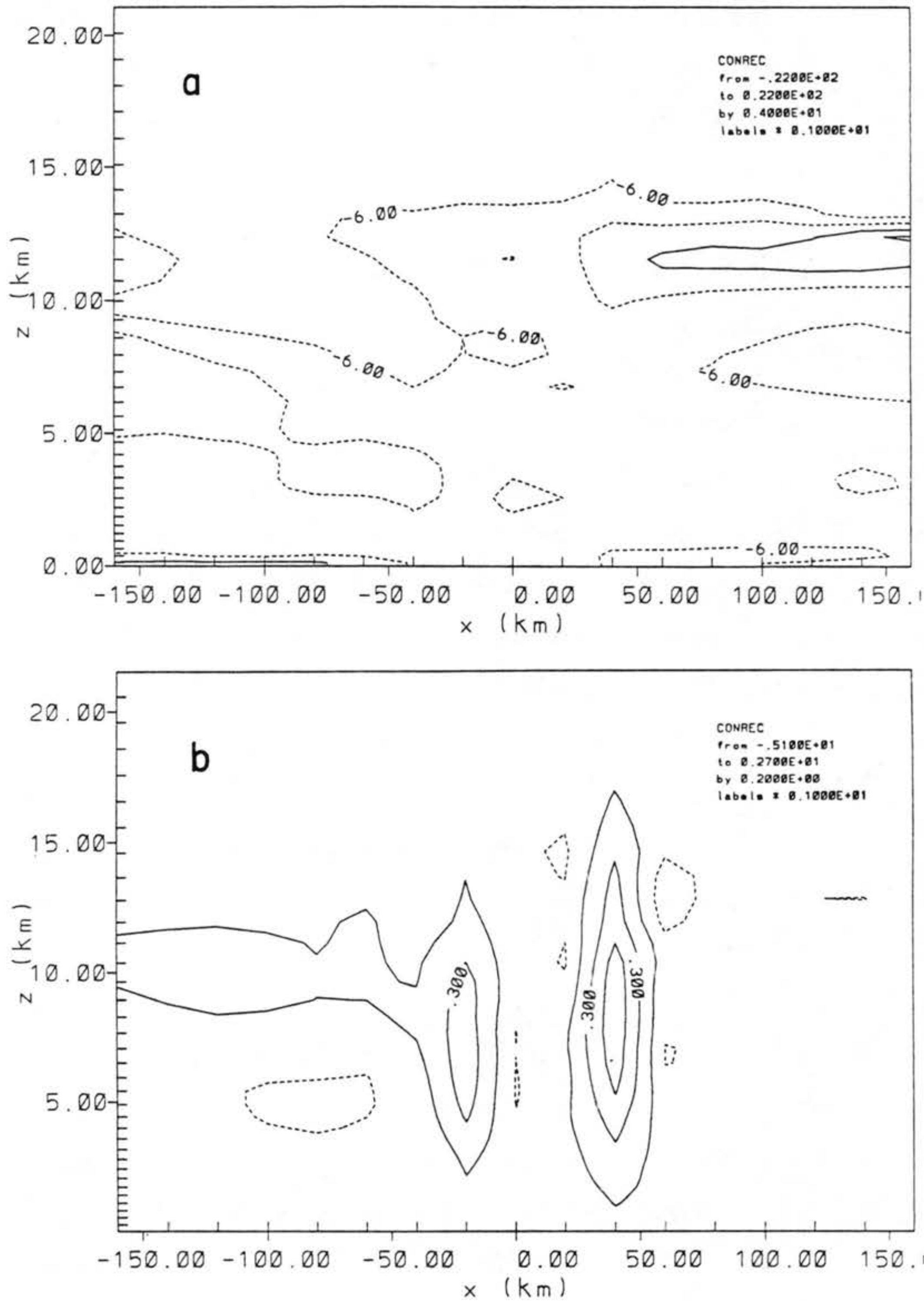

Figure 5.15: As in Figs. 5.6a-h except for the 20 km parameterized simulation with downdrafts and with precipitation.

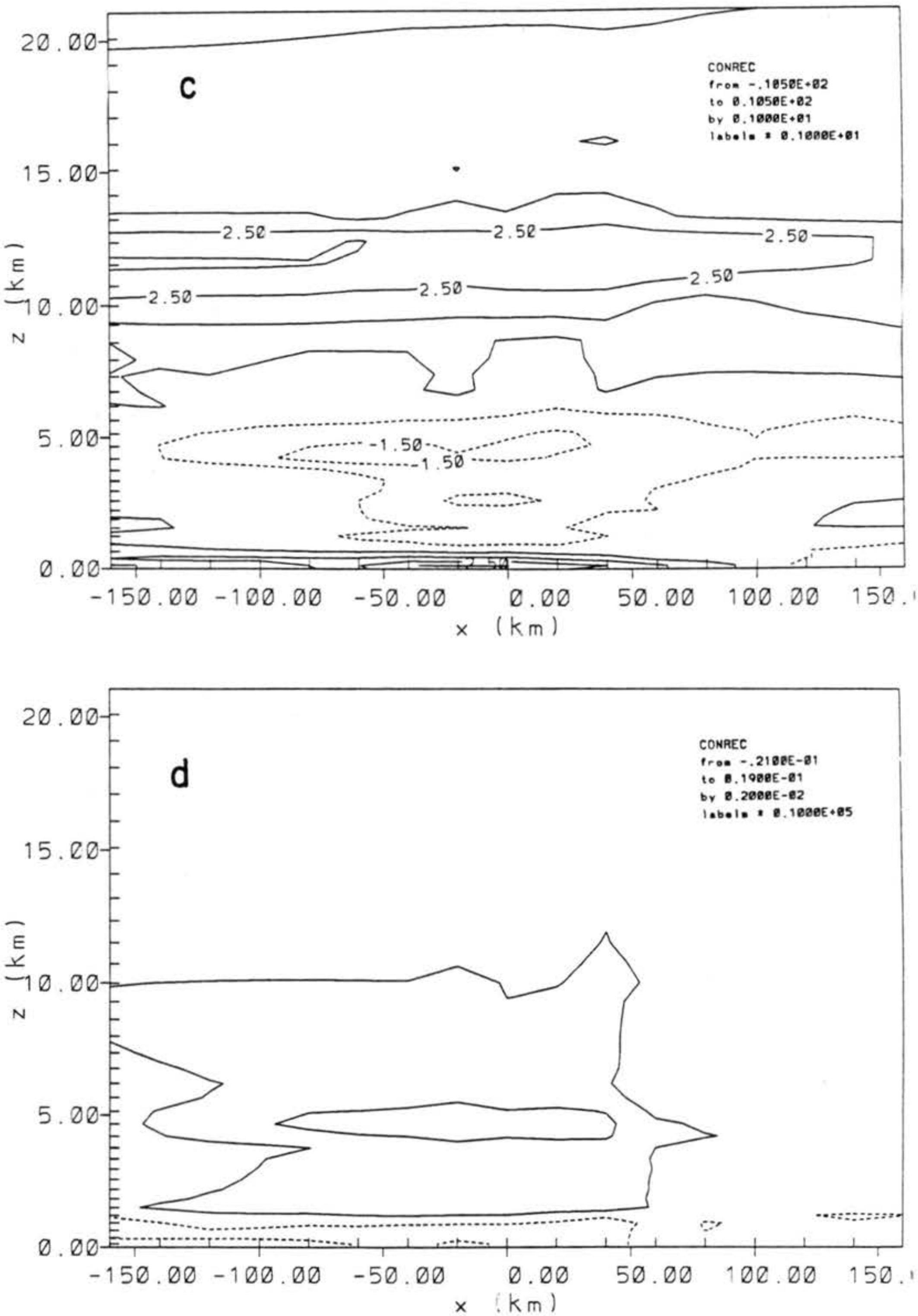

Figure 5.15: Continued.

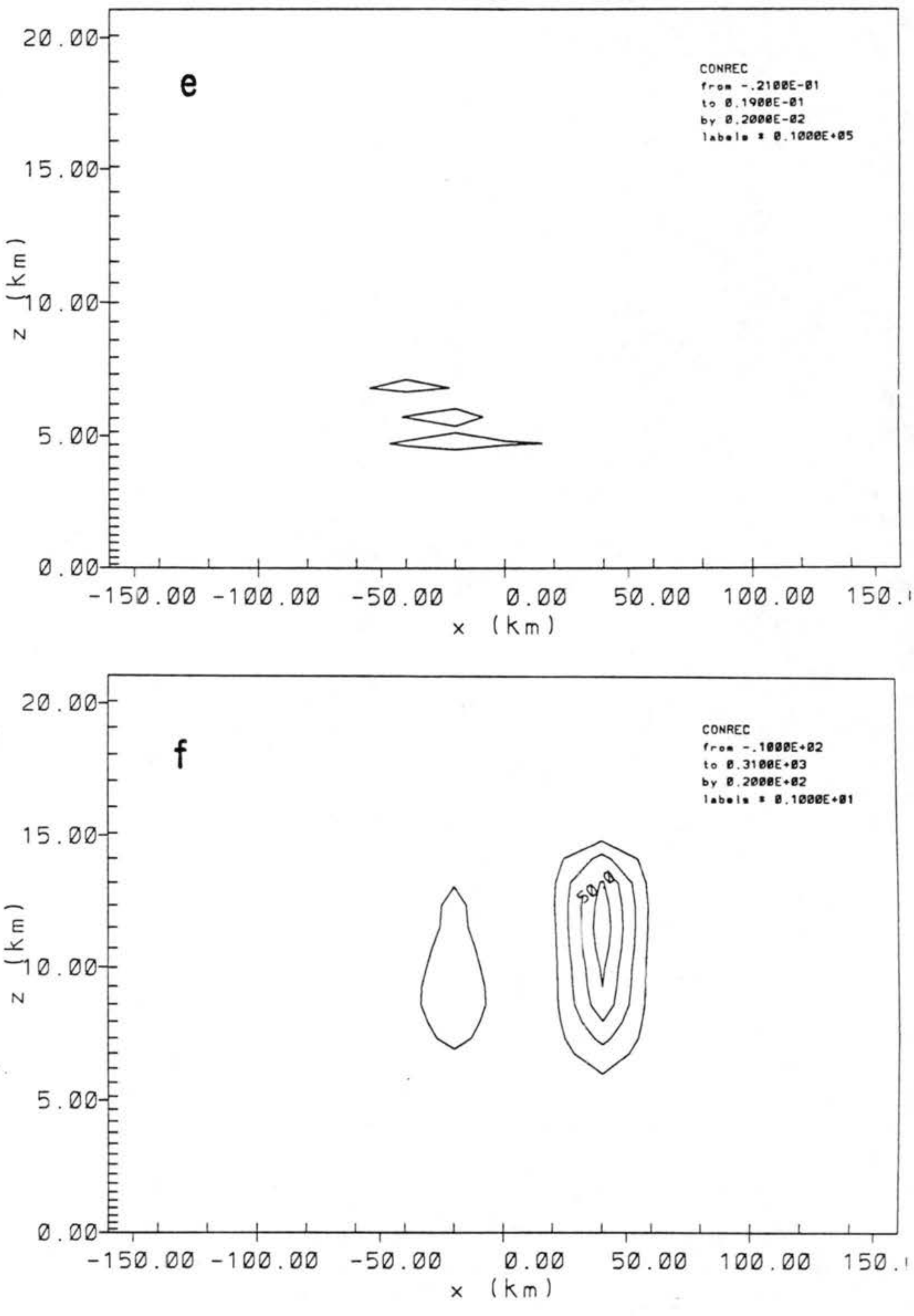

Figure 5.15: Continued.

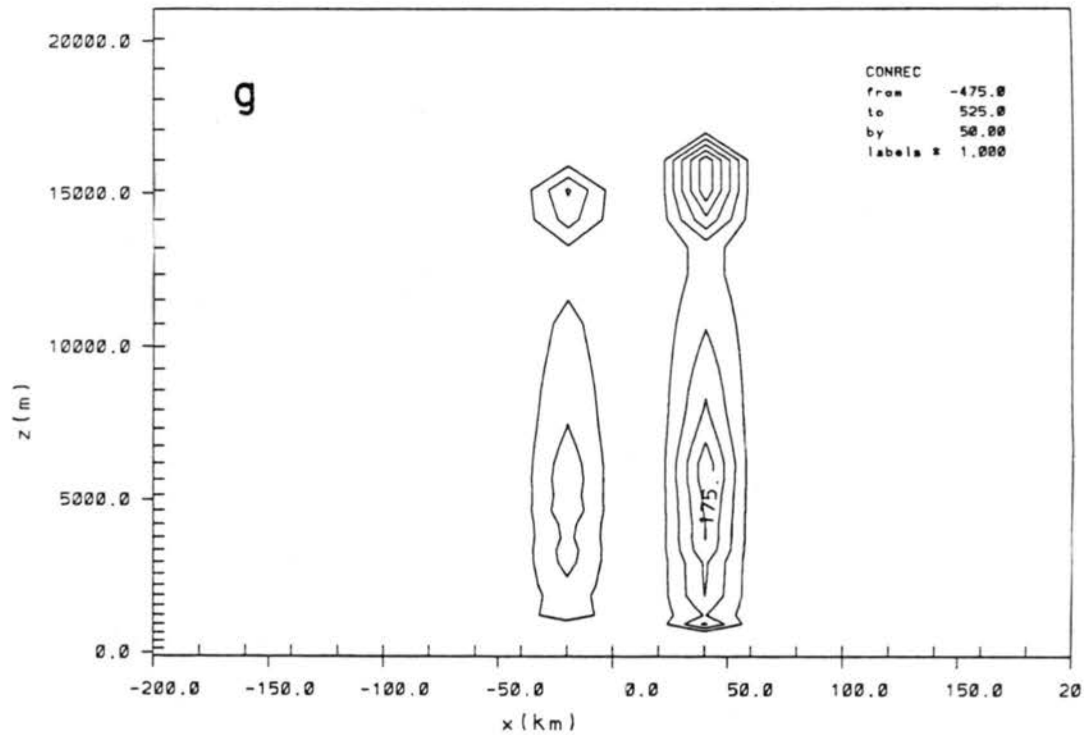

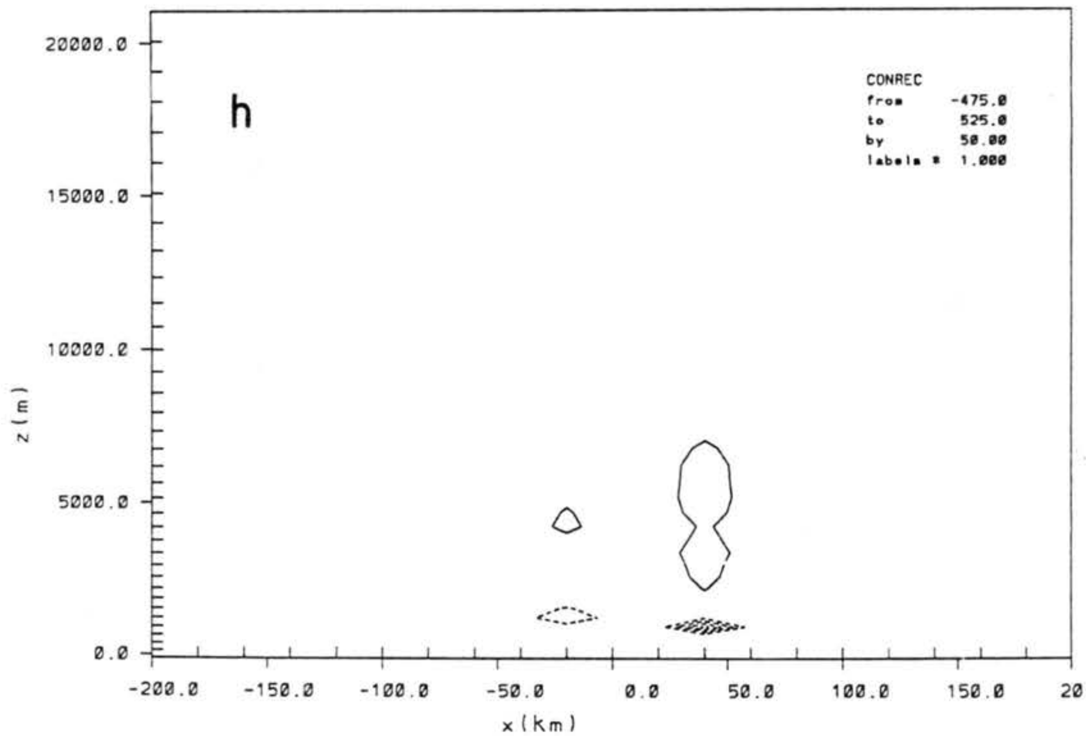

Figure 5.15: Continued.

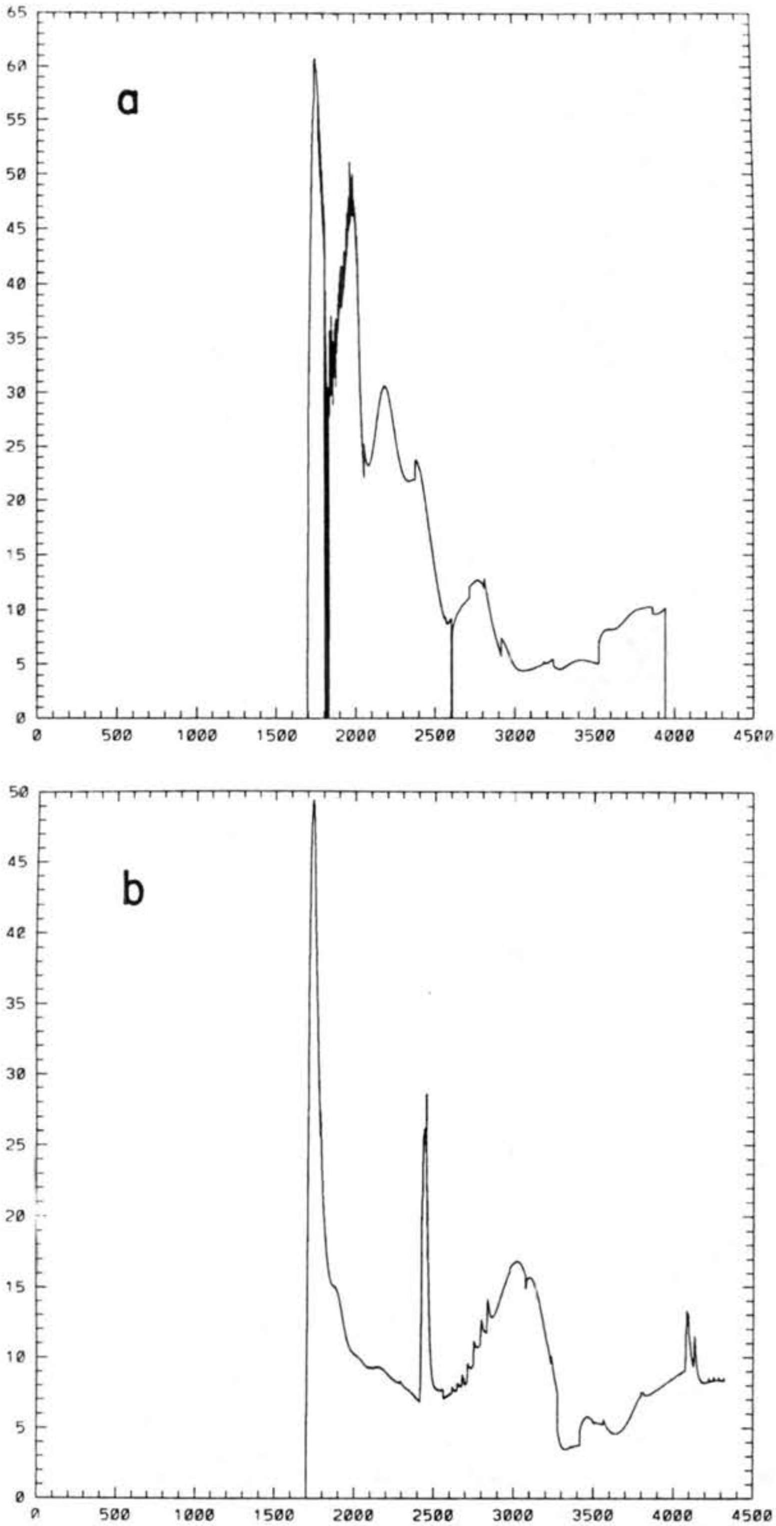

Figure 5.16: Temporal evolution (12 hrs) of the condensate rate in mm/hr for the parameterized simulations on a 20 km grid (a) without downdrafts and without precipitation, (b) with downdrafts and without precipitation.

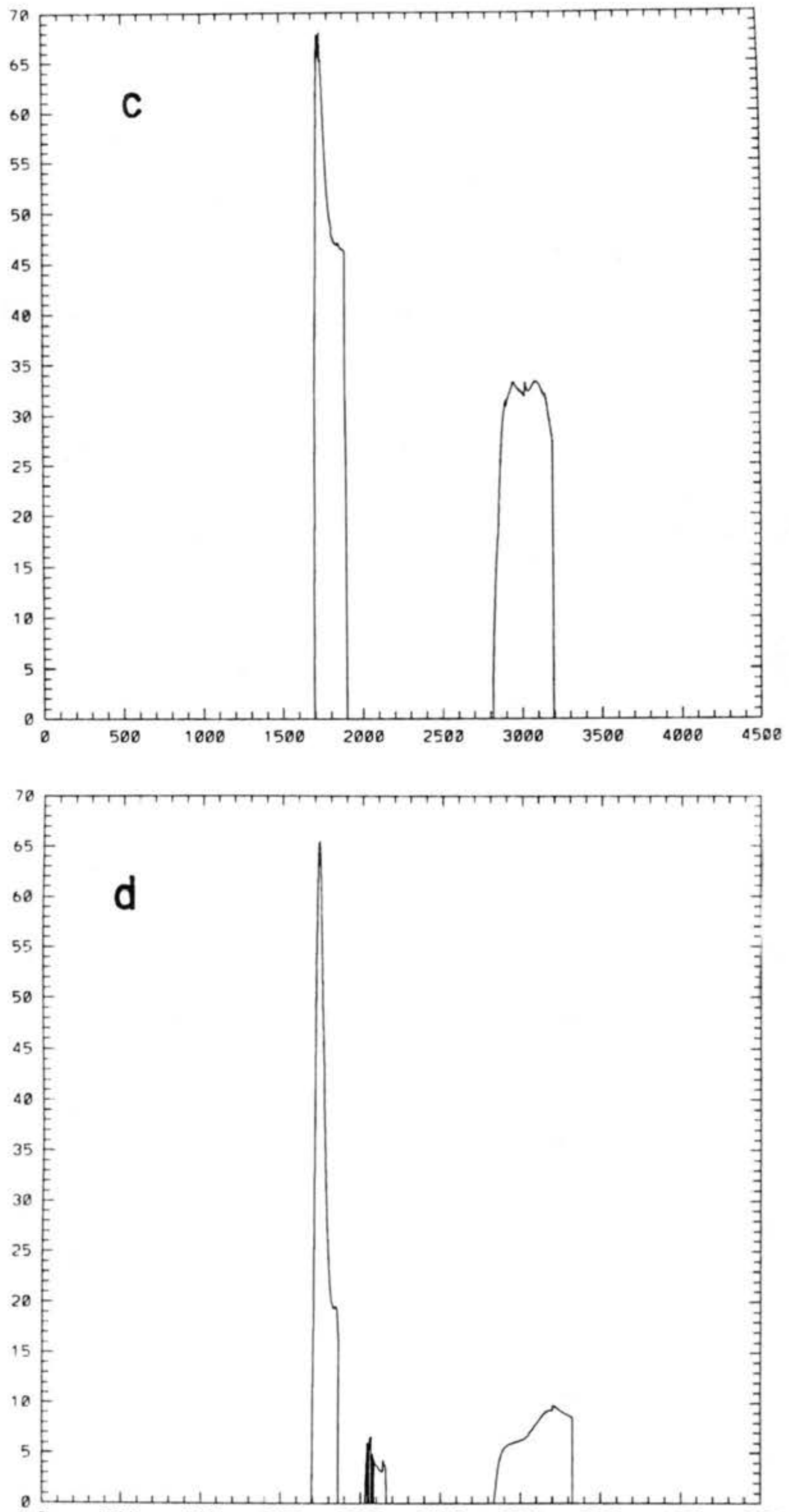

Figure 5.16: Continued. (c) without downdrafts and with precipitation, and (d) with downdrafts and with precipitation.

convection is steadier and more long-lived. It also appears that the parameterization is far too robust during supposedly transient events; this is perhaps due to the lack of moisture consumption by the parameterized cumulus within the PBL or the parameterization scheme being constructed around a steady-state model. The neglect of entrainment may also contribute to the excessive strength of the cumulus convection early in the numerical simulation. However, the transport of moisture by the convective cores is reproduced and the subsident circulation in the resolved circulations is apparent.

5.2.2 The explicit and parameterized simulations on a 5 km grid

The explicit simulation with 5 km running averages and the parameterized simulation on a 5 km grid are analyzed in this section. This will be done separately at 1400 local time and 1700 local time.

The explicit simulation at 1400 local time

In general, the 5 km running averages are similar in appearance to the 20 km running averages except the magnitudes are higher (Figs. 5.17a - 5.17h) This can be seen by comparing the peak values of the salient fields in Table 5.3 to those in Table 5.1.

Table 5.3: As in Table 5.1 except for the 5 km simulation at 1400 local time.

Simulation	W (m/s)	T (K)	Rt (g/kg)	COND (g/kg)	$\overline{w'w'}$ ($\frac{m^2}{s^2}$)
explicit	2.4	1.2	7.0	6.0	2.8
nodn/nomc	6.0	2.4	9.9	5.7	85.
dn/nomc	3.2	1.8	5.6	4.2	76.
nodn/ mc	7.0	4.8	7.2	2.2	850
dn/ mc	2.8	3.5	4.5	1.9	250

Interestingly, the magnitudes and scale of the temperature perturbations and divergent circulations are similar. These fields have similar scale and magnitude since they are affected by the geostrophic adjustment process, *i. e.* as the convection perturbs the mass field through localized heating, gravity waves are launched which distribute mass and momentum so that the final fields are in geostrophic balance. The temperature fields and divergent circulations should then exhibit similar final states as long as the averaging

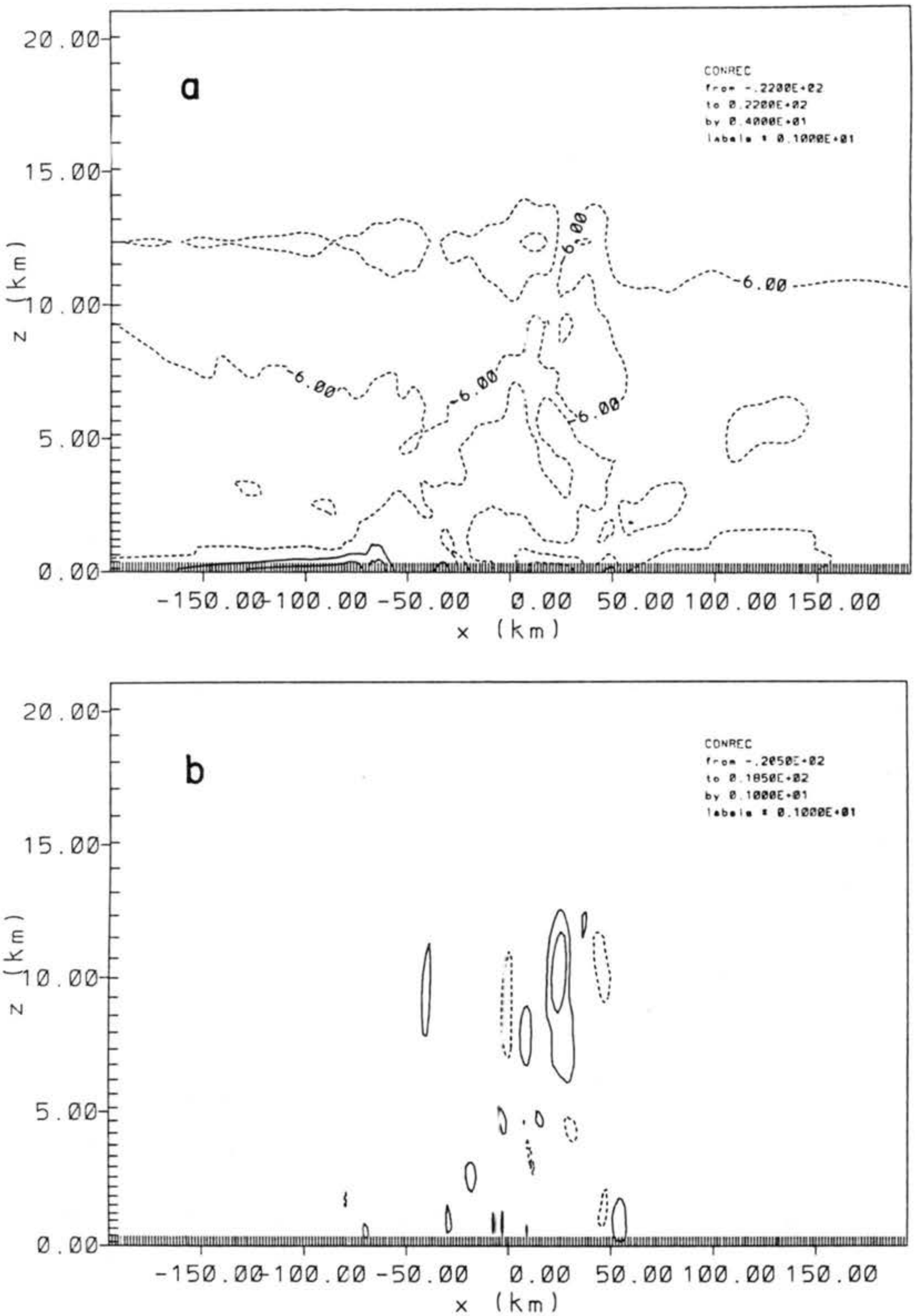

Figure 5.17: As in Figs. 5.6a-h except for the 6 km running averages of the explicit simulation at 1400 local time.

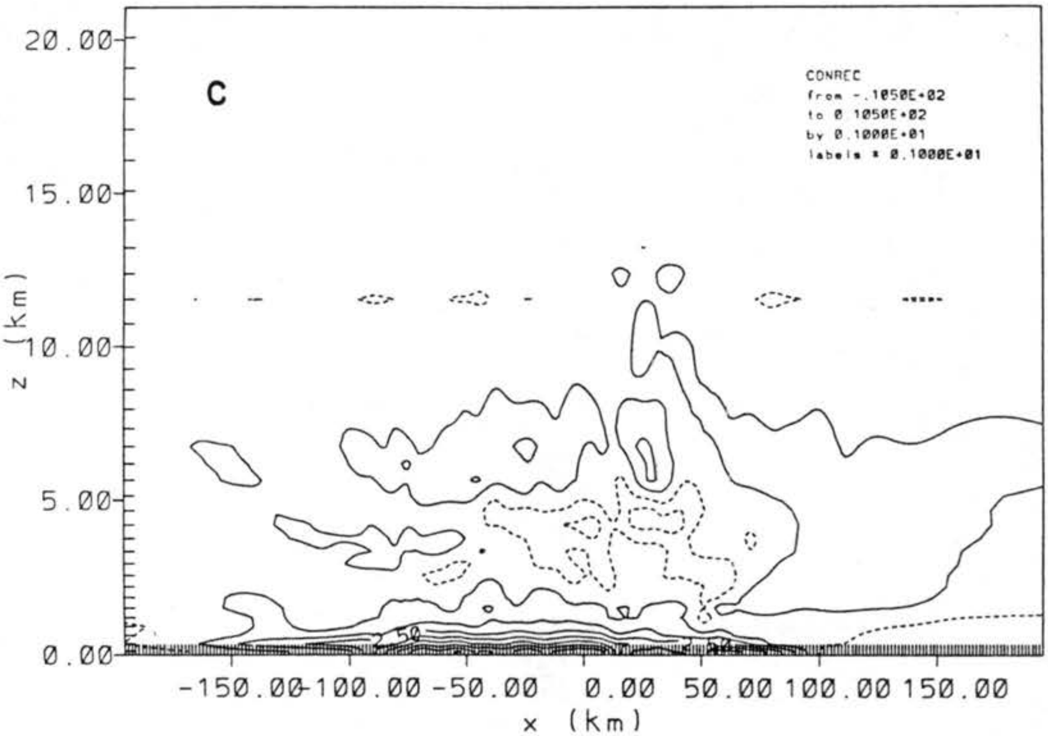

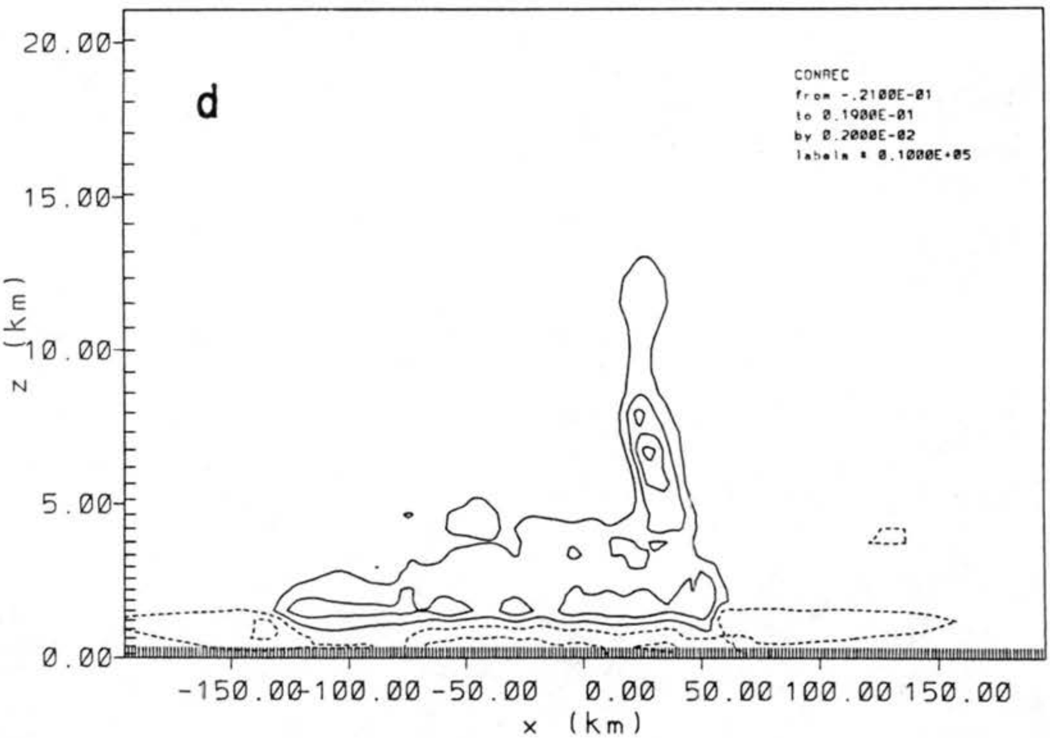

Figure 5.17: Continued.

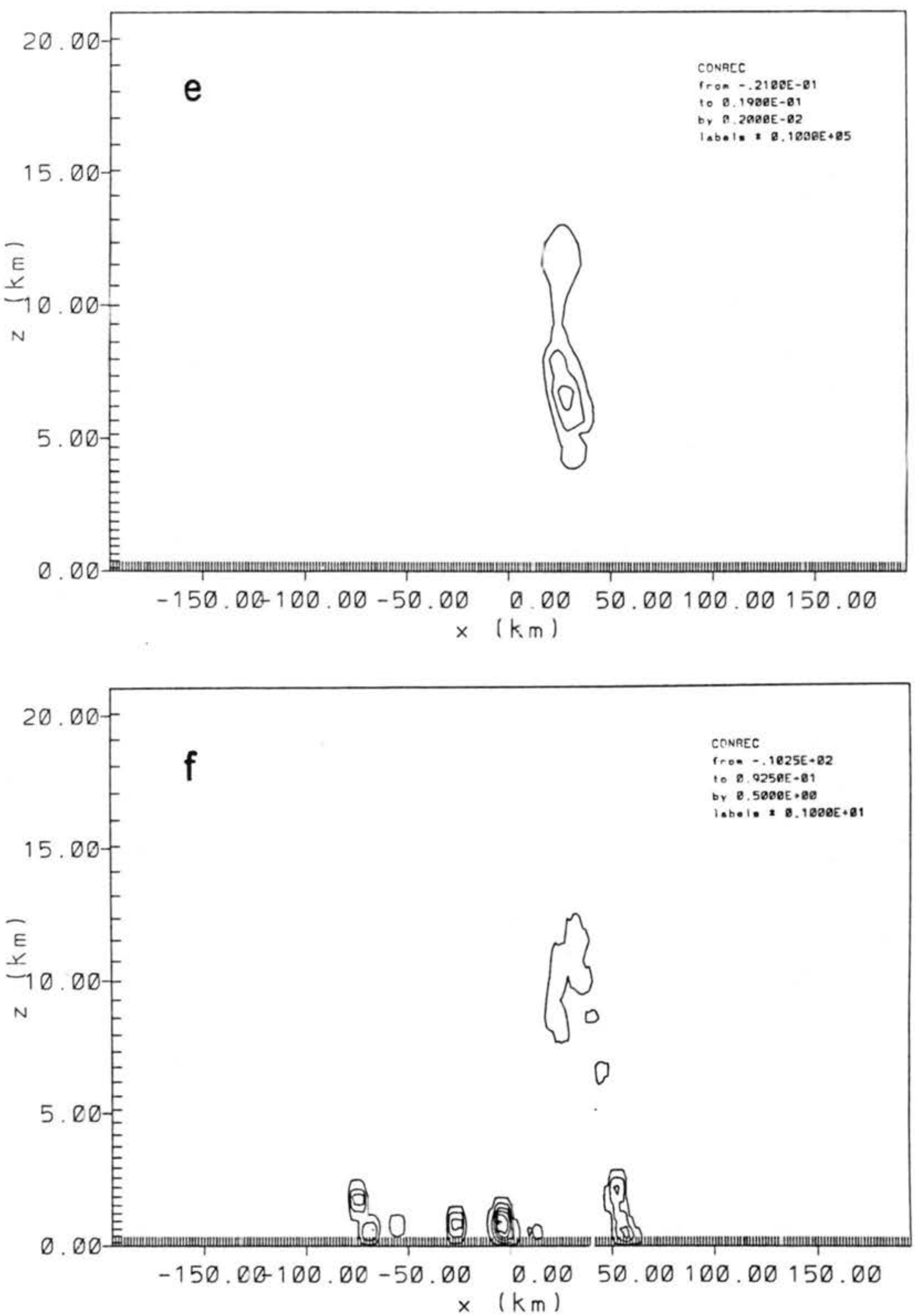

Figure 5.17: Continued.

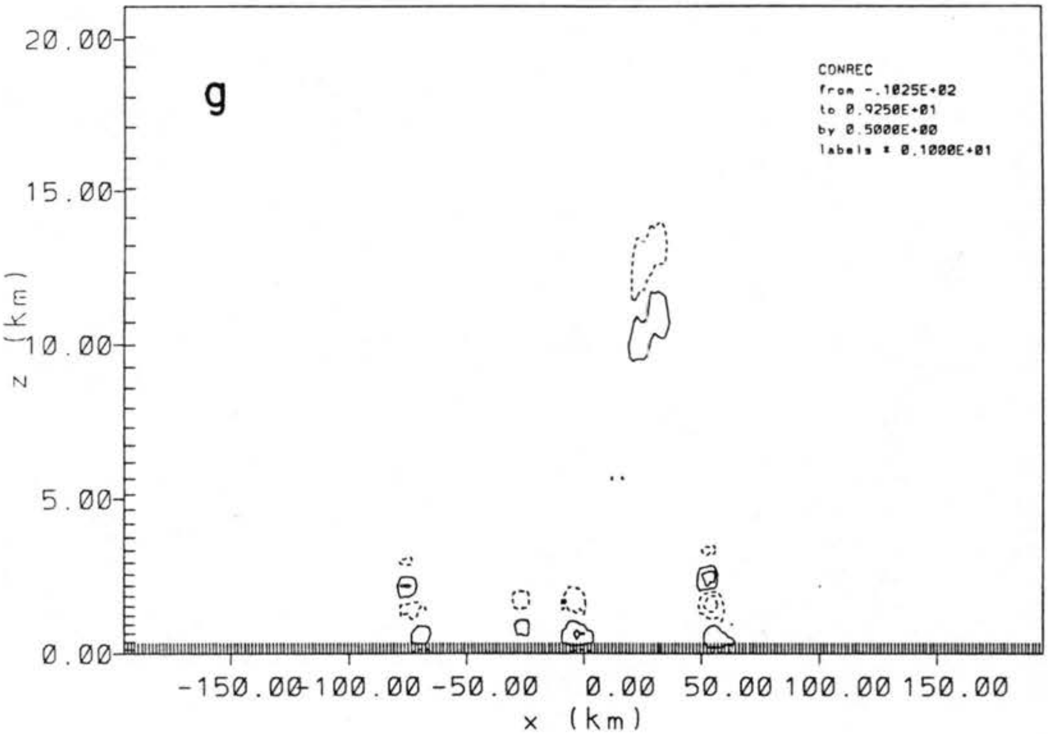

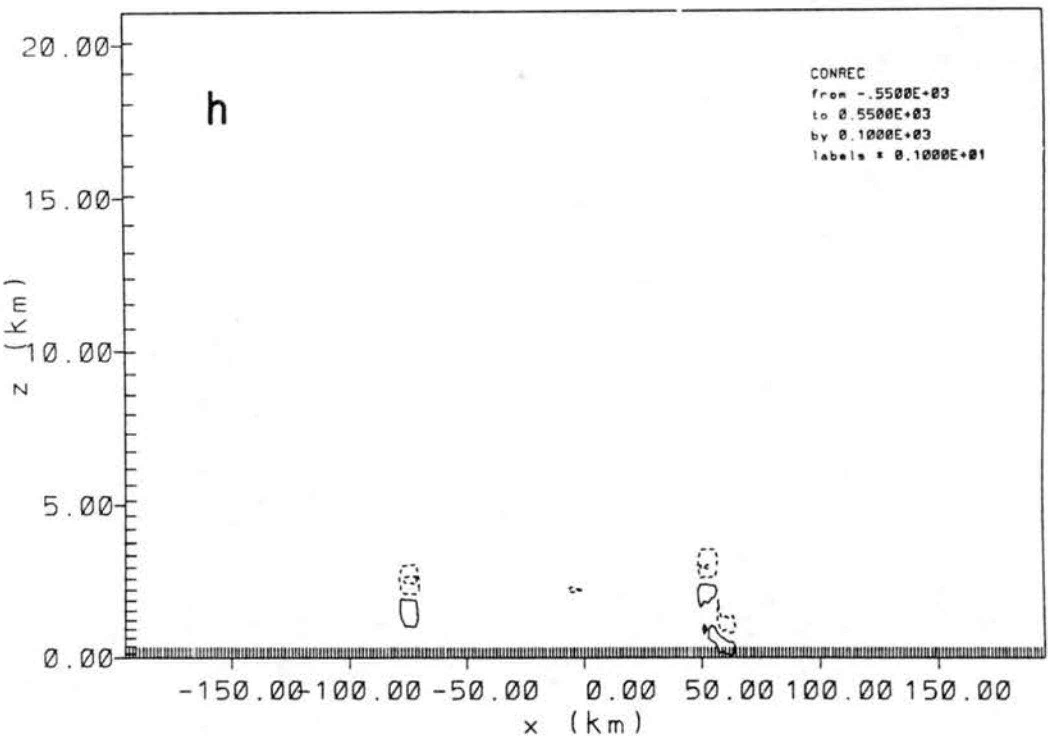

Figure 5.17: Continued.

operator is applied at scales less than the Rossby radius of deformation. Furthermore, the magnitudes of the vertical variance are also similar in magnitude between the two time periods as are the values of the eddy heating and moistening rates with a 5 km averaging scale.

The cumulus parameterization at 1400 local time

When the parameterization is run on a 5 km grid with no downdrafts and no precipitation (Figs. 5.18a - 5.18h), a two celled structure is clearly evident with this and the other three parameterization runs at 1400 local time. As discussed with the 20 km parameterization runs, this is not surprising since there is convergence and thus cumulus forcing on both the east and west propagating sea-breeze fronts. The parameterization is too robust in this case, thus prolonging the more transient cumulus events. The resolved vertical motion is three times stronger than the explicit simulation while the temperature perturbations are twice as strong. The robustness of the parameterization is indicated by peak vertical velocity variances of 120 $\frac{m^2}{s^2}$. Scalar transport through the convective cores is clearly evident in the perturbation total water mixing ratio and condensate mixing ratio fields.

As in the 20 km simulations, the decrease in peak magnitudes of the salient variables when downdrafts are added is indicated in Figs. 5.19a - 5.19h and Table 5.3. Although $\overline{w'w'}$ has increased slightly, mean vertical motion and perturbation temperature and total water mixing ratio are now in line similar to the explicit simulation.

When precipitation is added with no downdrafts (Figs. 5.20a - 5.20h), the condensate fields are more realistic. The robustness of this parameterization is indicated by $\overline{w'w'}$ values of 340 $\frac{m^2}{s^2}$ and mean vertical motions and perturbation temperatures twice as strong as the explicit simulation.

The addition of downdrafts to the precipitation simulation (Figs. 5.21a - 5.21h) indicate that several cells form on each sea breeze front. Peak values are similar to the no downdraft case.

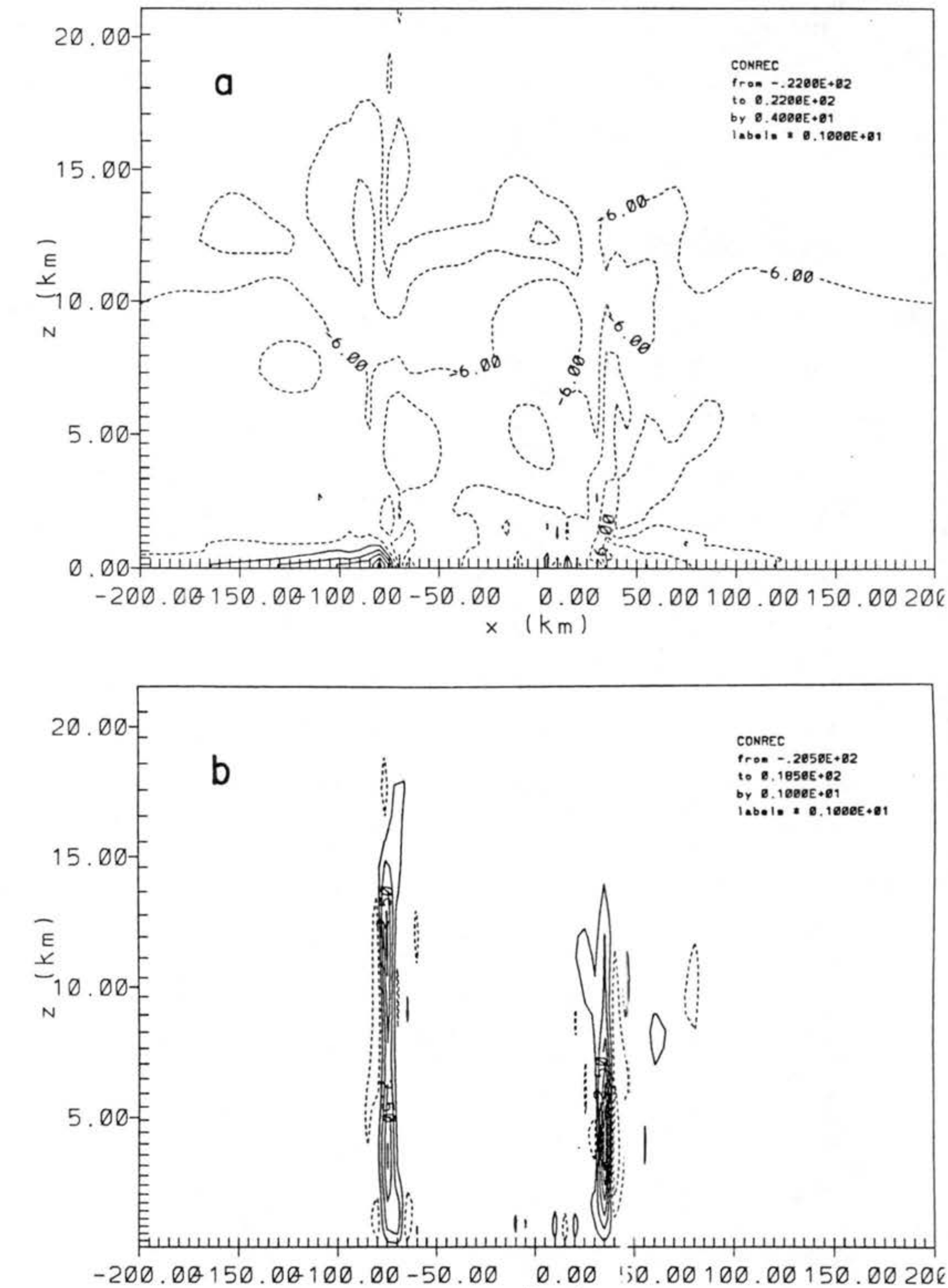

Figure 5.18: As in Figs. 5.6a-h except for the 5 km parameterized simulation without downdrafts and without precipitation.

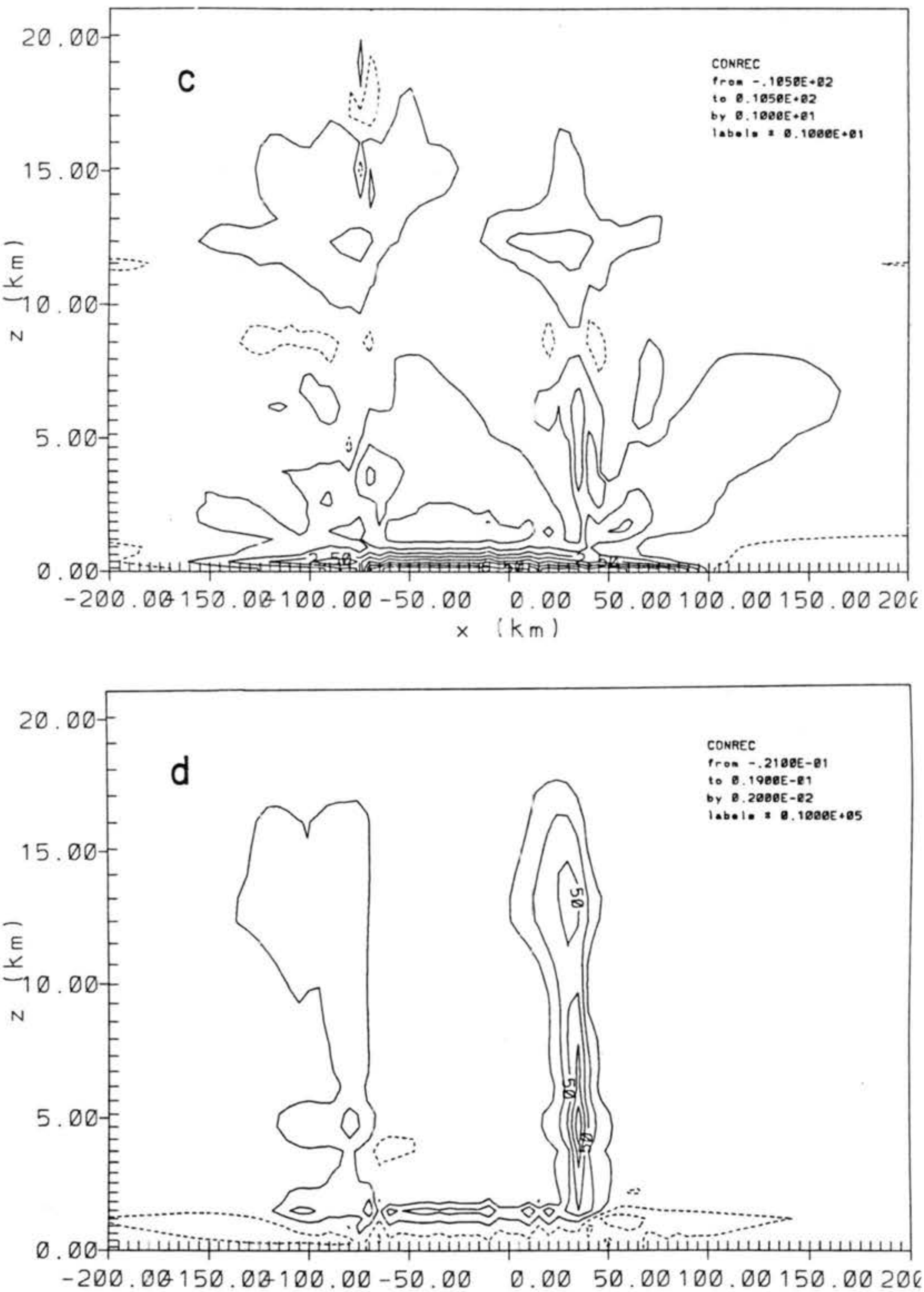

Figure 5.18: Continued.

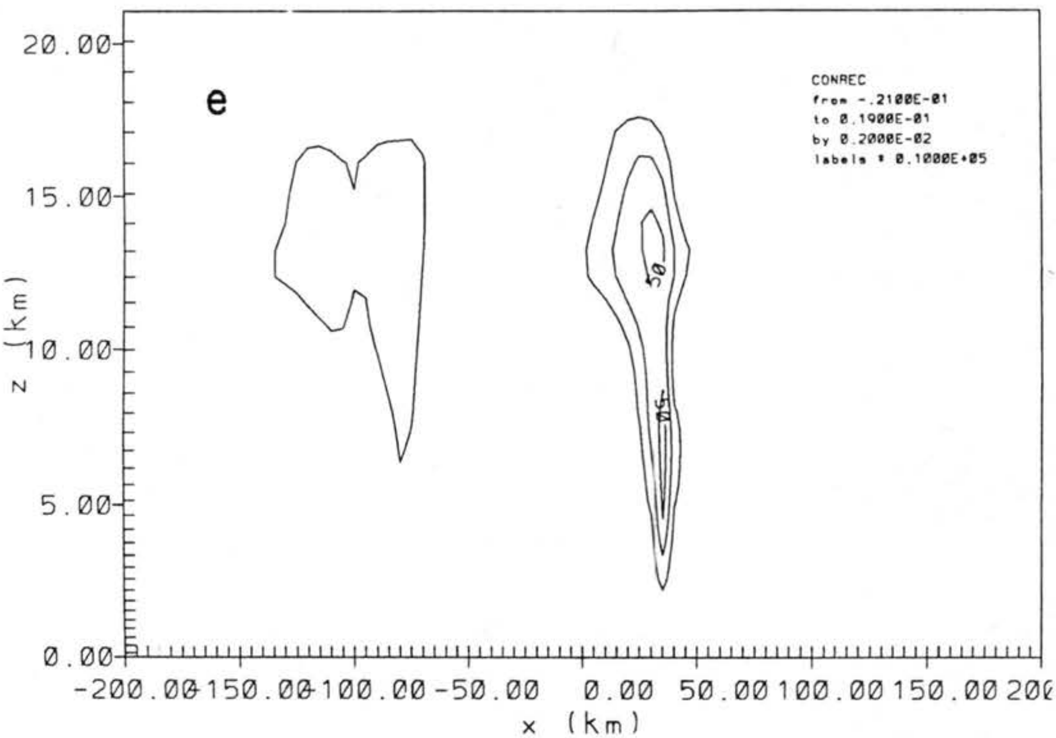

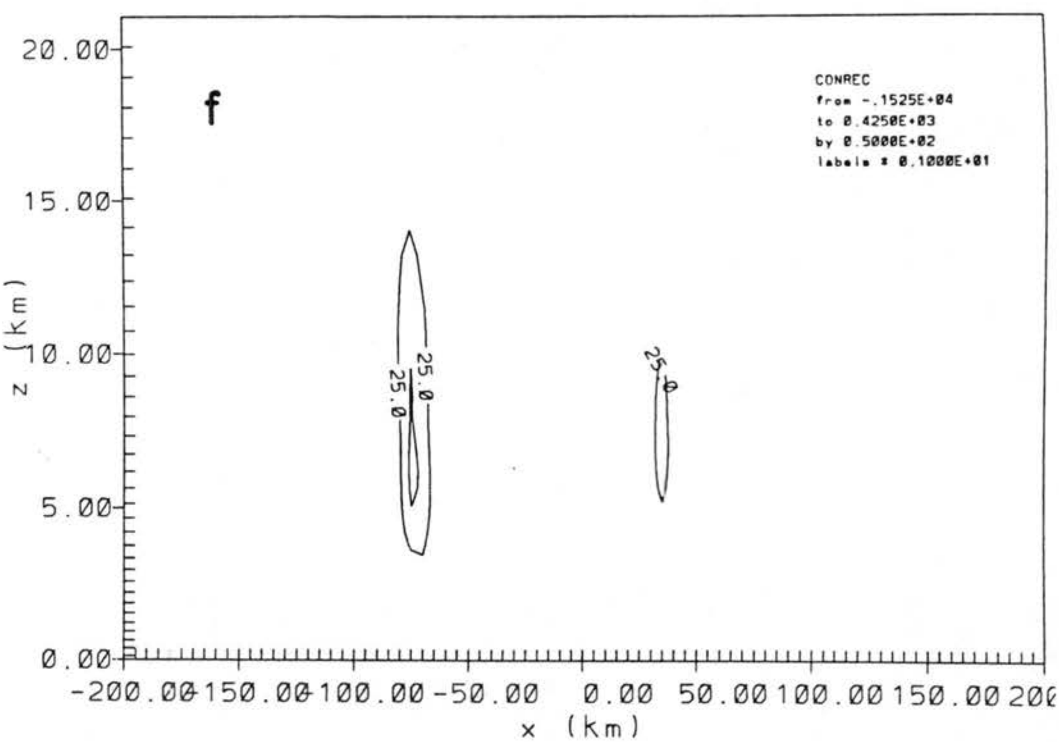

Figure 5.18: Continued.

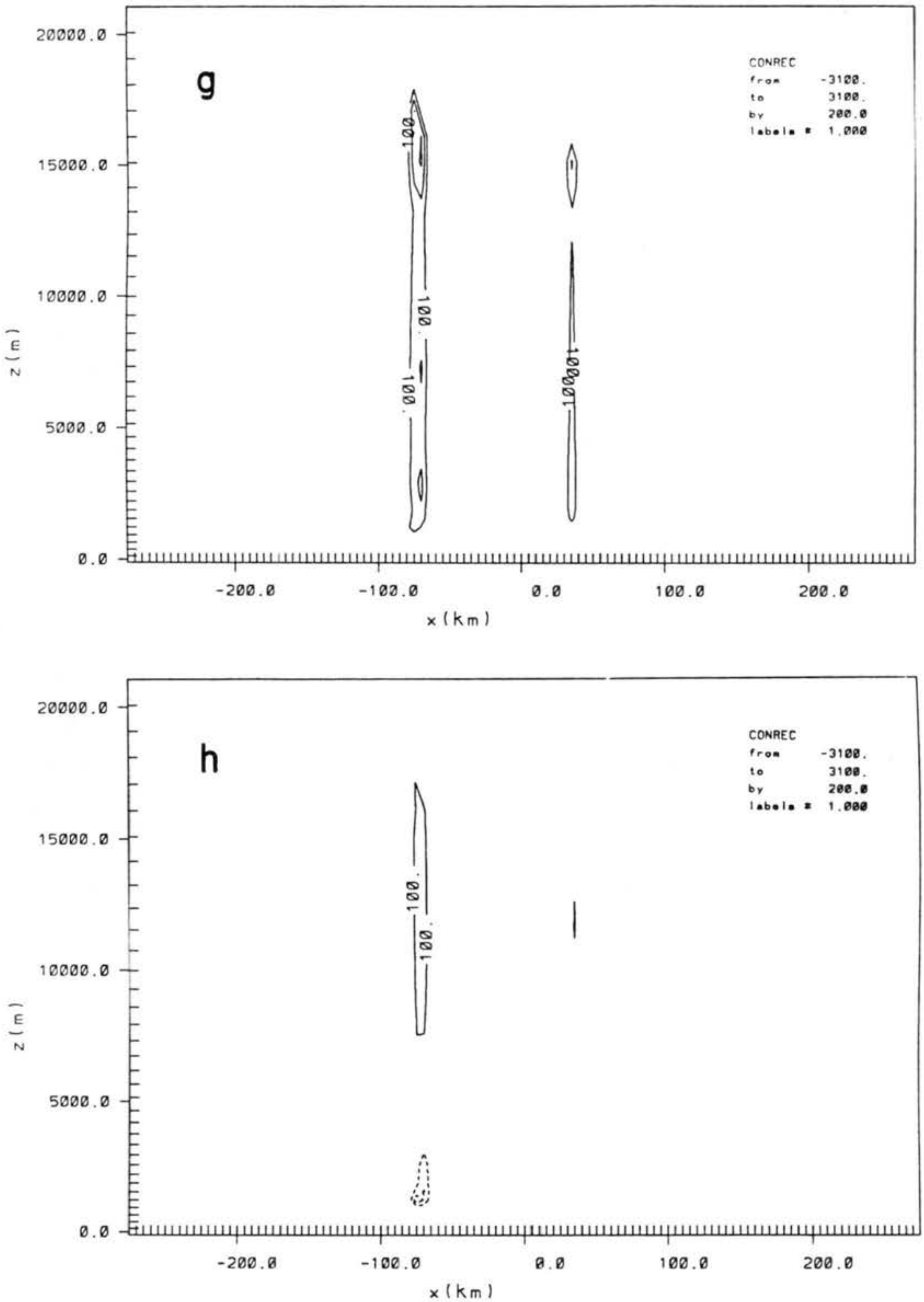

Figure 5.18: Continued.

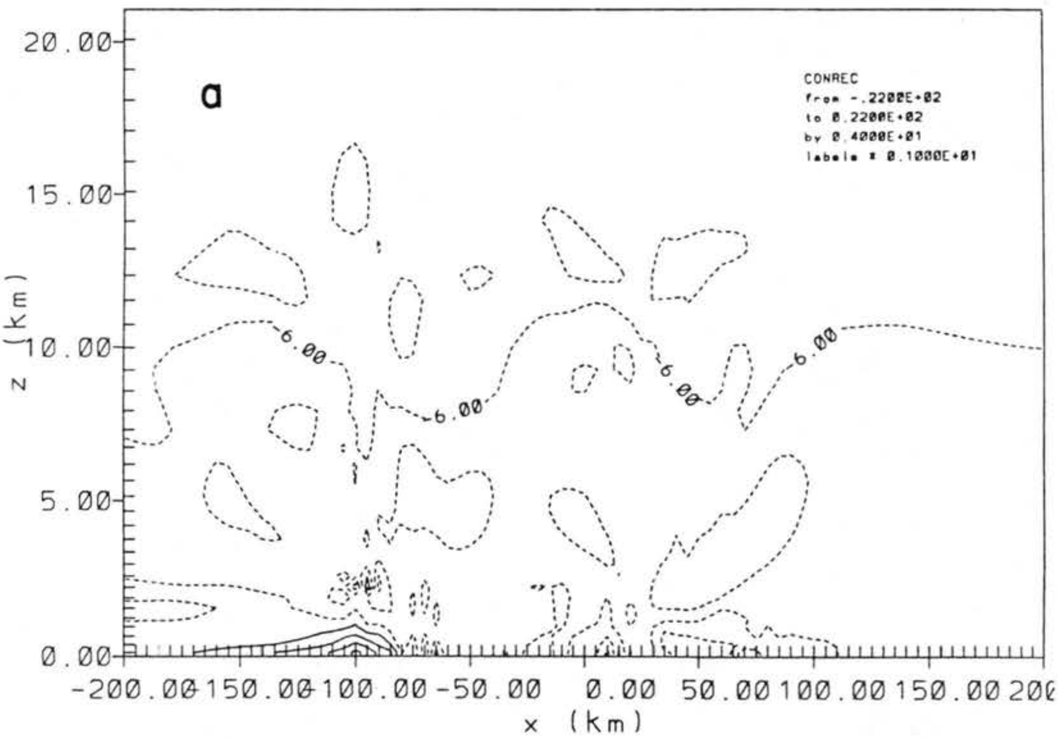

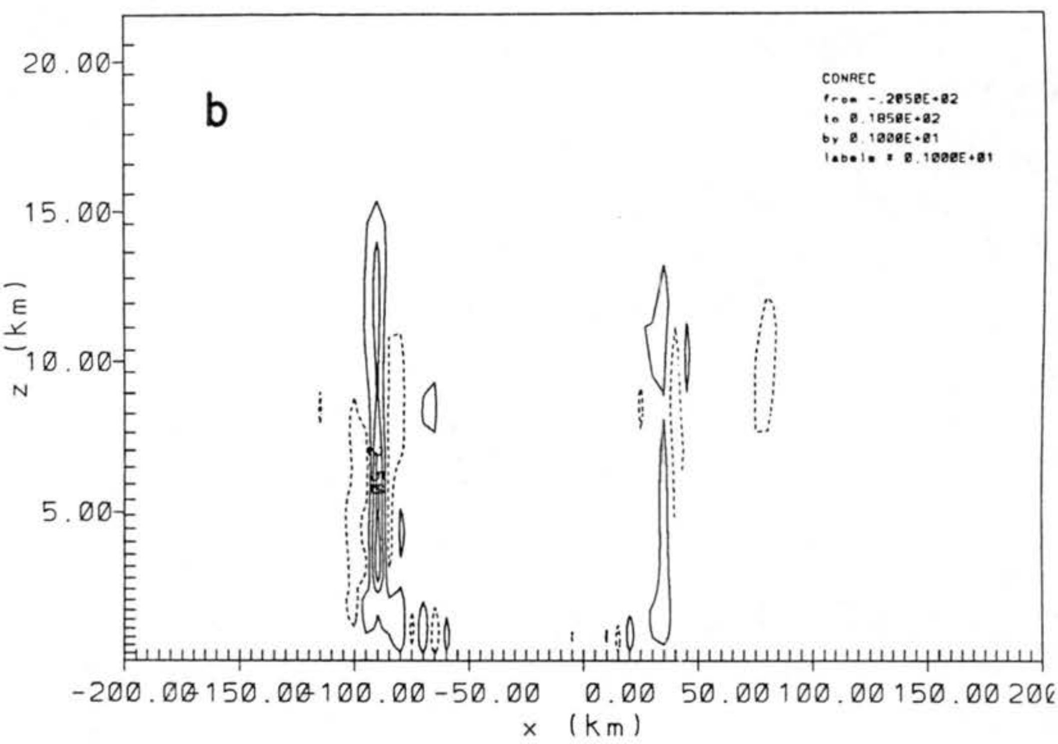

Figure 5.19: As in Figs. 5.6a-h except for the 5 km parameterized simulation with downdrafts and without precipitation.

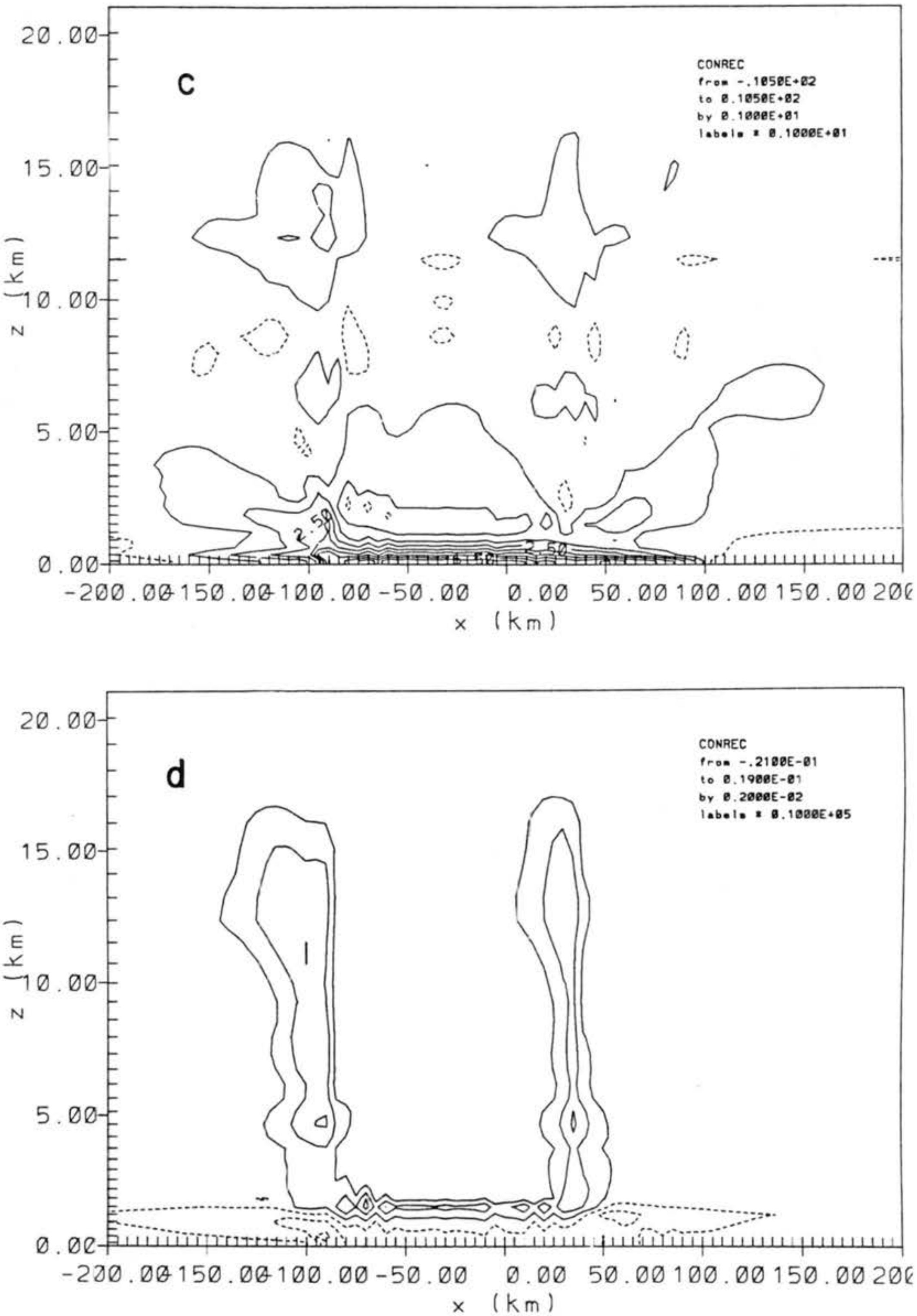

Figure 5.19: Continued.

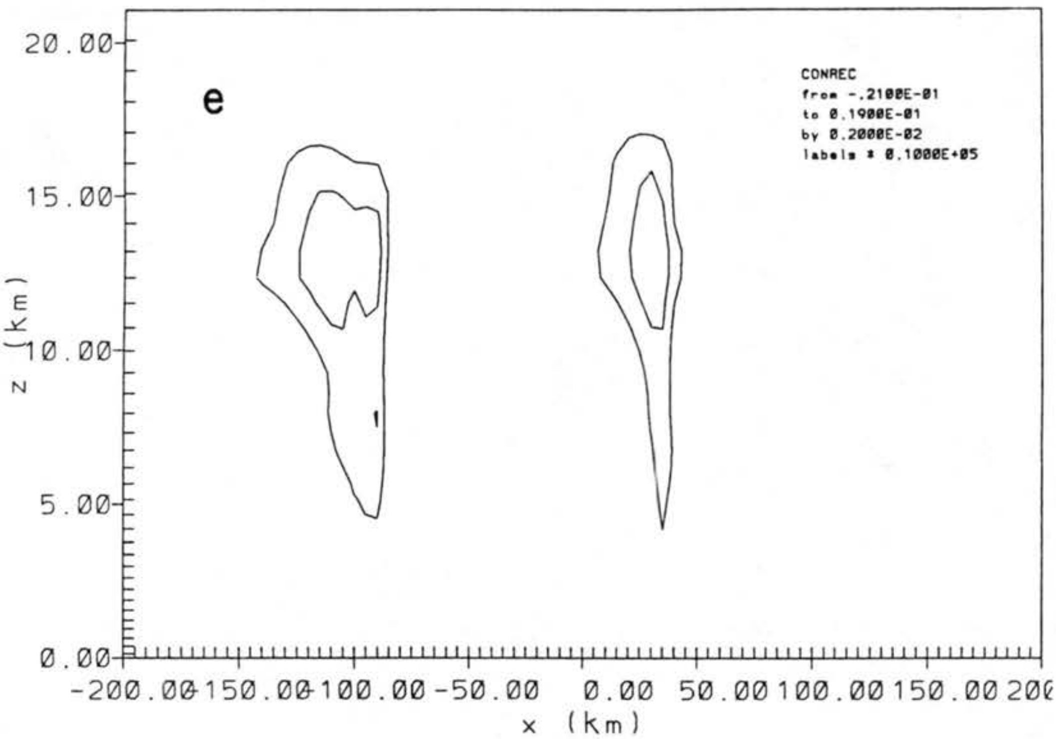

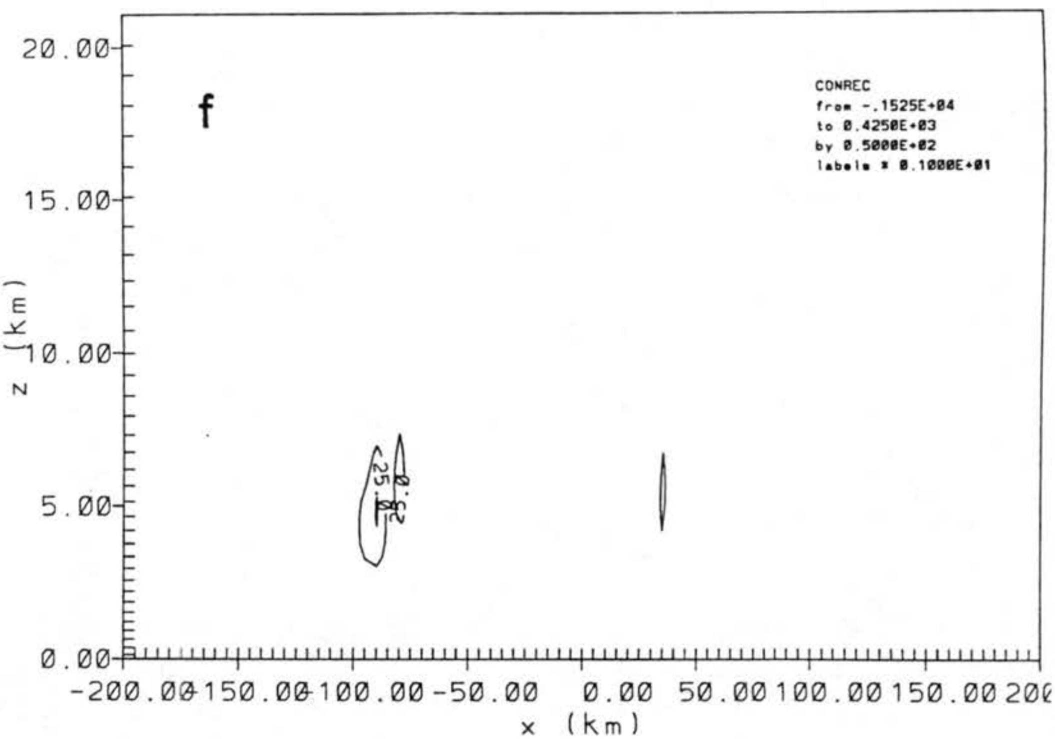

Figure 5.19: Continued.

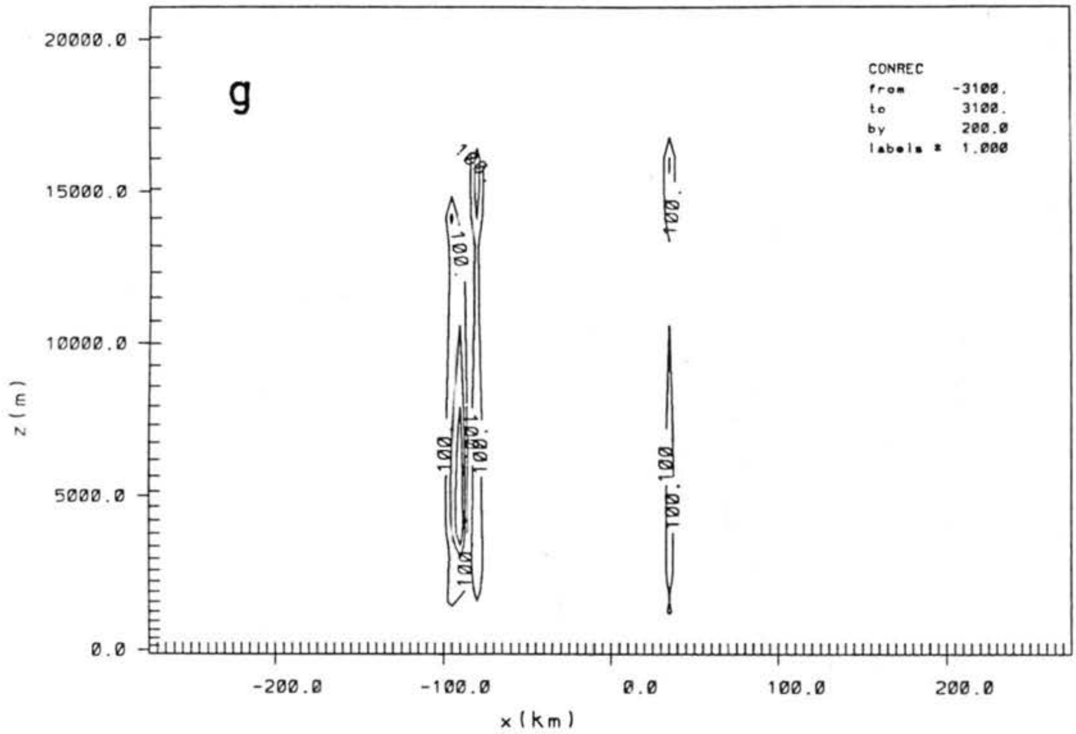

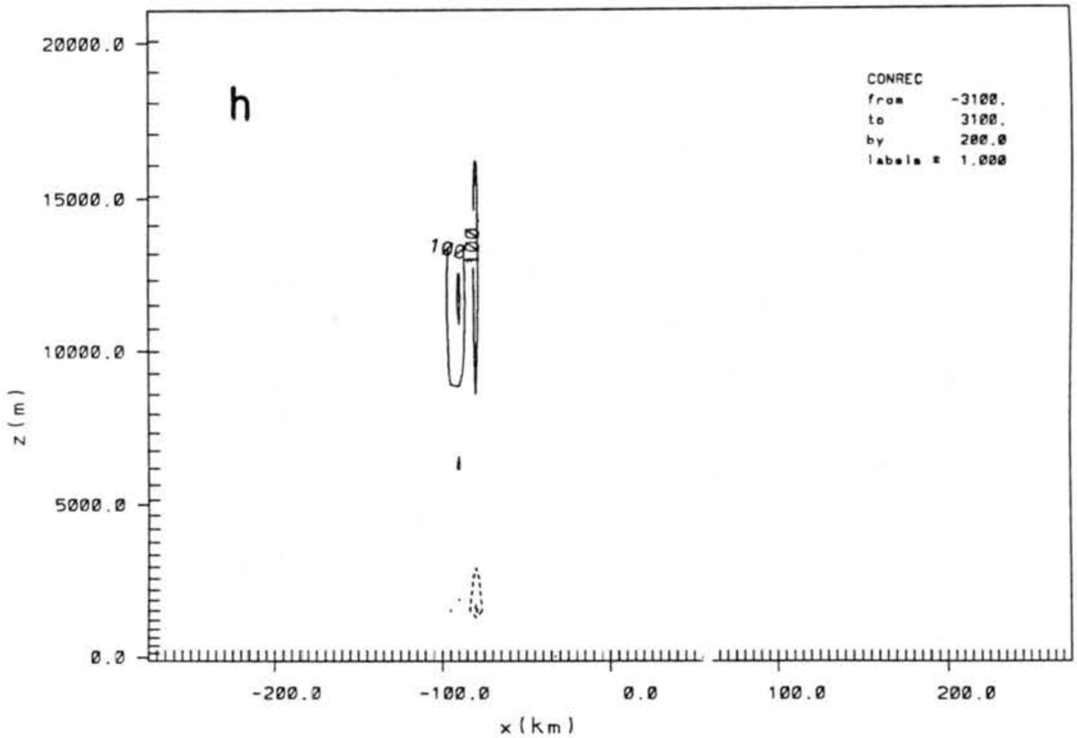

Figure 5.19: Continued.

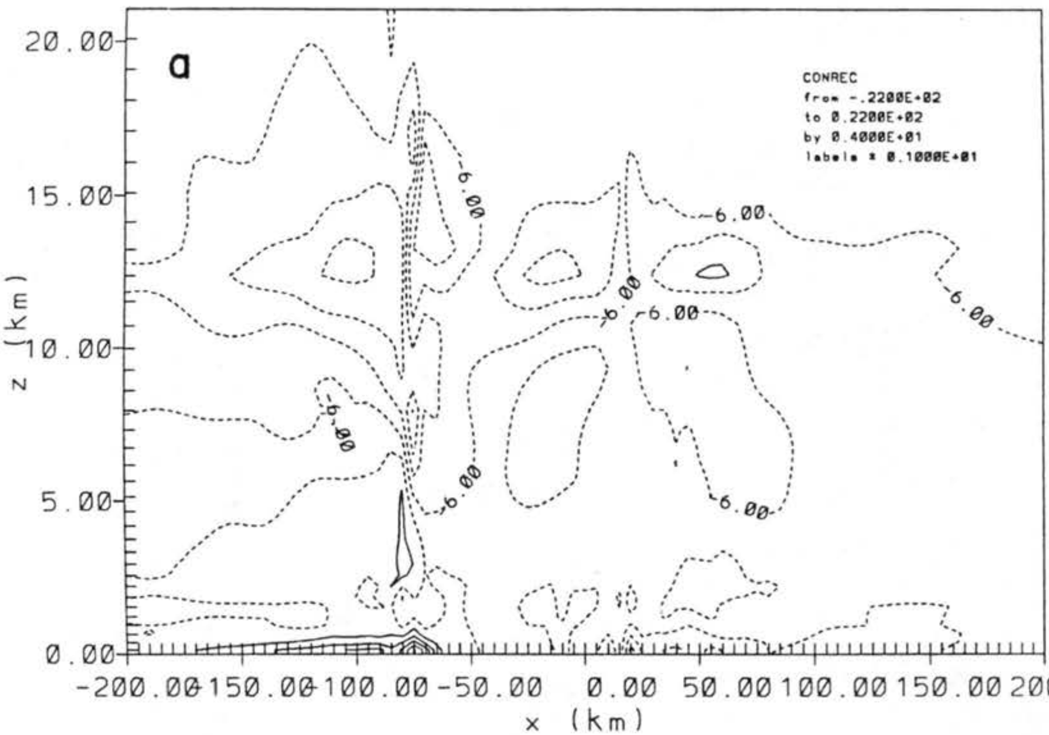

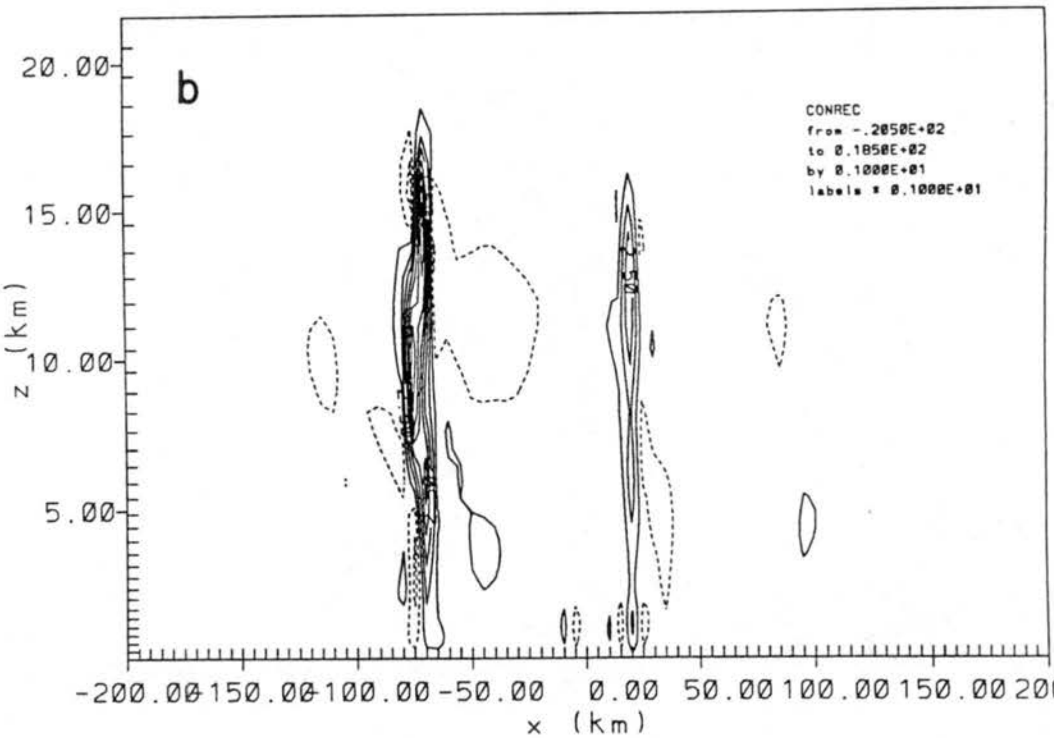

Figure 5.20: As in Figs. 5.6a-h except for the 5 km parameterized simulation without downdrafts and with precipitation.

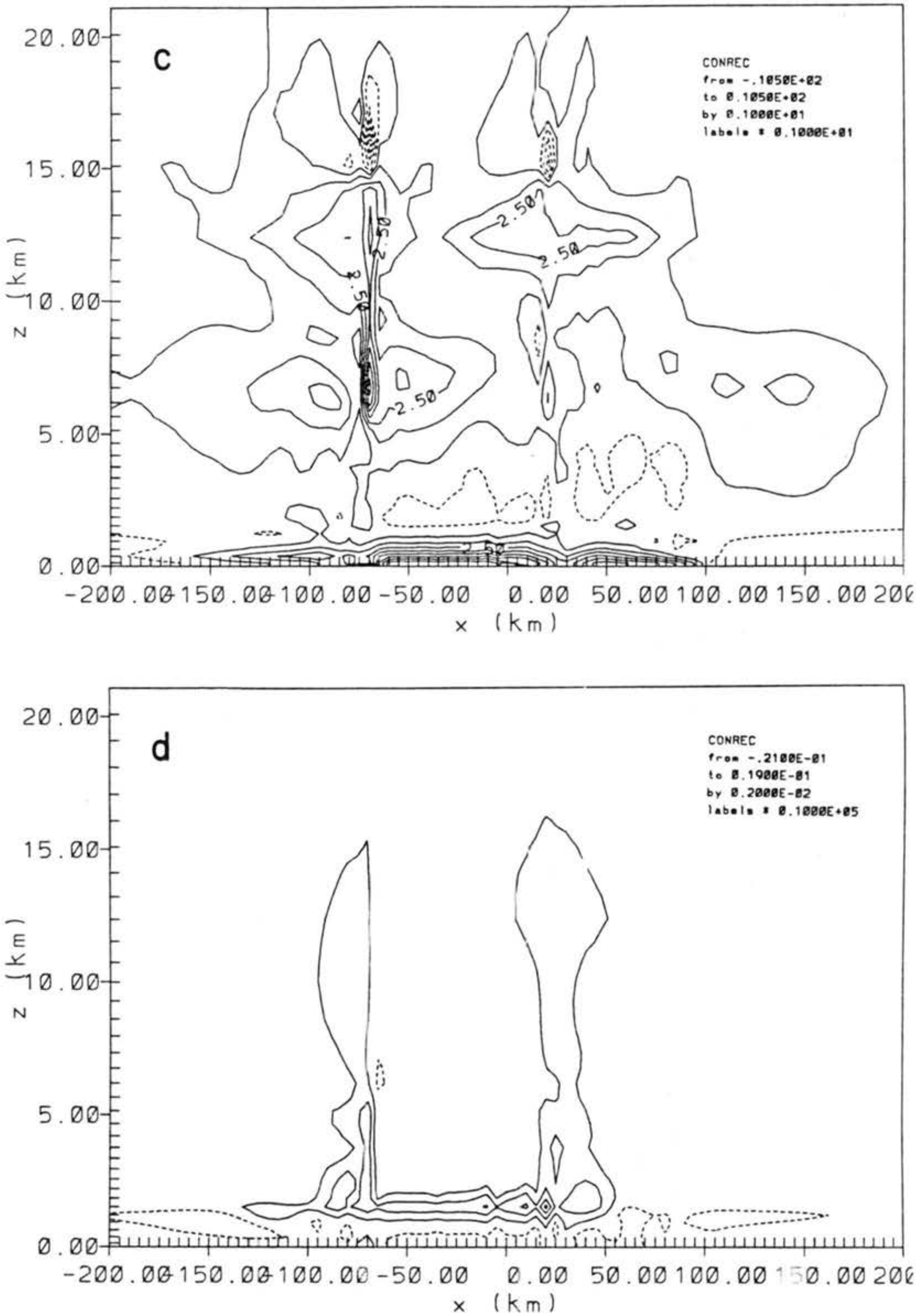

Figure 5.20: Continued.

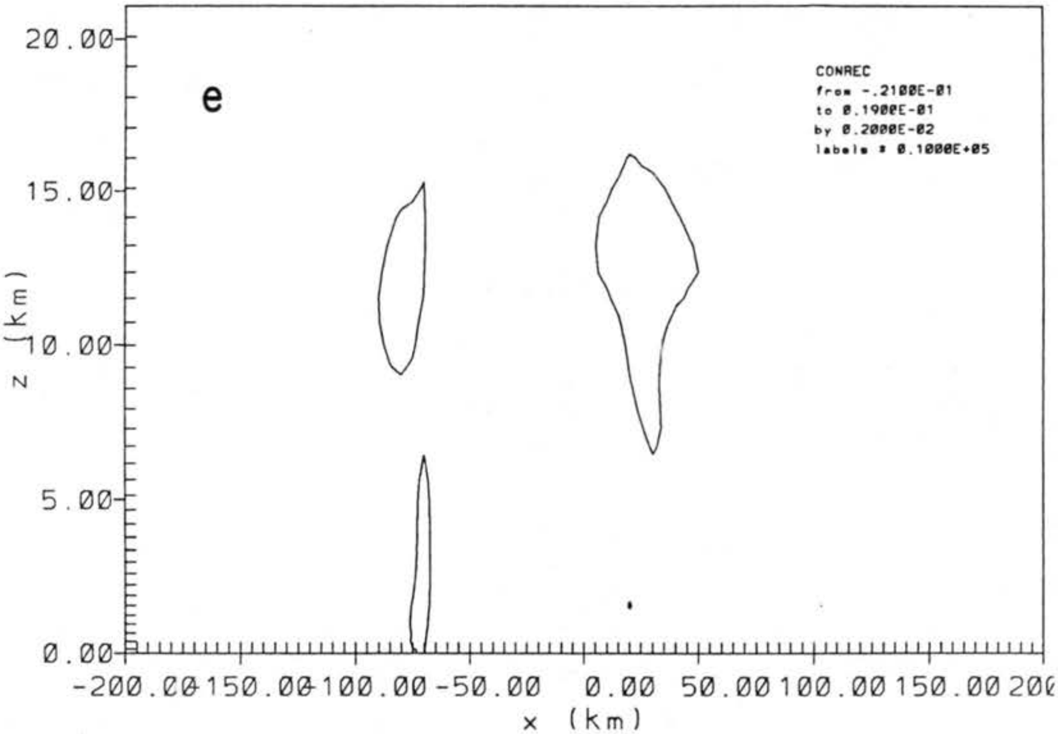

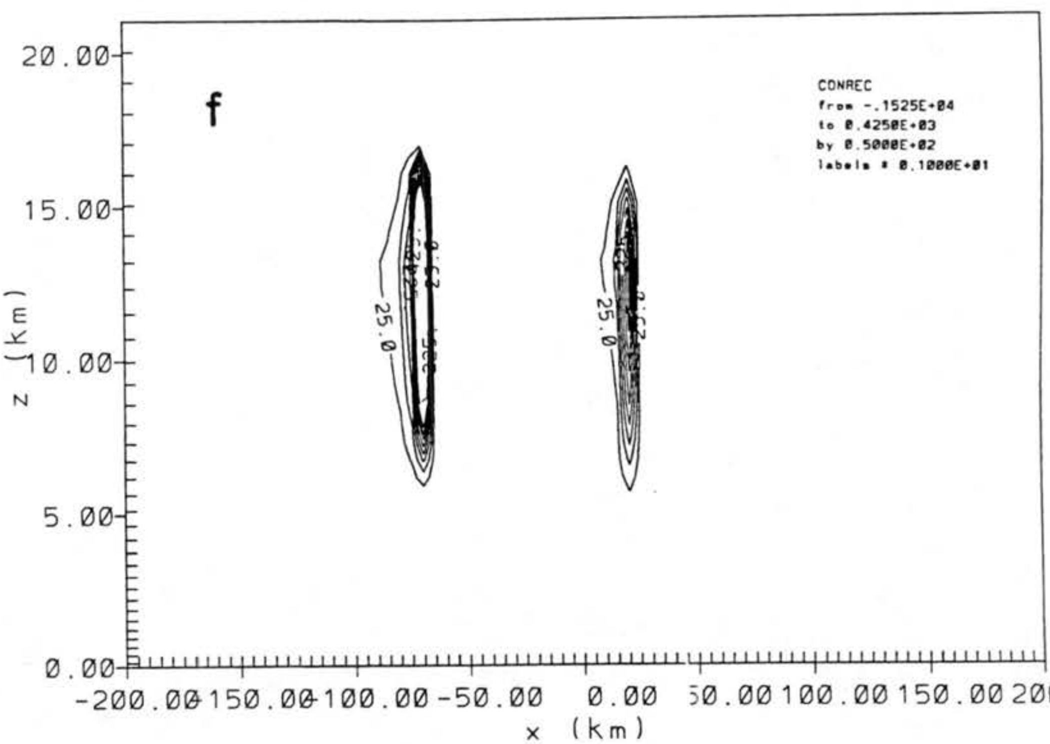

Figure 5.20: Continued.

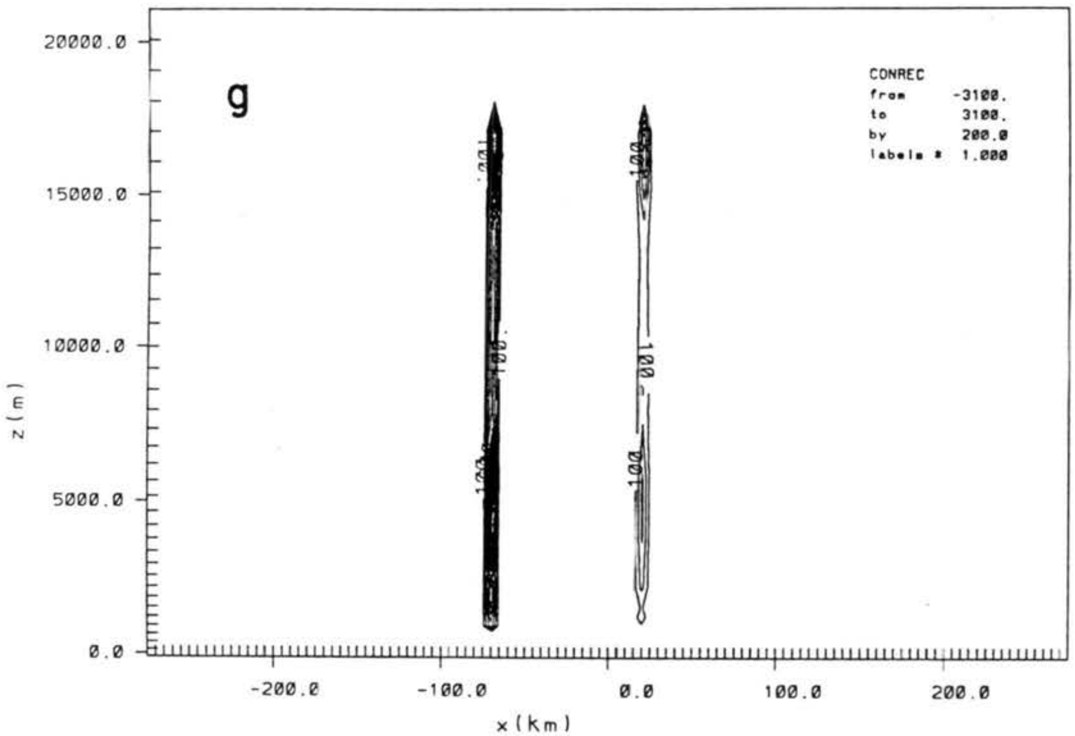

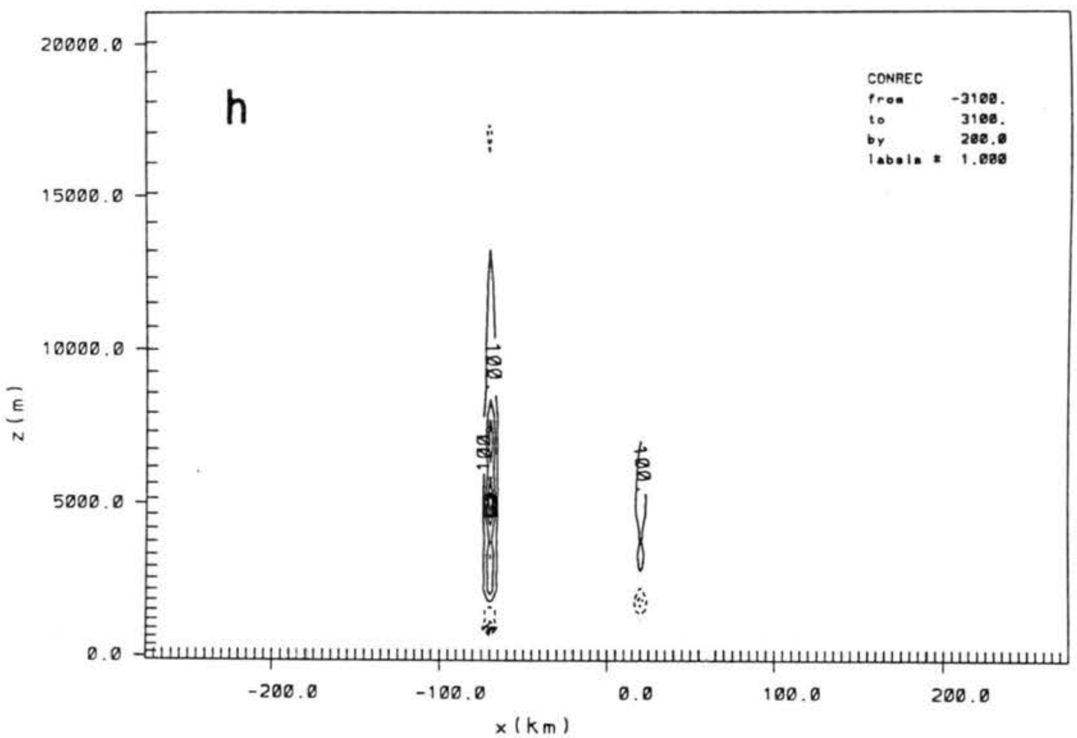

Figure 5.20: Continued.

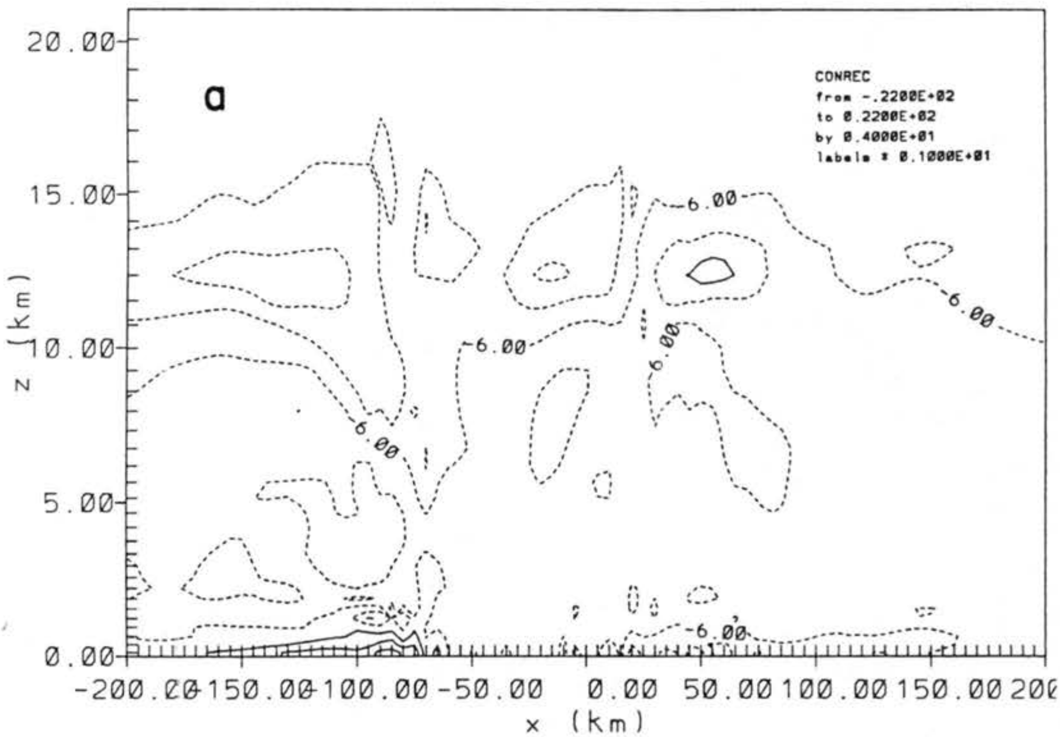

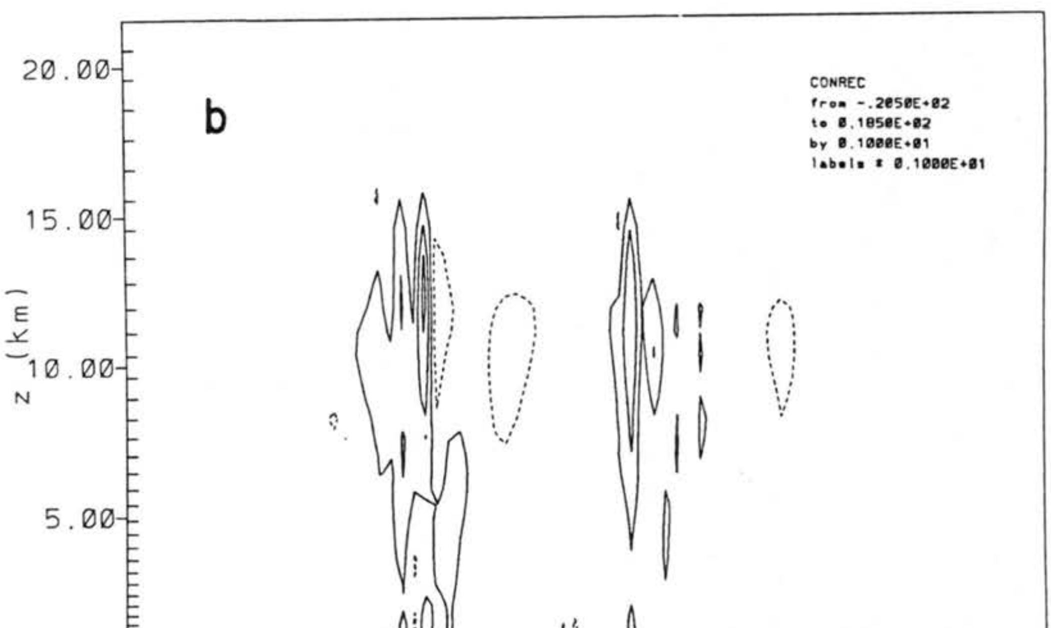

Figure 5.21: As in Figs. 5.6a-h except for the 5 km parameterized simulation with downdrafts and with precipitation.

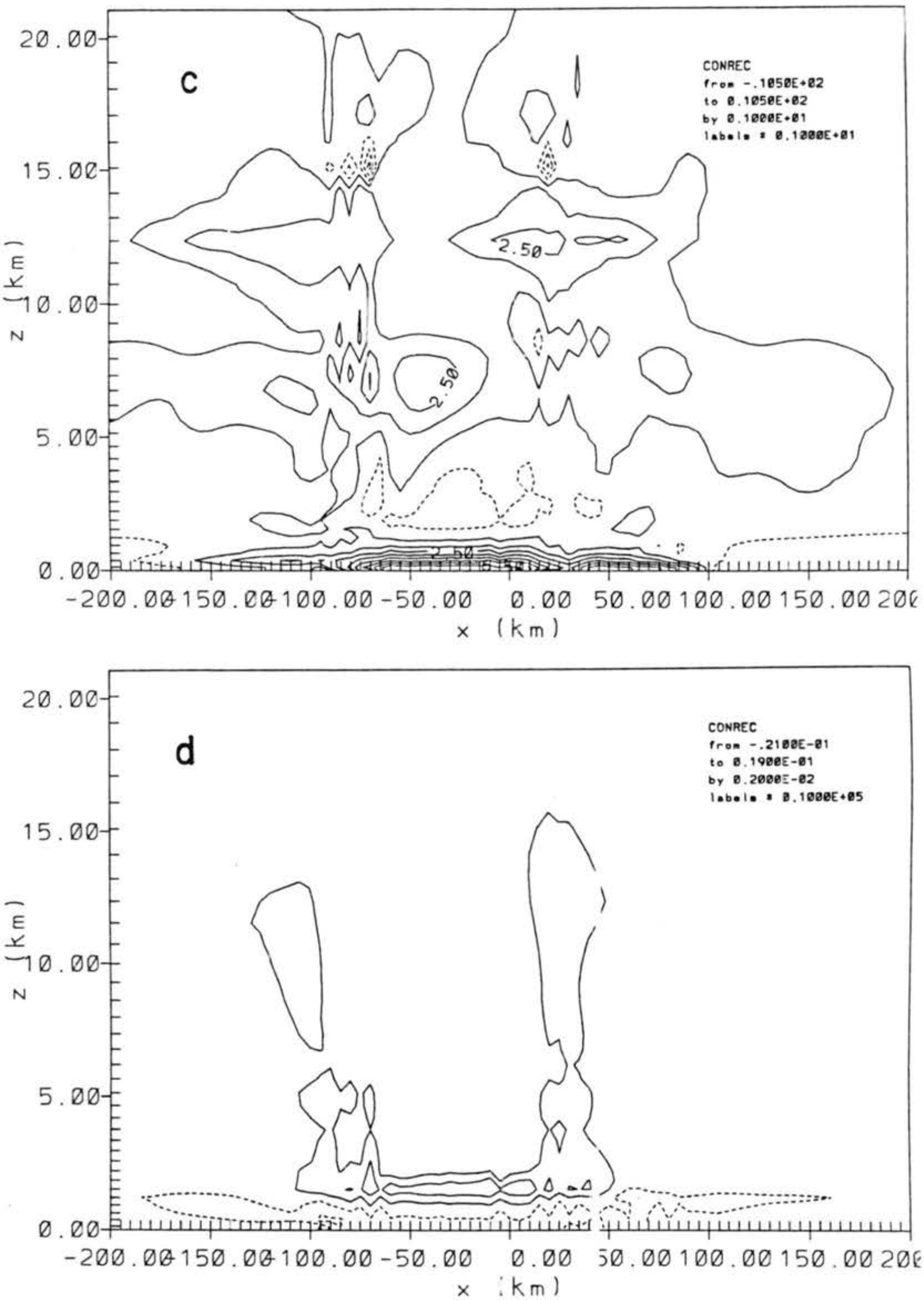

Figure 5.21: Continued.

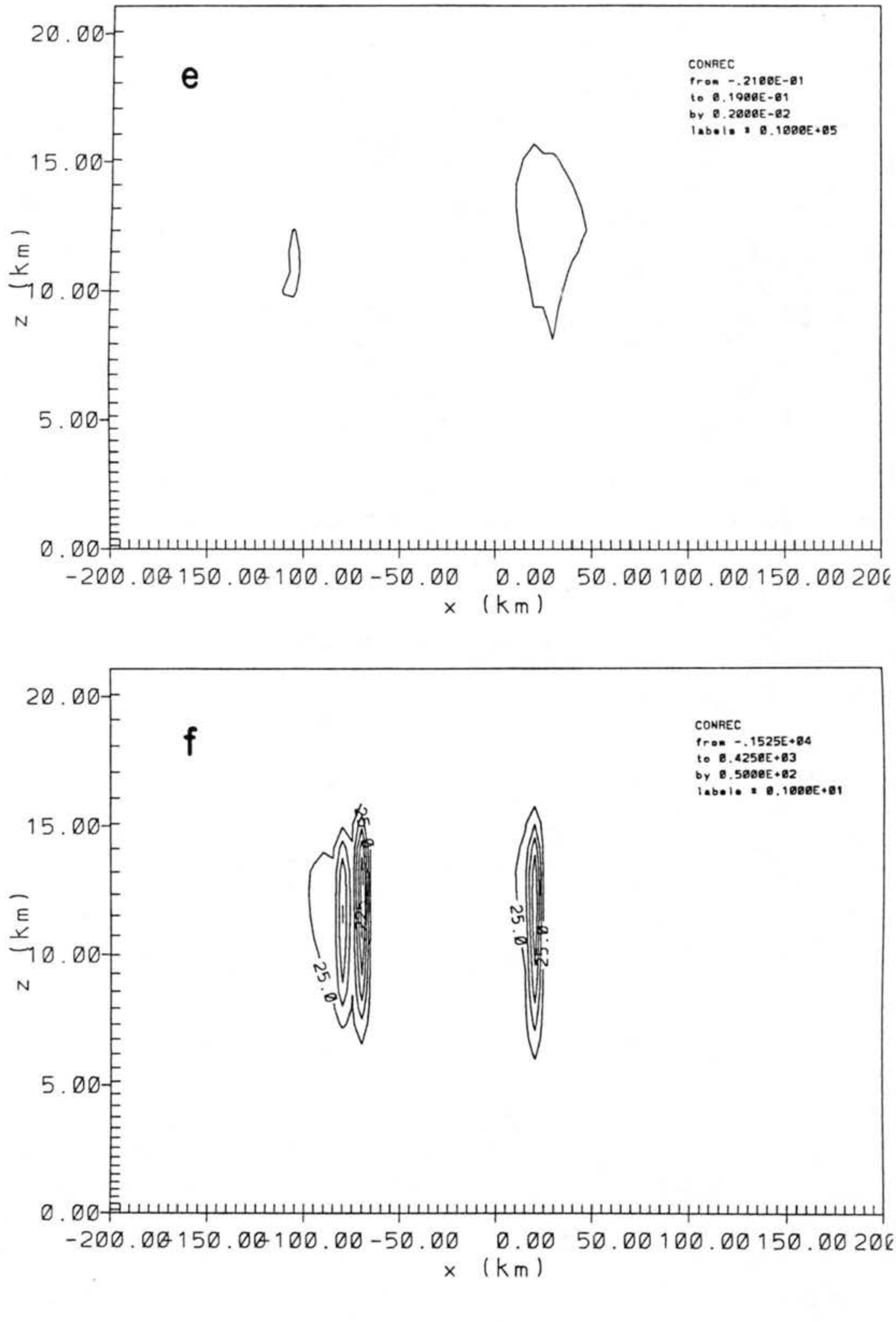

Figure 5.21: Continued.

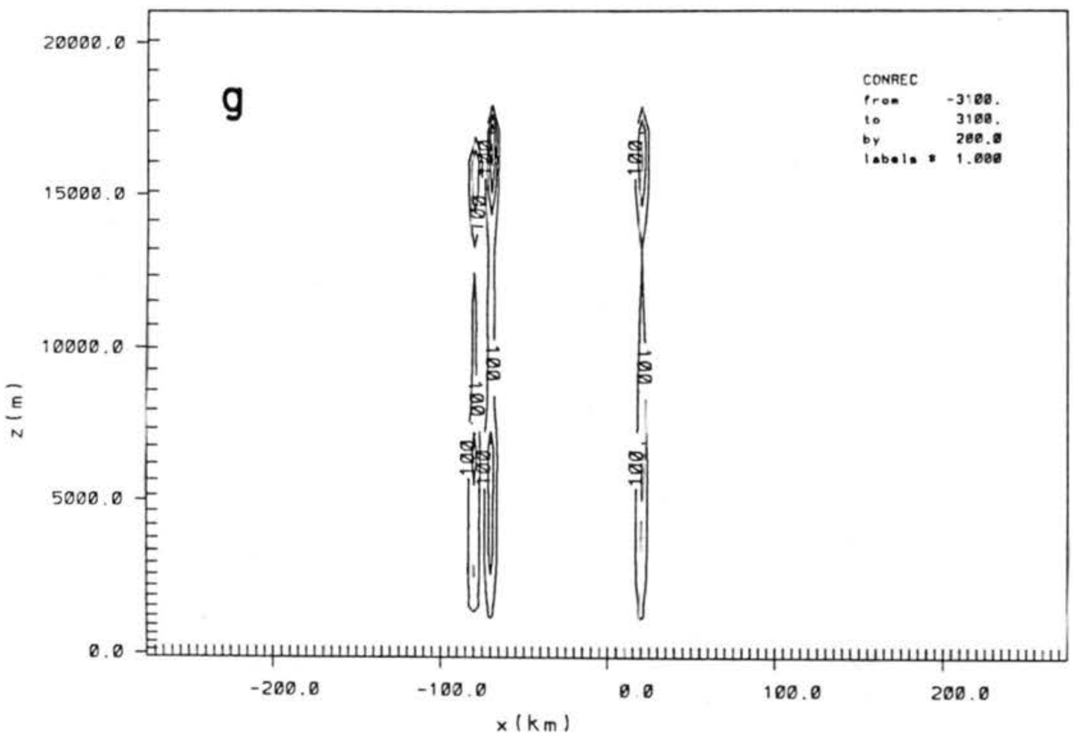

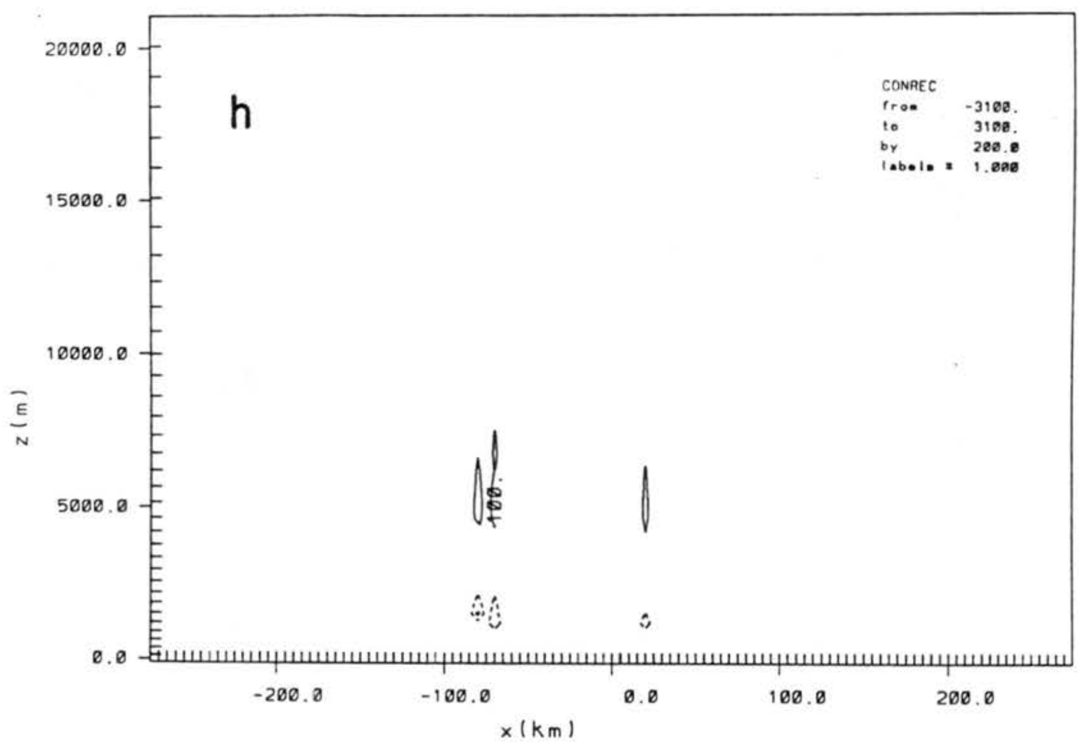

Figure 5.21: Continued.

The explicit simulation at 1700 local time

Finally, the explicit simulation three hours later (Figs. 5.22a - 5.22h) is examined. As at 1400 local time, the magnitudes of the 5 km-averaged fields are higher than the 20 km averaged fields except for the temperature perturbations, as indicated by comparing Table 5.4 to Table 5.2 and the divergence fields, seen by comparing Figs. 5.22a and 5.11a. These are similar due to the mass rearrangement resulting from the geostrophic adjustment process. The vertical variance is also similar confirming the notion that this variable is less scale dependent than the mean vertical motion.

Table 5.4: As in Table 5.1 except for the 5 km simulation at 1700 local time.

Simulation	W (m/s)	T (K)	Rt (g/kg)	COND (g/kg)	$\overline{w'w'}$ ($\frac{m^2}{s^2}$)
explicit	9.3	2.5	7.0	7.0	2.8
nodn/nomc	3.0	2.4	9.9	8.5	72.
dn/nomc	5.5	2.2	5.6	4.8	1300
nodn/ mc	6.0	2.8	9.9	9.0	63.
dn/ mc	1.6	3.0	5.4	2.3	110

The cumulus parameterization at 1700 local time

In Figs. 5.23a - 5.23h, the appearance of a single parameterized cell is evident; as in the 20 km parameterized simulation, the 5 km parameterization with no precipitation and no downdrafts place this cell about 40 km too far east. Mean vertical motion is half as strong as the explicit simulation and the temperature perturbations occupy too large a horizontal scale. However the deep transport scalars in the parameterized cumulus cores is apparent. In addition, the vertical variance is now similar, although slightly high, as compared to the explicit simulation.

The addition of downdrafts, shown in Figs. 5.24a - 5.24h, again appear to anchor the parameterized cumulus convection so that a single cell does not form near the western half of the peninsula at this later time. Instead, the parameterized cumulus appear to remain near where they were first initiated. All peak values are lower compared to the no downdraft simulation except vertical variance which increases slightly.

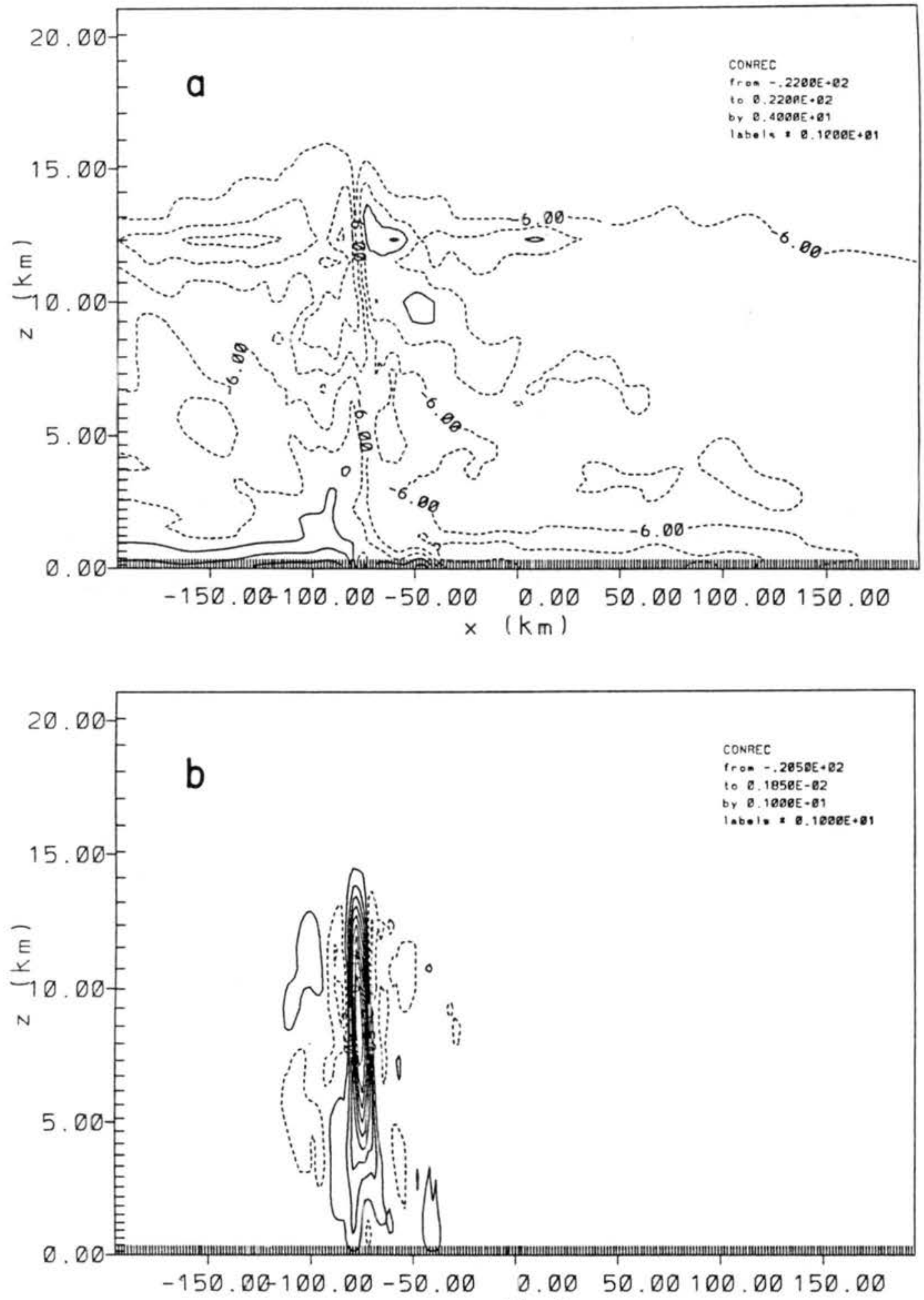

Figure 5.22: As in Figs. 5.6a-h except for the 5 km running averages of the explicit simulation at 1700 local time.

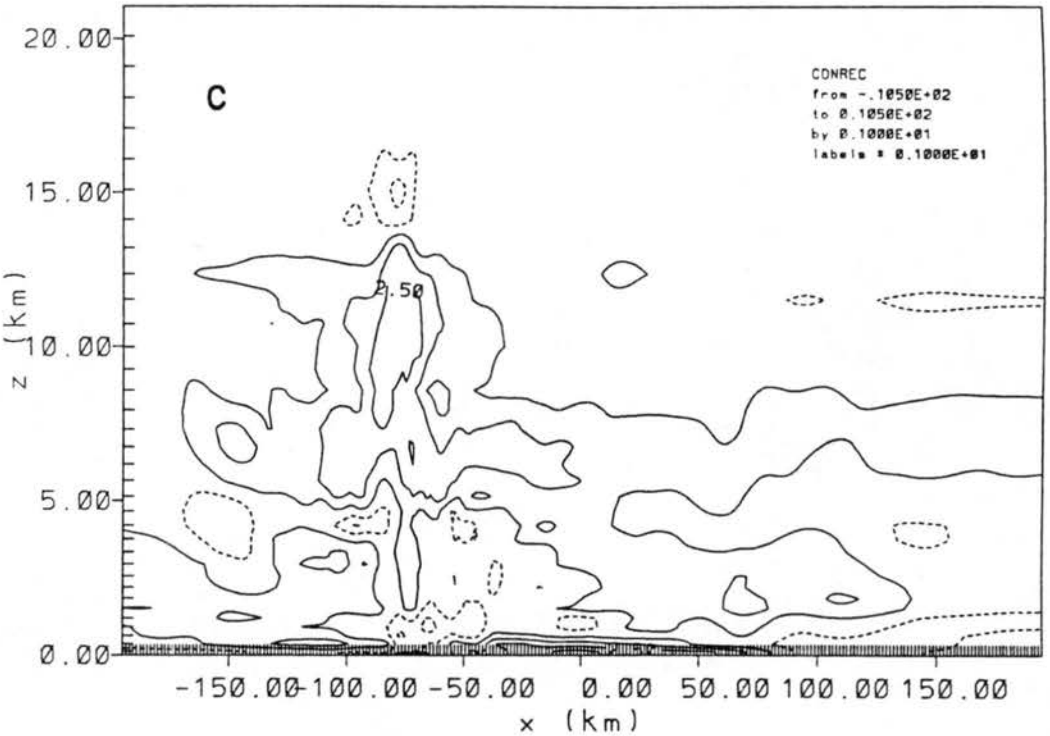

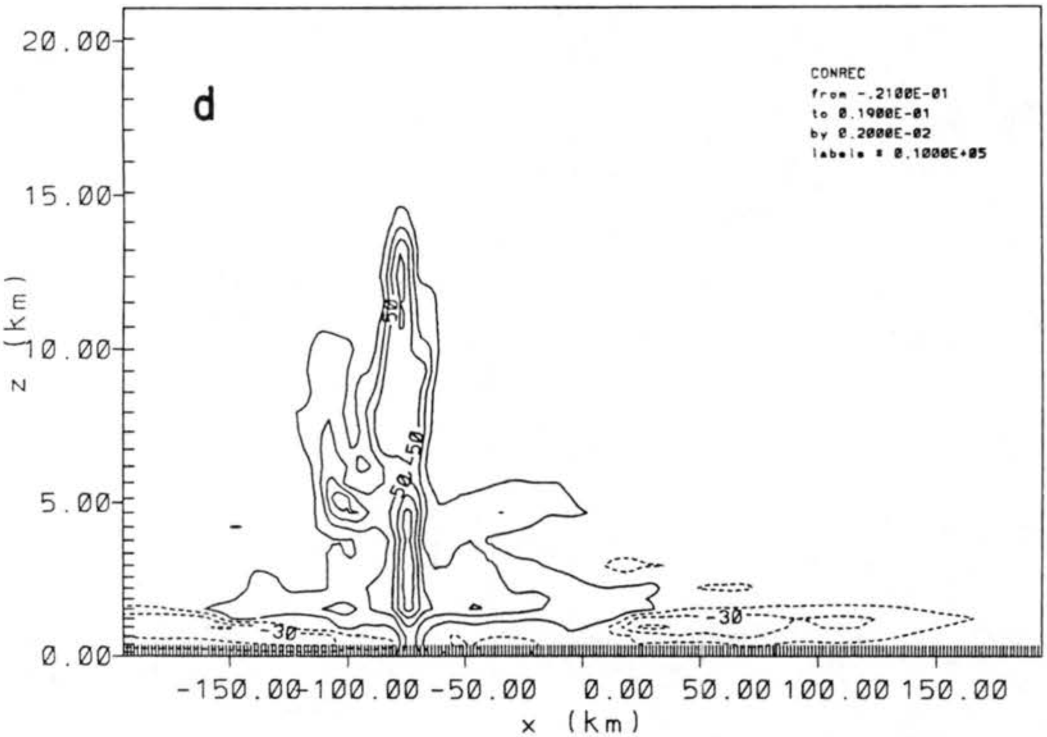

Figure 5.22: Continued.

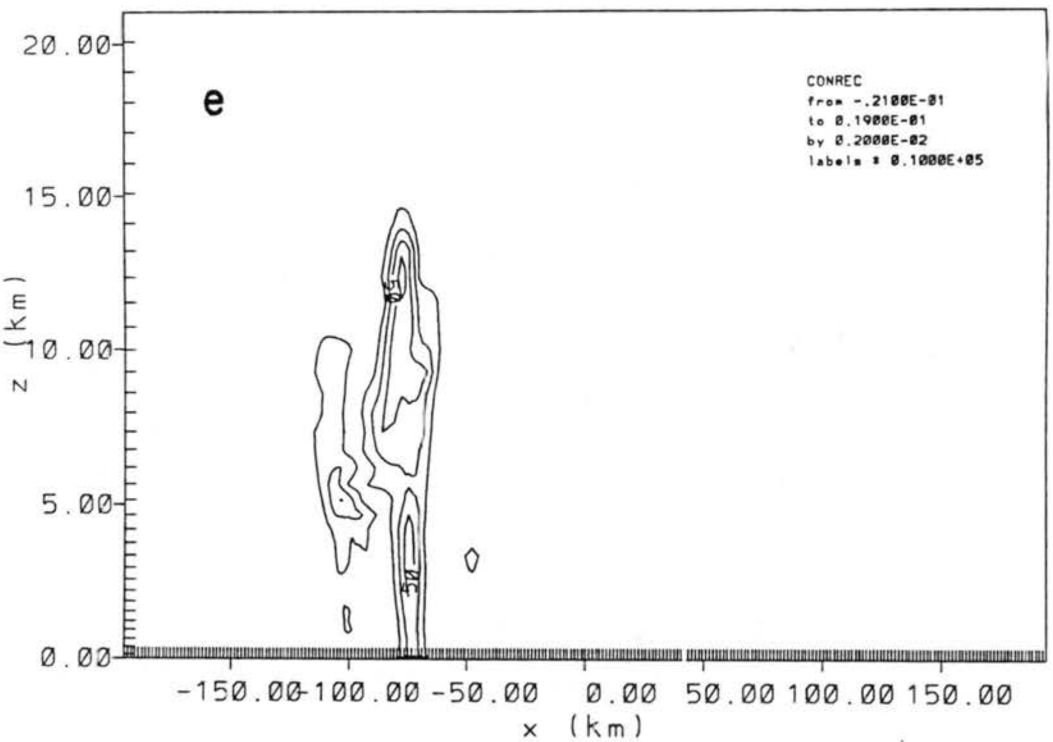

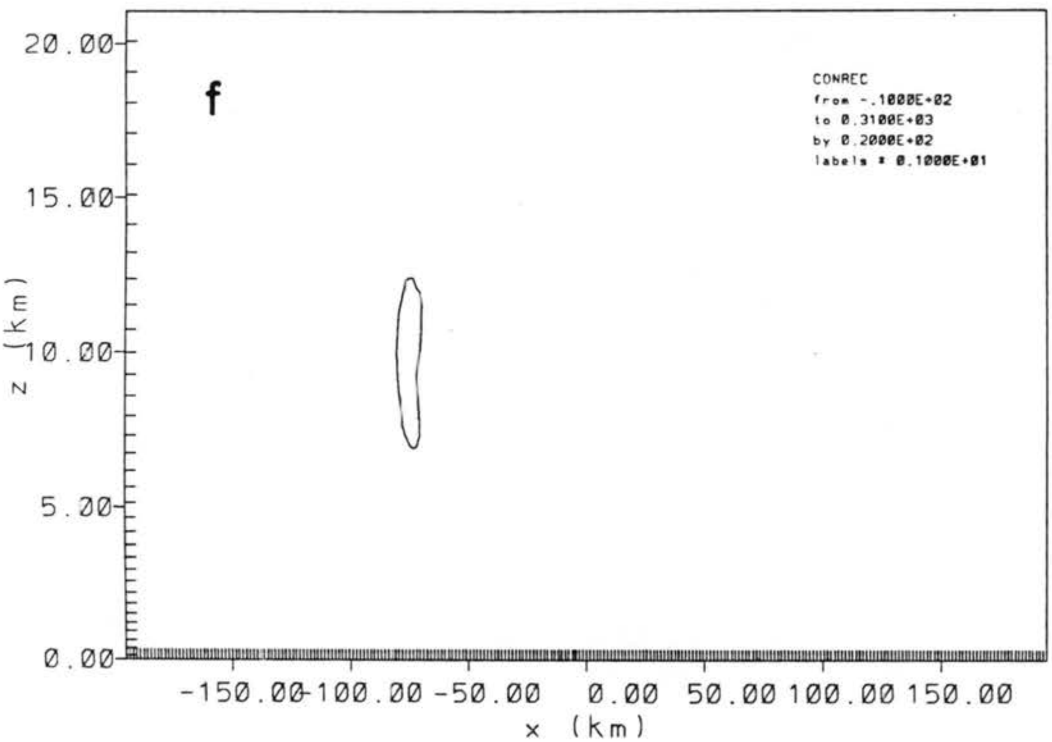

Figure 5.22: Continued.

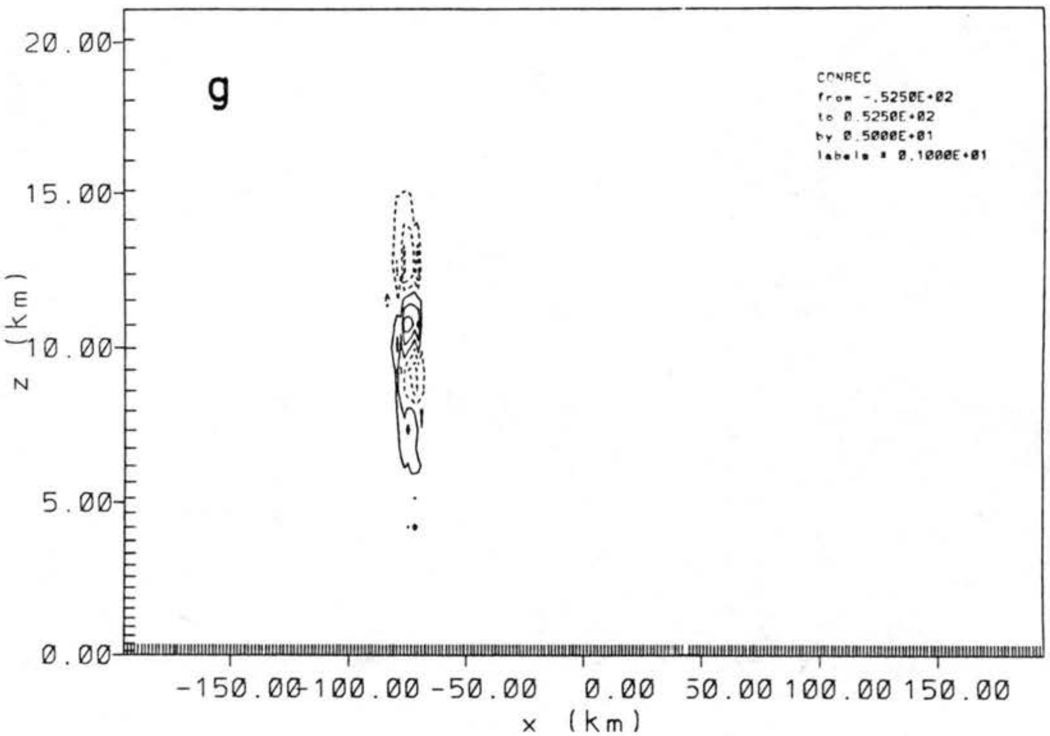

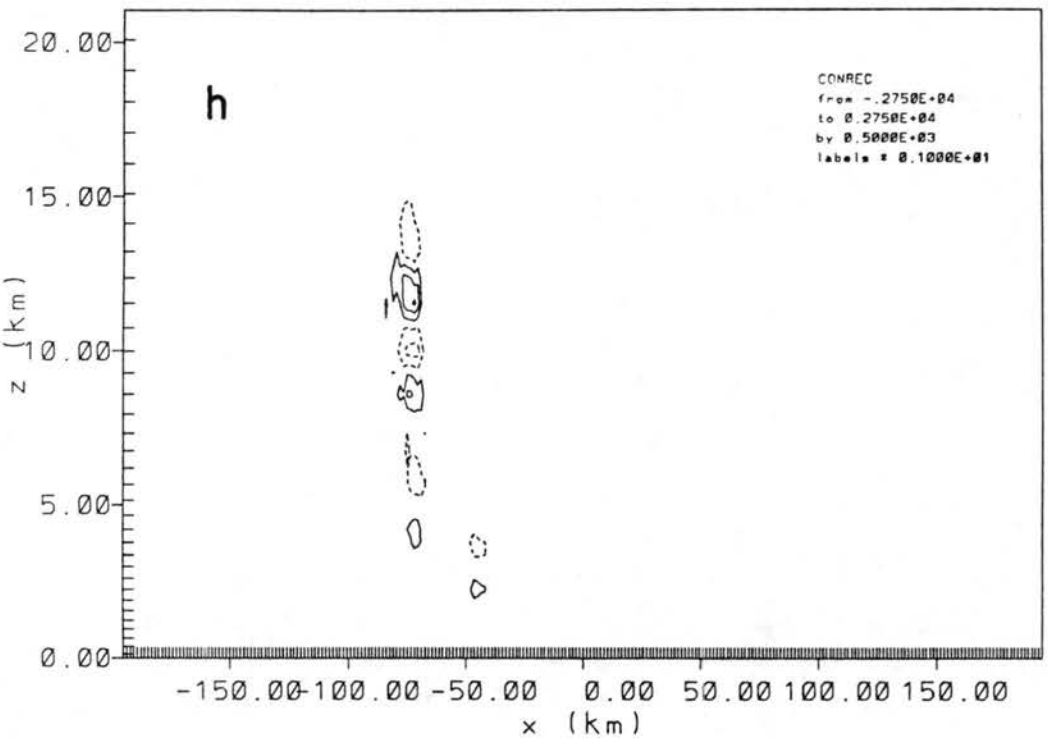

Figure 5.22: Continued.

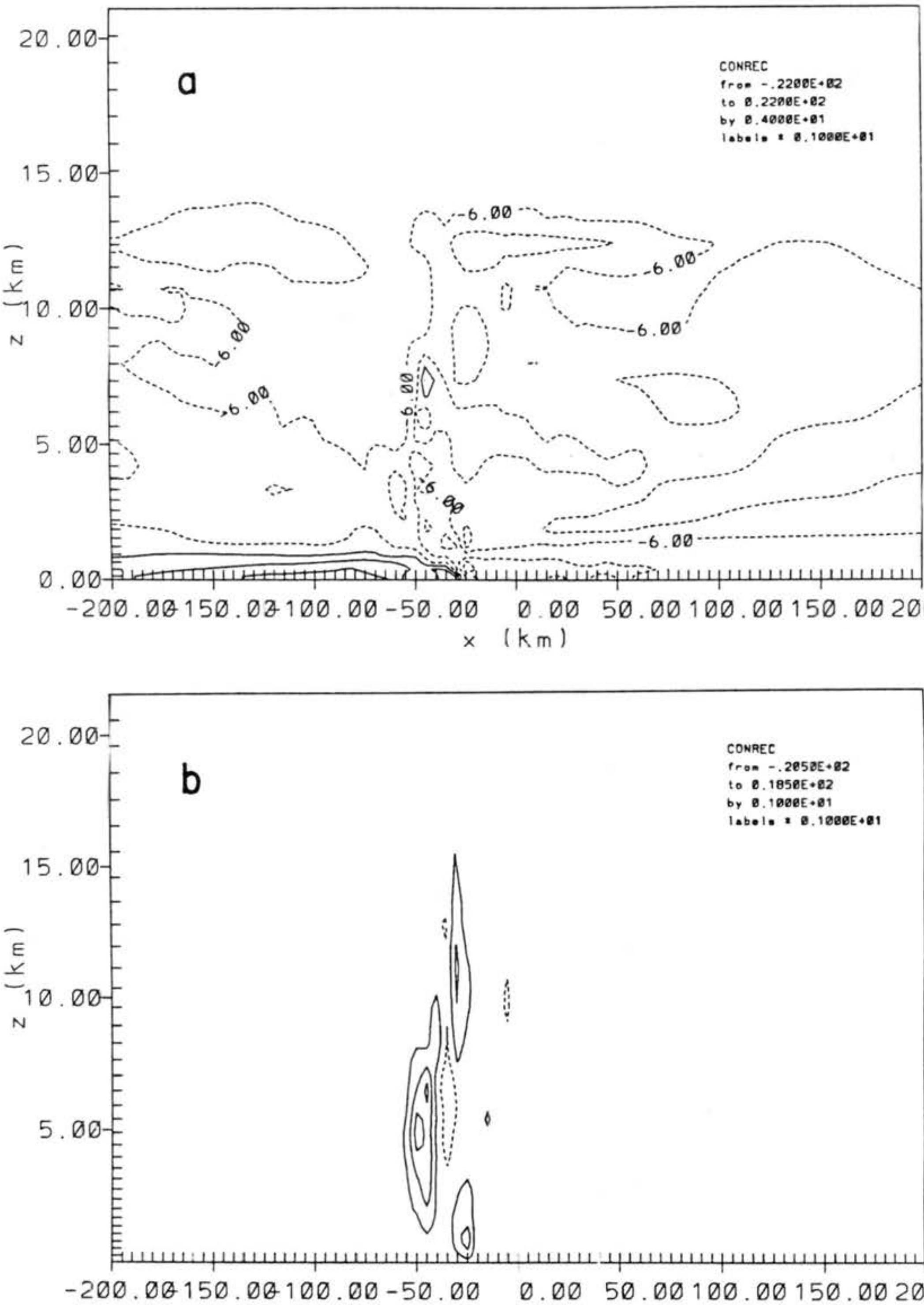

Figure 5.23: As in Figs. 5.6a-h except for the 5 km parameterized simulation without downdrafts and without precipitation.

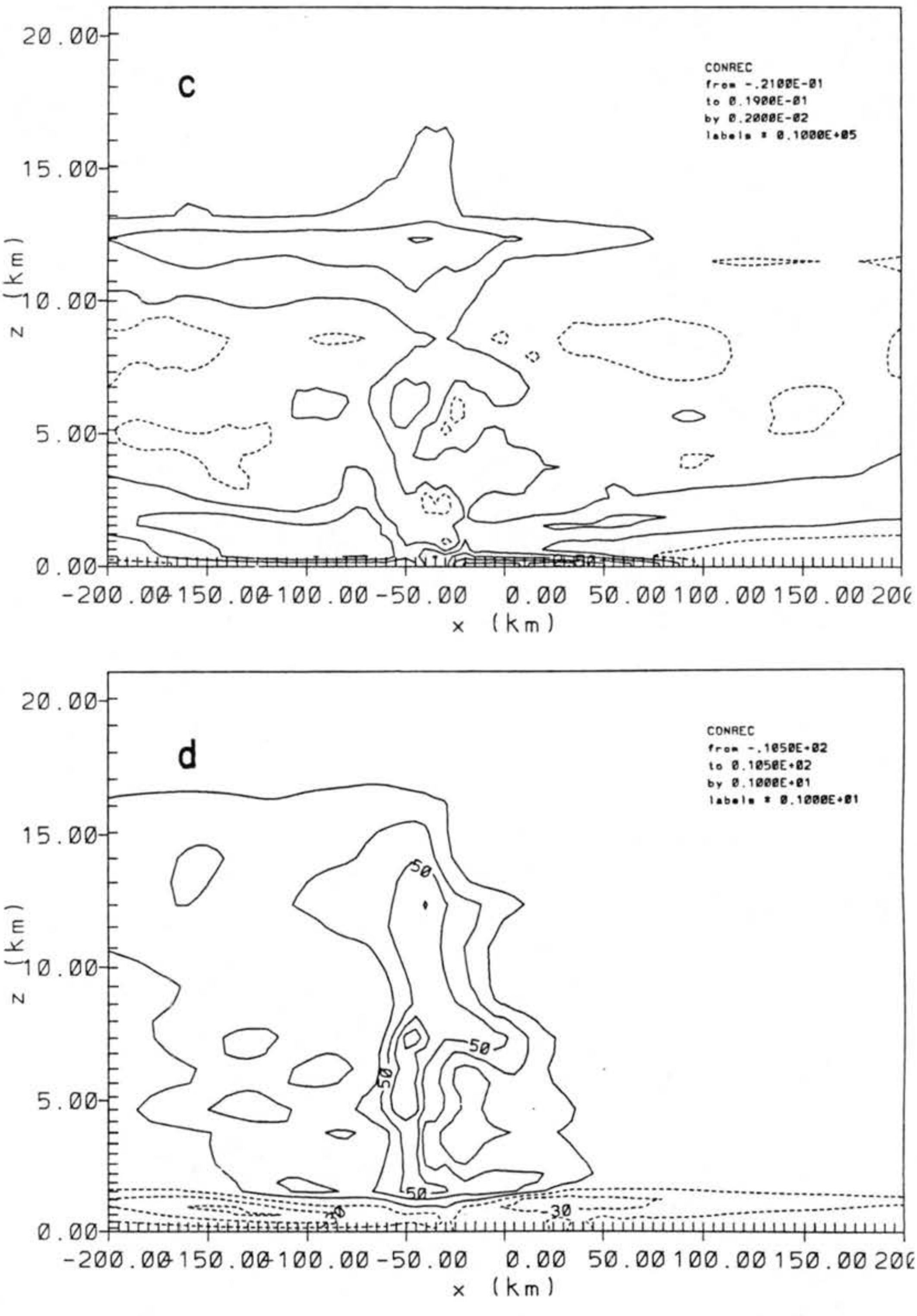

Figure 5.23: Continued.

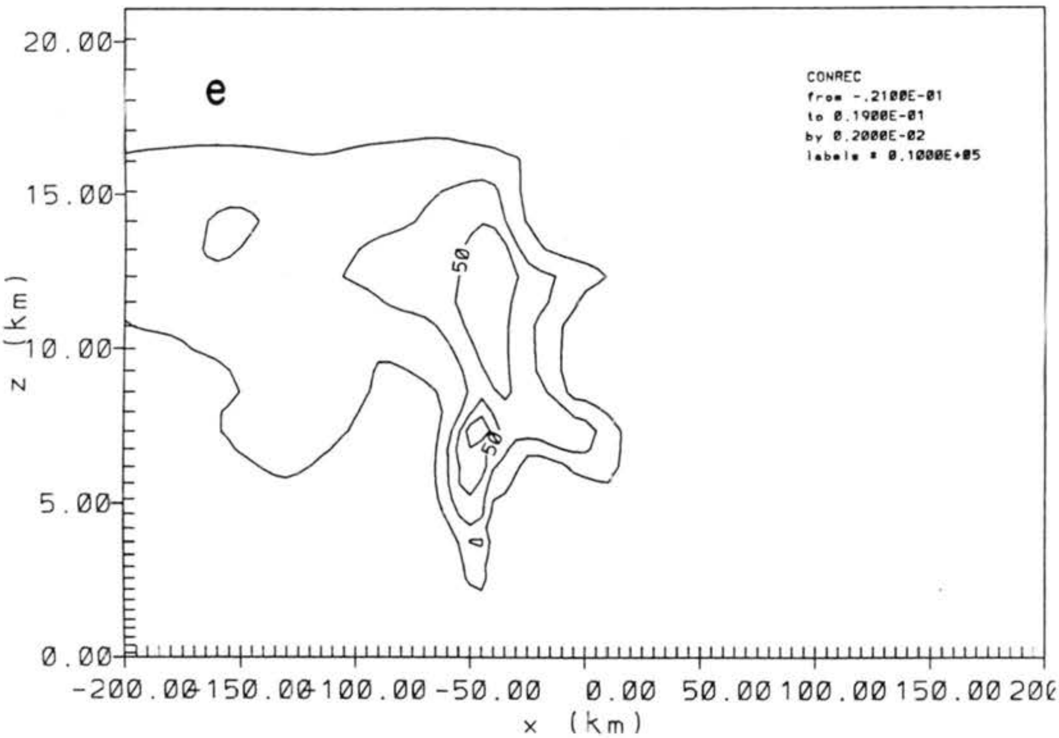

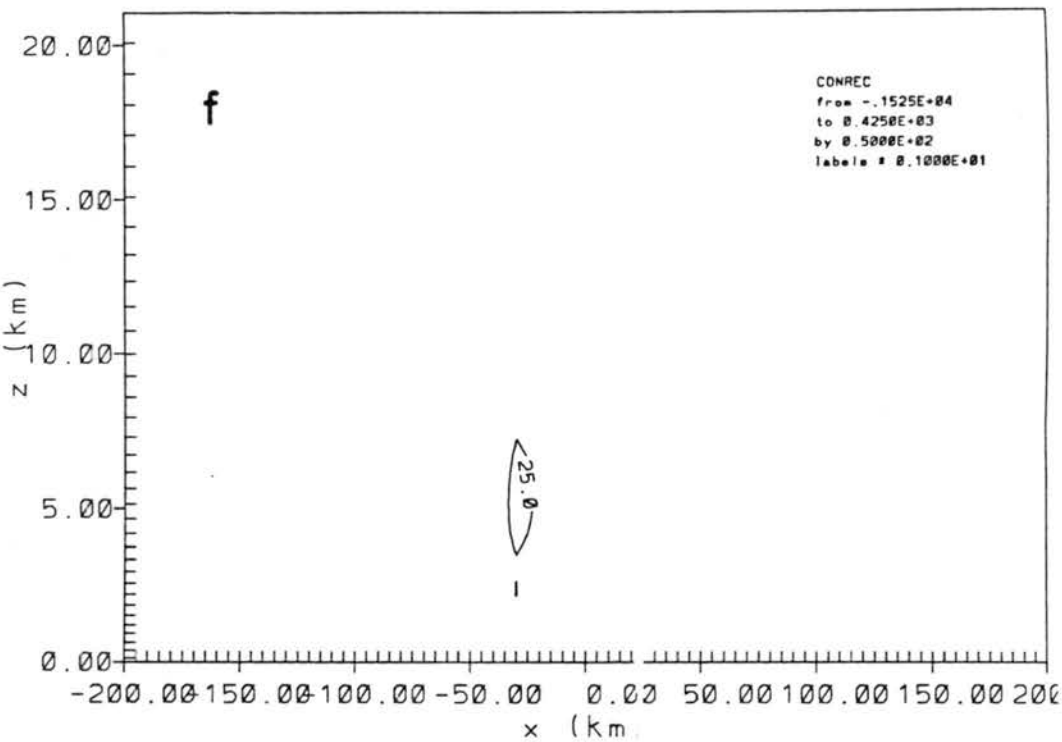

Figure 5.23: Continued.

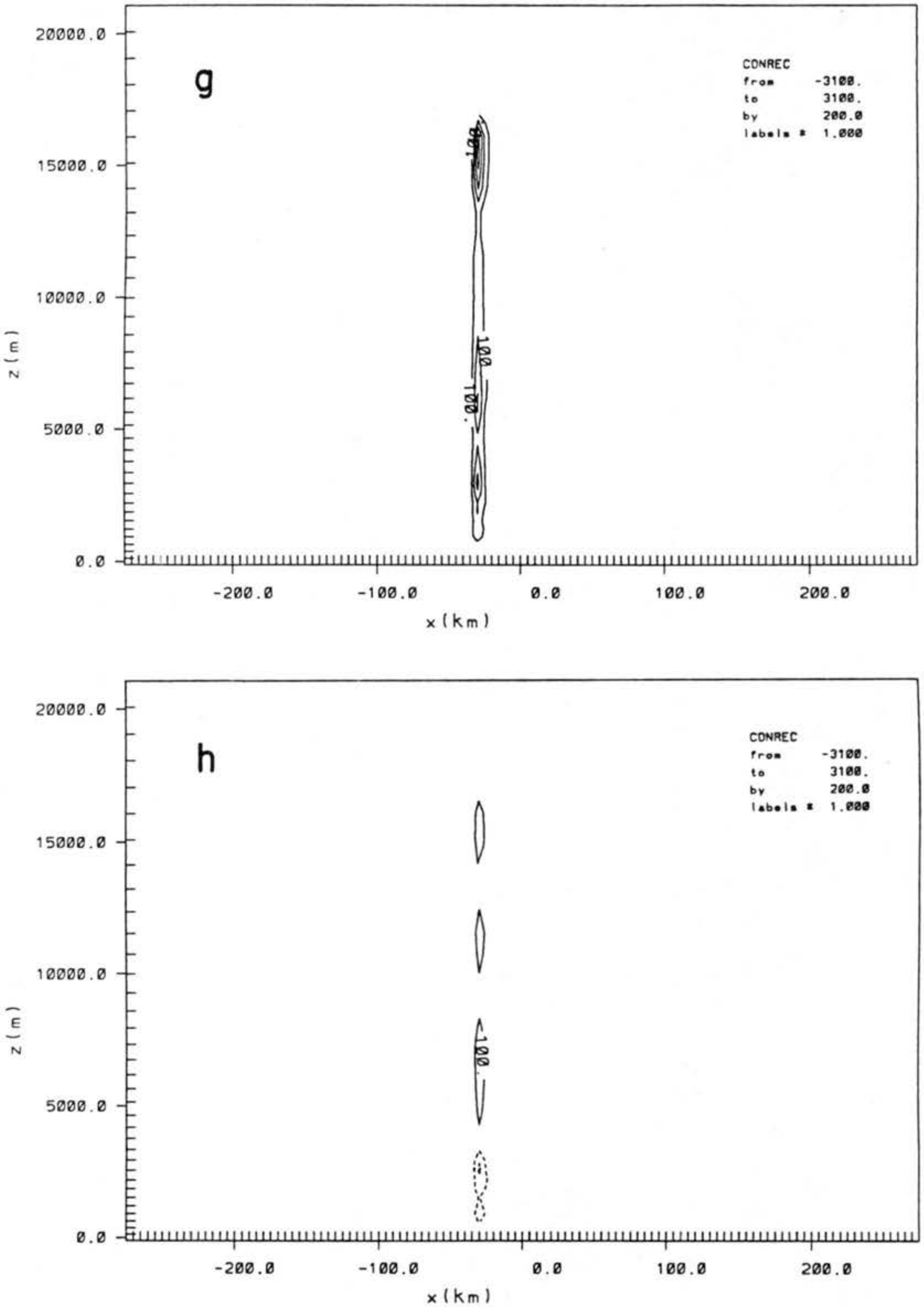

Figure 5.23: Continued.

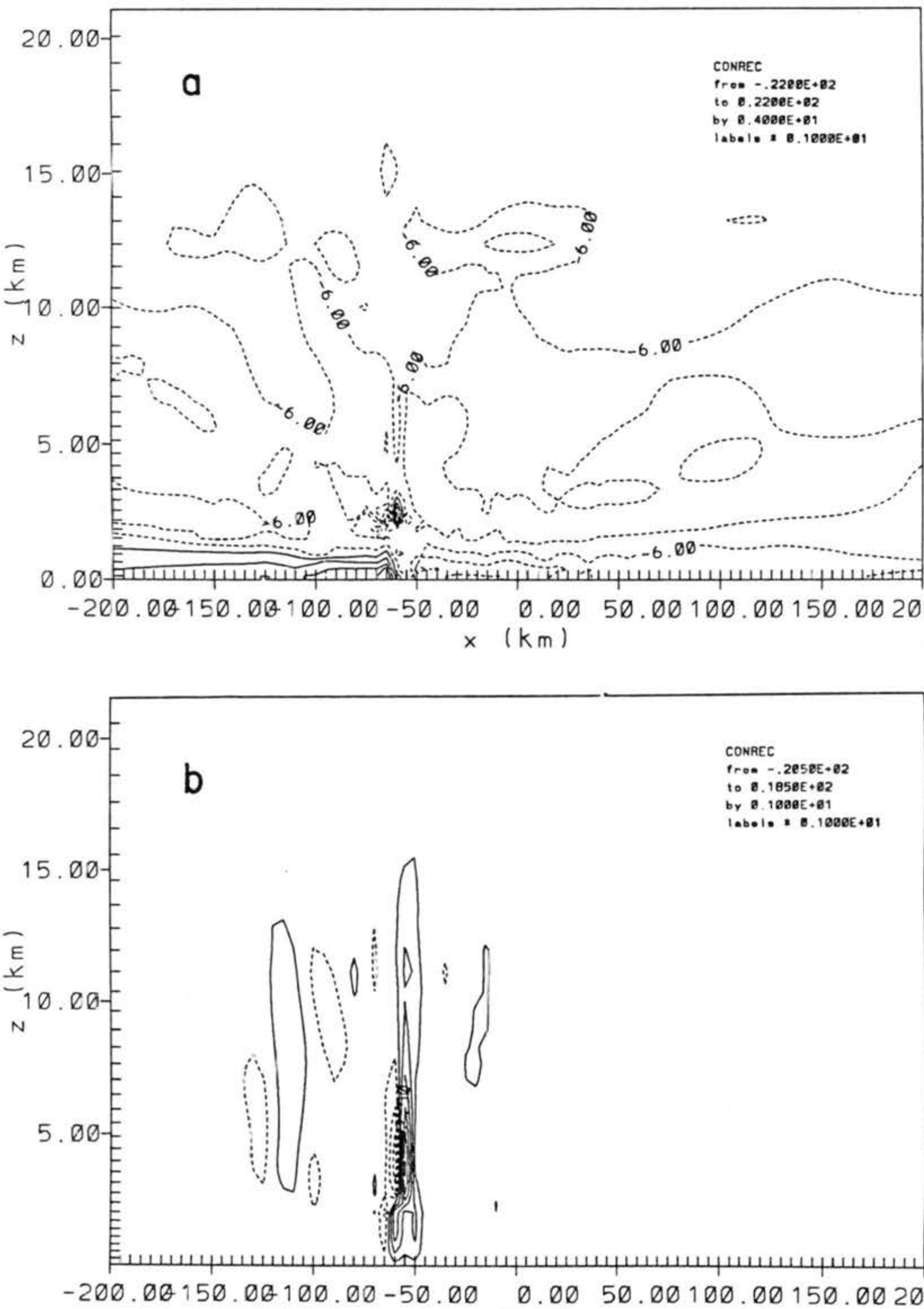

Figure 5.24: As in Figs. 5.6a-h except for the 5 km parameterized simulation with downdrafts and without precipitation.

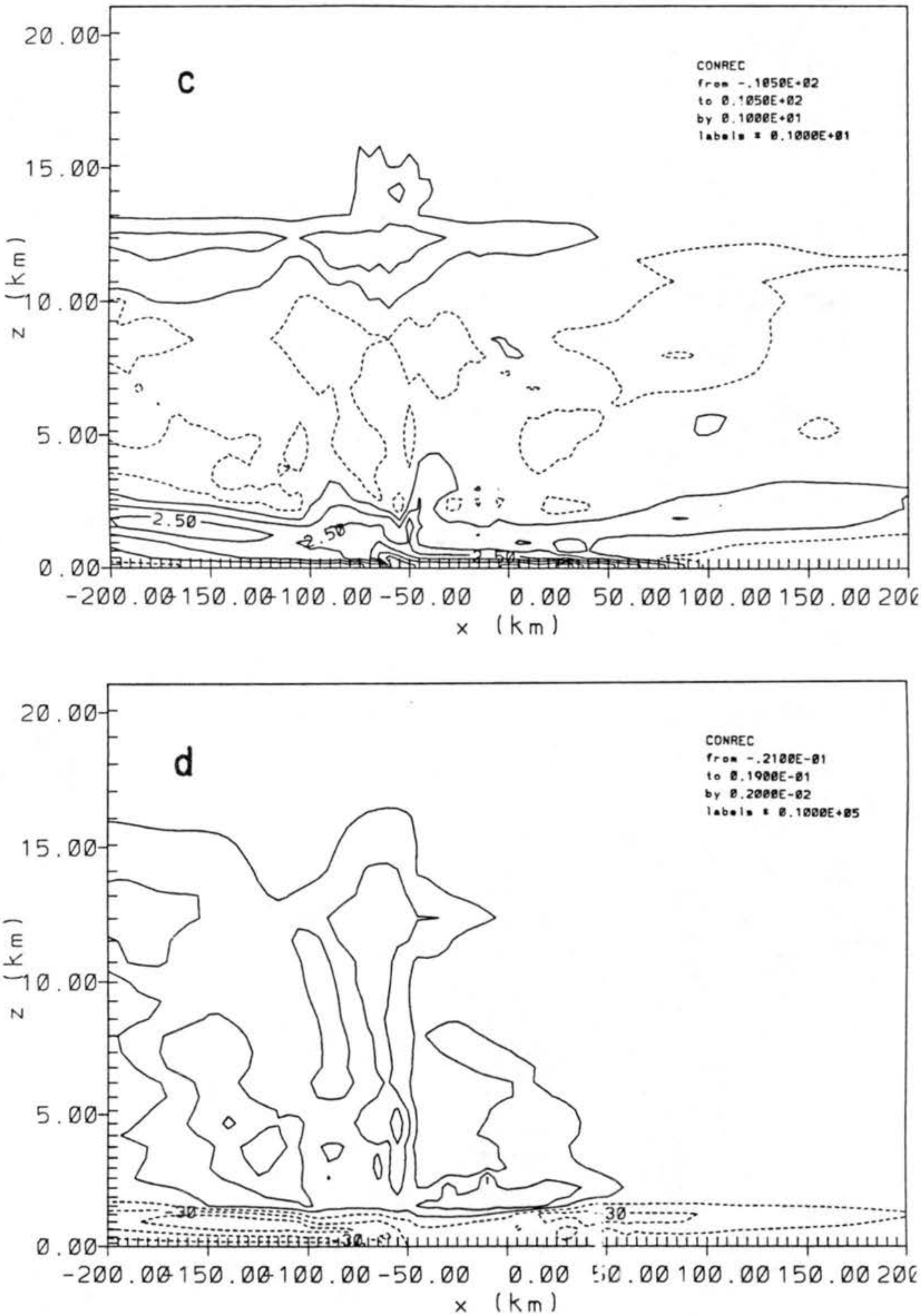

Figure 5.24: Continued.

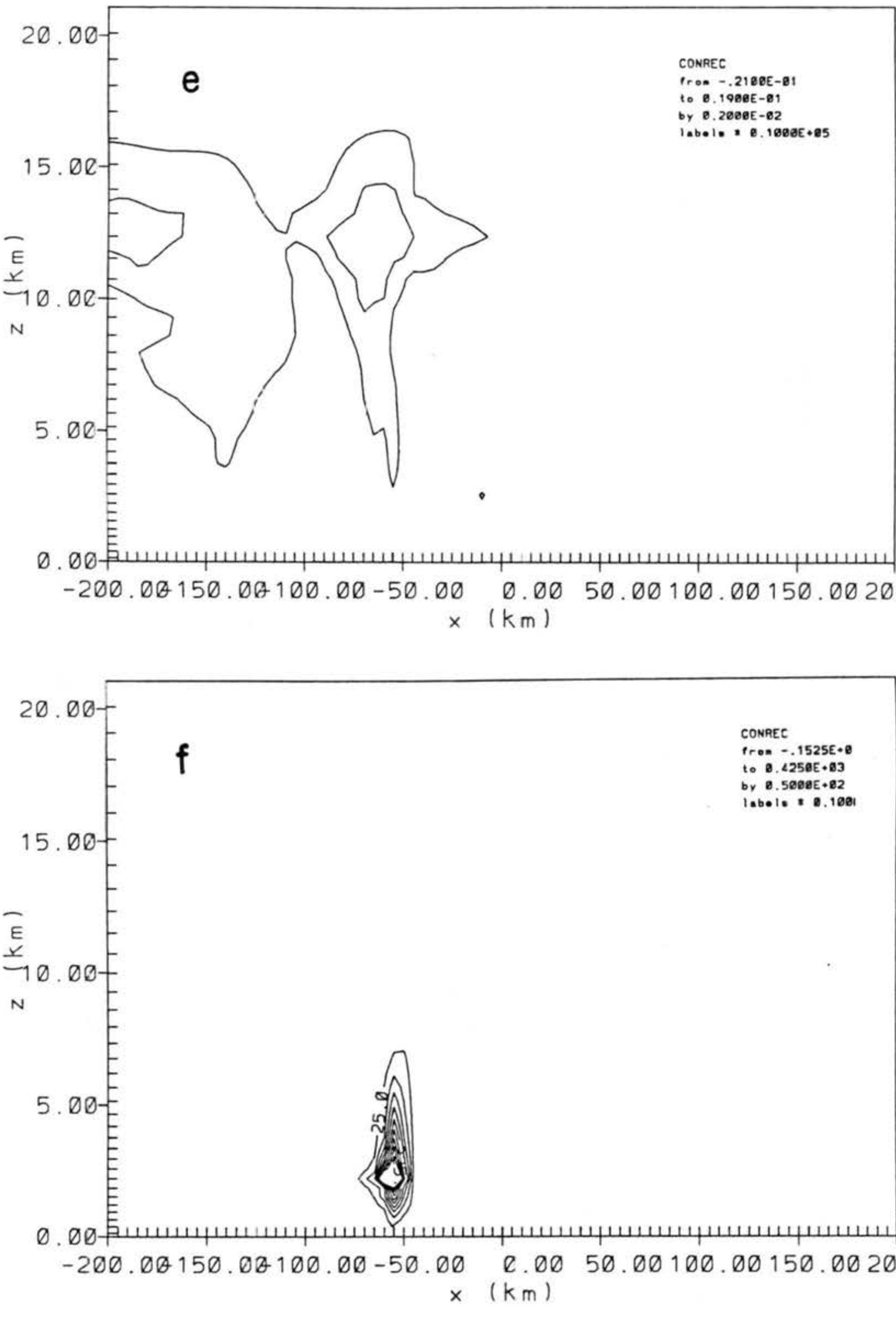

Figure 5.24: Continued.

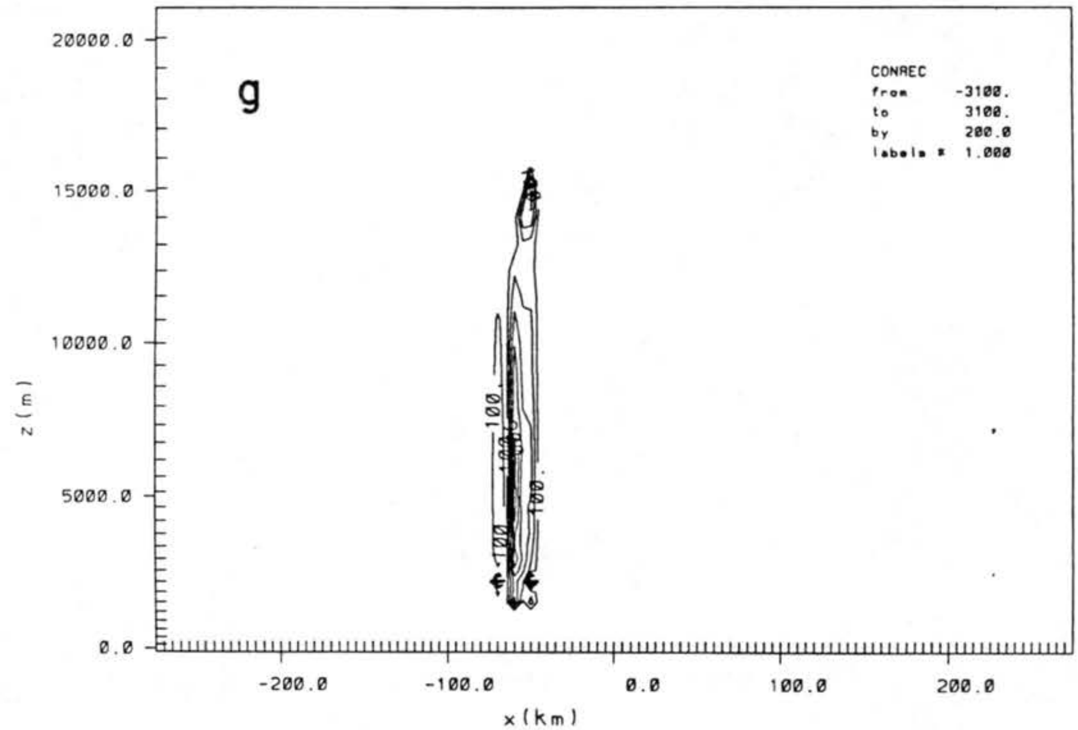

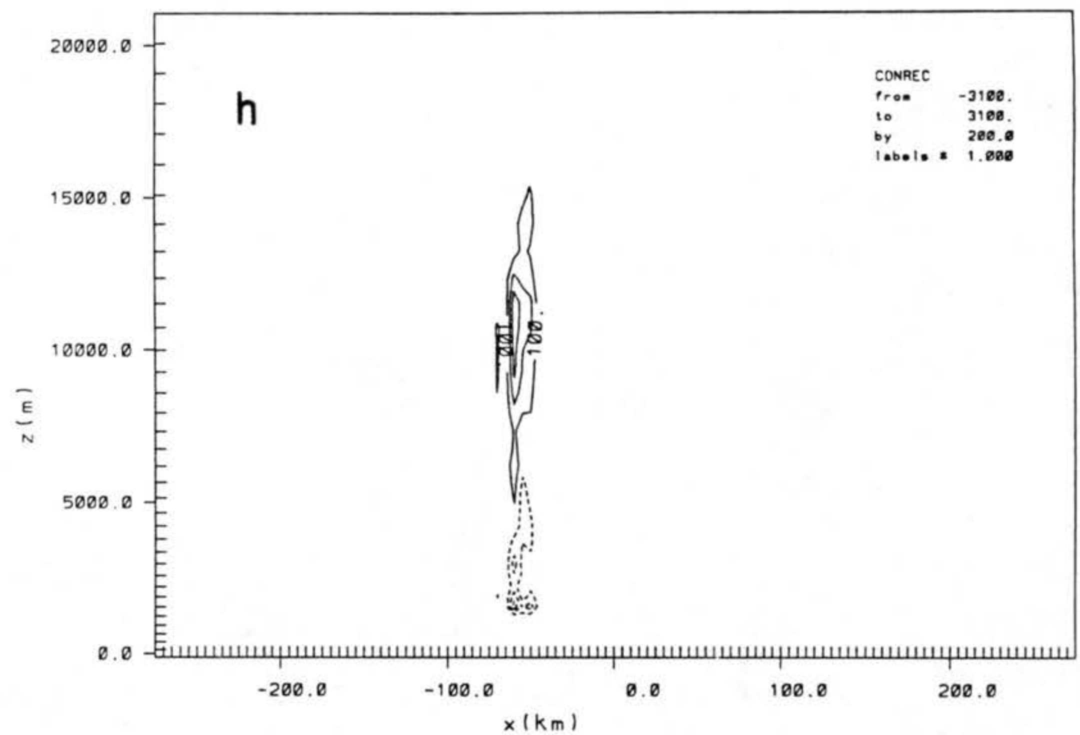

Figure 5.24: Continued.

When the parameterization with precipitation and no downdrafts is run (Figs. 5.25a - 5.25h), a single parameterized cumulus cell appears. Peak values are similar to the explicit simulation except for the perturbation total water mixing ratio which is twice as high, especially near 5 km. The vertical variance at this time is half as large as the explicit simulation.

In Figs. 5.26a - 5.26h, the results from the parameterization with downdrafts and precipitation is shown. Similar to the 20 km parameterized simulation at this time period, the convection is anchored to its initiation location. The vertical variance is an order of magnitude high while mean vertical motion, perturbation total water mixing ratio and condensate mixing ratio are all too small. This is probably the result of the cumulus convection remaining in the same location for the entire simulation.

The temporal evolution of the condensate rates are shown in Figs. 5.27a-5.27d for all four simulations at a grid point near the center of the peninsula. Unlike the 20 km simulation, the peak condensate rates for the runs without precipitation are nearly equal at 30 mm/hour. However, similar to the 20 km simulation are the peak rates near 50 mm/hour for the precipitation case without downdrafts. Also similar is the decrease of the condensate rate to one third of this value when downdrafts are added to the simulation with precipitation.

5.3 Summary

To summarize, the strengths and weaknesses of the parameterization on the 5 km grid are similar to those on the 20 km grid. In general, best agreement with both timing, location and transport of scalars by cumulus convection appears to occur when the parameterization is run with precipitation but no downdrafts; downdrafts anchor the convection to a location near its initiation. Downdrafts also weaken the parameterized cumulus convection, presumably due to the decrease of moist static energy within the PBL. This decrease is due to the cooling and also drying since the parameterized cumulus convection does not deplete the moisture within the PBL. The transport of scalars within the cumulus core is reproduced as are the resolved subsident circulations within the mesoscale model.

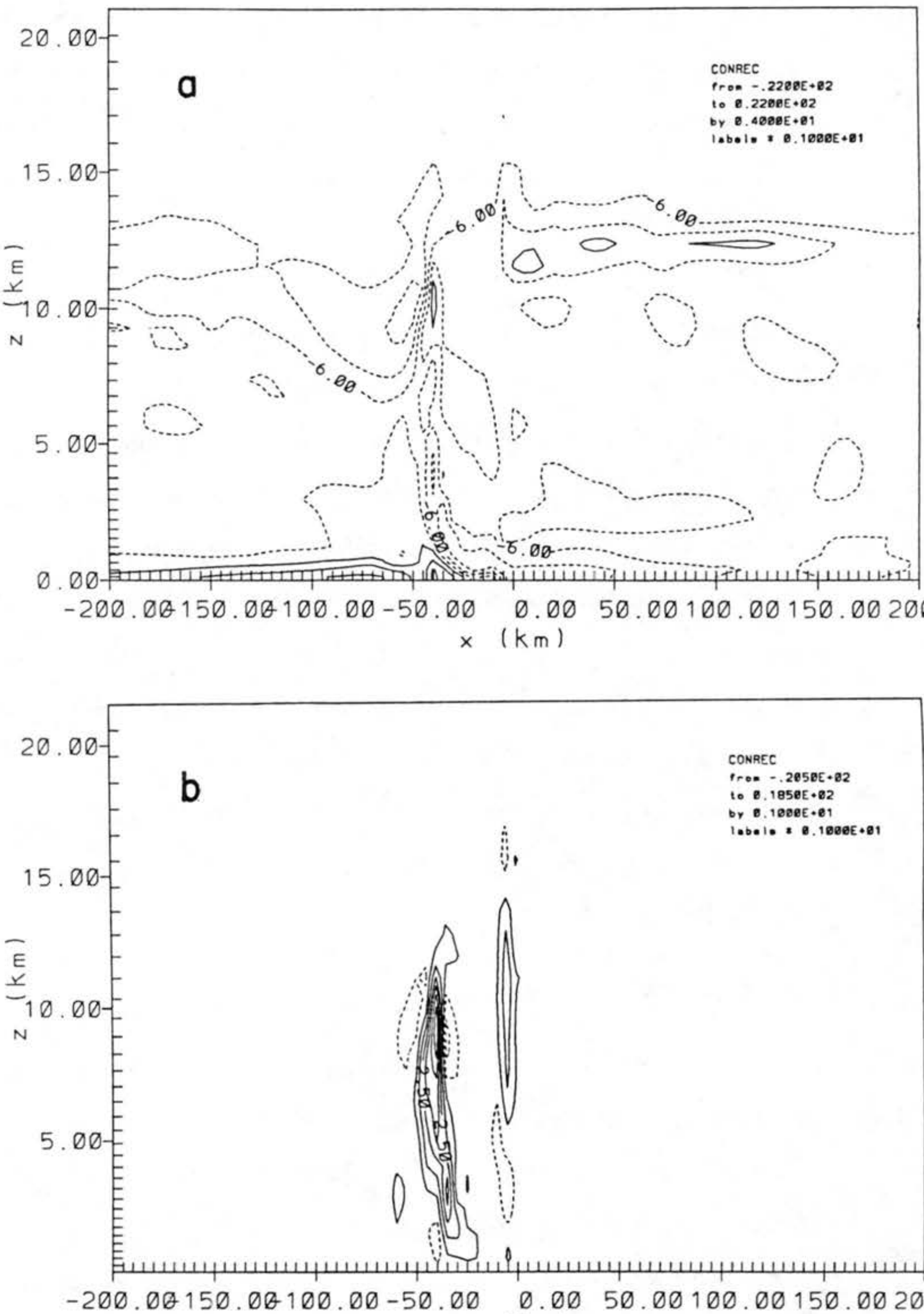

Figure 5.25: As in Figs. 5.6a-h except for the 5 km parameterized simulation without downdrafts and with precipitation.

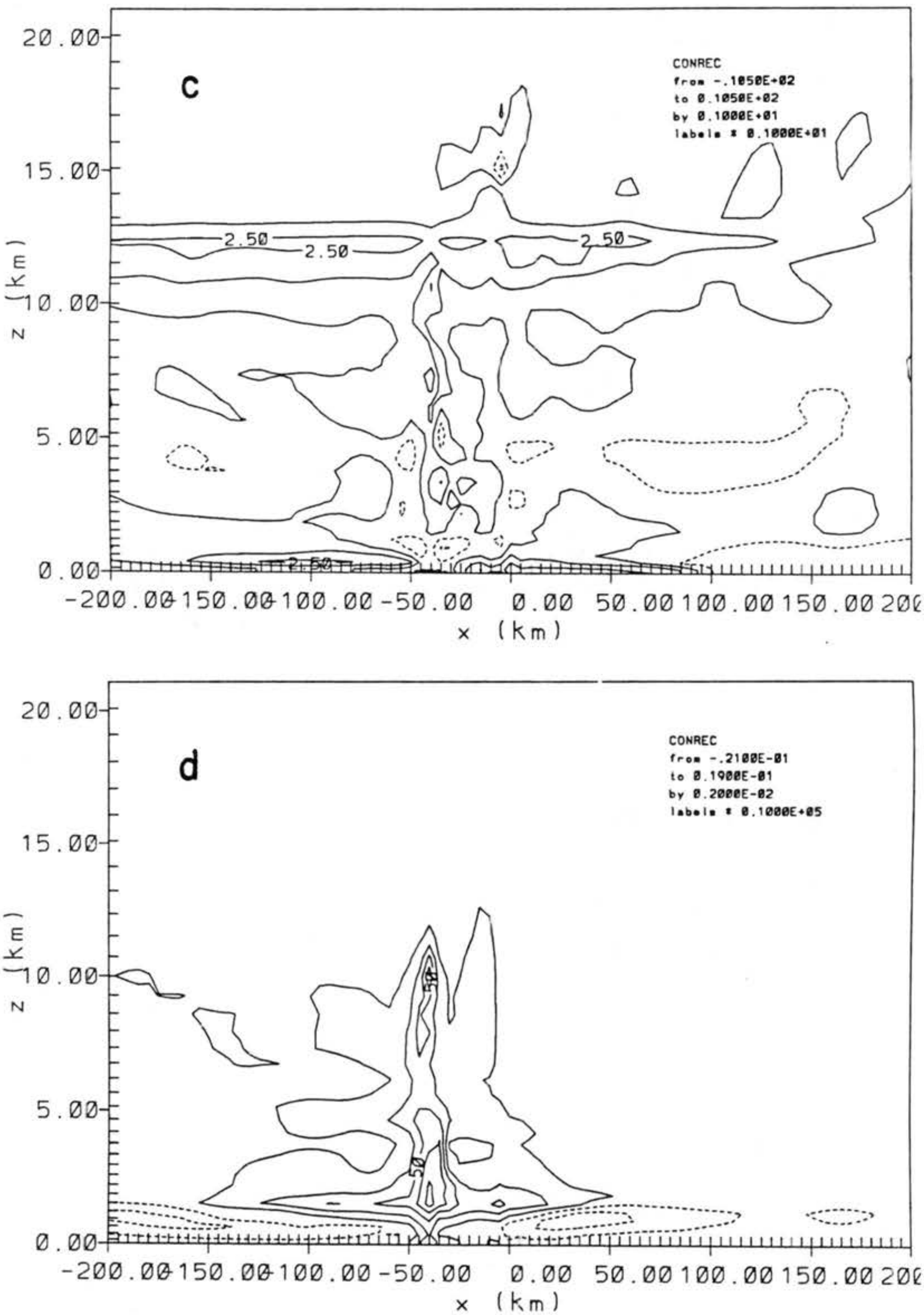

Figure 5.25: Continued.

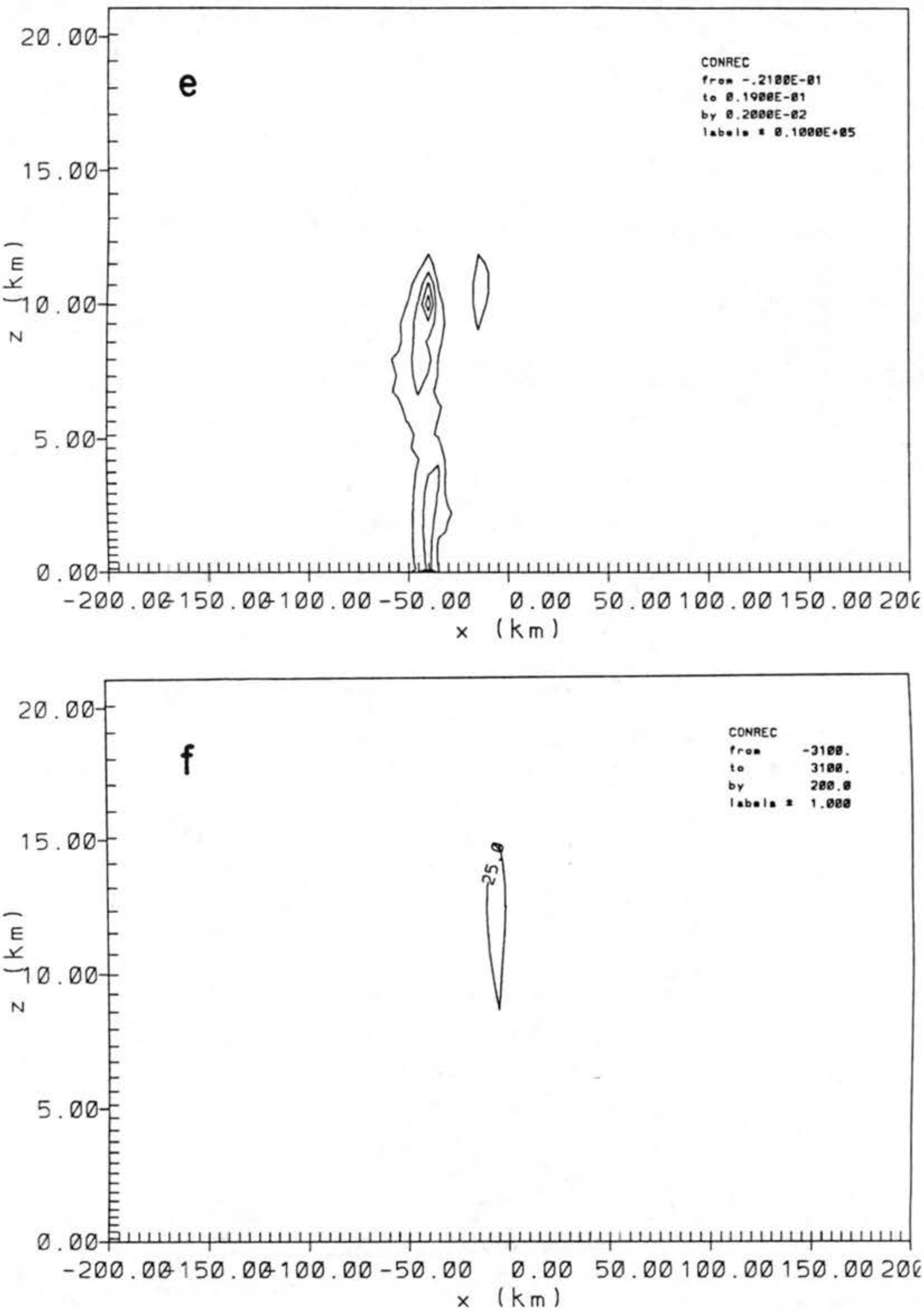

Figure 5.25: Continued.

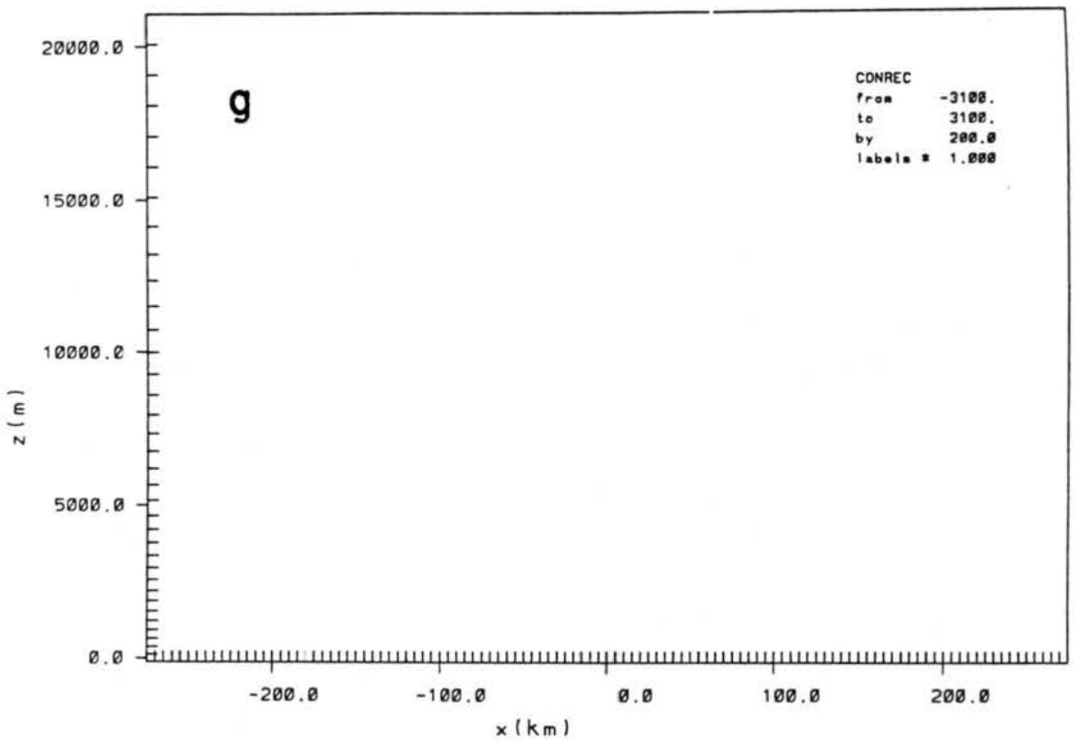

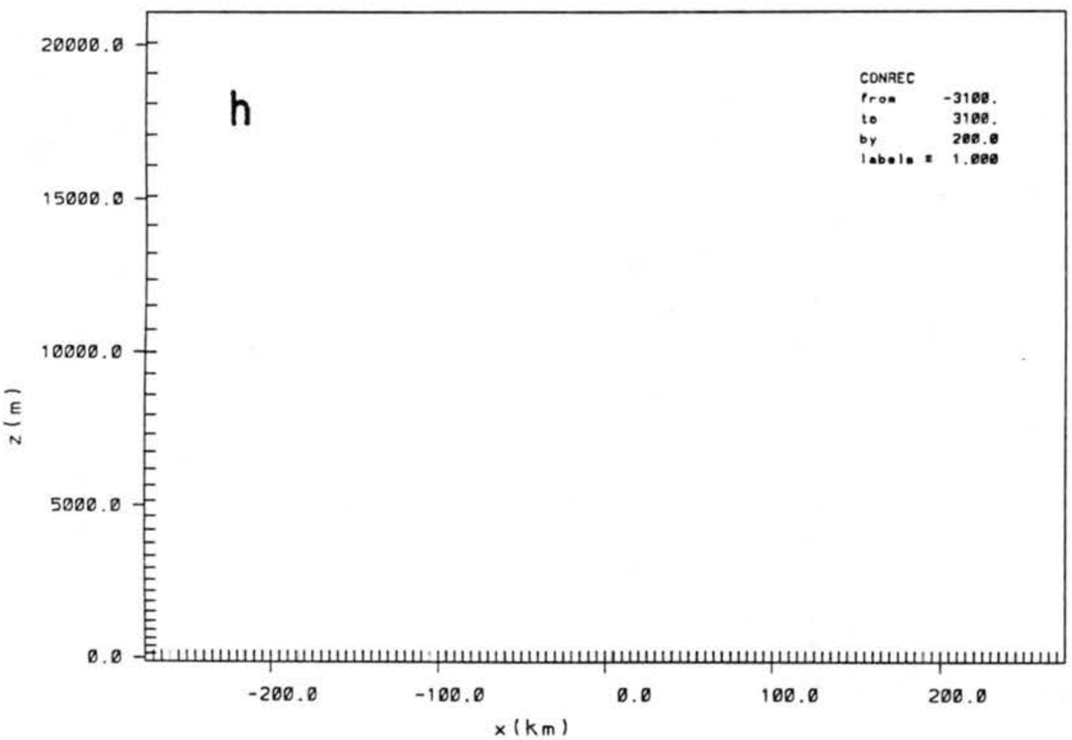

Figure 5.25: Continued.

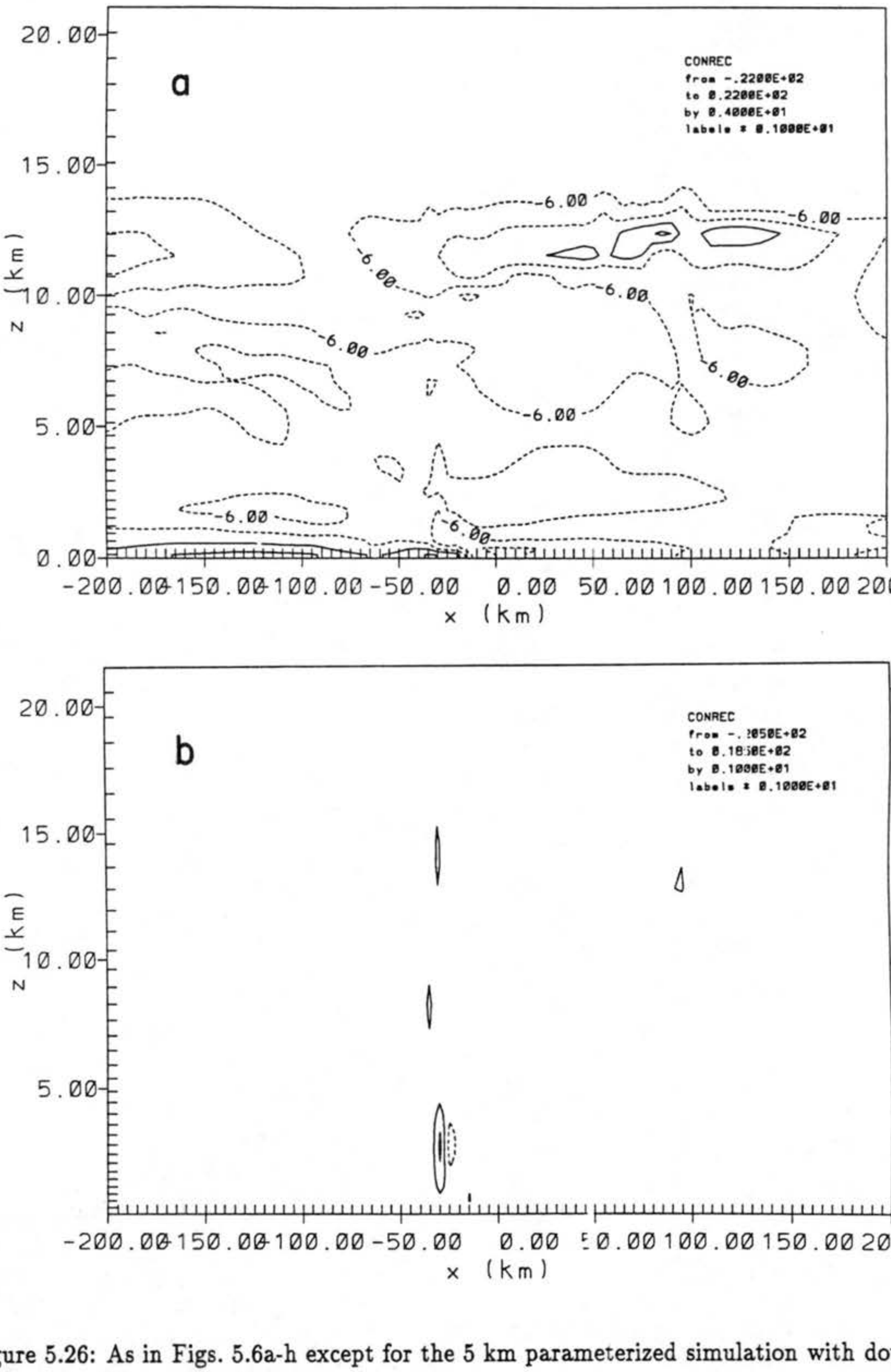

Figure 5.26: As in Figs. 5.6a-h except for the 5 km parameterized simulation with downdrafts and with precipitation.

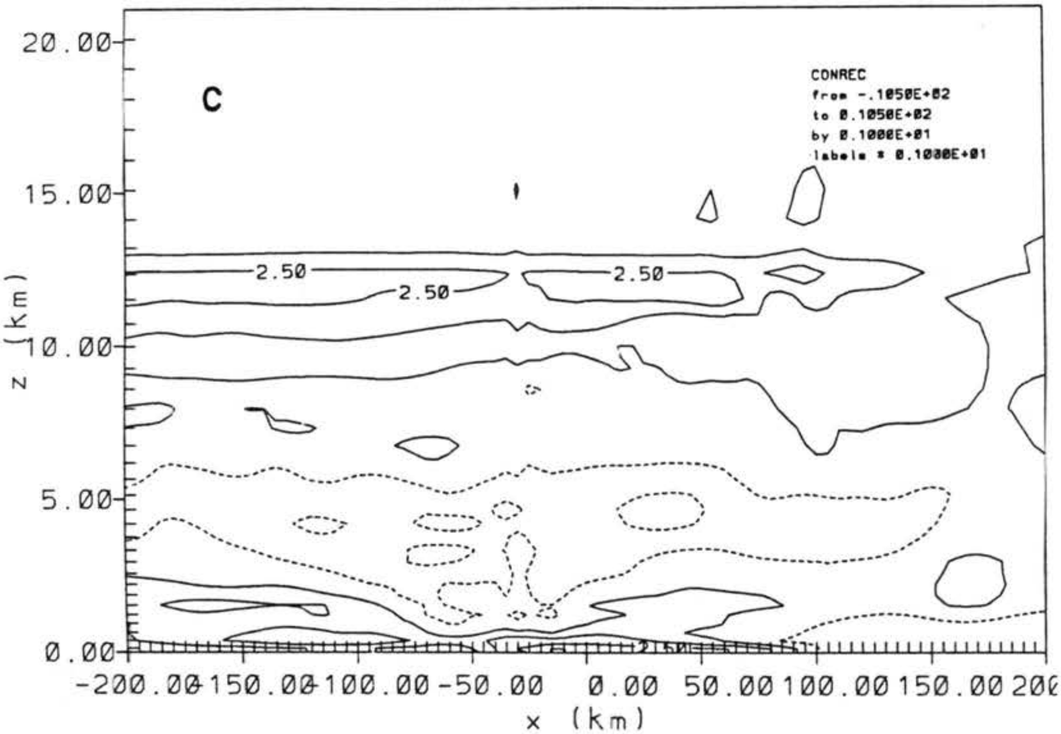

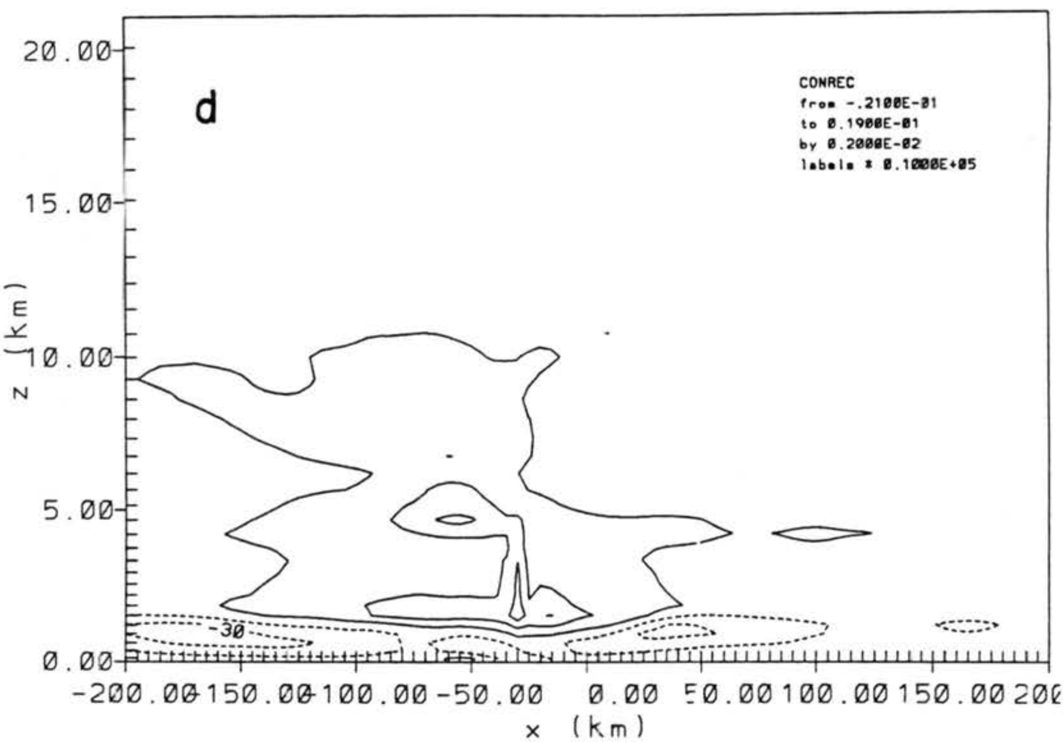

Figure 5.26: Continued.

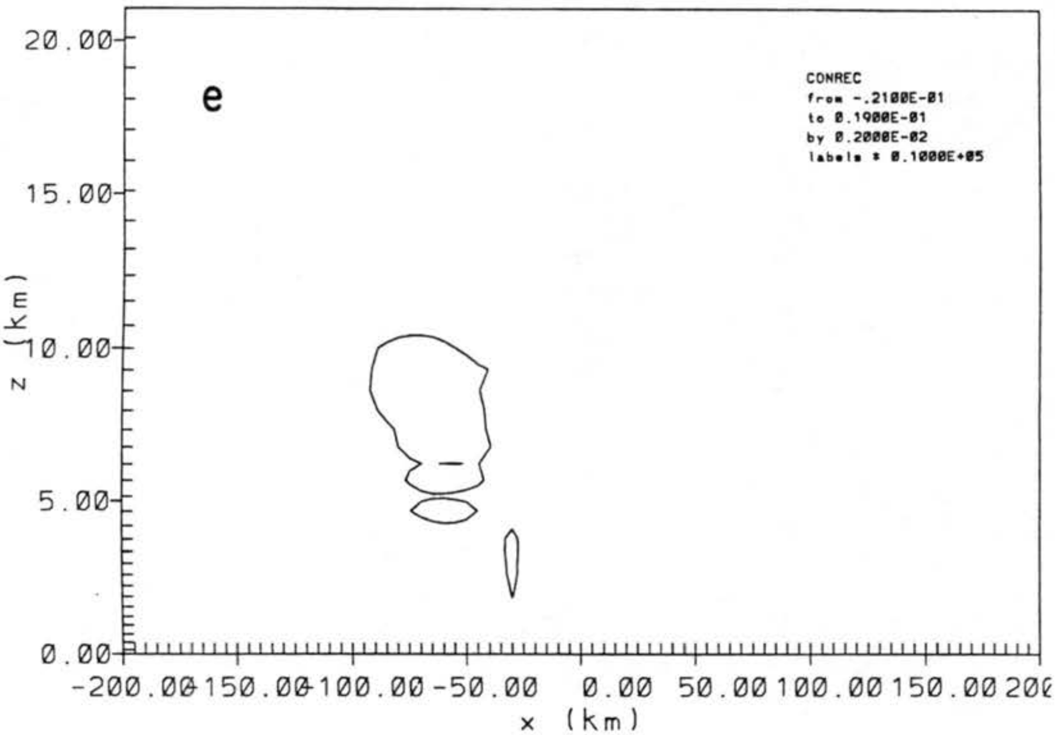

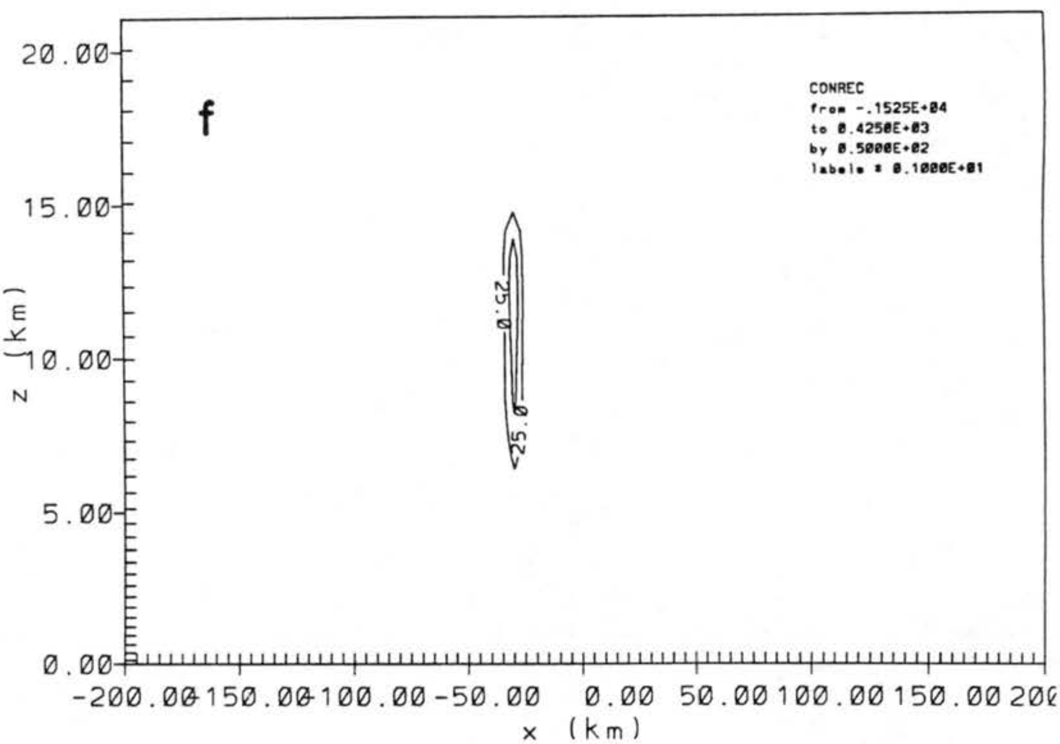

Figure 5.26: Continued.

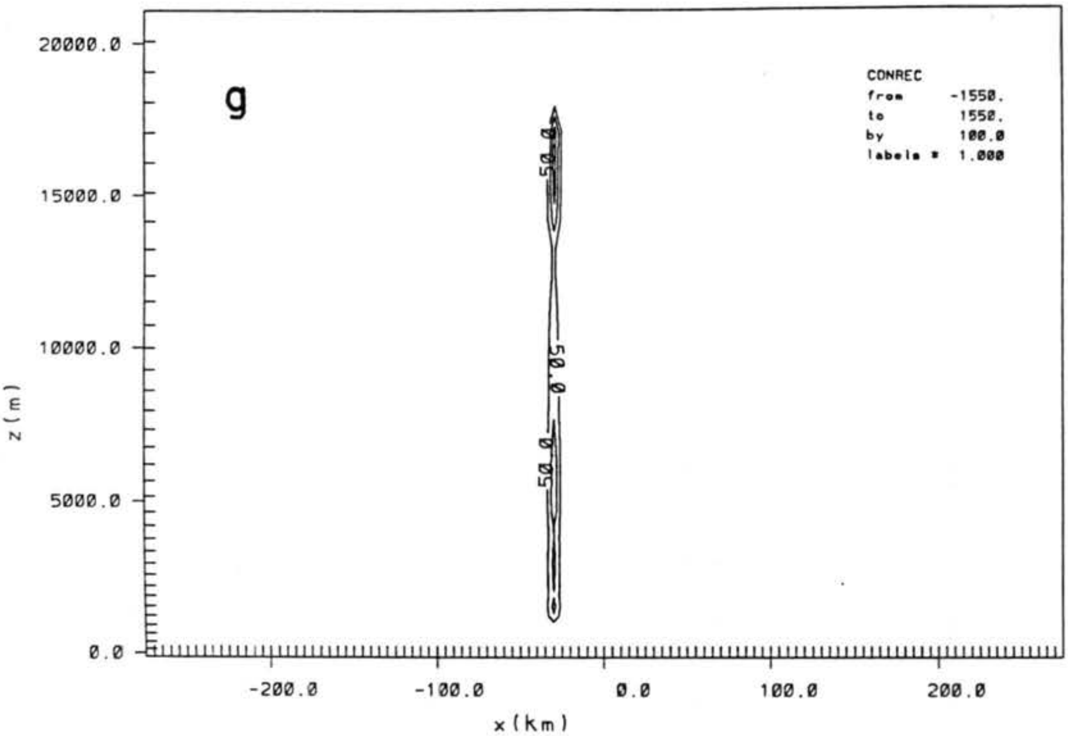

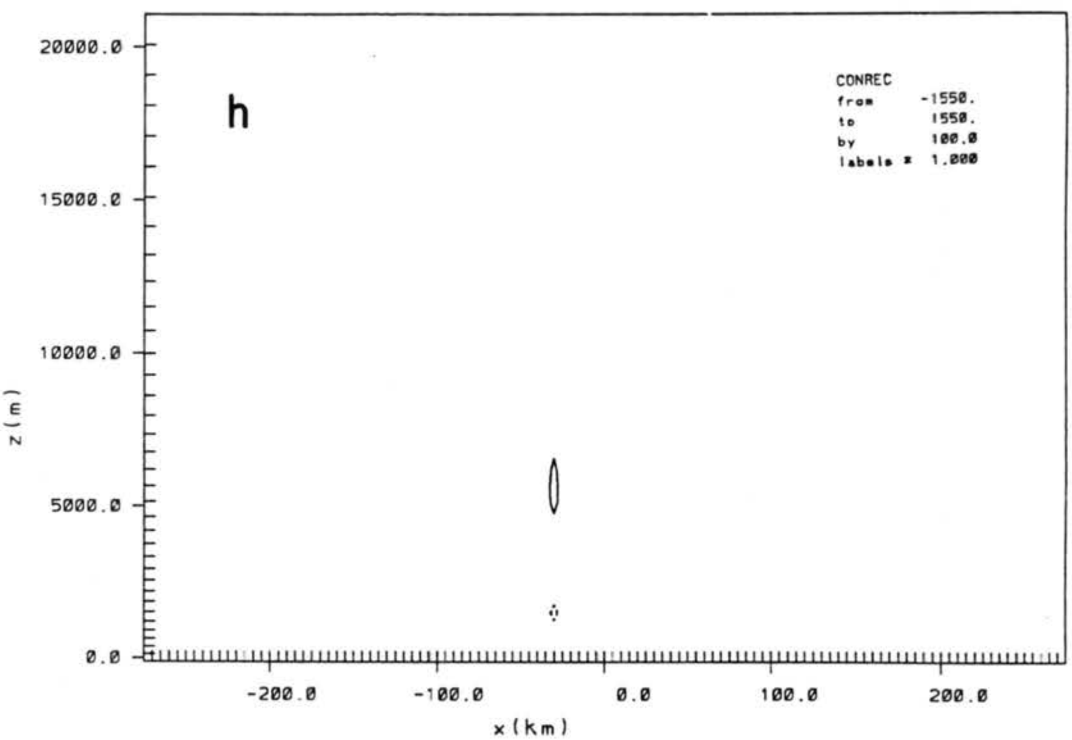

Figure 5.26: Continued.

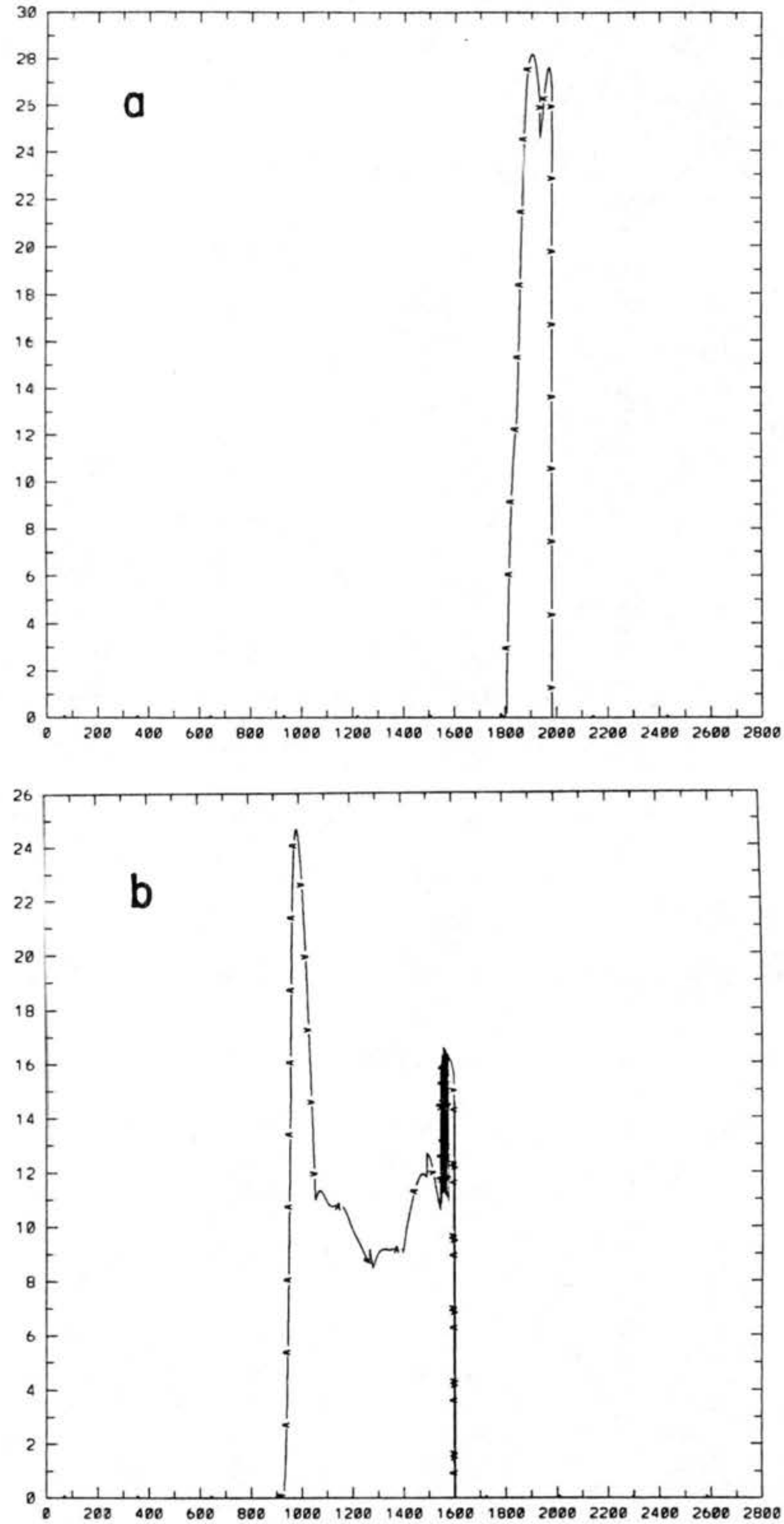

Figure 5.27: Temporal evolution (12 hrs) of the condensate rate in mm/hr for the parameterized simulations on a 5 km grid (a) without downdrafts and without precipitation, (b) with downdrafts and without precipitation.

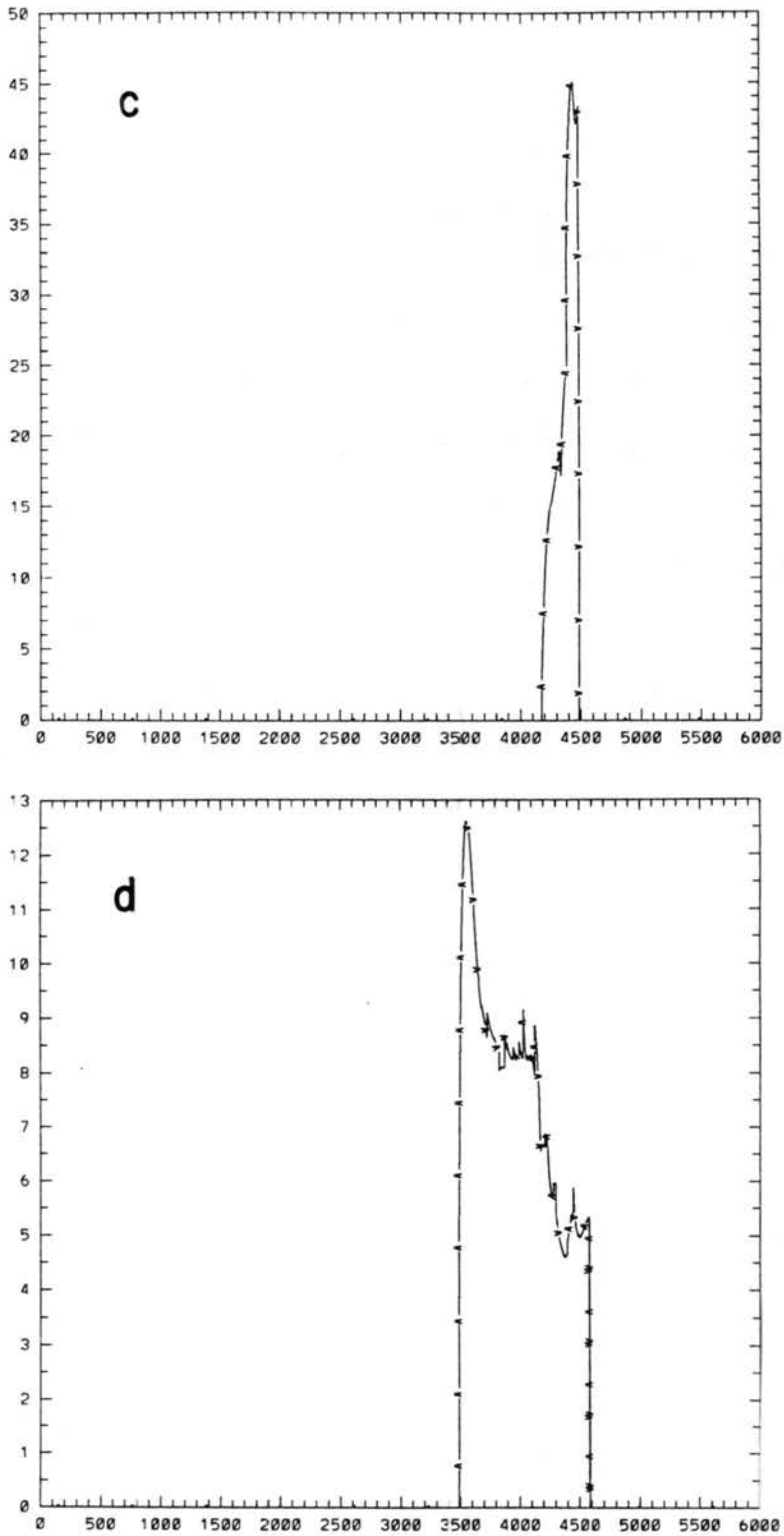

Figure 5.27: Continued. (c) without downdrafts and with precipitation, and (d) with downdrafts and with precipitation.

However, the parameterization is far too robust during the earlier transient events and this may be due to the neglect of moisture depletion within the PBL by the parameterized cumulus or the parameterization scheme being constructed around a steady-state model. The high heating rates in the upper troposphere are caused by the stability there and is manifested through the compensation term in 4.20. The strong parameterized heating should be offset by the cooling associated with the induced upward resolved motions, however high perturbation temperatures indicate that this is not happening as completely as it should. Choosing another form for w^{**} rather than assuming it to be constant with height might alleviate this problem. Allowing entrainment within the cloud would also decrease the effects of the parameterization scheme in the upper levels.

In addition, other experiments indicate there appears to be a weakly grid dependent criteria on the selection of the threshold value of $\overline{w'w'}$ for the initiation of convection. This threshold value is probably also dependent upon the type of convection being simulated. Fortunately though, these values appear confined to within a fairly narrow range and may need to be specified by the user through trial and error.

Chapter 6

SUMMARY AND CONCLUSIONS

A new cumulus parameterization scheme is presented which is designed for use in mesoscale models having a wide range of grid sizes. The basis for the scheme is derived from the explicit simulations of a mid-latitude supercell and a tropical squall line; these storms show striking similarity in the vertical profiles and temporal evolution of the vertical variance and the other vertical covariances. The scheme is an extension of the Mellor and Yamada (1976) level 2.5 closure which uses TKE as the only predictive variable. Their equations are modified to include saturation and precipitation and predict only on $\overline{w'w'}$, therefore this model is termed a 2.5w scheme. Furthermore, the closure formulation of Zeman and Lumley (1976) is used for the eddy transport and pressure-diffusion terms which are important in driving the prediction of $\overline{w'w'}$.

Since the level 2.5w model is inadequate in representing the effects of deep convection, a deep cumulus updraft and downdraft scheme based on convective adjustment is added. This cumulus part includes a convective adjustment term modulated by a time scale based on the integrated value of $\overline{w'w'}$ and a mesoscale compensation term which offsets the advection of scalars by the resolved vertical motion; this eliminates any double-counting between the cumulus parameterization scheme and the mesoscale model. The compensation term is formed by multiplying a constant determined through a moist static energy balance by the vertical gradient of a scalar.

Although this model is tested assuming a non-entraining updraft, 'tunable' parameters at this point include the entrainment rate of the updraft, the evaporative pressure scale for the downdraft, the updraft and downdraft core condensation efficiencies (which are not needed if the the condensed water is taken to be the difference between the total water mixing ratio and the saturation water mixing ratio within the cloud), the condensate partitioning terms for the updraft and downdraft and the threshold values of $\overline{w'w'}$ and mean vertical motion needed to activate convection. Many of these parameters are determined from conditionally sampling the aforementioned explicit simulations of a supercell and tropical squall line.

Four one dimensional simulations including no downdrafts/no microphysics, downdrafts/no microphysics, no downdrafts/microphysics and downdrafts/microphysics indicate that the limiting states of the parameterization scheme adequately represent a non-entraining cloud. These four versions of the cumulus parameterization scheme are exercised in a fully prognostic two dimensional simulation of Florida sea breeze convection on grid resolutions of five and twenty kilometers assuming a non-entraining cloud. General agreement is found when the fields of horizontal and vertical wind, perturbation temperature, perturbation total mixing ratio and condensate mixing ratio are compared to the appropriately averaged fields derived from an explicit simulation. Best agreement is found when microphysics are included and downdrafts are excluded since downdrafts tend to anchor the cumulus convection. Downdrafts also weaken the convection by decreasing the moist static energy within the PBL.

However, temperature perturbations are too strong in all parameterized simulations; this is supported by the high cumulus heating rates. These high heating rates should be moderated by the adiabatic cooling associated with the resolved upward motions, however model results indicate that this does not happen as completely as it should. The specification of a vertical profile for the constant in the compensation term may alleviate the unrealistically high perturbation temperature fields observed as might allowing cloud entrainment. Furthermore, the cumulus parameterization scheme is too robust during the transient events; this may be due to the neglect of moisture depletion within the PBL by the parameterized cumulus or to the scheme being designed around a steady-state model.

This scheme is unique since it extends a traditional PBL closure to the free atmosphere. It also predicts on $\overline{w'w'}$, which is an intuitive and direct measure of convective activity, and thus allows the communication of convective activity between contiguous grid cells. This hopefully overcomes the limitations that has prevented the use of previous cumulus parameterization schemes on a wide range of grid sizes. Furthermore, this cumulus parameterization provides an explicit source of hydrometeors for the mesoscale model which is important, for example, in the parameterization of mesoscale convective systems (MCSs). While hydrometeors may form in the broad area of mesoscale ascent, the detrainment of hydrometeors by parameterized convection is also important in contributing to the total hydrometeor content of the MCS.

6.1 Future research

The first step is to incorporate the cumulus parameterization scheme into a three dimensional model in order to allow for moisture depletion within the PBL by the parameterized cumulus. This will determine whether the inability of the scheme to replicate supposedly transient effects is due to the artificial constraints imposed in this work or to the scheme being designed around a steady state model. Perhaps a life-cycle may have to be incorporated into the cumulus parameterization scheme if allowing moisture depletion within the PBL does not produce transience. This life-cycle may include a downdraft lag as in some other cumulus parameterization schemes. And, although the cloud model in this study is called at every timestep, greater efficiency in program code and perhaps better results may be obtained by calling the cloud model less frequently.

Cloud entrainment also needs to be incorporated into future studies to determine its effect in reducing the unrealistically high heating rates and associated temperature perturbations within the upper troposphere. Choosing another form for the compensation term may more accurately mimic the mesoscale vertical motion profiles and thus also reduce the excessive temperature perturbations in the parameterized simulations. In addition experiments could be performed which specify the compensation term and diagnose the convective adjustment term.

The ability of the downdrafts to anchor the convection needs to be explored since this did not happen in the explicit simulation. Furthermore, in reality, the downdrafts and updrafts are physically separated in space so that the cool downdraft air is not drawn into the updraft. In this parameterization scheme, the downdrafts cool the entire PBL volume so that the cumulus cell is weakened. In order to more closely represent reality, the grid volume may have to be divided into a part cooled by downdrafts and a part which feeds the updraft.

Analysis of more explicit simulations will allow the appropriate free variables, including the condensate efficiencies and the condensate partitioning parameters to be further generalized. In fact, the explicit simulation and analysis of a MCS is planned so that this parameterization scheme can be extended to that class of storm. The explicit simulations do not need to be limited to supercells or squall lines, however; anvil-generated cirrus, stratocumulus-cumulus and small broken field cumulus can also be analyzed to generalize this parameterization scheme. It may be critical, for example, to accurately determine the condensate partitioning parameter for different cloud types.

It would also be interesting to implement this scheme in a GCM to determine its applicability in balanced-flow models. Since Bougeault (1985) has designed a cumulus parameterization scheme for GCMs which has a form very similar to this, hope exists that a single parameterization scheme might be able to accurately emulate deep convection on all grid sizes.

One last problem that may need to be further explored is the specification of the fall speeds of hydrometeors within the mesoscale model. An explicit simulation will provide the vertical mixing ratio profiles of hydrometeors which are supported by the resolved updraft velocities. Inconsistencies between the resolved vertical motion of the larger scale mesoscale model and the parameterized source profiles within the cloud model may develop, thus causing the hydrometeors to fall at unrealistically high speeds.

REFERENCES

Andre, J. C., G. De Moor, P. Lacarrere, and R. Du Vachat, 1976: Turbulence approximation for inhomogeneous flows: Part I. The clipping approximation. *J. Atmos. Sci.*, **33**, 476—481.

Andre, J. C., G. DeMoor, P. Lacarrere, and R. Therry, G. du Vachat, 1978: Modeling the 24 hour evolution of the mean and turbulent structures of the planetary boundary layer. *J. Atmos. Sci.*, **35**, 1861—1883.

Arakawa, A., 1969: Parameterization of cumulus convection. In *Proc. WMO/IUGG Symp. Numerical Weather Prediction*, 26 November - 4 December, Japan Meteor. Agency, Tokyo, IV,8,1-6.

Arakawa, A. and W. H. Schubert, 1974: Interaction of a cumulus cloud ensemble with the large-scale environment, Part I. *J. Atmos. Sci.*, **31**, 674—701.

Betts, A. K., 1975: Parametric interpretation of trade-wind cumulus budget studies. *J. Atmos. Sci.*, **32**, 1934—1945.

Betts, A. K., 2986: A new convective adjustment scheme. Part I: Observational and theoretical basis. *Quart. J. Roy. Meteor. Soc.*, **112**, 677—691.

Betts, A. K. and M. J. Miller, 1986: A new convective adjustment scheme. Part II: Single column tests using GATE wave, BOMEX, ATEX and arctic air-mass data sets. *Quart. J. Roy. Meteor. Soc.*, **112**, 677—691.

Blackadar, A. K., 1962: The vertical distribution of wind and turbulent exchange in neutral atmospheres. *J. Geophys. Res.*, **67**, 3095—3102.

Bougeault, P., 1981: Modeling the trade-wind cumulus boundary layer. Part II: A high-order one-dimensional model. *J. Atmos. Sci.*, **38**, 2429—2439.

Bougeault, P., 1985: A simple parameterization of the large-scale effects of cumulus convection. *Mon. Wea. Rev.*, **113**, 2108—2121.

Bretherton, C. S. and P. K. Smolarkiewicz, 1989: Gravity waves, compensating subsidence and detrainment around cumulus clouds. *J. Atmos. Sci.*, **46**, 740—759.

Brown, J. M., 1979: Mesoscale unsaturated downdrafts driven by rainfall evaporation. A numerical study. *J. Atmos. Sci.*, **36**, 313—338.

Businger, J. A., J. C. Wyngaard, Y. Izumi, and E. F. Bradley, 1971: Flux profile relationships in the atmospheric surface layer. *J. Atmos. Sci.*, **28**, 181—189.

Byers, H. and R. R. Braham, 1949: The thunderstorm. Technical report, U. S. Government Printing Office, Washington, D. C., 287. NTIS PB-234-515.

Chen, C. and W. R. Cotton, 1987: The physics of the marine stratocumulus-capped mixed layer. *J. Atmos. Sci.*, **44**, 2951—2977.

Cheng, M.-D., 1989a: Effects of downdrafts and mesoscale convective organization on the heat and moisture budgets of tropical cloud clusters. Part I: A diagnostic cumulus ensemble model. *J. Atmos. Sci.*, **46**, 1517—1538.

Cheng, M.-D., 1989b: Effects of downdrafts and mesoscale convective organization on the heat and moisture budgets of tropical cloud clusters. Part II: Effects of convective-scale downdrafts. *J. Atmos. Sci.*, **46**, 1540—1564.

Cotton, W. R. and R. A. Anthes, 1989: *Storm and cloud dynamics*, volume 44 of *International Geophysics Series*. Academic Press, 883.

Cotton, W. R., M. A. Stephens, T. Nehrkorn, and G. J. Tripoli, 1982: The Colorado State University cloud/mesoscale model—1982. Part II: An ice phase parameterization. *J. Rech. Atmos.*, **16**, 295—320.

Cotton, W. R., G. J. Tripoli, R. M. Rauber, and E. A. Mulvihill, 1986: Numerical simulation of the effects of varying ice crystal nucleation rates and aggregation processes on orographic snowfall. *J. Climate Appl. Meteor.*, **25**, 1658—1680.

Cram, J. M., 1990: *Numerical simulation and analysis of the propagation of a prefrontal squall line.* PhD thesis, Colorado State University, Dep't of Atmospheric Science, Fort Collins, Co. 80523, 332.

English, M., 1973: *Alberta Hailstorms*, volume 14 of *Meteorological Monographs.* Amer. Meteor. Soc., 37—98. ISBN 0-933876-39-4.

Flatau, P. J., 1985: Study of second-order turbulence closure technique and its application to atmospheric flows. Master's thesis, Colorado State University, Dep't of Atmospheric Science, Fort Collins, Co. 80523, 79.

Frank, W. M., 1983: The cumulus parameterization problem. *Mon. Wea. Rev.*, **111**, 1859—1871.

Frank, W. M. and C. Cohen, 1987: Simulations of tropical convective systems. Part I: A cumulus parameterization. *J. Atmos. Sci.*, **44**, 3787—3799.

Fritsch, J. M. and C. F. Chappell, 1980: Numerical prediction of convectively driven mesoscale pressure systems. Part I: Convective parameterization. *J. Atmos. Sci.*, **37**, 1722—1733.

Gregory, D. and M. J. Miller, 1989: A numerical study of the parameterization of deep tropical convection. *Quart. J. Roy. Meteor. Soc.*, **115**, 1209—1241.

Haltiner, G. J. and R. T. Williams, 1980: *Numerical prediction and dynamic meteorology.* John Wiley and Sons, 477.

Hassid, S. and B. Galperin, 1983: A turbulent energy model for geophysical flows. *Boundary-Layer Meteor.*, **26**, 397—412.

Hearn, A. C., 1984: *REDUCE users manual, Ver. 3.0.* The RAND Corp., Santa Monica.

Kanamitsu, M., 1975: *On numerical prediction over a global tropical belt.* PhD thesis, Florida State University, Dept. of Meteor., Tallahassee, Fl 32304, 281.

Kao, C.-Y. J. and Y. Ogura, 1987: Response of cumulus clouds to large-scale forcing using the Arakaw-Schubert cumulus parameterization. *J. Atmos. Sci.*, **44**, 2437—2458.

Klemp, J. B. and R. B. Wilhelmson, 1978: The simulation of three-dimensional convective storm dynamics. *J. Atmos. Sci.*, **35**, 1070—1096.

Knupp, K. R., 1985: *Precipitating convective cloud downdraft structure: A synthesis of observations and modeling.* PhD thesis, Colorado State University, Dep't of Atmospheric Science, Fort Collins, Co., 80523, 296.

Knupp, K. R., 1987: Downdrafts within High Plains cumulonimbi, Part I: General kinematic structure. *J. Atmos. Sci.*, **44**, 987—1008.

Konig, W. and E. Ruprecht, 1989: Effects of convective clouds on the large-scale vorticity budget. *Meteorol. Atmos. Phys.*, **41**, 213—229.

Kreitzberg, C. W. and D. J. Perkey, 1976: Release of potential instability: Part I. a sequential plume model within a hydrostatic primitiveequation model. *J. Atmos. Sci.*, **33**, 456—475.

Krishnamurti, T. N., M. Kanamitsu, R. Godbole, C. B. Chang, F. Carr, and J. Chow, 1976: Study of a monsoon depression (II), Dynamical structure. *J. Meteor. Soc. Japan*, **54**, 208—225.

Krishnamurti, T. N., Y. Ramanathan, H.-L. Pan, R. J. Pasch, and J. Molinari, 1980: Cumulus parameterization and rainfall rates I. *Mon. Wea. Rev.*, **108**, 465—472.

Krueger, S. K., 1988: Numerical simulation of tropical cumulus clouds and their interaction with the subcloud layer. *J. Atmos. Sci.*, **45**, 2221—2250.

Kuo, H. L., 1965: On the formation and intensification of tropical cyclones through latent heat release by cumulus convection. *J. Atmos. Sci.*, **22**, 40—63.

Kuo, H. L., 1974: Further studies of the parameterization of the influence of cumulus convection on large-scale flow. *J. Atmos. Sci.*, **31**, 1232—1240.

Lindzen, R. S., 1974: Wave-CISK in the tropics. *J. Atmos. Sci.*, **31**, 156—179.

Lumley, J. L., O. Zeman, and J. Siess, 1978: The influence of buoyancy on turbulent transport. *J. Fluid Mech.*, **84**, 581—597.

Manabe, S., J. Smagorinsky, and R. F. Strickler, 1965: Simulated climatology of a general circulation model with a hydrologic cycle. *Mon. Wea. Rev.*, **93**, 769—798.

Manton, M. J. and W. R. Cotton, 1977: Parameterizations of the atmospheric surface layer. *J. Atmos. Sci.*, **34**, 331—334.

Marwitz, J. D., 1972: Precipitation efficiency of thunderstorms on the High Plains. *J. Rech. Atmos.*, **6**, 367—370.

Mason, B. J., 1956: On the melting of hailstones. *Quart. J. Roy. Meteor. Soc.*, **82**, 209—216.

Mellor, G. L., 1973: Analytic prediction of the properties of stratified planetary surface layers. *J. Atmos. Sci.*, **30**, 1061—1069.

Mellor, G. L. and T. Yamada, 1974: A hierarchy of turbulence closure models for planetary boundary layers. *J. Atmos. Sci.*, **31**, 1791—1806.

Miller, L. J., J. D. Tuttle, and C. A. Knight, 1988: Airflow and hail growth in a severe northern High Plains supercell. *J. Atmos. Sci.*, **45**, 736—762.

Moeng, C.-H., 1984: A large-eddy-simulation model for the study of planetary boundary-layer turbulence. *J. Atmos. Sci.*, **41**, 2052—2062.

Moeng, C.-H., 1986: Large-eddy simulation of a stratus-topped boundary layer. Part I: Structure and budgets. *J. Atmos. Sci.*, **43**, 2886—2900.

Moeng, C.-H., 1987: Large-eddy simulation of a stratus-topped boundary layer. Part II: Implications for mixed-layer modeling. *J. Atmos. Sci.*, **44**, 1605—1614.

Moeng, C.-H. and A. Arakawa, 1980: A numerical study of a marine subtropical stratus cloud layer and its stability. *J. Atmos. Sci.*, **37**, 1661—2676.

Moeng, C.-H. and D. A. Randall, 1984: Problems in simulating the stratocumulus-topped boundary layer with a third-order closure model. *J. Atmos. Sci.*, **41**, 1588—1600.

Moeng, C.-H. and J. C. Wyngaard, 1984: Statistics of conservative scalars in the convective boundary layer. *J. Atmos. Sci.*, **41**, 3161—3169.

Molinari, J., 1985: A general form of kuo's cumulus parameterization. *Mon. Wea. Rev.*, **113**, 1411—1416.

Molinari, J. and T. Corsetti, 1985: Incorporation of cloud-scale and mesoscale downdrafts into a cumulus parameterization: Results of one- and three-dimensional integrations. *Mon. Wea. Rev.*, **113**, 485—501.

Moncrieff, M. W. and S. A. Green, 1972: The propagation and transfer properties of steady convective overturning in shear. *Quart. J. Roy. Meteor. Soc.*, **98**, 336—352.

Monin, A. S. and A. M. Obukhov, 1954: Basic laws of turbulent mixing in the atmosphere near the ground. *Akademiia Nauk SSSR*, **24**, 163—187.

Nicholls, M. E., R. A. Pielke, and W. R. Cotton, 1991a: A two-dimensional numerical investigation of the interaction between sea breezes and deep convection over the Florida peninsula. *Mon. Wea. Rev.*, **119**, 298—323.

Nicholls, M. E., R. A. Pielke, and W. R. Cotton, 1991b: Thermally forced gravity waves in an atmosphere at rest. *J. Atmos. Sci.*, accepted for publication.

Nicholls, M. E. and M. J. Weissbluth, 1988: A comparison of two-dimensional and quasi-three-dimensional simulations of a tropical squall line. *Mon. Wea. Rev.*, **116**, 2437—2452.

Ogura, Y. and C.-Y. J. Kao, 1987: Numerical simulation of a tropical mesoscale convective system using the Arakawa-Schubert cumulus parameterization. *J. Atmos. Sci.*, **44**, 2459—2476.

Ooyama, K. V., 1982: Conceptual evolution of the theory and modeling of the tropical cyclone. *J. Meteor. Soc. Japan*, **60**, 369—379.

Orlanski, I., 1986: Localized baroclinicity: A source for meso-α cyclones. *J. Atmos. Sci.*, **43**, 2857—2885.

Orlanski, I. and B. B. Ross, 1977: The circulation associated with a cold front. Part I: Dry case. *J. Atmos. Sci.*, **34**, 1619—1633.

Payne, S. W., 1981: The inclusion of moist downdraft effects in the arakawa-schubert cumulus parameterization. In *Preprint Volume: Fifth Conf. on Numerical Weather Prediction*, Amer. Meteor. Soc., Monterey, Calif., 277—284.

Raymond, D. J., 1975: A model for predicting the movement of continuously propagating convective storms. *J. Atmos. Sci.*, **32**, 1308—1317.

Raymond, D. J., 1976: Wave-CISK and convective mesosystems. *J. Atmos. Sci.*, **33**, 2392—2398.

Raymond, D. J., 1983: Wave-CISK in mass flux form. *J. Atmos. Sci.*, **40**, 2561—2572.

Raymond, D. J., 1984: A wave-CISK model of squall lines. *J. Atmos. Sci.*, **41**, 1946—1958.

Raymond, D. J., 1986: Prescribed heating of a stratified atmosphere as a model for moist convection. *J. Atmos. Sci.*, **43**, 1101—1111.

Rosenthal, S. L., 1979: The sensitivity of simulated hurricane development to cumulus parameterization details. *Mon. Wea. Rev.*, **107**, 193—197.

Rutledge, S. A. and J. Houze, R. A., 1987: A diagnostic modeling study of the trailing stratiform region of a midlatitude squall line. *J. Atmos. Sci.*, **44**, 2640—2656.

Schlesinger, R. E., 1990: Feedback of deep moist convection to its near environment as dignosed from three-dimensional numerical model output: Results from an early experiment. *J. Atmos. Sci.*, **47**, 1390—1412.

Shapiro, L. J. and H. E. Willoughby, 1982: The response of balanced hurricanes to local sources of heat and momentum. *J. Atmos. Sci.*, **39**, 378—394.

Sommeria, G., 1976: Three-dimensional simulation of turbulent processes in an undisturbed trade wind boundary layer. *J. Atmos. Sci.*, **33**, 216—241.

Soong, S.-T. and Y. Ogura, 1980: Response of tradewind cumuli to large-scale processes. *J. Atmos. Sci.*, **37**, 2035—2050.

Soong, S.-T. and W.-K. Tao, 1984: A numerical study of the vertical transport of momentum in a tropical rainband. *J. Atmos. Sci.*, **41**, 1049—1061.

Sun, W.-Y. and Y. Ogura, 1980: Modeling the evolution of the convective planetary boundary layer. *J. Atmos. Sci.*, **37**, 1558—1572.

Tremback, C. J., 1990: *Numerical simulation of a mesoscale convective complex: Model development and numerical results.* PhD thesis, Colorado State University, Dep't of Atmospheric Science, Fort Collins, Co. 80523, 247.

Tripoli, G. J. and W. R. Cotton, 1981: The use of ice-liquid water potential temperature as a thermodynamic variable in deep atmospheric models. *Mon. Wea. Rev.*, **109**, 1094—1102.

Tripoli, G. J. and W. R. Cotton, 1982: The Colorado State University three-dimensional cloud/mesoscale model—1982. Part I: General theoretical framework and sensitivity experiments. *J. Rech. Atmos.*, **16**, 185—220.

Tripoli, G. J. and W. R. Cotton, 1989: Numerical study of an observed orogenic mesoscale convective system. Part 2: Analyis of governing dynamics. *Mon. Wea. Rev.*, **117**, 305—328.

Weisman, M. L. and J. B. Klemp, 1982: The dependence of numerically simulated convective storms on vertical wind shear and buoyancy. *Mon. Wea. Rev.*, **110**, 504—520.

Zeman, O. and J. L. Lumley, 1976: Modeling buoyancy driven mixed layers. *J. Atmos. Sci.*, **33**, 1974—1988.

Zeman, O. and H. Tennekes, 1975: A self-contained model for the pressure terms in the turbulent stress equations of the neutral atmospheric boundary layer. *J. Atmos. Sci.*, **32**, 1808—1813.

Zipser, E. J. and M. A. LeMone, 1980: Cumulonimbus vertical velocity events in GATE. Part II: Synthesis and model core structure. *J. Atmos. Sci.*, **37**, 2458—2469.